BEDFORM MIGRATION AND ASSOCIATED SAND TRANSPORT ON A BANNER BANK: APPLICATION OF REPETITIVE MULTIBEAM SURVEYING AND TIDAL CURRENT MEASUREMENT TO THE ESTIMATION OF SEDIMENT TRANSPORT

GARRET PATRICK DUFFY

March 2006

BEDFORM MIGRATION AND ASSOCIATED SAND TRANSPORT ON A BANNER BANK: APPLICATION OF REPETITIVE MULTIBEAM SURVEYING AND TIDAL CURRENT MEASUREMENT TO THE ESTIMATION OF SEDIMENT TRANSPORT

Garret Patrick Duffy

Department of Geodesy and Geomatics Engineering
University of New Brunswick
P.O. Box 4400
Fredericton, N.B.
Canada
E3B 5A3

March 2006

PREFACE

This technical report is a reproduction of a dissertation submitted in partial fulfillment of the requirements for the degree of Doctor of Philosophy in the Department of Geodesy and Geomatics Engineering, March 2006. The research was supervised by Dr. John Hughes Clarke.

As with any copyrighted material, permission to reprint or quote extensively from this report must be received from the author. The citation to this work should appear as follows:

Duffy, G. P. (2006). *Bedform Migration and Associated Sand Transport on a Banner Bank: Application of Repetitive Multibeam Surveying and Tidal Current Measurement to the Estimation of Sediment Transport.* Ph.D. dissertation, Department of Geodesy and Geomatics Engineering, Technical Report No. 237, University of New Brunswick, Fredericton, New Brunswick, Canada, 228 pp.

ABSTRACT

A new integrated method of measuring bedload transport using repetitive multibeam surveys of a sand bank in Mispec Bay, Saint John, NB, has been developed. Migration rate and morphometric parameters, all derived from the bathymetric dataset, are used to calculate net sediment transport that is expressed as migrating bedforms. This bedform associated sediment transport value was tested for validity by combining observed median grain size and observed hydrodynamic data from one of three M2 tidal current measurement cycles, the latter initially conducted to investigate the nature of the current field in Mispec Bay. The maximum bedform associated bedload transport value of 30 kg/m/tide falls in the range predicted by a pre-existing sediment transport model of the area. At the least, the bedform associated bedload transport value is a good lower estimator of bedload transport. This is because of the unknown component of bedload not expressed in bedform migration.

A conceptual model for the formation and maintenance of the Cape Spencer sand bodies has been proposed. Comparison of observed hydrodynamic data with pre-existing hydrodynamic and sedimentary models of headland localities reveals that the asymmetric coastline of Cape Spencer has an impact on its local current field and consequently sand bank development. With respect to ebbing currents, the coastline of Cape Spencer has an elliptical aspect ratio greater then the threshold necessary to advect a major tidal eddy in Mispec Bay. Thus, the tidal eddy advected in Mispec Bay locally induces major tidal asymmetry, with a line of net bedload reversal, inferred from hydrodynamic observations, separating the flood dominated and ebb dominated regions. Mispec bank has built up inshore of this line and sediment is continually advected from its tip, where there is an

increasing net sediment transport rate; a portion of this sediment ends up being redeposited on the distal end of the bank only to be recirculated around the bank. Given the static nature of the overall bathymetry of Mispec Bank, a steady state recirculation appears to maintain the bank. In contrast, for opposing flood currents the elliptical aspect ratio is less than the eddy advection threshold to the east so a major eddy is not advected on this tidal phase. The lack of an advected tidal eddy dictates less tidal asymmetry on the east side of Cape Spencer and thus the sand bank there occurs as a stretched sand sheet with much lower thickness than the Mispec Bank.

TABLE OF CONTENTS

LIST OF FIGURES

C h a p t e r   1 :   I n t r o d u c t i o n

1.1.   Opening Statement

The observable phenomenon of the transport of matter along and above the sediment-water interface ("sediment transport") depends on two fundamental components: the hydrodynamics of the water column and the properties of the sediment. Direct field measurement of sediment transport by suspension now appears to be logistically practical using optical and acoustic sensors [*Huntley and Hanes*, 1987; *Hanes et al.*, 1988] whereas direct field measurement of bedload transport by sediment traps, especially in a marine environment, is often logistically difficult [*Huntley et al.*, 1991]. Over the years, laboratory studies comparing the controlled quantities of hydrodynamics and sediment properties with the resultant measured (by means of sediment traps) bedload transport rate have resulted in a number of empirical formulations of bedload transport rate. Workers employ these mathematical predictors using hydrodynamic measurements and measurements of bottom sediment to estimate bedload transport.

Sediment transported at the seabed as bedload often expresses itself morphologically as measurable migrating sand dunes or ripples[*]. Naturally, if these dynamic bedforms can be remotely sensed, this presents an opportunity to measure bedload transport without the necessity to use sediment traps [*Engel and Lau*, 1980; *Van den Berg*, 1987]. Remotely sensing the migration rate of sand dunes, in order to estimate the bedload transport, has been done by many workers with different approaches over the years. In the early 1980's,

---

[*] From hereon, all bedforms will be referred to as "dunes". In this thesis, this morphologic term is favoured above other genetic or metric terms for reasons of clarity.

because of uncertainty in marine positioning, *Langhorne* [1982] carried out repetitive

direct measurements of a staked cross-section of a dune using divers instead of using

repetitive ship-based single beam or side-scan measurements. This dataset, although

highly temporally and spatially accurate, was also highly localized and did not give any

information about the larger scale migration regime. Other workers have used single

beam echosounders, to assess migration rates [*Simons et al.*, 1965; *Engel and Lau*, 1980;

Jinchi, 1992; *Ten Brinke et al.*, 1999; *Knaapen*, 2004]. This approach is subject to (for old

archived data) positional inaccuracies and such one dimensional measurements of crest

migration are subject to errors due to the unknown orientation of the crest-line. Figure 1.1

illustrates the potential over-estimate of crest-line displacement arising from using a

single-beam echosounder. Of course, single-beam echosounder lines are usually run

closely spaced and in parallel enabling estimation of the crest-line orientation and

adjustment of the displacement estimate. Still other workers have used sidescan sonar

[*Van den Berg*, 1987] and stationary bottom photography [*Wilkinson et al.*, 1985; *Huntley

et al.*, 1991] to assess migration rates. Sidescan sonar has absolute position accuracy

issues, so is unreliable for repeated observations in the absence of stationary bottom

features for registration. Bottom photography, although highly precise in a local

coordinate system, is limited to closely spaced bedforms.

Figure 1.1 Illustration of over-estimate of crest displacement resulting from surveying a sand dune twice.
The track line is the dotted line and the positions of the crest at times t_1 and t_2 are indicated. A better estimate
based on tracking the morphology of the crest-line is represented by the solid arrow.

The most recent advance in bedform remote sensing is the use of multibeam echosounders. A multibeam echosounder that can provide near continuous coverage of bottom topography together with a GPS system at least as precise as the smallest beam footprint, is potentially the optimal data collection system for measuring sand dune migration. The two main sources of uncertainty, namely position and the orientation of the crest, are minimised with this measurement system. Knowledge of migration rate together with bedform height, all derived from multibeam data, theoretically enable the calculation of sediment transported within the migrating bedforms or "bedload transport".

This thesis will test the primary hypothesis that: "Repetitive multibeam surveying may be used to assess bedload transport rate in a tidal environment". A secondary objective of this work, arising from the primary hypothesis, is to test or modify existing models of headland associated sand banks for applicability to the study area. These objectives were arrived at by executing a multi-disciplinary data collection field program over a prominent sand dune covered sand bank in Mispec Bay, New Brunswick. Morphometric parameters of the migrating dunes were combined with migration velocity information (elucidated by cross-correlating serial multibeam surveys) to estimate bedform-associated sediment transport. In addition, tidal currents were measured over the sand bank and used as a basis to predict the variation of hydrodynamic sediment transport over the field area. This in turn was compared with results from general mathematical and conceptual models of the variation of sediment transport in the vicinity of a headland.

1.2. Motivation

The main motivation of this work is to use time-lapsed multibeam bathymetric data as a source of dynamic data, in this case bedload transport, rather than just a series of singular "static" passive datasets. Whereas subtracting bathymetric DTMs provides a direct representation of the volumetric change of the seabed, the accuracy of this technique is subject to tidal errors or long period heave artifacts both of which can affect the difference DTM. An alternative 2D dune tracking technique that will be proposed in this thesis is for use in repeat survey operations that employ accurate 2D positioning, for example, code DGPS. Only accurate 2D positioning is necessary, making this technique widely applicable to many repeat survey operations. Accurate, but at present logistically difficult, 3D positioning such as that afforded by real-time kinematic GPS is not necessary for the performance of the proposed technique.

The technique proposed in this thesis will have two main "products": (1) bedform migration vector field and (2) an image describing observed bedload transport.

1. Bedform Migration Vector Field

The bedform migration field is an important dataset that describes the dynamic behaviour of bedforms and can be used to answer questions concerning the behaviour of bedforms in a non uniform flow field [*Rubin and Hunter*, 1985; *Rubin and Hunter*, 1987; *Rubin*, 1998] and questions concerning the spatial variability of migration rate.

2. Observed Bedload Transport

Observed bedload transport rate can be used to calibrate and check mathematical models of sediment transport rate that are used to predict impacts of coastal engineering installations. For example, knowledge of bedload transport rate in Mispec Bay could be of use to engineers installing the proposed new wharf adjacent to Irving Canaport off Black Head, as long as one recognises that bedform associated bedload transport figure represents a lower limit on total sediment transport due the unaccounted for suspension and traction carpet components.

In addition, given a region of known sediment transport rate, we can predict how pollutants (only those that act as bedload particulates however), such as those from urban sewage outfalls or dredging spoils, will be dispersed.

1.3. Physical Setting of the Mispec Bank

Mispec Bay is the body of water that lies between the headlands of Mispec Point and Cape Spencer and is located 11 km south-east of the city of Saint John, New Brunswick. Mispec Bay is especially open to wind and waves with directions from the east to the south-west inclusive since winds from all other directions come off the land from where there is insufficient fetch to generate any waves of consequence.

The rocks around Mispec Bay fall into two categories, one of them faulted against the other. The promontories of Mispec Point and Cape Spencer are comprised of one or other of these rock types and this difference in composition is expressed in their geomorphology. Mispec Point is composed of the Pennsylvanian (320 Ma) aged Balls

Lake Formation of red conglomerate, sandstone, siltstone and shale. Its easily eroded

lithology is reflected in the symmetrical hyperboloidal coastline of Mispec Point. Such a

shape is typical of headlands composed of massive, easily eroded litholgies.
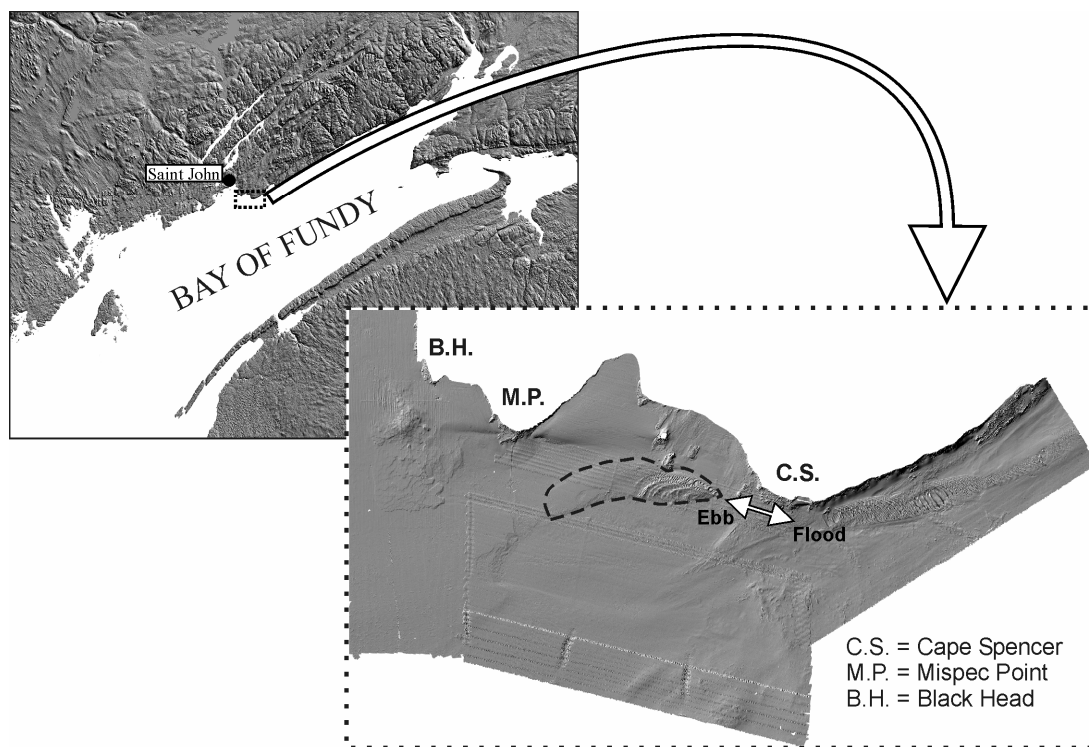
Figure 1.2 Overview of study area in relation to Bay of Fundy (top left). Mispec Bank is denoted by the dashed line above. Ebb and flood current directions are also indicated. Shaded relief data are from Geological Survey of Canada cruises in 2000 and 2001 and were compiled by Ian Church (Ocean Mapping Group).

In contrast to Mispec Point, the asymmetrical Cape Spencer and its coastline to the

west is composed of a much older (Cambrian (550 Ma) and Pre-Cambrian) and more

resistant complex of intrusive and sedimentary rocks. These rocks are separated from the

rocks of Mispec Point by a major northeast-southwest trending fault. The geomorphology

of Cape Spencer reflects the more resistant lithological composition. It is readily seen that

Cape Spencer is markedly more convex on it eastern side because of the existence of more

resistant rocks.

The asymmetry of Cape Spencer has an impact on the formation of tide induced transient eddies attached to the headland and consequently an impact upon sedimentation around Cape Spencer. This will be discussed further later.

The bathymetry of Mispec Bay consists of two topographic elements, one superimposed upon the other. The first element, regarded as the 'background' topography is a typical 'profile of equilibrium' [*Duff*, 1994] that consists of a flat shallow (5 – 15 m below chart datum) part that drops to 40 m within a kilometre. The second element is a sand bank, which is a positive topographic feature formed by deposition. It is superimposed upon the profile of equilibrium in water depths greater than 20 m below chart datum and, on the basis of contour interpolation, is estimated to be eight metres thick at its thickest point (and shallowest point, at 22 m below chart datum). In plan view it is a boomerang-shaped feature only half of which, of rough dimension 2.5 by 1 km, closest to the headland is possessed of actively migrating sand dunes. The remainder of the banner bank is featureless and apparently moribund. The seaward edge of the sand bank sharply terminates forming a well defined continuous delineation between the sediments of the sand bank and the sea floor. The landward edge of the sand bank is more gradual and nebulous with discontinuous 30 cm high ripples persisting landward of the sand bank.

Mispec Bay, being in the Bay of Fundy, experiences a large diurnal tide range of 5 metres (neaps) and 8.5 metres (springs). Therefore, water depth over the shallowest point ranges between 24 and 29 m during a neap tide and 22.5 and 31 metres during a spring tide. The highest predicted tidal current in the Saint John Harbour and Approaches region is 1.4 m/s adjacent to Cape Spencer on the Bay of Fundy side for the spring flood and ebb tide [*Li et al.*, 2003].

The migrating bedforms on the active part of Mispec Bank, the subject of this dissertation, change in morphology moving towards the headland. The facing directions of all the active bedforms indicate net sediment transport towards the tip of the headland Cape Spencer. Within the 'tail' of the sand bank and along the seaward slope of the sand bank in the deep water, maximum dune height is 40 cm with a typical spacing of 10 m, these dunes also are markedly asymmetric with facing directions towards the headland. More sinuous, higher and longer dunes become more dominant towards the shallower part of the sand bank where maximum height and spacing grow to 3.5 m and 50 m respectively. Along the landward edge of the sand bank, closest to Cape Spencer, there is a broad (100 m wide) shallow (2.5 m deep) channel in base of which discontinuous ripples and lunate megaripples (15 – 20 m spacing) are found with facing directions which are parallel to the channel and towards the sand bank tip.

1.4.   Methodology

The Mispec Bay banner bank was selected as an ideal field area for this research. Four previous Geological Survey of Canada cruises in 2000 and 2001 showed that there were actively migrating sand dunes. Bedrock was also present, which was necessary to confirm registration between surveys. Logistically, it was the best expressed bedform field within a reasonable daily operational distance from the port of Saint John.

To resolve the net migration of the sand dunes, six Simrad EM-3000 multibeam surveys were carried out over the sand bank from April to September in 2002. To resolve detectable migration during a tidal cycle, a single multibeam survey was also carried out during a tidal current measurement epoch on 4th October 2002. During this survey, the

same patch of seafloor was surveyed approximately every 30 minutes. The sequential surveys were processed and compared in order to derive the migration measurements, which were combined dune height and form factor information to estimate the bedform-related bedload transport rate. A suite of computer programs were written to achieve these goals.

It is important to emphasise that since bedform associated bedload is based on net tidal displacement of a bedform, the bedload estimate is theoretically a *tidally averaged* bedload estimate. In order to test the primary hypothesis that repetitive multibeam surveying may be applied to the measurement of sediment transport rate, at least one other independent measurement of sediment transport rate needs to be made as a check on the multibeam tidally averaged rate. No direct measurements (sediment traps) of active sediment transport have been made so only indirect measurements have been possible. One utilises mathematical expressions [*Van den Berg*, 1987; *Madsen*, 1991; *Nielsen*, 1992 comprise the expressions used in this thesis] of current and grain size to predict instantaneous bedload transport rate. This calculated instantaneous bedload transport rate (using observed currents and grain size) is then integrated over a tidal cycle to yield the predicted net sediment transport rate. Another is based on the spatial distribution of grain size parameters [*McLaren*, 1981; *McLaren and Bowles*, 1985; *Gao and Collins*, 1991; *McLaren and Bowles*, 1991; *McLaren et al.*, 1993; *Vanwesenbeeck and Lanckneus*, 2000]. It was proposed initially by *McLaren* [1981] that systematic spatial variation of grain size, sorting and skewness indicated sediment transport direction. Even though this method only gives information of sediment transport direction (not magnitude), it is still a useful way to check the repetitive multibeam method.

A multi-disciplinary approach combining the distinct fields of hydrography, current measurement and ground-truthing has therefore been taken and various techniques have been developed in this thesis to process and integrate the data.

1.5. Thesis Outline

This thesis will devote a chapter to the acquisition, processing and interpretation of each data type: multibeam sonar, hydrodynamics and ground-truthing. Then there will be two chapters concerning the two main techniques developed in this work: bedform migration measurement and the estimation of bedform associated sediment transport. The final chapter will discuss the sedimentary processes maintaining the sand bank, discovered from the repeat surveys.

Chapter 2: Multibeam System and Survey Results

This chapter will describe the acquisition method, sensor integration and post-processing of the primary dataset of this research, namely the six consecutive bathymetric surveys of the banner bank. An overview will be given of the specifications of the Simrad EM3000 multibeam and the various ancillary sensors used for surveying.

Factors influencing the resolution of the digital terrain models will be described together with how the data was reduced for gridding. Accuracy estimation by means of cross-line analysis will also be described.

How the surveys were designed for optimal spatial and temporal resolution of the dunes will be described and also the processing steps required to create accurate digital terrain models.

2.1. Survey Equipment

CSL *Heron* was a state-of-the-art 34ft survey launch fully equipped with a wide array of hydrographic, geophysical and oceanographic equipment. She was owned by the Canadian Hydrographic Service (CHS) and was on a 10 year loan to the Ocean Mapping Group at the University of New Brunswick (UNB). The loan was part of a Joint Partnership Agreement between the CHS and UNB. She was provided for the purposes of conducting Ocean Mapping related research and training. An accident on 29th July 2005 in Quebec City resulted in her untimely demise. However, at time of writing there are plans for *Heron mk. II* to be working in 2006.

These surveys were carried out early in *Heron*'s career as an Ocean Mapping Group vessel, before there was a permanent integrated survey system. A motion sensor, Motion Reference Unit ("MRU-6"), and the Simrad multibeam were the only fixed equipment during the survey period. Other ancillary sensors were available for short trial periods only. The result of this was that each of the surveys had different survey equipment; this was especially prevalent for the measurement of attitude and heading. The configuration of *Heron*'s ancillary sensors is given in Table 2.1.

Table 2.1 Ancillary Sensors used on Heron, April to September 2002.

Survey	"April" 23/4, 24/4	"May" 18/5	"June" 30/6	"July" 1/8	"August" 27/8	"September" 2/10, 3/10
GPS	DGPS	DGPS	DGPS	DGPS	DGPS	DGPS
Attitude	Seapath 200 RTK (incl. MRU-5)	Seapath 200 RTK (incl. MRU-5)				
	MRU-6[*]	MRU-6[*]	MRU-6[*]	MRU-6	MRU-6	MRU-6
					POS-MV 320	POS-MV 320
Heading	Seapath 200 RTK	Seapath 200 RTK				
			Gyro-compass	Gyro-compass	Gyro-compass	Gyro-compass
					POS-MV 320	POS-MV 320

[*]Not speed and heading aided

2.1.1. Motion Sensors

On a dynamic surveying platform such as *Heron*, continuous measurements of the heave and attitude (roll, pitch and heading) of the vessel must be fed into the multibeam so that the position and depth of the measured sounding reflects accurately the true (vessel relative) position and depth of that point so that the final produced DTM will be free of motion artifacts.

2.1.1.1   MRU-6

This motion sensor is manufactured by Kongsberg Seatex and is capable of measuring roll, pitch, heave (by means of a triaxial accelerometer and triaxial gyro) and heading (by means of a triaxial fluxgate compass). It was located as close as possible to where the measurements where going to be applied, i.e. the multibeam, and was 30 cm above the transducer. The functioning of the MRU's magnetic compass was compromised by its proximity (15 cm) to the spinning metal flywheel of the ship's motor so this was disabled. The MRU was therefore employed as a motion sensor only; heading was input from another source.

When operated with ancillary speed and heading aiding, the MRU-6 has a stated roll and pitch measurement accuracy of $\pm\, 0.05°$ (rms) and a stated heave accuracy of $\pm\, 5$ cm (rms) within a heave period range of 0 to 25 s. It is a high-grade motion sensor and is specially designed for high precision motion measurements in marine applications. Importantly, it can output high frequency 100 Hz attitude data directly into the Simrad processing unit. In the absence of external aiding, it employs a Vertical Gyro Algorithm (VGA) to locate the vertical reference axis around which roll, heading and heave are measured. Without velocity aiding from a GPS VTG string (as was the case for the April,

May and June surveys), especially relevant when the vessel is cornering, the VGA outputs a heave and roll artifact because of the addition of a turning centrifugal force which distorts the vertical reference axis. This meant that special post-processing had to be done at the start of lines to eliminate the heave artifact (see later Section 2.4).

During data acquisition, the MRU-6 was supplied with heading from a 1 Hz magnetic compass situated in the cockpit and away from any electromagnetic noise. For the April, May and June surveys, a course over ground (COG) string was supplied to the MRU-6 instead of a velocity string but this still helped prevent heave anomalies after turning.

An MRU can also be used as a component of an aided inertial navigation system, the Simrad Seapath 200RTK system, which has an MRU-5 with no internal magnetic compass since it is not required for heading. In the Simrad Seapath 200RTK system, attitude data is blended with heading and speed data derived from a pair of dual-frequency GPS antennas in order to derive high accuracy heading, attitude and heave (this latter set-up was used for the April and May surveys). Speed and heading aiding ensure that distortion of the vertical does not happen when cornering so heave and roll anomalies are eliminated. One of the GPS antennas may be supplied with DGPS-RTK corrections for high accuracy positioning and heave measurements even when the vessel is turning. The Seapath 200-RTK comes with its own GPS base station and radio antenna to transmit RTK corrections. A Seapath 200 base station was erected for some of the surveys but its radio link was intermittent in real time so the data quality was poor.

2.1.1.2   POS-MV 320

This instrument was manufactured by Applanix (now Trimble). It is another "total measurement" solution instrument that measures position, attitude and heading and is a rival to the Seapath 200/200RTK instrument. It was used on loan from Applanix and was used for the August and September surveys, mainly for testing and comparison with the MRU-6, which is the default motion sensor on *Heron*. The POS-MV320 comes with twin dual-frequency GPS antennas and thus can output heading (derived by calculating the azimuth between the GPS antennas) already. This GPS heading is inertially smoothed through its inertial measurement system.

2.1.1.3   Heading Sensors

Three different sensor types were used to measure the heading of the vessel: (a) GPS (accuracy ~0.10-0.05° (rms)); (b) magnetic compass (accuracy ~1.0-2.0° (rms)) and (c) gyrocompass (accuracy ~0.50-0.75° (rms)).

GPS derived heading is given by the Seapath and POS systems and its accuracy far exceeds that necessary for hydrographic survey (typically 0.5 – 1.0°). However the POS-MV heading, which utilises a GPS Azimuth Measurement System (GAMS), was found to be unreliable and prone to failure. The POS-MV input its heading into the Simrad but when its GAMS heading solution was used to merge attitude and construct a DTM, there was an obvious heading bias evinced by dune crest misalignment. Other users (CHS Atlantic) of POS-MV have encountered this problem with the GAMS solution.

Typically, either a stand-alone magnetic compass or a gyrocompass was used to input heading into the MRU-6. The 1 Hz heading string input into the MRU was inertially smoothed by the 100 Hz angular rate of change data about an absolute vertical axis logged

by the MRU. This angular rate of change data, which is insensitive to turning, is used to adjust the input heading, which *is* subject to biases when turning. The heading then outputted at 100 Hz by the MRU is thus a "blended" heading solution and is not subject to turning errors.

2.1.2. Global Positioning System

Measurements of position are necessary so the absolute position of the sounding is as accurate as possible. One of the initial aims of this research was to test the use of RTK navigation in measuring crest displacements. However, the RTK-GPS system of a base station set up at the Irving Canaport and a rover installed on Heron proved quite troublesome and prone to failure. Therefore, the planned RTK project was taken no further.

Instead, Canadian Coastguard DGPS was used that received differential corrections from the nearby Partridge Island beacon transmitter. In order to assign accurate horizontal positions to the soundings, a lever arm correction had to be applied in post-processing to translate the position measured by the DGPS antenna (which was input directly as a GPGGA string into the Simrad Processing unit) to the transducer face.

2.1.3. Multibeam Echosounder

Specifications of the Simrad EM3000S multibeam follow.

- Mills cross array of two orthogonal line arrays of transducers
- Nominal Centre Frequency: 300 kHz
- Number of beams: 127
- Min-max depth: 0.5-150 m

- Pulse length: 0.05 ms continuous wave (CW) pulse and receive bandwidths of 4 to 8 kHz

- Beam geometry:

    Transmit beamwidth: 1.5° along track and 120° across track,

    Receive beamwidth: 30° along track and 1.5° across track

    Total effective beamwidth (intersection of transmit and receive cones): 1.5° x 1.5° but the across-track receive beamwidth grows with the secant of the steering angle relative to the transducer (1.5°*sec[steering angle]), e.g. at 60° from the vertical would produce a receive beam width of 3°, whereas at nadir, the receive beamwidth would be 1.5°. This means that the across-track dimension of the beam footprint increases dramatically across-track, while the along-track dimension increases only slightly, so the spatial resolution of a single beam decreases further away from nadir.

- Angular beam spacing: increases angularly away from nadir with the secant of the beam steering angle (0.9°*sec[steering angle]). At nadir, beam spacing is 0.9°, and at 60°, the spacing is 1.8° apart. Therefore, there is considerable across-track overlap of beams, ensuring good depth resolution across-track. However, this across-track overlap condition comes at the expense of sounding density away from nadir, meaning that soundings are very dense at nadir but not so away from nadir.

- Pitch stabilised

‒ Not roll stabilised, but in calm conditions (less than 5° of roll), the beam

 sector is extended to the full ±65°, however if there is greater than 5° of

 roll, a narrower sector of ±60° is used instead.

‒ Ping rates: generally 4-5 Hz in the water depths encountered in this study.

A description of the resolution and accuracy of the EM3000 is given in Section 2.3.1.

2.1.4. Sound Speed Sensor

An Applied Microsystems Ltd. (AML) Conductivity-Temperature-Depth (CTD)

sensor housed in a Brooke Ocean towbody was used to measure the salinity and

temperature of the water column. These measurements, together with the depth were then

used to calculate (in software, using accepted empirical formulae) the sound speed in

water so that refraction-of-sound effects were mitigated. *Heron* was not equipped with a

free-fall winch at this time so CTD 'dips' were taken while the vessel was stationary.

Calculated sound speed profiles were input into the Simrad processing unit so that that

profile would be used for refraction corrections from that point on. Inspection of

multibeam swaths for refraction artifacts during acquisition confirmed that this "dip and

run" method was sufficient to account for refraction so post-processing was therefore not

necessary with the exception of the June survey when an old sound speed profile was

used. This was remedied by remerging the correct sound speed profile using code

developed by Jonathan Beaudoin (Ocean Mapping Group), *newMergeAtt*.

2.1.5. Tide Gauge

The Canadian Hydrographic Service operated tide gauge at Saint John was used for

tidal reduction of soundings. 15 minute ASCII data were downloaded via modem at UNB

and then reformatted so that they could be merged into the observed sounding depths.

Cross-line analysis was carried out to see what phase and amplitude errors, if any, were incurred by extrapolating the observed water level to the field site 10 km away.

2.2. Survey Planning and Acquisition

In this research, the purpose of surveying was to construct DTMs that reflected the true bathymetry and morphology as accurately as possible. Positional accuracy, coverage and sounding density are the main factors that decide whether the DTM produced is the best possible for a given multibeam sonar with a given angular beam spacing and these factors are determined by line spacing and vessel speed. As stated in Section 2.1.3, the EM3000 sounding density and spatial resolution is strongly nadir biased so line spacing must be chosen so that the dense nadir soundings of a line overlap the lower density soundings of an adjacent line. The degree of overlap should be at least 50%; to cause the depth of an area of seafloor to be sampled by soundings from at least two adjacent lines. An error in the Simrad hardware (remedied in 2003) had two consequences: (a) when *Heron* was rolling heavily a "pinched" swath width of roughly twice, instead of potentially 3.4 times the water depth was achieved; and (b) highest ping rates were limited to 4 Hz (in the shallowest and deepest parts of the field area). Ping rates of 7 Hz should be achievable in the shallowest part of the field area but this was not possible.
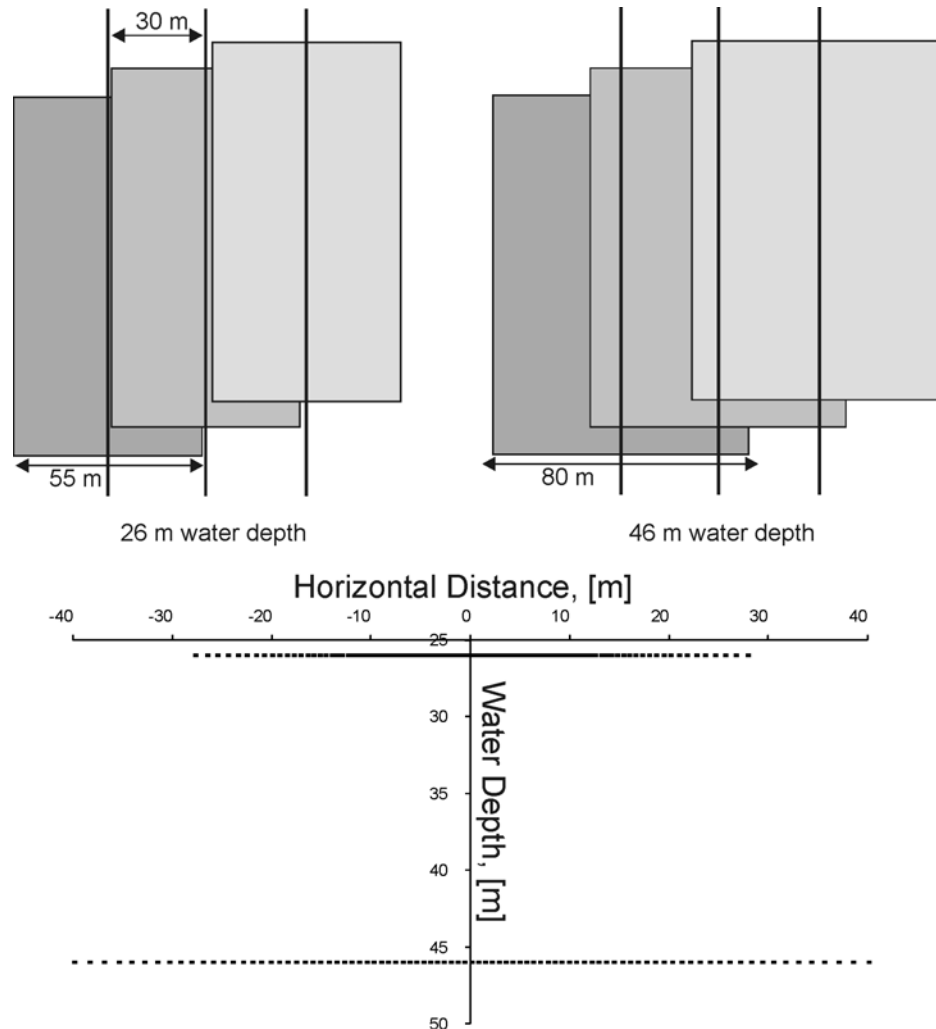
Figure 2.1 (TOP) Illustration of change in overlap water depth if the same line spacing is maintained into deeper water. (BOTTOM) Illustration of theoretical change in sounding density with different water depths.

For these reasons, a close line spacing of 30 m was deemed more then sufficient to achieve 50% overlap in the shallowest part of the sand bank (Figure 2.1). Given the narrow depth range of 26 m to 46 m (taking into account average tide range of 6 m) and the small extent of the field area, it was considered reasonable to extend this line spacing into the deeper water rather than increasing the line spacing into the deeper water (Figure 2.1 shows that by running lines in this fashion, greater than 50% overlap is achieved in water depths greater than 30 m).

Average vessel speed was kept at the normal survey speed of 10.5 kts. This meant that for on average 17 survey lines 4 km in length, survey time was typically 7 – 8 hours duration, including one hour transit time. At depths shallower than 40 m, the limited ping rate had a detrimental effect on along track coverage (Figure 2.2) because swath spacing is fixed (to 4 Hz instead of a maximum of 25 Hz) and depth invariant. This effect is worst at nadir where along-track swath coverage at nadir ranged from 50% in shallow water to 80% in deeper water (Figure 2.2(left)) because the beam footprints are smallest here. In contrast, the effect lessens across track where beam dimensions become larger and coverage ranges from over 70% in shallow water to over 100% in deeper water (Figure 2.2(right)). The considerable across track overlap between adjacent lines made up for this shortcoming somewhat, increasing the overall sounding density.
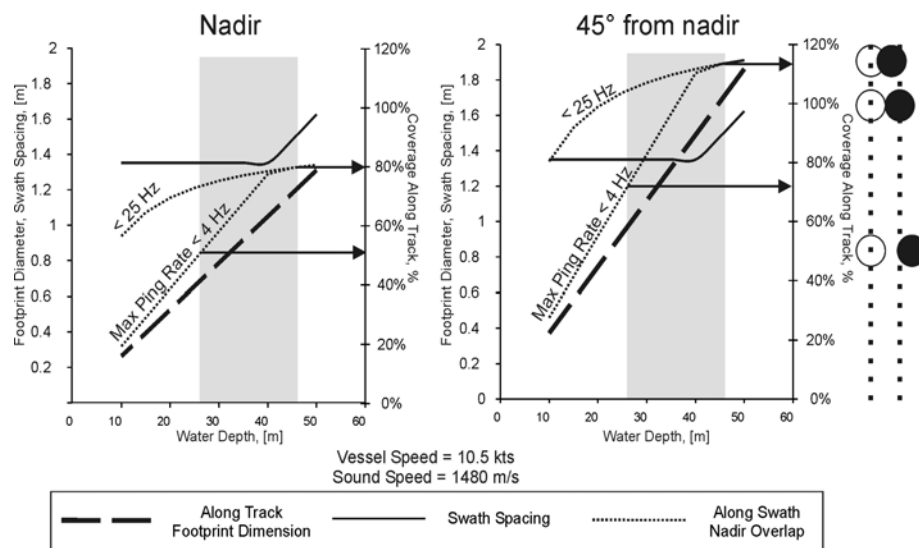
Figure 2.2 Effect on limited ping frequency on inter swath overlap (denoted by the straight diagonal dotted line). (LEFT) Nadir along track overlap; (RIGHT) along track overlap at 45° from nadir. The grey rectangle and the horizontal arrows denote the range in along track overlap over the depth of the study area. Also shown on the right is a definition sketch of along track coverage.

2.2.1. Survey Practice

Most of the surveys adhered to the design specifications outlined in the last section. However, in the May survey, dense concentrations of buoys attached to lobster pots forced

the skipper to ignore the survey line plan and instead carry out this survey 'free-hand'. He

attempted to steer lines so that the nadir beam of successive survey lines just touched the

outermost beams of the previous line. Therefore, the line spacing was not the 30 m as

planned but 50% overlap throughout was still achieved (as opposed to increased overlap in

deeper water if the survey plan was followed) running lines in this in this fashion. Figure

2.3 illustrates the difference in the configuration of survey line layout.
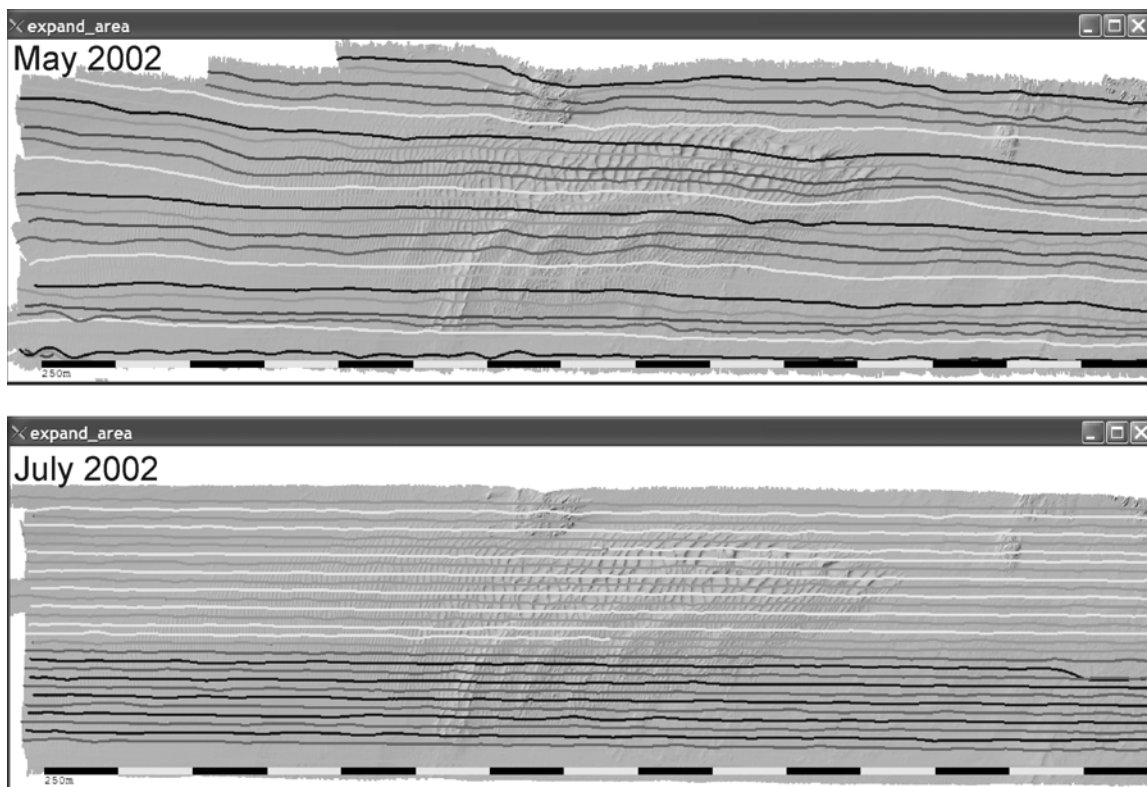
Figure 2.3 Figure Illustration of difference between 'free-hand' line running of May survey and line running according to the line plan (July survey shown for contrast).

To mitigate against refraction artifacts, the geometry of the swath was monitored as

the multibeam was running to see if 'frowns' or 'smiles' were occurring. The water

column in the field area was typically vertically homogenous in terms of sound speed so

usually only one or two CTD dips were necessary.

2.3. Processing

All the steps of multibeam data processing were carried out using Ocean Mapping Group's in-house developed suite of software, *SwathEd*, developed and written by Dr. John Hughes Clarke.

2.3.1. Gridding

After cleaning the soundings of outliers, merging the tide correction and geo-referencing the sounding positions, the soundings were gridded using *weighgrid*, a component of the *SwathEd* suite.

In terms of survey resolution, the footprint area of each sounding places a limit on the depth resolution of the individual sounding. As can be seen in Table 2.2 a single nadir sounding is returned for a circular area of diameter of roughly 65 cm in 26 m of water and 100 cm in 46 m of water [*Hare*, 1995] (this depth range defines the sand bank). The equivalent values for the elliptical footprints at 45° away from nadir, with footprints become increasingly eccentric away from nadir, are: in 26 m of water, 100 cm along-track by 200 cm across-track and in 46 m, 170 cm along-track by 350 cm across-track. This is satisfactory resolution for studying the bedforms in this area that have larger dimensions than this resolution [*Hughes-Clarke*, 1998] (the smallest spacing of dunes resolved in 40 m depth is 10 m).

Table 2.2 Geometrical parameters of the Simrad EM-3000, which has 127 beams with a nadir beamwidth of 1.5° by 1.5°. Depths depicted are typical of the sand bank. The beam footprints are spaced within a swath so that they overlap each other across-track by 50%. The values in the penultimate row of the table are the number of soundings per square metre if there was no overlap between the lines. The values in the last row are measured using *SwathEd* using actual data showing the distribution of soundings.

	26	46
Water Depth, [m]	26	46
Vessel Speed Over Ground [kts]	10.5	10.5
Ping Rate, [Hz]	4	4
Soundings Along Track at nadir, [m^{-1}]	0.74	0.74
Soundings Across Track at nadir, [m^{-1}]*	2.6	1.70
Soundings Along Track at 45°, [m^{-1}]	0.74	0.74
Soundings Across Track at 45°, [m^{-1}]*	0.9	0.6
Beam Footprint Area at nadir, [m^{2}]	0.3	0.9
Beam Footprint Area at 45°, [m^{2}]	1.4	3.5
Average No. Soundings, 100% coverage, [m^{-2}]†	1.3	0.8
Average No. Soundings, actual coverage, [m^{-2}]	2.8	2.1

* Angular beam separation = 0.9*sec[steering angle].
† Equals average of product of along track and across track sounding density within 65° of nadir.

The quantity of interest for producing an accurate DTM is the sounding density and this has been measured on images of sounding distribution (using a modification to *SwathEd* by Jonathan Beaudoin) to between 2 – 3 m^{-2} (variation is with water depth) thanks to the overlap between lines. These repeat measurements of the same patch of seafloor also average out random depth and horizontal errors making the depth estimate of a bin more robust. As evinced by apparent displacement of the bedrock, there is still of course the possibility that positional uncertainty can cause outliers in the DTM. Considering first of all the sounding density, sonar resolution and worst possible DGPS error, a grid resolution of one square metre per pixel was decided upon. The resulting

DTMs were sun-illuminated to inspect any attitude or refraction artifacts which may have affected the data.

Careful processing of the surveys was especially important in this thesis since the accuracy of the digital terrain model of the sand dunes has a direct effect on the temporal accuracy of movement. Fortunately, the study area has two stationary rock outcrops that could be used as reference markers for testing the registration of the consecutive surveys. From inspection of the migration vectors, to be discussed later in this thesis, apparent displacement of these bedrock obstacles was less than 1.5 metres for all the surveys.

2.3.2. Refraction Correction

An error in the June survey caused an incorrect sound speed profile to be exported to the Simrad processing unit and used during acquisition at the start of the survey. The soundings from the first 11 of 29 lines were adversely affected by this error. Figure 2.4 shows the result of using *newMergeAtt* to apply the correct sound speed profile. The along track artifacts arising from using the wrong profile have been visibly reduced.
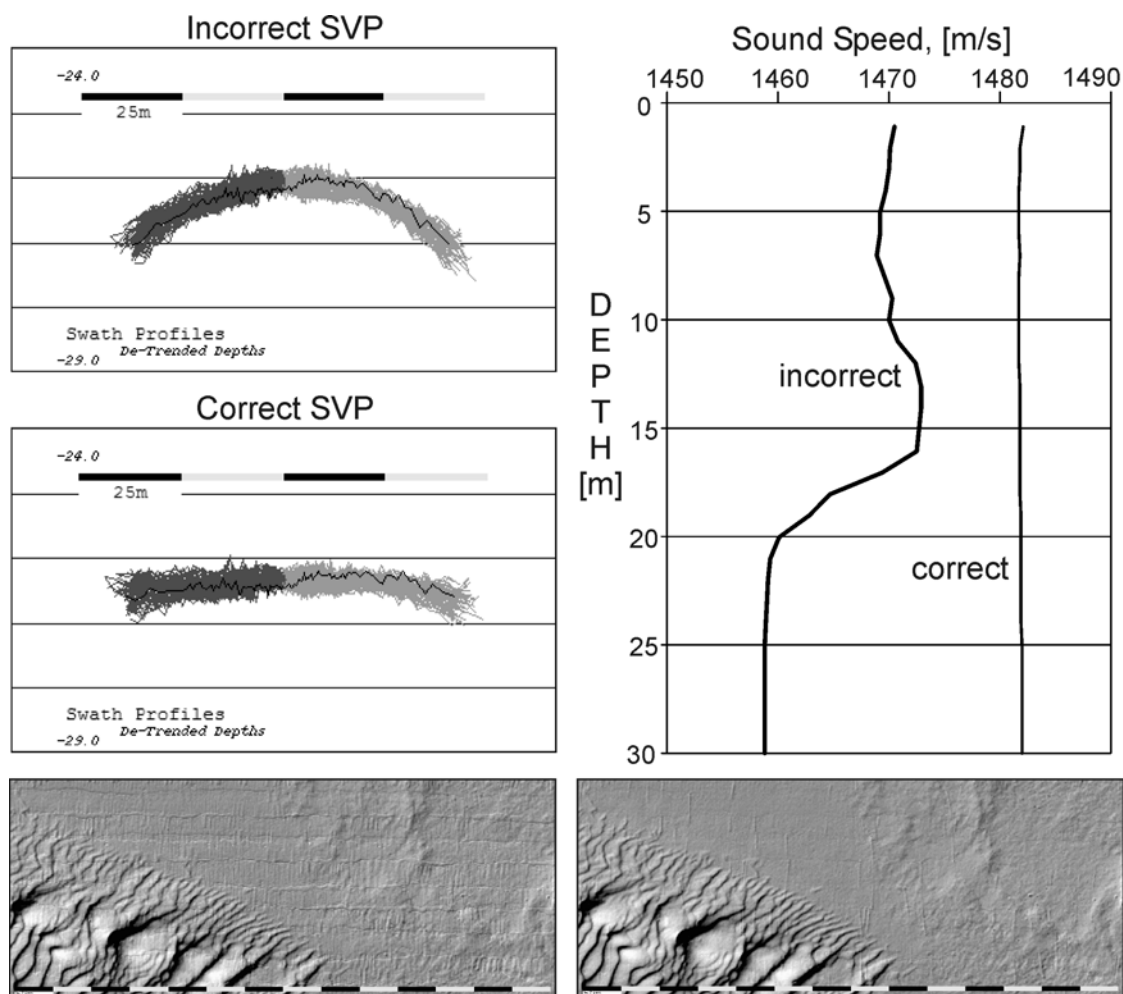
Figure 2.4 Effect of using incorrect sound speed profile. The cross-sections depict the "frown" from using the incorrect SVP and the subsequent improvement when the correct SVP is merged. Also shown is the qualitative improvement shown on the sun-illuminated images.

2.3.3. Latency and Sensor Misalignment Correction

Sand dunes, being linear features, are ideal for spotting sensor misalignment biases because such biases result in easily detectable artifacts such as crest line twinning and mis-matching. 'Twinning', where the crest of a sand dune appears twice in different locations, results when the crest feature on opposing lines do not line up (Figure 2.5). If the artifact is independent of vessel speed (as was the case here), a pitch correction is often necessary to better resolve the feature. This was especially relevant for the MRU which tended to slip about its pitch axis in its housing between surveys so usually it was necessary to apply a pitch correction of a few degrees for each survey. Note that it is assumed here that only

misalignments between the motion or attitude sensors and the multibeam exist; misalignments of the multibeam and motion or attitude sensors with the vessel's reference axes are assumed to have negligible effect. Such vessel reference frame misalignment errors only have appreciable impact for centimetre-level positioning accuracy and smaller beam footprints than those used in this study [*Hughes-Clarke*, 2003].
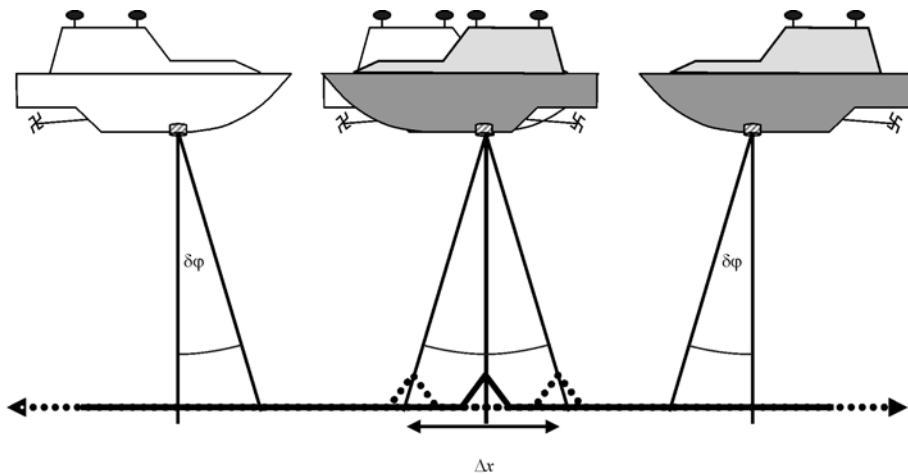
Figure 2.5 Schematic illustration of feature twinning arising because of pitch misalignment between motion sensor and multibeam.

2.4. Quality Control

2.4.1. Tide Issues

Cross-lines were surveyed for two reasons: (a) to quantify the accuracy of each survey and (b) to investigate the applicability of the observed tides at Saint John tide gauge to tidal reduction in Mispec Bay. The locations of cross-lines relative to the field area are indicated in Figure 2.6.

April	↑	July	↑	↑
May	↓	Aug	↑	↓
June	↑	Sept	↑	↓
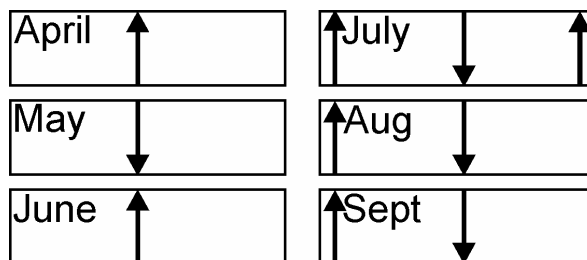
Figure 2.6 Location and direction of cross-lines relative to field area.

Cross-line analysis is performed by subtracting a pair of DTMs composed of the cross-line soundings only and the survey-line soundings only. Cross-sections are then taken through this narrow difference DTM and analysed for bias and standard deviation. Ideally, such a section will have zero bias and any deflections away from zero are due to dune crest-line mismatching due to horizontal positional inaccuracy. Sometimes the cross-section will have spatially persistent biases away from zero and these are often attributed to long period heave that is induced by a sudden acceleration, that 'leak' through the motion sensor (since the period is too long for the motion sensor, which is of finite bandwidth sensitivity, to detect it) into the bathymetry. The usual cause of such acceleration is turning of the vessel and the resulting induced oscillation effect is usually evident in the bathymetric data for the first few minutes of the following survey line. Another cause of this artifact is sudden acceleration of the vessel along a survey line.
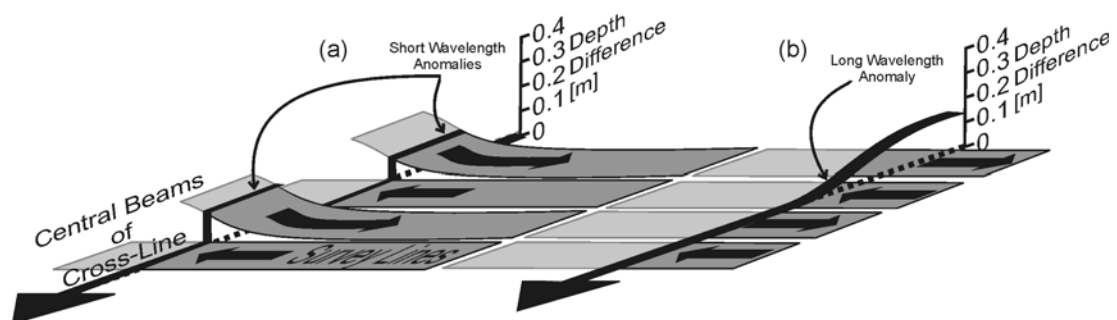
Figure 2.7 (a) Series of heave anomalies that result from a zero-bias cross-line traversing a beginning or an end of a survey line; (b) Heave anomaly that results from a biased cross-line that traverses zero bias survey lines.

Figure 2.7 illustrates the two possible end members of the bathymetric anomaly.

Figure 2.7(a) shows the expected difference DTM anomalies at either end of the surveyed

area, where every second *survey* line displays the long period heave artifact because they

start just after turning; in this case, the *cross*-line displays no such long period heave

artifact and is zero bias. The difference DTM cross-section is zero when the cross line

crosses an *end* of the survey lines but non zero when crossing a *beginning* of a survey line,

resulting in theoretical abrupt departures from zero bias. Figure 2.7(b) shows the expected

difference DTM anomaly in the centre of the surveyed area, where the survey lines do not

display the long period heave anomaly and are zero bias; however, now the cross-line

exhibits the long period heave anomaly and this shows in the difference DTM cross-

section as a long wavelength change in bathymetry. In reality, both the survey lines and

the cross line may exhibit long period heave so the bathymetric anomaly will be a

combination of the two cases.

Any such biases from the difference DTM cross-section need to be removed so that

any remaining long term biases can not be attributed to long period heave effects. This is

done by using the OMG tool *DelayEditor,* developed by Dr. John Hughes-Clarke, which

high-pass filters the heave signal using a cosine squared tapered high-pass filter with a

user specifiable time constant ($\pm$ 10 seconds in this case). This effectively removes the

long period heave induced by oscillation of the motion sensor after turning or after sudden

changes in speed and makes the difference DTM less biased in these areas (Figure 2.8).
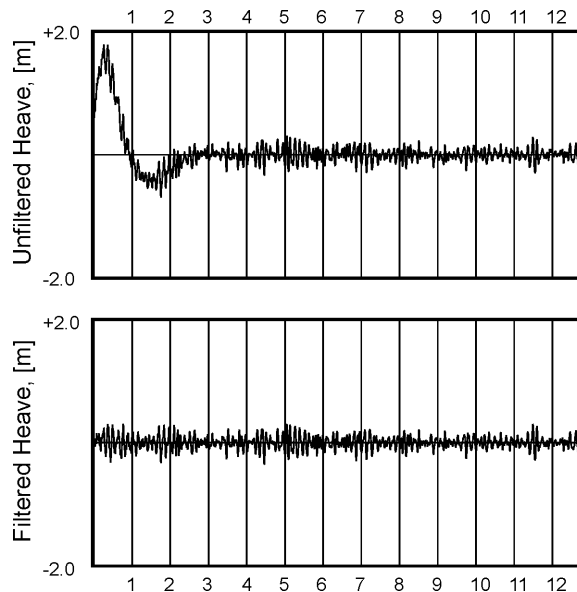
Figure 2.8 Sample heave time series from a June 2002 survey line showing removal of induced heave anomaly. (TOP) Unfiltered; (BOTTOM) Filtered.

The effect of removal of the acceleration induced heave artifact in the cross line is clear in Figure 2.9 especially in the June, July and September surveys. The heave artifact which affects the entire cross-section is attributable to the slow oscillation of the motion sensor after turning onto the cross-line (Figure 2.7(b)) whereas the biases of lesser horizontal scale are attributable to survey lines which started close to the cross-line (Figure 2.7(a)). These latter biases are readily observed on cross-lines that traversed either end of the survey area rather than traversing through the centre of the survey area, by which time the motion sensor would have settled down and any turn related heave artifact in the survey lines would have diminished to zero (although that assumes no evasive manoeuvring along the line, not the case when trying to avoid a lobster pot!). Such cross-lines were carried out in the July, August and September surveys (locations shown in Figure 2.6). Arrows in the left columns of Figure 2.11 and Figure 2.12 show bathymetric anomalies caused by heave leakage at the start of the survey lines and their subsequent removal by applying the dynamic heave correction.

After removing the heave-related biases, one would expect all the difference DTMs to become close to zero bias. Interestingly, this was not the case for the April and May surveys. Changing the relative phase of the merged tide resulted in the discovery that when the tide was merged ten minutes later than that at the Saint John tide gauge, the result was closer to the desired zero bias solution. The observed tide was compared with predicted tide to see if there was some inherent phase error in the observed tide that would explain why the observed tide arrived 10 minutes later in April and May than it did in later months. A plot of observed tides superimposed on predicted tides is given in Figure 2.13. It is clear from the figure that there was no significant phase difference between the predicted and observed tide for Saint John tide gauge. A possible reason for this discrepancy is that the water levels at the tide gauge and field area were not equivalent at this time because of the effect of the spring freshet on the water level at the tide gauge (note arrows in Figure 2.13 denoting elevated low water level in April). This effect is localised to the estuary (where the tide gauge is situated); it is unlikely that the effect of the spring freshet will be felt at the field area in the open sea.

Bias and standard deviation statistics for the difference DTM cross-sections in Figure 2.10, Figure 2.11(g,h) and Figure 2.12(c,d). Statistics for the conditions with and without heave correction and with and without the phase delay are displayed. Note how the dynamic heave correction substantially decreases the standard deviation of the difference surface; this is especially true of the difference surfaces at either end of the surveyed area (depicted in Figure 2.11 and Figure 2.12) where a lot of the error is due to the starting of survey lines at either end, an error for which the heave correction is designed to minimise.

Note how the standard deviation of the centre cross-line remains large even after dynamic heave corrections applied (Figure 2.10). This is mostly because the seafloor beneath this cross-line is not featureless and a lot of the scatter is due to feature mismatching after subtracting the surfaces. The seafloor beneath the other cross-lines was relatively featureless and so the error bars are smaller for these cross-lines after correcting for dynamic heave (Figure 2.11(g,h) and Figure 2.12(c,d)).
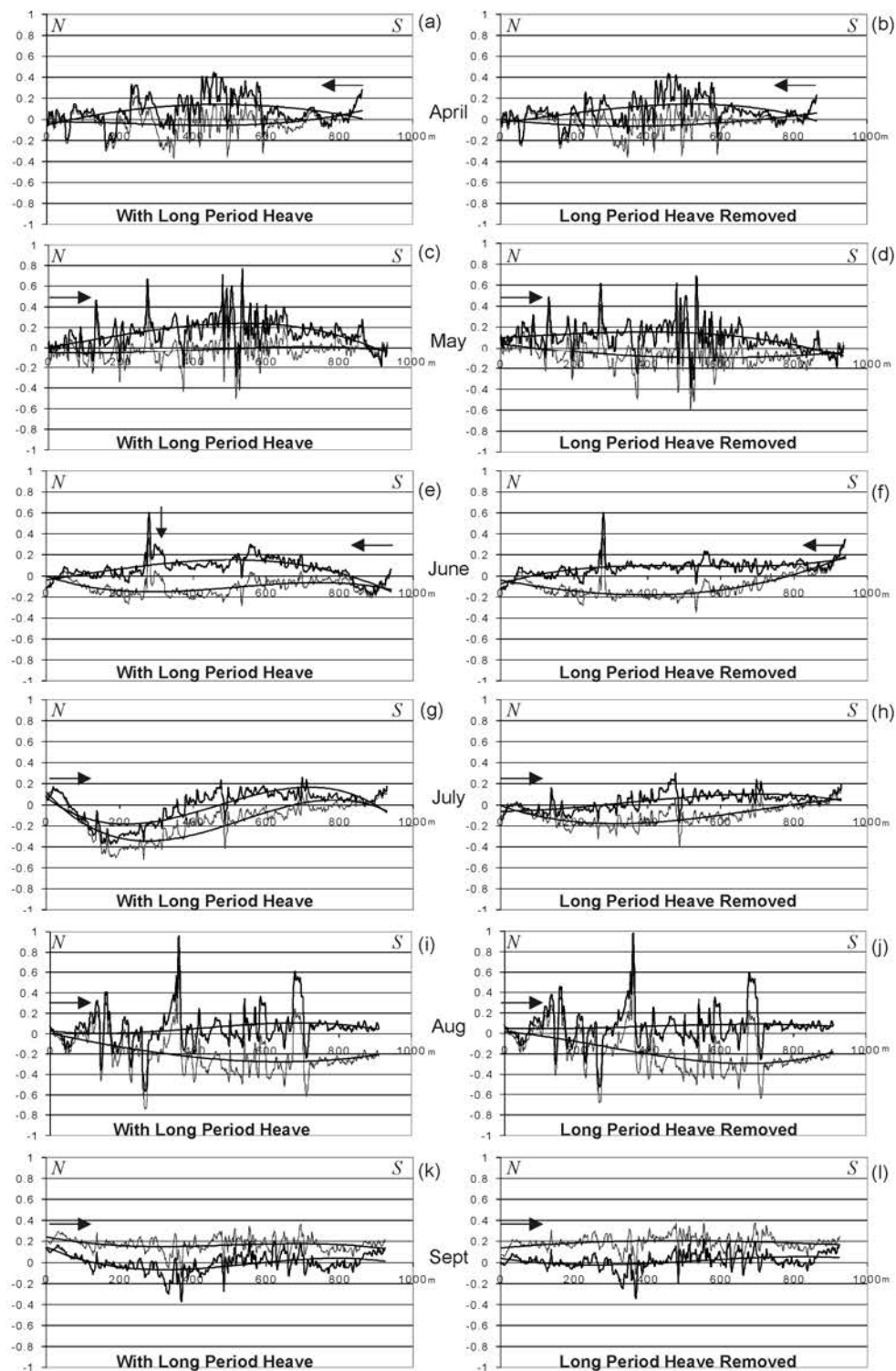
Figure 2.9 Cross-sections through the centre check-line difference DTM (units of metres) for the different surveys at different time delays (black: in phase with Saint John tide gauge; lighter colour: 10 minutes later than Saint John tide gauge). Horizontal arrow indicates cross-line direction. Left column is with long period heave present. Right column is with long period heave removed in both check-line and survey lines. Smoothed differences are also displayed.
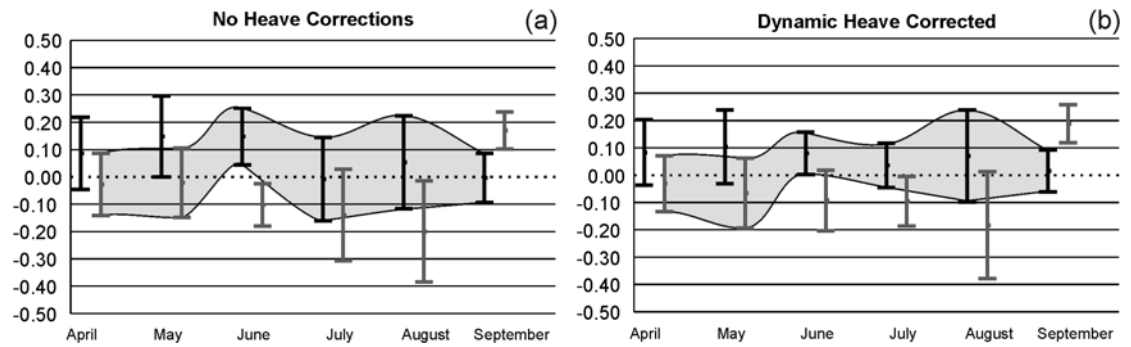
Figure 2.10 Bias and standard deviation plots for sections through the difference DTM for the centre cross-line (black error bars: in phase with Saint John tide gauge; grey error bars: 10 minutes later than Saint John tide gauge), (a) long period heave present; (b) long period heave removed.
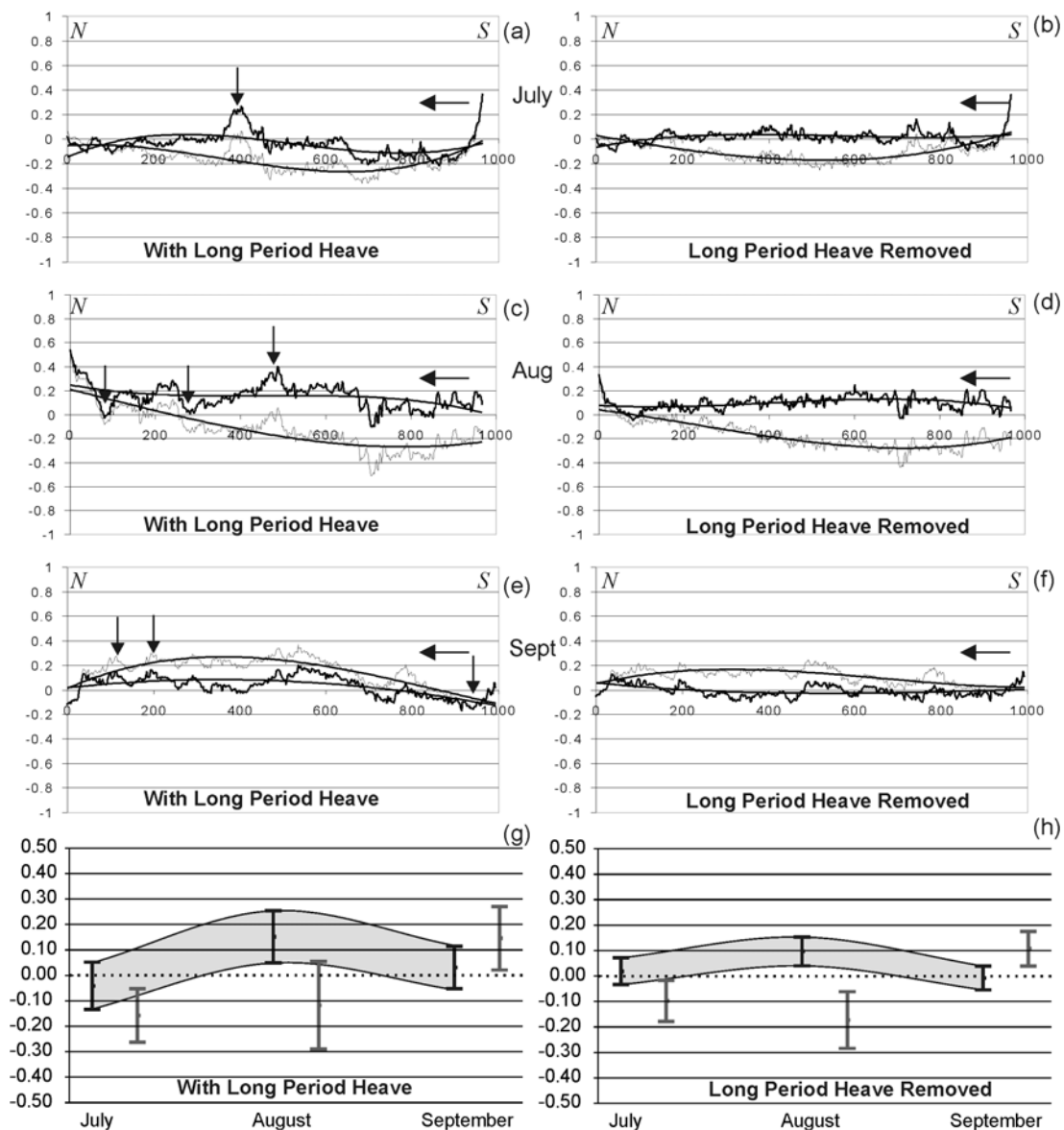
Figure 2.11 (a-f) Difference DTM cross sections at the western extremity of the survey area (black: in phase with Saint John tide gauge; lighter colour: 10 minutes later than Saint John tide gauge). Horizontal arrow indicates cross-line direction; vertical arrows depict deviations caused by heave anomalies at the start of survey lines; (g,h) Bias and standard deviation plots for sections through the difference DTM, (g) long period heave present; (h) long period heave removed.
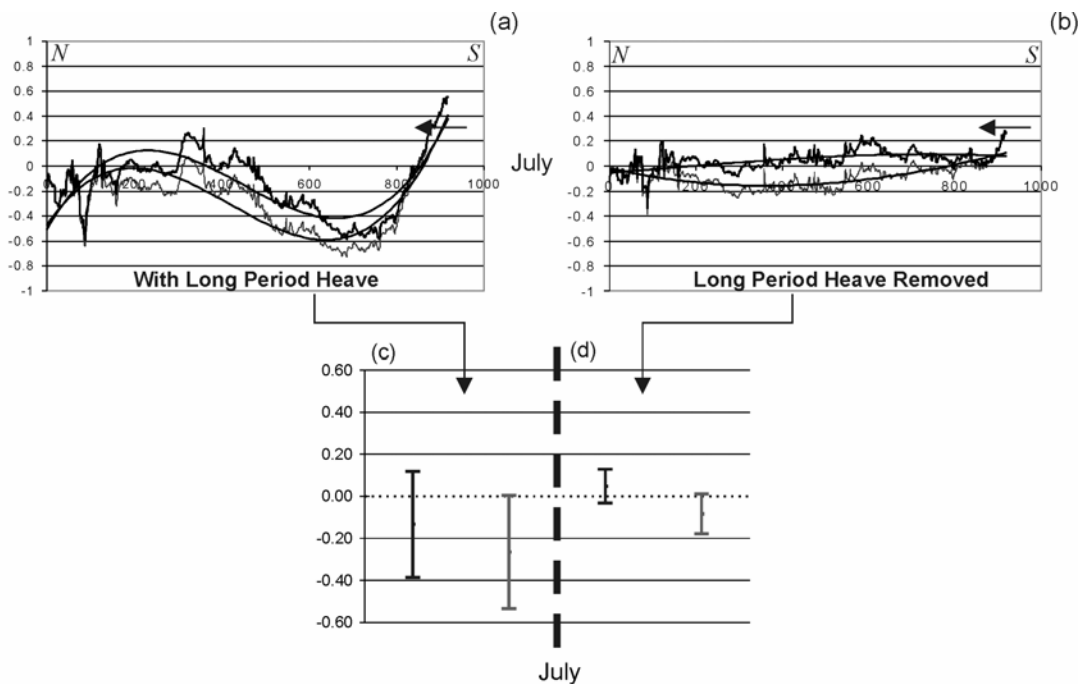
Figure 2.12 (a,b) Difference DTM cross section at the eastern extremity of the survey area (black: in phase with Saint John tide gauge; lighter colour: 10 minutes later than Saint John tide gauge). Horizontal arrow indicates cross-line direction. The long period aberration is the cross-line heave anomaly leaked into the depth data. (c,d) Bias and standard deviation plots for the cross-section, (c) long period heave present; (d) long period heave removed.
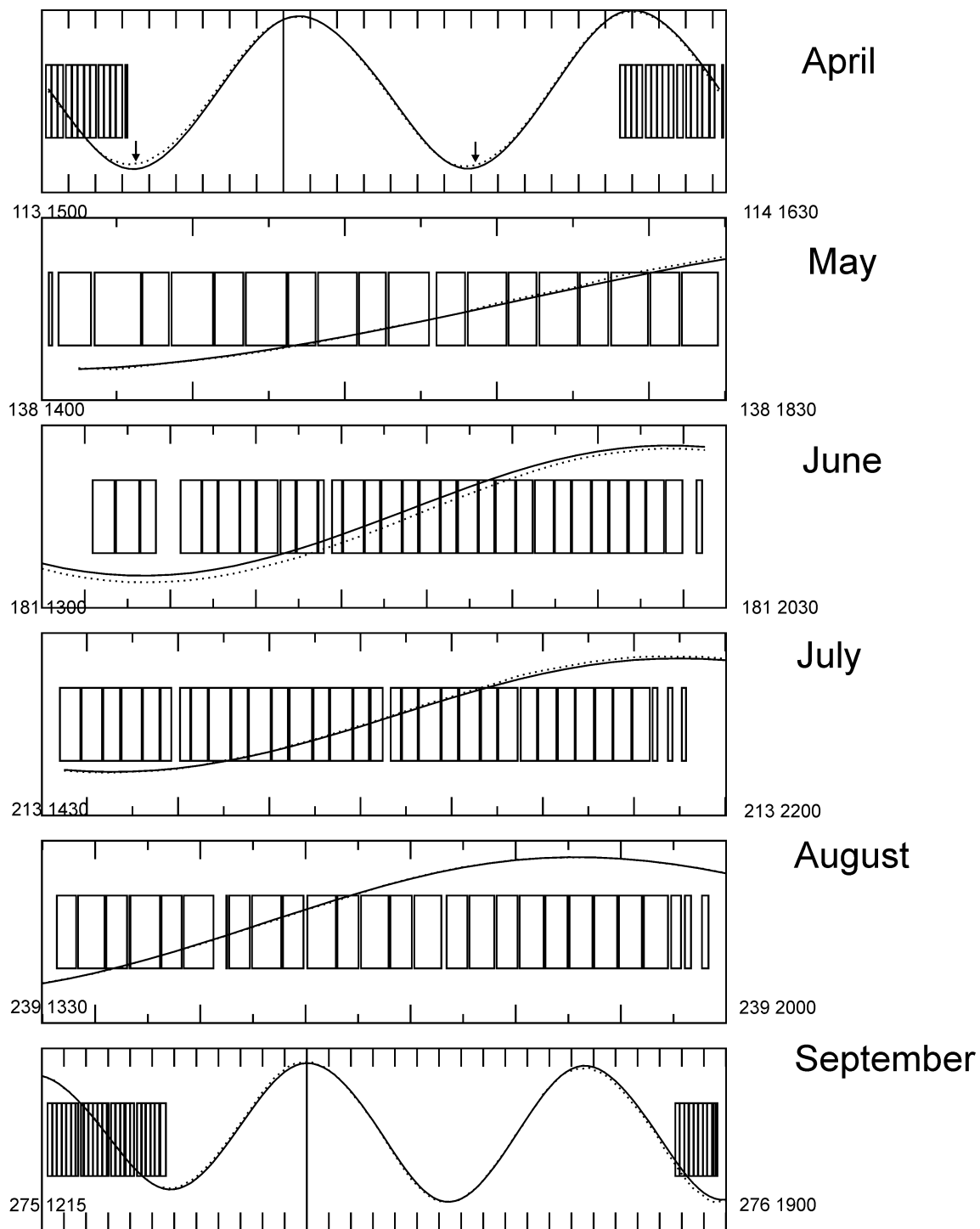
Figure 2.13 Observed tide (dotted line) and predicted tide (solid line) for the monthly surveys. Duration of each survey line is depicted by the width of the rectangular boxes. Arrows in the April tides depict elevated low water level because of the Saint John River freshet.

2.5.   Conclusion

Each of the bathymetric surveys was carefully processed so that perceived displacements were real and not artifacts due to motion sensor and multibeam relative misalignment. Sand dune crests, being continuous curvilinear features, were highly amenable to the detection and elimination of such misalignments.

Cross-line analysis enabled the quantification of bias and accuracy of each survey; removal of turning related long-period heave substantially improved the accuracy of the digital terrain models. The water level at the field area was equivalent to that at Saint John tide gauge, roughly ten kilometres away, except for the months of April and May when the effect of the spring freshet caused an elevated water level at the gauge which was not felt at the field area.

C h a p t e r   3 :   H y d r o d y n a m i c s

To better understand the hydrodynamic regime over the sand bank, three current measurement cycles of duration 12.42 hours, or one M2 tidal cycle, were conducted using a vessel mounted Acoustic Doppler Current Profiler (ADCP). Current measurement was carried out for two reasons: to investigate the effect of the tidal eddy on the horizontal and vertical current structure in Mispec Bay and to provide actual current measurements for predicting sediment transport rates, rather than using mathematical model predictions.

Interpretation of the current data shows that there is a high degree of spatial variability and some vertical variability in the current regime over the sand bank because of the disturbing effect of Cape Spencer. Currents flowing towards and away from the headland possess predictable temporal trends of duration and magnitude depending on proximity to the headland. In addition, analysis of residual, i.e. tidally averaged, currents and current ellipses show that residual currents increase landwards and towards the headland and that in the lee of the headland there is a zone where residual current is greater than the semi-major axis of the current ellipse. Salinity and temperature profiles taken over a tidal cycle point to the influence of the Saint John River on the surface water chemistry. On the flooding tide, currents sweep the warmer, fresher Saint John River plume, which had flowed into the Bay on the previous ebb tide, over the field area.

Because of its relevance to this study, a theory of headland eddy generation is discussed and the predictions arising from the theory are applied to the Mispec eddy.

3.1.   Principles of Doppler Current Profiling

An ADCP mounted on a moving platform has an advantage over stationary Eulerian current measurement devices (impellers, S4 current meters) for this type of investigation because the spatial variability of current is of interest. The ADCP has the added advantage of being able to vertically bin the current velocity, allowing the possibility of examining the variability of currents with depth as well as space.

The RD Instruments Workhorse ADCP is composed of an array of 4 x 600 kHz transducers all pointed away from each other and at 20° from the line perpendicular to the plane of the back-plate of the instrument [*RD-Instruments*, 1996]. Each transducer simultaneously transmits a pair of coded pulses (a "ping") and then, after a period of ringing of the transducer, the 'blanking period', receives a continuous signal of backscattered sound as the ping propagates through the water column ensonified by its beam. Because of scatterers moving with the water column, the backscattered sound for a given beam will have a Doppler frequency shift imparted to it so its frequency will be altered (positive shift if the scatterers are moving towards the transducer, negative shift if the scatterers are moving away from the transducer). This Doppler shift (directly proportional to the component of velocity projected along the beam axis) is measured by auto-correlating the received signal twice, separated by a system defined 'lag time'; if the temporal location of the peak in the auto-correlation function is anything other than the lag time, then the Doppler shift is directly proportional to this shift in correlation time. Each beam then registers a single *along-beam* component of motion.

After the transmission of a ping and the blanking period, a backscattered continuous signal is received from the beam volume at the transducer as the ping propagates through the water column scattering from particles as it does so. This returned signal is divided into intervals by the instrument circuitry, each corresponding to overlapping depth cells, through a process of 'time gating'. The measured velocity of each depth cell is the average velocity for that cell, linearly weighted toward the velocity of the scatterers in the centre of cell (since the centre of the cell is the only part of the cell encountered by both the leading and trailing edge of the finite length ping). The overlapping of the cells arises because of the finite pulse length of the ping: a given amplitude in the backscattered signal is the sum of the interactions of the trailing edge of the pulse with cell *x* and the leading edge of the pulse with the deeper cell *x+1* that arrive at the transducer contemporaneously.

The minimum achievable depth cell length is explicitly related to the inter pulse interval, i.e. the ping length, which is in turn related to the bandwidth of the pulse. High frequency (e.g. 1200 kHz) broadband ADCPs are capable of taking many measurements of velocity in a small volume so a depth cell size of 1 m is valid for this frequency of operation. However, such high frequencies are of course subject to more attenuation in the water column and therefore may not be used in water depths greater than 18 m. Medium frequency (600 kHz) ADCPs have an optimal depth cell size of 2 m with a maximum range of 58 m [*RD-Instruments*, 1996].

Figure 3.1 illustrates how two ADCP beams resolve a coplanar current vector. ***T*** represents such a coplanar vector and is a true component of some 3D current vector. The deflection from horizontal of ***T***, the angle θ, is exaggerated for clarity. Each beam can

only detect a component of motion parallel to it, i.e. the projection of *T* onto each of the beams, and this measured component is represented by the double-headed arrows in Figure 3.1. These measured components are then summed to give *S*. The expression for *S* is given in Figure 3.1. Note that to convert the measured 2D vector *S* to the true 2D current vector *T*, *S* needs to be adjusted for the configuration of the beams, i.e. the deflection from the vertical of the beams, the angle A. This calculation elucidates the *i* and *j* components of *T*: *T*cos(θ)* and *T*sin(θ)*, and is described in Figure 3.1 by the arrow graphic.
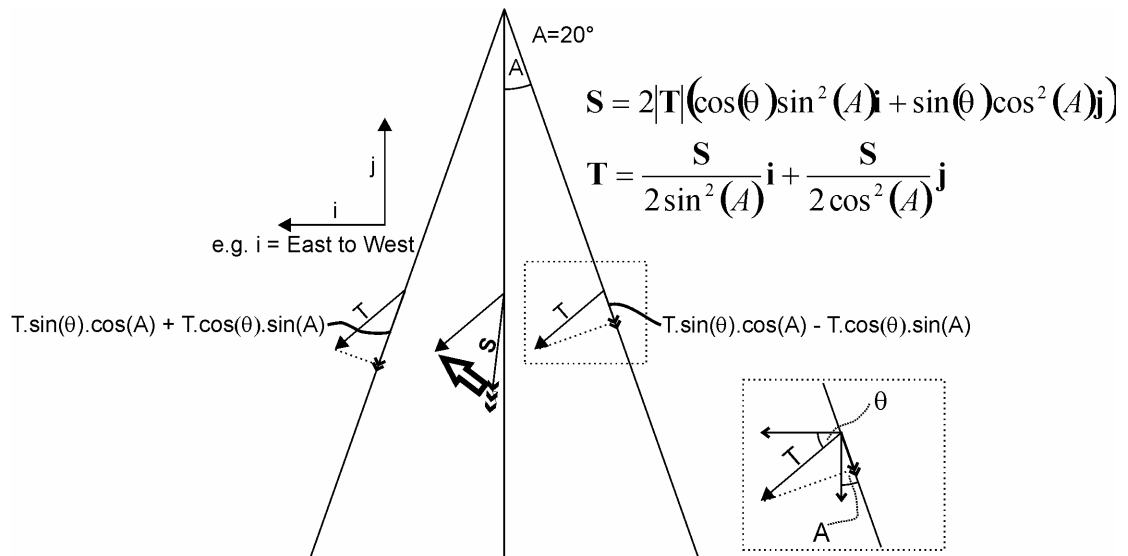
Figure 3.1 Resolution of a current vector in a given plane (e.g. east-west-up plane). Note how the current vectors in both beams are the same; this is necessary for the calculation of the resultant vector, *S*. The *i* and *j* components of *S* need to be divided by 2*sin²(A) and 2*cos²(A) respectively in order to yield the *i* and *j* components of *T*. This operation is denoted by arrow graphic.
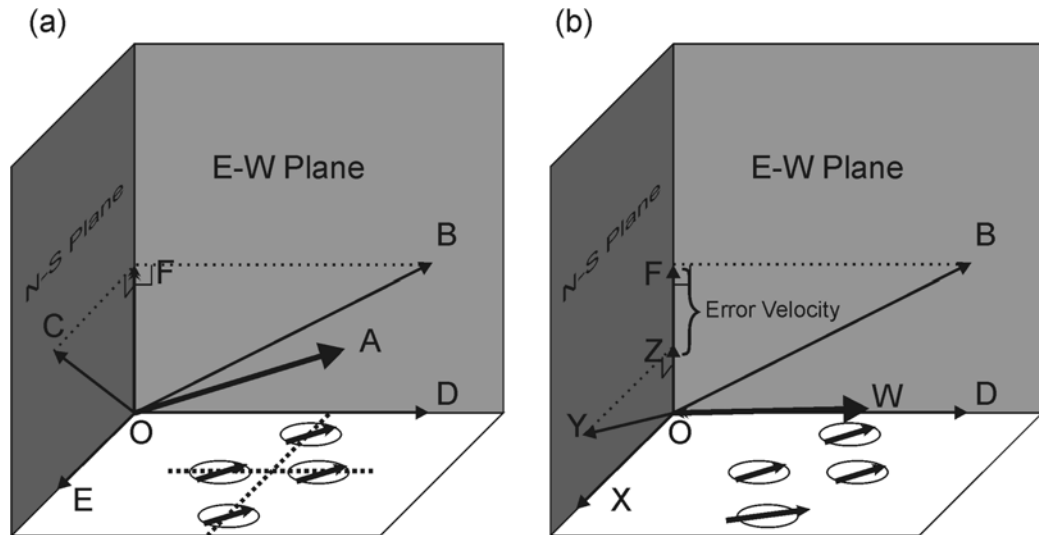
Figure 3.2 Illustration of how current vectors are summed using the ADCP and the importance of the homogeneous current assumption. (a) illustrates the ideal situation where the current vectors in all four beams are equal in magnitude so the vertical component of both planar vectors is the same, then *OA=OD+OE+OF*, where *OF* is one of the measurements of the vertical component; (b) illustrates the importance of having the fourth beam which makes possible the second measurement of the vertical component. Here there is a large discrepancy between measurements of vertical component, *OF* and *OZ*; this has an effect on the resultant vector *OW*, which is quantified by the error velocity |*OF-OZ*|.

The ADCP processes the beam-relative velocities by pairs of beams to resolve two orthogonal horizontal components and two measurements of the vertical velocity. For instance, if the ADCP is oriented in the cardinal directions, the ADCP calculates the east-west and up component with one pair of beams and the north-south and up component with the other pair of beams (Figure 3.2(a)). The figure also illustrates the horizontal uniformity assumption upon which the successful operation of the ADCP rests. Horizontal uniformity does not mean that the currents are assumed to be flowing horizontally; rather it means that at a given depth, the same current exists in all four beams. This is where the redundancy afforded by the second measurement of vertical velocity is useful: if, in one of the four beams the current is different from the other three, then the vertical component of this pair of beams will be different from the other beam pair. The difference in vertical velocity measurement is called the error velocity and is a useful figure for testing data quality.

The ADCP converts the measured velocities from being relative to the vessel to absolute by subtracting the apparent velocity of the bins that include the bottom echo ("bottom tracking"), which is effectively the velocity vector of the vessel. External heading may be input into the ADCP but it is recommended that bottom tracking should always be used if available since any errors in the bottom track measurement are also present in the vessel-relative current measurement, so they cancel out in the subtraction process [*RD-Instruments*, 1996].

3.2. Theory of Transient Eddy Formation around Headlands

Since this chapter deals extensively with the hydrodynamic effects of a headland eddy, the theory of headland eddies will now be discussed.

Signell and Geyer [1991] produced the most authoritative work into the controlling factors of headland associated eddy formation. Their central idea was that headland associated eddies are formed as a result of "injection" of vorticity, which was generated within a narrow shoaling region around the headland, into a flat region downstream of the headland whereupon the injected vorticity is dissipated. This "injection" happens when the rotating fluid in the shoaling layer "separates" from the headland (in plan view) because of a change from negative to positive pressure gradient at the headland tip.

The following discussion of the theory of headland eddy generation will expand on the latter concepts and discuss: (a) where and how vorticity is generated; (b) flow separation as the mechanism of vorticity "injection" and (c) the evolution of this injected vorticity (the "eddy") in the area downstream of the headland.

3.2.1. Vorticity Generation Mechanisms

To illustrate the controlling factors on vorticity generation, the depth-averaged vorticity equation will be derived (derivation modified after *Randall* [2004]) and expanded to identify pertinent terms. The derivation of the depth-averaged vorticity equation is arrived at by manipulation of the depth-averaged horizontal momentum Equation (3.1), which describes the change in momentum per unit mass on a parcel of water, and the depth-averaged shallow water mass conservation Equation (3.2). For derivation of these two starting equations see *Randall* [2004].

$$\frac{d\mathbf{u}}{dt} + f(\mathbf{k} \times \mathbf{u}) = -g\nabla\eta - \left(\frac{C_D|\mathbf{u}|}{h+\eta}\right)\mathbf{u} + \nabla(A_H(\nabla \bullet \mathbf{u}))$$

where:

$$\frac{d\mathbf{u}}{dt} = \frac{\partial\mathbf{u}}{\partial t} + (\mathbf{u} \bullet \nabla)\mathbf{u}$$

$$f = 2\Omega\sin\phi$$

(3.1)

$$\frac{\partial\eta}{\partial t} + \nabla \bullet [\mathbf{u}(h+\eta)] = 0$$

(3.2)

where $\mathbf{u} = (u,v)$ is the horizontal depth-averaged velocity vector, f is the Coriolis parameter, Ω is the angular speed of the earth (2π in 23h 56m 4s (1 sidereal day)), ϕ is latitude, $\mathbf{k}$ is the vertical unit vector pointing away from the earth's centre, g is the acceleration due to gravity, h is the water depth below mean sea level, η is the water surface elevation above mean sea level, C_D is the drag coefficient and A_H is the viscosity (specifically, the horizontal eddy viscosity).

The shallow water equation (3.1) describes the contributing force vectors on a parcel of water. The first term on the left hand side is the 'total derivative' of the velocity

comprising the sum of the temporal and spatial derivatives of velocity for non-steady, non-uniform flow. The terms on the right hand side of (3.1) represent the true forces on the body of water. The first term on the RHS represents the horizontal pressure gradient force caused by the instantaneous slope of the water surface, using the hydrostatic assumption that the absolute pressure depends only on the height of the water column, i.e. water density is depth invariant (the barotropic condition). The second and third terms are frictional terms and describe the loss of momentum through bottom friction (proportional to the square of velocity) and internal friction respectively.

Note that in the event of curvilinear or circulating flow, the $(u \bullet \nabla)u$ term, which represents the change of u in the direction of u, is the sum of radial and tangential components of acceleration. To clarify this latter point, the useful vector calculus identity $(u \bullet \nabla)u = \nabla[(u \bullet u)/2] + (\nabla \times u) \times u$ is employed to re-write and re-arrange (3.1) as:

$$\frac{\partial \mathbf{u}}{\partial t} + (\zeta + f)\mathbf{k} \times \mathbf{u} = -\nabla(g\eta + K) - \left(\frac{C_D|\mathbf{u}|}{h + \eta}\right)\mathbf{u} + \nabla(A_H(\nabla \bullet \mathbf{u}))$$

where
$$\text{Vorticity}, \zeta = \mathbf{k} \bullet (\nabla \times \mathbf{u})$$
$$K = (\mathbf{u} \bullet \mathbf{u})/2$$

(3.3)

The cross product term on the LHS of (3.3) represents the total radial acceleration (perpendicular to u, because of $k \times u$) at a point which includes planetary (from Coriolis) and local centrifugal components. Note how vorticity has been introduced at this early step.

The equation describing the rate-of-change of depth-averaged vorticity, ζ, is derived by taking the curl of (3.3) (more specifically carrying out the operation $(\nabla \times) \bullet k$ on (3.3)

and substituting for $\nabla \bullet \boldsymbol{u}$ from (3.2) whilst making the necessary statement that the total

change in elevation, η, with time is the same as the total change in depth H with time and

that for a small area the spatial gradient of total vorticity, $\nabla(\zeta + f)$, is approximated by $\nabla(\zeta)$

since the planetary vorticity will not change over a small area.

$$\frac{\partial \zeta}{\partial t} + \boldsymbol{u} \bullet \nabla(\zeta) = \frac{\zeta + f}{H}\left[\frac{dH}{dt}\right] - C_D\left[\nabla \times \frac{|\boldsymbol{u}|}{H}\boldsymbol{u}\right] \bullet \boldsymbol{k} + A_H \nabla^2 \zeta$$

$\quad$ A $\qquad$ B $\qquad\qquad$ C $\qquad\qquad$ D $\qquad\qquad$ E

where $\qquad\qquad\qquad\qquad\qquad\qquad\qquad\qquad\qquad\qquad$ (3.4)

$$\frac{d}{dt} = \frac{\partial}{\partial t} + \boldsymbol{u} \bullet \nabla$$

$$H = h + \eta$$

Equation (3.4) is the depth-averaged vorticity equation. It states that the total *change*

in vorticity following a parcel of fluid of fixed mass (L.H.S. of (3.4)) depends on three

principal terms. Term C modifies *existing* vorticity by squashing or stretching the water

column as the bathymetry changes in time *and* space (since the total derivative operator is

used) and is the only way vorticity changes in the absence of bottom friction (Figure 3.3

(a)). In coastal regions, the frictional (hence the C_D term) term D becomes important and

is the curl of the depth normalised stress that describes the twisting of the water column

produced by the torque arising from spatially varying bottom shear stress (Figure 3.3

(b,c)). Thus term D describes a mechanism whereby new vorticity is generated. Term E

expresses the diffusion of vorticity due to horizontal mixing processes quantified by the

inherent viscosity (specifically eddy viscosity) of the fluid.

Term D may be expanded (see Appendix A) to see more clearly the way bottom friction generates vorticity. When bottom friction exists, it will be seen that there exist mechanisms for *both* the generation *and* dissipation of vorticity.

$$-C_D\left[\nabla\times\frac{|\mathbf{u}|}{H}\mathbf{u}\right]\bullet\hat{\mathbf{k}}=-C_D\frac{|\mathbf{u}|}{H^2}\left[\mathbf{u}\times\nabla\underset{\uparrow}{H}\right]\bullet\hat{\mathbf{k}}+C_D\frac{1}{H}\left[\mathbf{u}\times\nabla\underset{\uparrow}{|\mathbf{u}|}\right]\bullet\hat{\mathbf{k}}-C_D\frac{|\mathbf{u}|}{H}\zeta \qquad (3.5)$$

$$\text{I}\text{II}\text{III}$$

The two main vorticity generating mechanisms are terms I and II, being the cross products of velocity and depth gradient (depth positive downward) and velocity and velocity gradient respectively (note arrowed terms in (3.5)). Term I is the 'slope torque' [*Robinson*, 1981] and describes the generation of vorticity when there is a component of $\mathbf{u}$ parallel to the bathymetric contours (put another way: when there is a component of $\mathbf{u}$ is perpendicular to the depth gradient, ∇H, otherwise the cross product will vanish). Physically this means that a contour-wise flow of a certain velocity along a given slope of ∇H will feel a greater depth distributed drag force in shallow water than in deeper water (Figure 3.3 (c)). Term II is the 'speed torque' which arises when there is a component of velocity perpendicular to the velocity gradient, i.e. when there is lateral shear in the flow. Such a situation can come about if there is already vorticity present in the flow or if the flow accelerates around an obstacle such as a headland (Figure 3.3 (b)). Term III represents the vorticity dissipation by bottom friction and has no dependence on slope or shear.
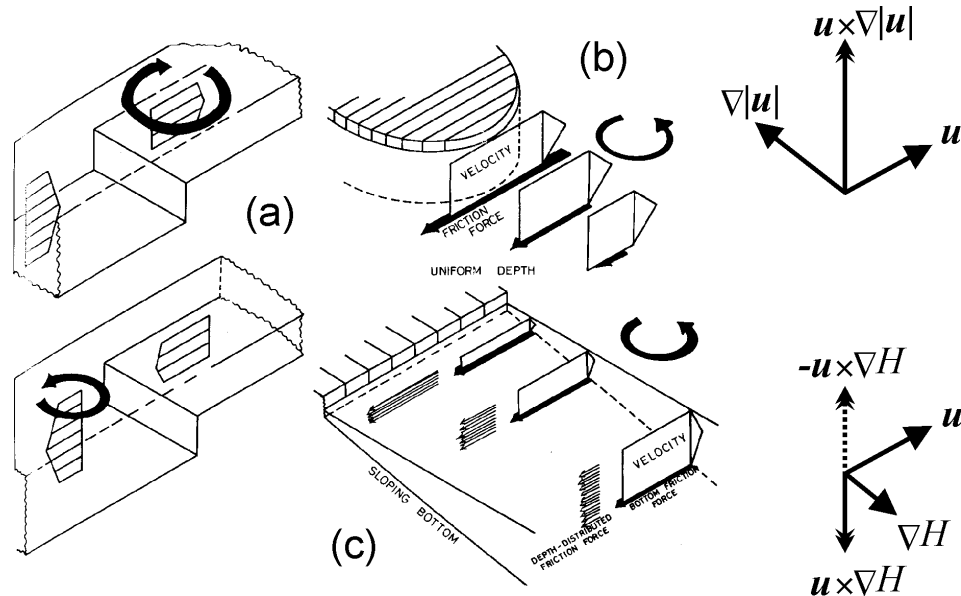
Figure 3.3 (a) the vorticity generating mechanism in the absence of bottom friction (term C in (3.4)); (b) vorticity generation by bottom friction caused by speed torque (Term II in (3.5)) and (c) vorticity generation by bottom friction caused by slope torque (Term I in (3.5)) (modified from *Robinson* [1983]).

Significance of Equation (3.5) to headland eddy generation

Therefore, in the vicinity of a headland the shallow water depth and relatively rapid bottom gradients lead to a significant vorticity *generating* mechanism embodied in the slope torque (Term I) and a vorticity *modifying* mechanism embodied in Term C of (3.4). In addition, the strong transverse shear as the current accelerates around the headland leads to a vorticity generating speed torque (Term II). The frictional vorticity mechanisms are illustrated in Figure 3.3 (b,c). Note that even though the vorticities in Equation (3.5) are of opposite sign, in the special case of a headland proximal flow, the velocity gradient is opposite to the depth gradient so the generated vorticities act in the same direction (positive). It has been noted elsewhere [*Pingree and Maddock*, 1979; *Robinson*, 1983; *Ridderinkhof and Zimmerman*, 1990; *Park and Wang*, 2000] that in most other cases the slope and speed torques are opposed. This generated vorticity is then enhanced by Term C of (3.4). Around the shoaling zone, the flat seafloor still possesses bottom friction but can only dissipate existing vorticity according to Term III, not generate it.

It would be remiss not to briefly mention the work of *Park and Wang* [2000], who took a slightly different approach to the study of vorticity generating mechanisms around a headland. They derived the *volume transport* vorticity equation, which expresses the vorticity of flux, $U = H\boldsymbol{u}$, (the latter in units of m²/s) of water, rather than the depth-averaged vorticity equation, as discussed above, which expresses the vorticity of depth-averaged velocity (the latter in units of m/s). *Park and Wang* [2000] allege that the major factor in vorticity generation is when isolines of the water surface cross the isobaths around the headland (according to *Park and Wang* [2000], this mechanism is roughly analogous to term C of (3.4)) and that bottom friction is not as important as alleged by *Signell and Geyer* [1991]. Nevertheless, the pattern of transport vorticity generated by the model of *Park and Wang* [2000] is very similar to the pattern of depth averaged vorticity. Whatever the origin of the vorticity, the mechanisms of vorticity injection and subsequent dissipation that are described in the following sections still apply.

3.2.2. Mechanism of Vorticity Injection

If the flow follows the coast, the vorticity produced in the shoaling area around the headland does not penetrate into the water mass above the flat seafloor and eddies are not likely to form. *Signell and Geyer* [1991] proposed that vorticity was injected in a similar fashion to the familiar aerodynamic problem of "stalling" of an aircraft wing when it cuts through the airflow (initially parallel to the wing) at too steep an angle. During "stalling", vorticity, which is continuously generated in a layer just above the interface with the air and the wing, is injected into the laminar flow above the boundary layer in the form of turbulence causing the wing to stop lifting. This phenomenon is known as flow separation and was proposed as the mechanism of injecting the produced vorticity.

The fact that the vorticity generating mechanisms were so localised around the headland led *Signell and Geyer* [1991] to adopt a general hydrodynamic model that had previously been applied to the hydrodynamics of a viscous fluid (air or water) flowing past an infinite smooth cylinder (or wing, for the stalling problem). In this type of model, vorticity is only generated in that part of the fluid where the velocity is affected by the no-slip condition with the interface, or the viscous "boundary layer". *Signell and Geyer* [1991] recognised that the shoaling zone around the headland within which vorticity is generated could be analogous to a "boundary layer" as described latterly and proposed to use the same infinite cylindrical model but with a seabed with bottom friction in addition to a viscous horizontal boundary layer as vorticity generators. Figure 3.4 illustrates these two boundary layers around the headland. Signell and Geyer argue that because the width of the shoaling layer where bottom friction causes vorticity is greater than the scale of the purely viscous boundary layer associated with a no-slip condition at the horizontal headland/water interface, bottom friction is more important than viscosity in controlling vorticity generation.

Point of Separation

Horizontal **viscous** boundary layer, dependant on viscosity and no-slip condition at the coast

HEADLAND

PLAN

Headland boundary layer, dependant on bottom slope (**I** in Eq. 3.5) and spatial gradient of current (**II** in Eq. 3.5)

VERTICAL SLICE

Boundary layer vorticity

Advected eddy

Current boundary layer, dependant on viscosity and bottom roughness
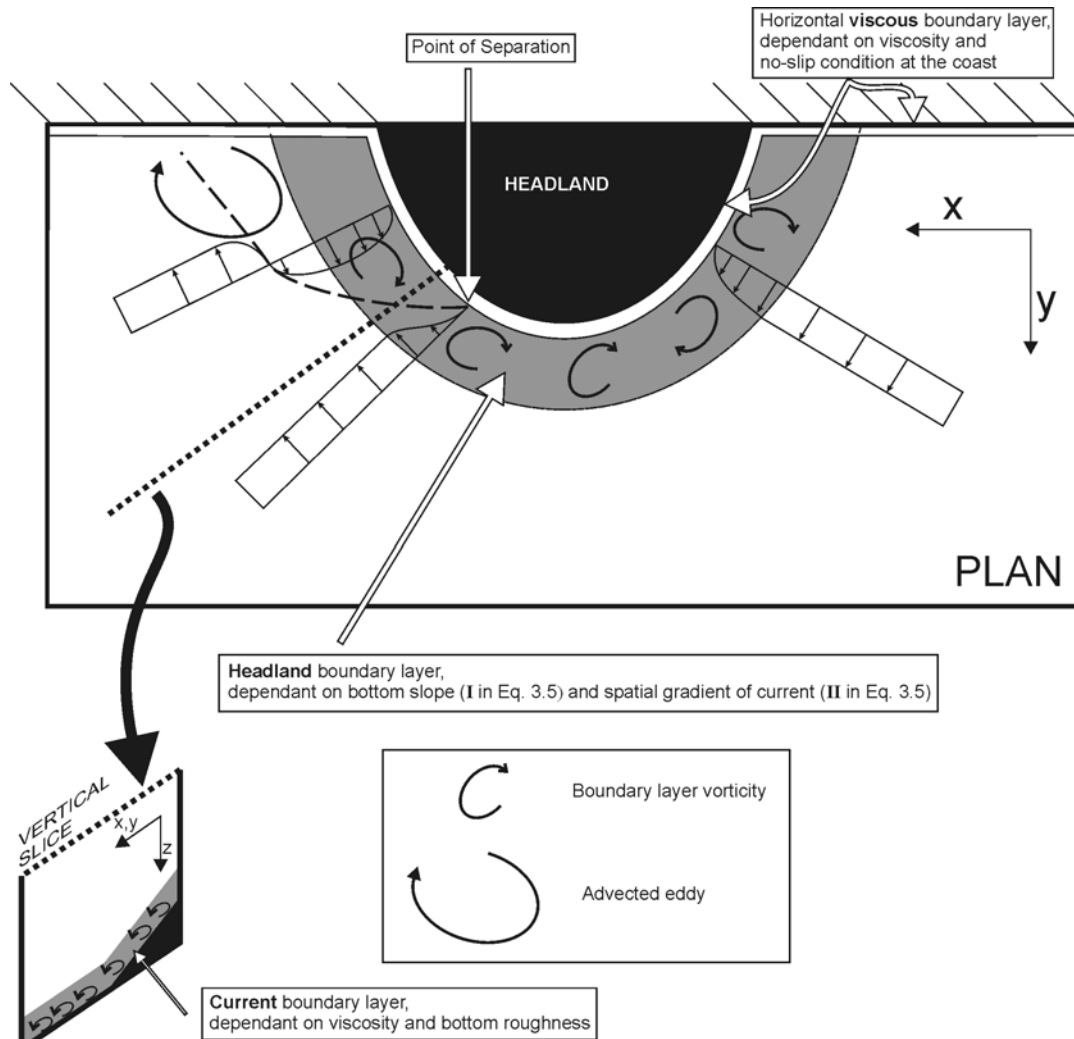
Figure 3.4 Illustration of the headland, viscous and current boundary layers. The changes in boundary-following velocity with distance from the headland are depicted as velocity "profiles".

Difference between current and headland boundary layers

It must be emphasised that the headland boundary layer is not the current boundary layer. The current boundary layer arises from the frictional interaction between the seabed and the viscous water above the interface. In the treatment described here, headland eddies arise from separation of the flow from the (horizontal) headland boundary layer, not from separation of the flow from the (vertical) current boundary layer.

Flow separation is intimately related to the variation of the pressure gradient downstream, which is dependent on the downstream change in flow velocity [*Schlichting*, 1968]. The theory, in the context of the headland model (the boundary layer is as defined latterly), is as follows:

1. Moving along a line normal to the shore, the horizontal boundary layer, as defined latterly, is the slowest moving, and therefore least energetic, part of the water body. This is depicted by the velocity "profiles" in Figure 3.4.
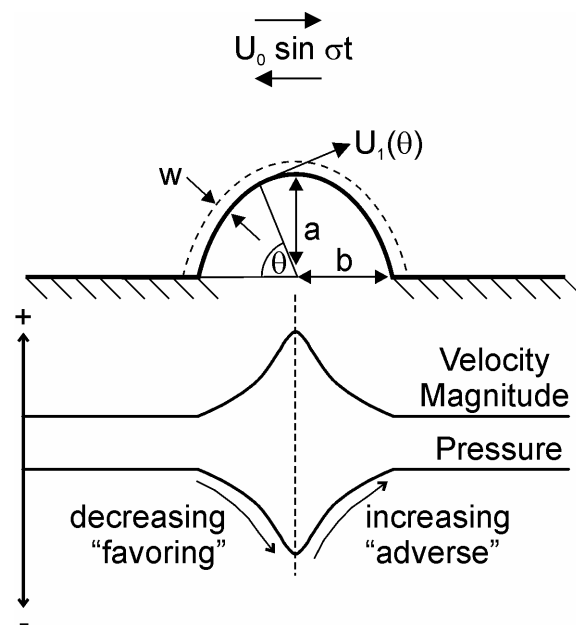
Figure 3.5 Schematic illustration of Signell and Geyer's [1991] model . A uniformly flat region of depth *H*, which cannot generate (only dissipate) vorticity, surrounds the headland. Vorticity is generated in the region *w* that shoals from *H* to H_0. Headland geometry is defined by the shore-normal and shore-parallel elliptical axes, *a* and *b*. The velocity magnitude and pressure are measured following the coastline.

2. So long as pressure on the horizontal boundary layer is constant or decreasing downstream (this is termed a "favouring" pressure gradient), this boundary layer remains "attached" to the interface and moves downstream. Pressure decreases to a minimum, with an accompanying sea-level drop, as the water body accelerates to a maximum due to the Venturi Effect approaching the

headland tip (see pressure and velocity curves in Figure 3.5). There is therefore a favouring pressure gradient as the water body approaches the headland tip.

3. Downstream of the headland tip, the water body decelerates and the pressure therefore increases. This positive along-shore pressure gradient (termed an "adverse" pressure gradient) has a major effect on the boundary layer, which as stated in point 1 above is a region of already low kinetic energy. The increasing pressure downstream causes the fluid in the boundary layer to slow down further and eventually reverse (see velocity "profiles" in Figure 3.4). This deceleration of the alongshore flow must be accompanied by on offshore flow to maintain continuity.

4. The point where this happens is called the point of separation (Figure 3.4) where vorticity in the boundary layer is advected into the headland's lee causing an eddy. An advected eddy is depicted in Figure 3.4.

The downstream change in pressure is schematically depicted in Figure 3.5. The nature of the along-shore pressure gradient was found by Signell and Geyer to be dependant on three separate factors, only one of which caused a change from favouring (negative or constant) to adverse (positive) pressure gradient, conducive to eddy formation. This was found by re-arranging (3.1) so that the pressure gradient term was on the LHS and then substituting the *coastline following* velocity, $U_1(\theta)$ (Figure 3.5) for $\boldsymbol{u}$. For a derivation of $U_1(\theta)$, see *Schlichting* [1968]. Note how $U_1(\theta)$ is maximum at the headland tip, where θ is $\pi/2$.

$$g\frac{\partial \eta}{\partial x_1} = -\left(\frac{\partial U_1}{\partial t} + U_1\frac{\partial U_1}{\partial x_1} + \frac{C_D U_1 U_0}{H}\right)$$

$$= -\left(\frac{\partial U_1}{\partial t} + U_1\frac{\partial U_1}{\partial \theta}\frac{\partial \theta}{\partial x_1} + \frac{C_D U_1 U_0}{H}\right)$$

$$\quad 1 \qquad 2\uparrow \qquad 3$$

where $\qquad\qquad\qquad\qquad\qquad\qquad$ (3.6)

U_0 is the amplitude of the far - field velocity parallel to the shore

$$U_1 = U_1(\theta) = U_0\sin(\sigma t)\frac{1+\alpha}{\sqrt{1+\alpha^2\cot^2\theta}}$$

$x_1 = $ coastline following coordinate

$\alpha = $ elliptical headland aspect ratio $= a/b$

Of these three terms, only the second arrowed term, the "advection" term, which depends on the alongshore change in along-shore velocity, was found to be conducive to flow separation, i.e. induced a change from negative to positive pressure gradient at the headland tip, this specific situation is illustrated in Figure 3.5(bottom), the other terms inhibited flow separation. Therefore, *Signell and Geyer* [1991] proposed that only when this term *dominates* the other two terms is flow separation possible. After expanding (3.6) and for pronounced headlands, they quantified the dominance of advection over the other two terms by two ratios.

$$\frac{\text{Term 2}}{\text{Term 3}} = \frac{\text{advection}}{\text{friction}} = \frac{H}{C_D b}\frac{\alpha(1+\alpha)}{3} = 2\left(\frac{H}{2C_D}\right)\frac{1}{b}\frac{\alpha(1+\alpha)}{3} = 2l_f\frac{1}{b}\frac{\alpha(1+\alpha)}{3}$$

$$\frac{\text{Term 2}}{\text{Term 1}} = \frac{\text{advection}}{\text{local acceleration}} = \frac{U_0}{\sigma b}\frac{\alpha(1+\alpha)}{3} = \frac{1}{2}\left(\frac{2U_0}{\sigma}\right)\frac{1}{b}\frac{\alpha(1+\alpha)}{3} = \frac{1}{2}l_t\frac{1}{b}\frac{\alpha(1+\alpha)}{3}$$

$\qquad\qquad\qquad\qquad\qquad\qquad\qquad\qquad\qquad\qquad$ (3.7)

α is the aspect ratio of the headland, or the ratio of the shore-normal to the shore parallel elliptical axes, *a/b*. It must be pointed out that these equations only apply to headlands with aspect ratios greater than 4/3; this has implications for the asymmetric

Cape Spencer, which has an aspect ratio greater than this value on the ebbing tide but less than the threshold on the flooding tide. From (3.7) it can be seen that for a given headland, increasing far-field depth, H, and decreasing bottom friction, C_D, act to increase the importance of tidal advection relative to friction and hence promote separation. Likewise, increasing tidal current amplitude, U_0, and decreasing tidal frequency, σ, promotes separation. Interestingly, the temporal change of the current vector at a point, or "local acceleration", only works against advection when the tidal frequency is increased, e.g with the addition of M4 or M6; increasing tidal amplitude only increases the effect of *advection* at the expense of local acceleration even though such an increase will also increase local acceleration.

For a given headland, an eddy will only form if the tidal advection is large enough to move it off the lee of the headland and bottom friction is not strong enough to retard the rotation over the distance of the tidal excursion.

3.2.3. Evolution of the eddy

The factors $H/2C_D$ and $2U_0/\sigma$ are parameterised into l_f, the frictional length scale (large values mean less friction), and l_t, the tidal excursion, which is defined as the distance water moves over half a tidal cycle.

When the flow separates, the ratios described formerly determine the post separation behaviour of the eddy (Figure 3.6).
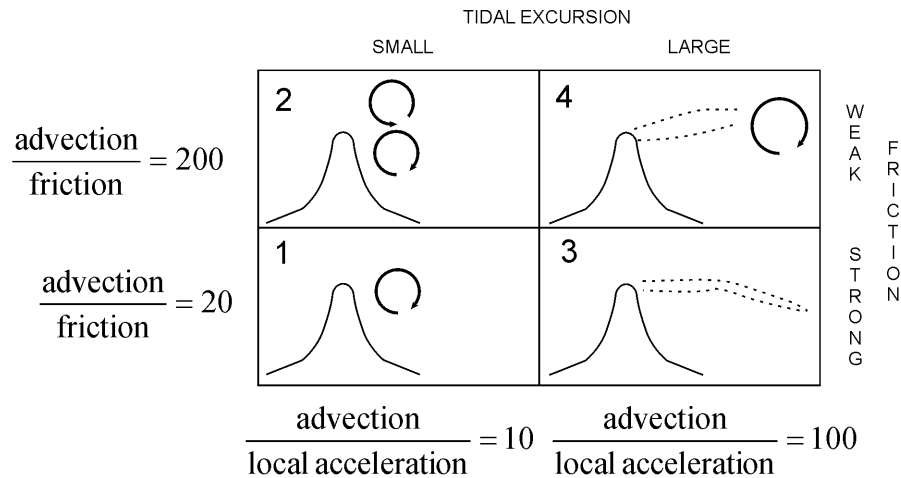
Figure 3.6 The four possible eddy types arising from weak or strong friction and short or long tidal excursion (after *Signell and Geyer* [1991]).

Cases one and two are the result of tidal excursion being on the same order of magnitude as headland length, *b*, but case one exhibits stronger bottom friction than case two. Stronger bottom friction means that the eddy will be spun down faster. Case two shows the situation when there is weaker bottom friction (either by increasing the depth or decreasing the drag). Here more than one eddy is generated and they are able to interact with each other.

Cases three and four are the result of much longer tidal excursion relative to headland length (either by increasing the tidal current amplitude or decreasing the tidal frequency, e.g. to diurnal). Case three shows the situation when strong bottom friction exists. A strong shear zone extends from the tip of the headland but strong bottom friction limits recirculation in the lee of the headland and there is stagnancy in this region. Case four shows the situation when there is weaker bottom friction. Here, the eddy is advected downstream without substantial spinning down.

The weak friction in cases two and four means that tidal eddies may interact on different phases of the tide. Strong friction in cases one and three means that eddies are spun down before the next phase of the tide.

According to *Signell and Geyer* [1991], for natural situations with M2 tides, friction length scales range from 7 to 21 km and tidal excursions range from 2 to 8 km (this empirical factor-of-two relationship between l_f and l_t is the reason for the scaling of Figure 3.6). The identification of different types of post separation behaviour of transient eddies based on the parameters l_f, l_t and α allows the testing of Signell's model with observed parameters from Cape Spencer and observed post-separation behaviour of the tidal eddy. This will be dealt with at the end of the chapter.

3.3. Data Acquisition and Processing

3.3.1. Experimental Design

For designing the ADCP tidal cycles, the same successful approach as used previously by OMG for tidal current investigations around the mouth of the Musquash estuary, New Brunswick, was adopted. *Geyer and Signell* [1990] also utilised a similar data acquisition strategy in their study of a tidal eddy in Martha's Vineyard, Massachusetts. The technique consisted of continuous steaming around a diamond-shaped track for an M2 tidal cycle and then offsetting the diamonds on successive tidal cycles to build up a larger spatial picture. Previous workers in the Bay of Fundy and Saint John Harbour have determined that, due to the resonant effect of the Bay of Fundy and the M2 tidal constituent, the M2 tidal constituent is the primary oscillation in this locale, all others are negligible [*Greenberg*, 1979; *Sankaranarayanan and McCay*, 2003]. Three square diamonds were

arranged so that the tidal current regime on the sand bank was captured (Figure 3.7, Table 3.1).

A similar data acquisition approach has also been taken by [*Geyer and Signell*, 1990] albeit more (nine) tidal cycles were executed. ADCP observations of an eddy associated with the headland Portland Bill were also carried out by *Bastos et al.* [2004] although the field technique was different in that currents along a single linear transect across the banner bank were sampled over a single spring tidal cycle.

Due to time and logistical constraints of fieldwork, no attempt was made to conduct the circuits at similar phases of the spring-neap cycle (Table 3.1 shows the acquisition days relative to the next spring tide). Figure 3.8 shows the dates of the circuits in relation to the spring-neap cycle. It is readily seen that the predicted peak flood currents vary by up to a factor of three over the spring-neap cycle. Therefore, any spatial variation in magnitude for the same phase of the tide but different day could be due to different phase in the spring-neap cycle, rather than an inherent hydrodynamic effect. However, current directional variation is assumed to be independent of spring-neap phase so therefore any interpretation of the current field must be confined to the directional pattern of the current vectors and only a broad interpretation of magnitudinal variation is possible. Furthermore, any spatial variation in magnitude for the same phase of the tide and same day can be interpreted to be an inherent hydrodynamic effect and not a spring-neap effect.
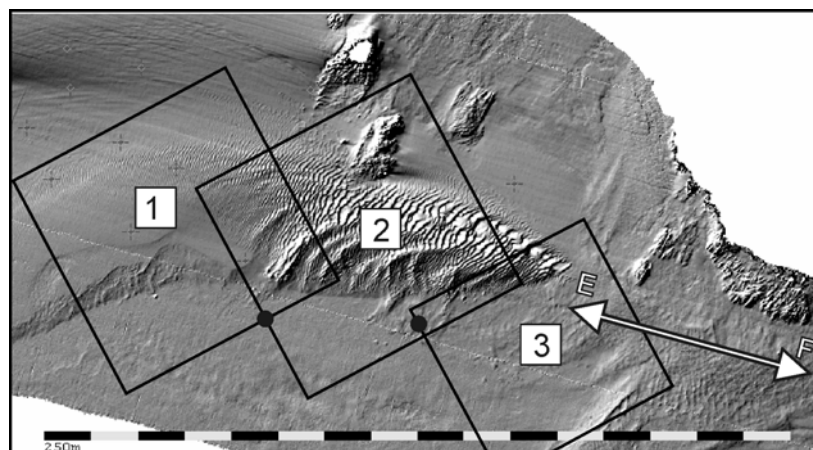
Figure 3.7 Location of the diamond tracks showing where currents were measured. Dots mark the position of the current sample locations in Figure 3.10. "E" and "F" indicate ebb and flood directions.
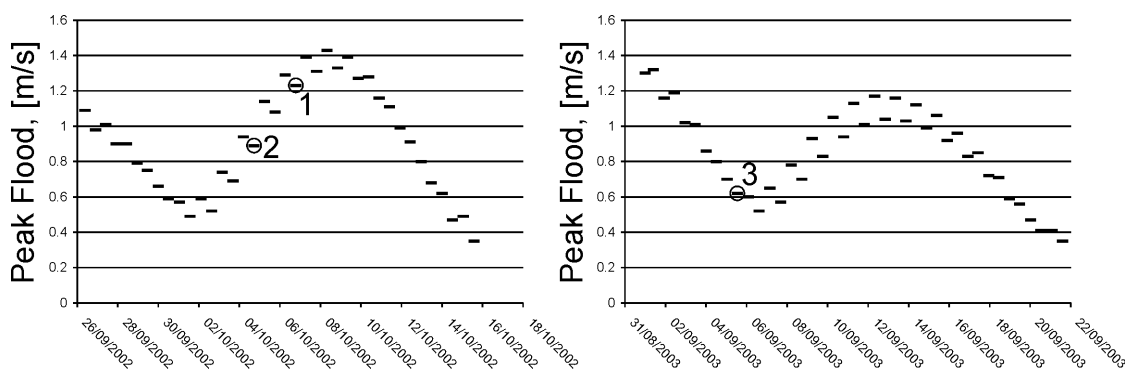
Figure 3.8 Predicted (from Nobeltec tidal prediction software) spring-neap peak flood currents over a tidal cycle at Cape Spencer showing the dates of the circuits measured in this work.

Table 3.1 Acquisition parameters of the ADCP cycles

Diamond	1	2	3
Date	6/10/2002	4/10/2002	5/9/2003
Days Relative to Spring Tide	-2	-4	-7
Side, km	1.2	1.2	1.0
Depth cell size, m	1	1	0.5
No. circuits	24	23.5	33.5

3.3.2. Data Processing

3.3.2.1   ADCP Data reduction

A data processing pipeline similar to *Geyer and Signell* [1990] was employed. Dr.

John Hughes Clarke developed and wrote the ASCII conversion utility *ReadADCP* and

the current gridding utility *CombineMultiADCP*.

Firstly, to process current vectors from different tidal cycles collected at different

times, one of the three tidal cycle surveys was deemed the reference survey and the

relative tidal phase shift of the other surveys was calculated and applied. To carry out this

last step it is of course necessary to assume the period of a tidal cycle. M2 was assumed to

be dominant in this case and the phase shifts were calculated the basis of this assumption.

When the phase shifts have been applied, the current vectors from different ADCP

measurement cycles are ready to be averaged together.

Secondly, depth-averaged current data that were collected within a 30 minute time

window (relative to the M2 tidal phase) were spatially averaged into a 75 m spatial grid.

In Figure 3.9(a), there is a pair of track lines with instantaneous current vectors indicating

that these data were collected within the time window, i.e. the time window is of

sufficiently long duration to capture one complete circuit. There is also another track line

in the figure from another diamond and collected at the same tidal phase. Figure 3.9(b)

depicts the spatially and temporally (for that time window) averaged vectors at the centre

of each grid cell. Processing a single tidal cycle in this fashion yields a single tidal cycle

time series at each grid cell (the superimposed vectors in Figure 3.9(c) are the averaged

current vectors for successive windows). Outlier rejection in this stacked vector field was

achieved by stacking the vectors in a 75 by 75 m cell only if it contained more than 50

ensembles (i.e. the total number of vectors in each cell in Figure 3.9(a)). The primary and residual (tidally averaged) current field were derived by stacking current vectors in 30 minute and 12.42 hour increments respectively. Calculation of tidal ellipses is done by using all the vectors in each cell of Figure 3.9(c).
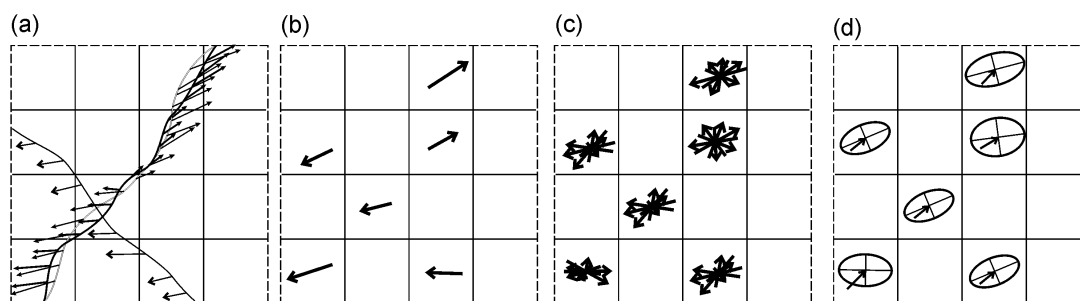
Figure 3.9 (a-d) Illustration of processing steps to derive current ellipses.
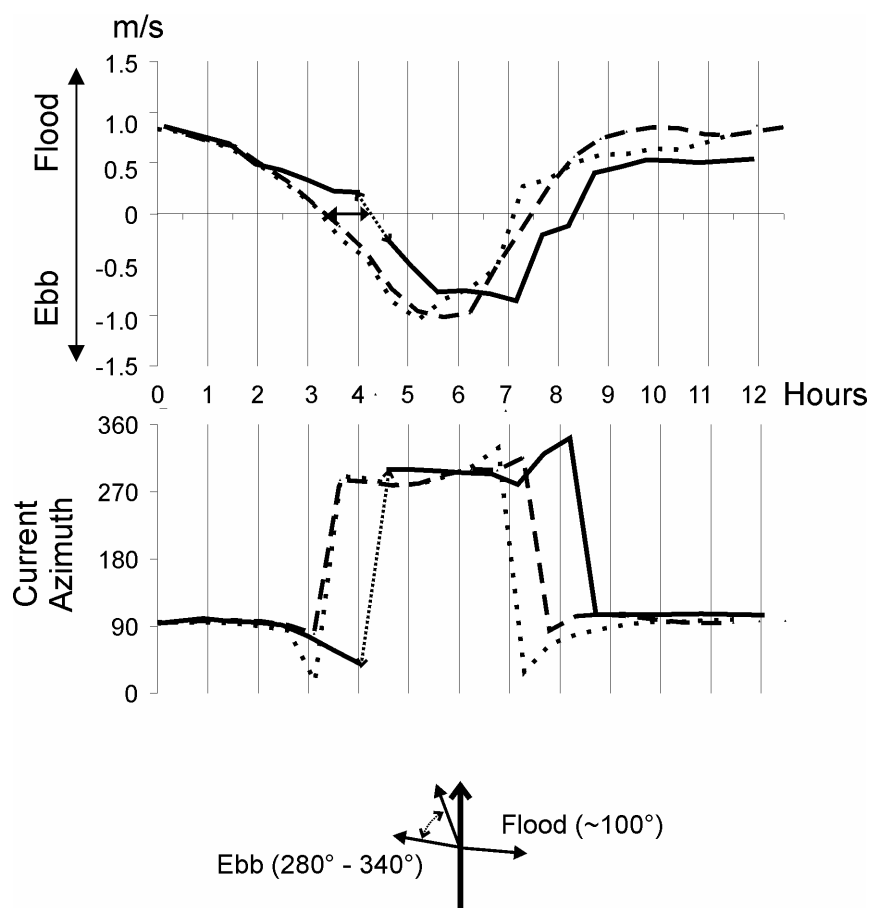
Figure 3.10 Comparison of phase of tidal cycle surveys in terms of magnitude and direction. Solid line denotes 2003 tidal cycle; broken lines denote 2002 surveys. Dotted double-headed arrow denotes interpolation of current in 2003 survey. Solid double-headed arrow denotes the ~1 hour delay between the 2002 and 2003 surveys.

Figure 3.10shows current magnitudes and azimuths plotted against phase relative to

the earliest 2002 survey. The locations of the points were chosen to be close together and

relatively offshore and are given in Figure 3.7. Clearly, the 2002 surveys line up well and

are in phase with each other. However, when comparing the transition between flood and

ebb currents, the 2003 survey is lagged ~1 hour (2 time samples) with respect to 2002

surveys. There was almost a year between the 2002 and 2003 surveys so the assumption

of pure M2 tidal component (denoted by the dotted line in Figure 3.11) for all that time

may be invalid.
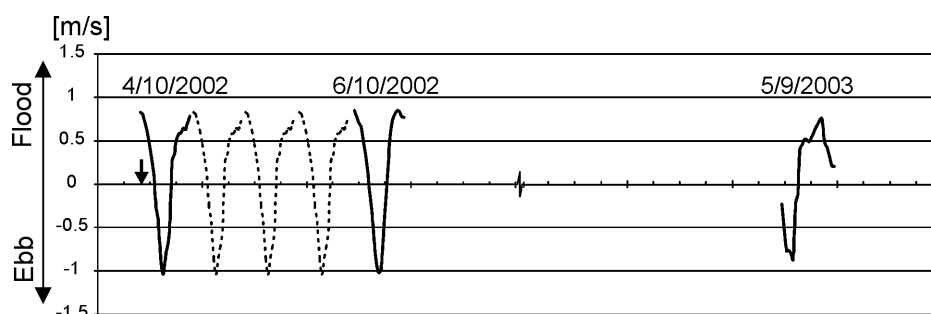
Figure 3.11 Time relationship of the three surveys. Major tick mark is 24 hours. Arrow denotes reference
time.

To test whether this was the case, each of the current measurement cycles was referred

to its preceding predicted high water at Saint John Tide gauge, such an operation should

minimise errors due to the accumulation of other constituents over the year. The results of

this are displayed in Figure 3.12.
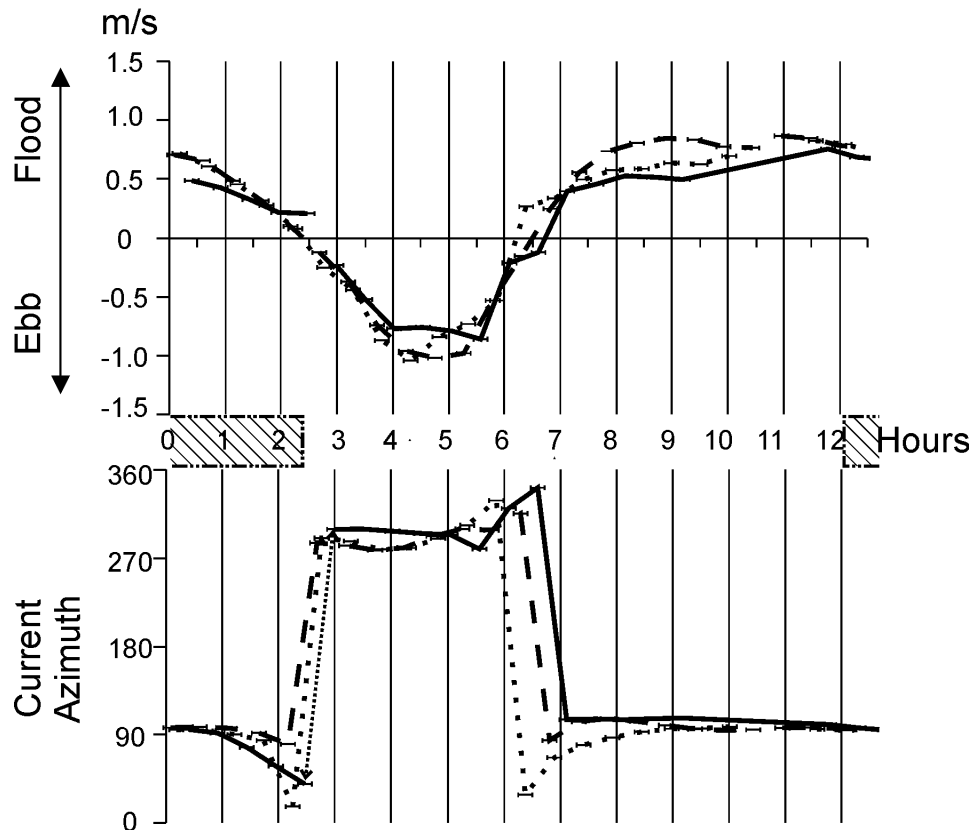
Figure 3.12 Phase relationship of the three surveys using their preceding predicted times of high water as reference times. The hatched box denotes the period of incursion of relatively fresher water from the advected plume of the Saint John River (to be discussed in Section 3.4.4).

The horizontal error bars indicate possible errors in predicted high-water times, ±7.5 minutes, this error value was arrived at through comparing observed high-water with predicted high-water. Comparison of Figure 3.10 and Figure 3.12 reveals that the phase error has been much decreased using the most recent predicted high-water reference times. The discrepancy is now less than the sampling frequency (~30 minutes). It's worth noting that the three tidal cycles are synchronized at the change from flooding to ebbing currents, but there is a discrepancy at the change from ebbing to flooding currents because of unequal durations of ebbing currents (possibly due to the dependence of the behaviour of a tidal eddy on its preceding peak ebb current, which was different for all three tidal cycles), not because of different phases.

In summary, simultaneous display of currents with the same relative phase enabled compilation and interpretation of "synoptic" maps of current vectors (Figure 3.15 to Figure 3.18).

3.3.2.2   Current ellipses

Calculating the major and minor axes of the current ellipse described by the locus of the instantaneous current vector, $u\mathbf{i} + v\mathbf{j}$, is the same as finding the eigenvalues of the two by two covariance matrix formed by σ^2_{UU} and σ^2_{VV} (the variances of u and v over the tidal cycle) as the diagonal elements and σ^2_{UV} (the covariance of u and v over the tidal cycle) as the off-diagonal elements [*Butman et al.*, 2002]. The solution is shown in Equation (3.8).

where

$$\mathbf{R} = \bar{u}\mathbf{i} + \bar{v}\mathbf{j}$$

$$a = \sqrt{4(\sigma^2_{UU} + \sigma^2_{VV} + X)}$$

$$b = \sqrt{4(\sigma^2_{UU} + \sigma^2_{VV} - X)}$$

$$\alpha = 90^\circ - \frac{1}{2}\tan^{-1}\left(\frac{2\sigma^2_{UV}}{\sigma^2_{UU} - \sigma^2_{VV}}\right)$$

$$e = 1 - \frac{b}{a}$$

$$X = \sqrt{\left(\frac{\sigma^2_{UU} - \sigma^2_{VV}}{2}\right)^2 + \left(\sigma^2_{UV}\right)^2}$$

$$\sigma^2_{UV} = \frac{1}{n}\sum(u - \bar{u})(v - \bar{v})$$

$$\sigma^2_{UU} = \frac{1}{n}\sum(u - \bar{u})^2$$

$$\sigma^2_{VV} = \frac{1}{n}\sum(v - \bar{v})^2$$

(3.8)

In some locations, observations of the tidal cycle were not possible at all phases of the tide, e.g. due to poor track following; ellipses plotted using these undersampled data will be biased. To counteract this effect, only current ellipses in areas where at least 97% of the tidal cycle (or at least 23 out of 24 half hourly observations) were sampled and plotted. Ellipses are plotted with their centres at the end of the residual current vectors (Figure 3.13).
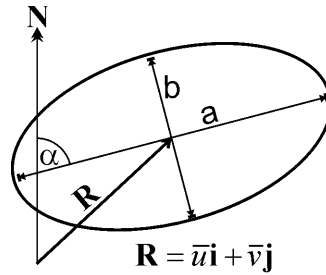
Figure 3.13. Definition sketch of tidal ellipse parameters.

Current ellipses are useful to investigate the degree of isotropy of the tidal currents at a point. A highly eccentric current ellipse means that the currents at that point are highly bi-polar over the tidal cycle. In contrast, as the current ellipse becomes more circular, this means that the current changes direction by gradually changing its azimuth rather than just flicking between one direction and the opposite direction. Tidal asymmetry, where the current in one direction has appreciably longer duration than that in the opposite direction, is expressed in the current ellipse by the length of the residual current vector.

3.3.2.3   Vertical Current Profile Calculation

The assumption of a logarithmic current velocity profile is generally assumed so that depth-averaged currents may be employed to estimate the bottom shear stress and thus sediment transport rate. This assumption was tested in this section.

For a variety of seabed types, the theoretical logarithmic vertical profile is closely approximated by a power law profile (Equation (3.9)) relating current speed, U, at a height above the seabed, z, to the depth-averaged current speed, $\bar{U}$ [*Soulsby,* 1997].

$$U(z) = \left(\frac{z}{0.32h}\right)^{1/7} \bar{U} \ \text{ for } \ 0 < z < 0.5h$$

$$U(z) = 1.07\bar{U} \ \text{ for } \ 0.5h < z < h$$
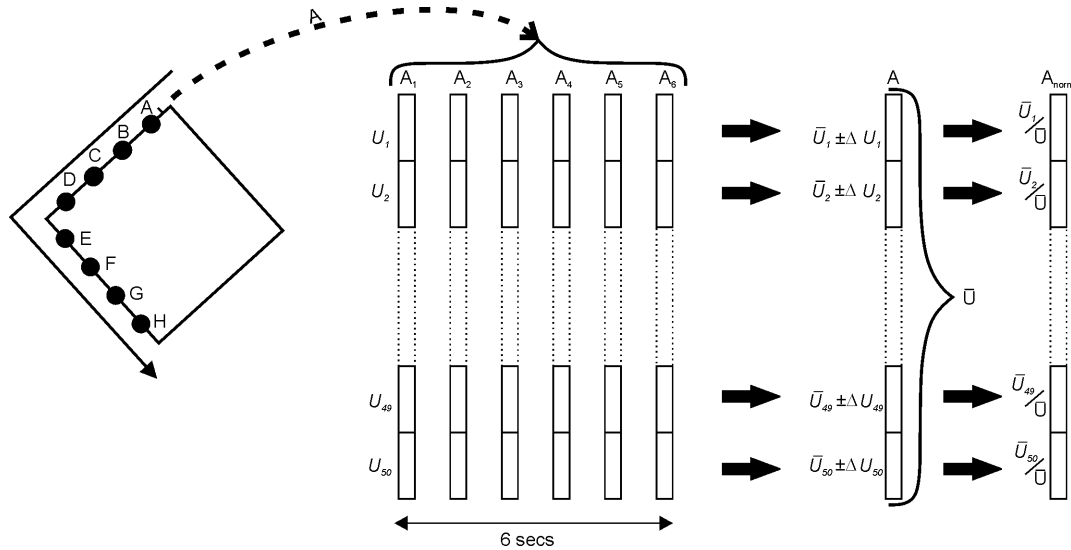
Figure 3.14 Illustration of averaging process to calculate normalized current velocity profiles. A-H denote locations of ensemble averaging along a transect denoted by the crooked arrow. Curly braces denote horizontal and vertical averaging.

Figure 3.29 to Figure 3.32 (to be discussed in detail later) show plots of the current relative to the depth-averaged current ($U/\bar{U}$) at a fractional height of the water column(z/h) for a sample of averaged ensembles (the different point symbols in Figure 3.29 to Figure 3.32 denote the results of averaging within circles A, B, etc.) for nine transects[*] taken throughout the tidal cycle on the Oct 6th 2002 measurement epoch. Figure 3.14 illustrates the process of calculating these profiles. $U(z)$ is calculated by a moving average of the north and east components of each bin, i.e. each bin is averaged horizontally over six ensembles (equivalent to six seconds), before the depth-averaged current, which is the vertical average of the bins comprising $U(z)$ that contain values, is calculated. Errors in the calculation of $U/\bar{U}$ arising from the horizontal averaging are calculated based on the standard deviation of the east and north components of a given bin. These error bars are

displayed for one averaged ensemble on each transect in Figure 3.29 to Figure 3.33 inclusive.

3.4.   Current Analysis and Interpretation

By comparing the currents to the observed tide stage, it was apparent that the headland had a major hydrodynamic influence on the current field in addition to the tide stage. As discussed in Section 3.3.1, an important proviso on current interpretation in this work is that, because of the extreme change (as much as 20% (Figure 3.8)) in peak tidal current from day to day over the spring-neap cycle, it is difficult to make general statements about spatial patterns in current magnitude across the three diamonds. However, it is assumed that spatial trends in current azimuths may be interpreted to be independent of phase in the spring-neap cycle.

3.4.1. Temporal current field variation

From sequentially examining the current fielding 31 minute increments, it was possible to make an interpretation by sketching streamlines of the tidal flow (Figure 3.15 to Figure 3.18). Immediately evident is the dominance of the primary tidal eddy on the ebbing tidal current field. As it is advected away from the headland, its clockwise rotation induces currents over the sand bank to flow opposite to the expected ebb current direction, i.e. they flow towards the headland instead of away from the headland.

---

[*] A "transect" is taken here to mean one half of a circuit moving either onshore to offshore or the opposite direction.
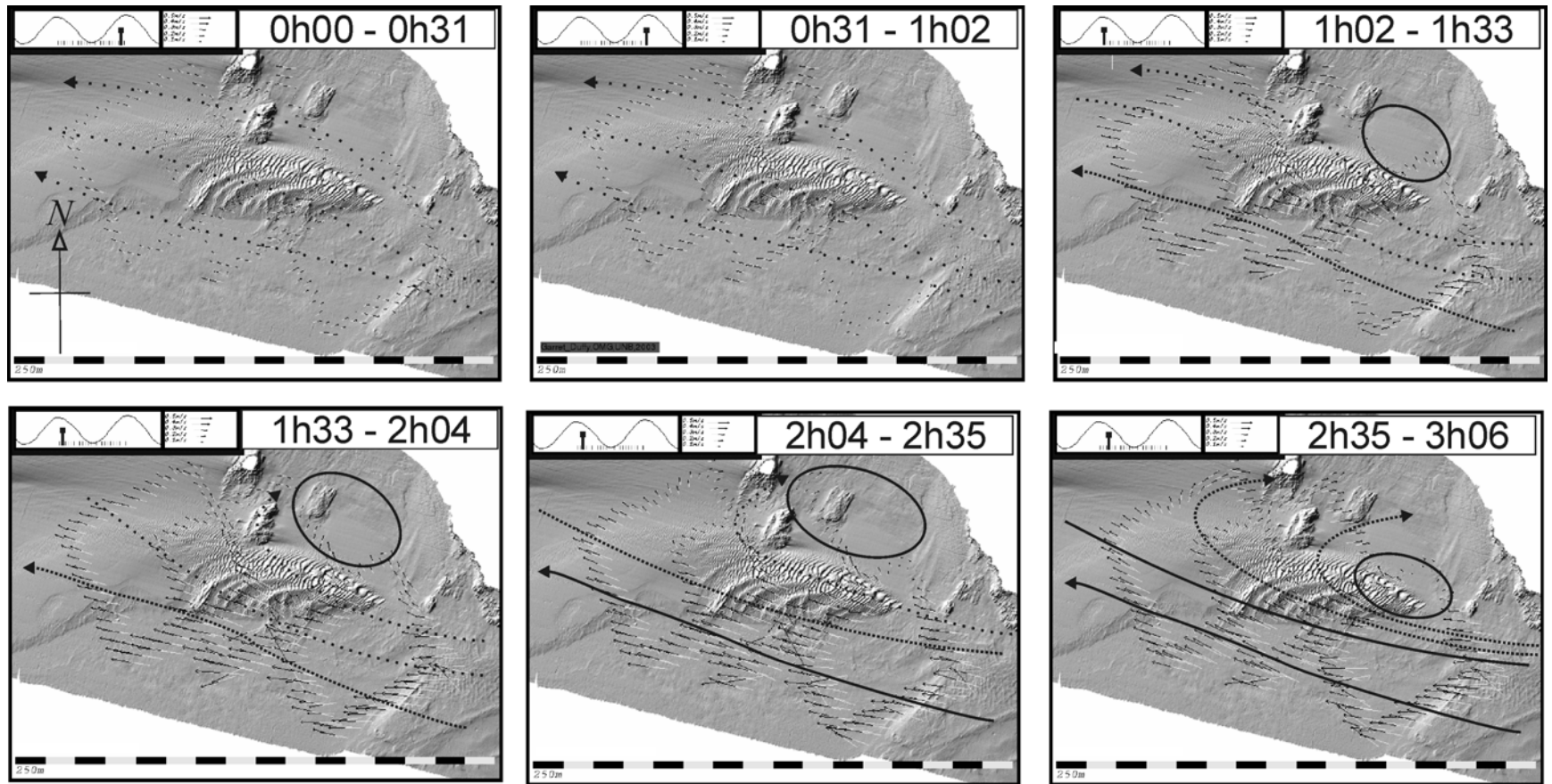
Figure 3.15 Interpretation of the first quarter of a tidal cycle in increments of 1/24th of a tidal cycle starting from slack before ebb. In the inset of each is the phase of the tide.
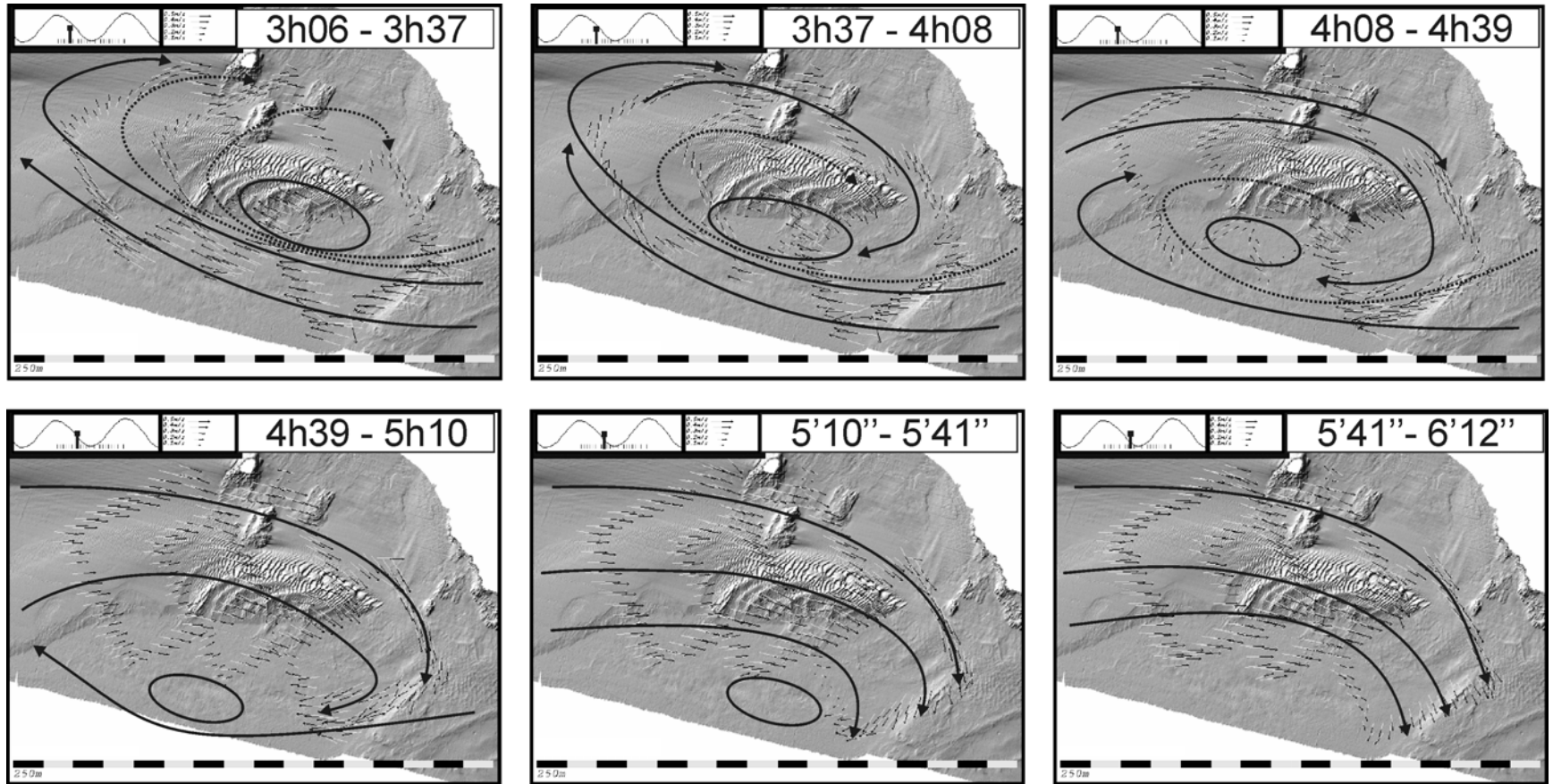
Figure 3.16 Interpretation of the second quarter of a tidal cycle in increments of 1/24th of a tidal cycle. In the inset of each is the phase of the tide.
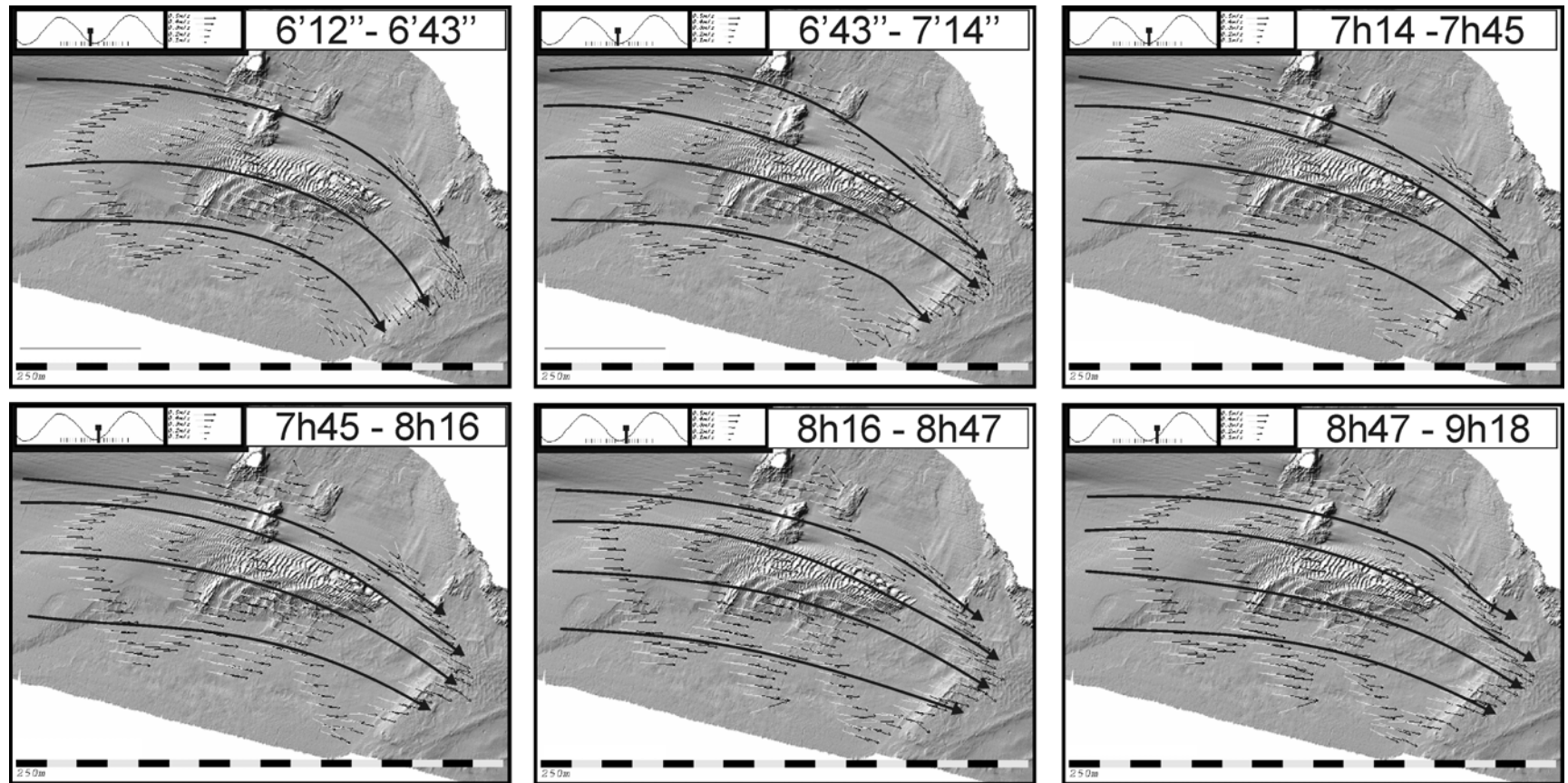
Figure 3.17 Interpretation of the third quarter of a tidal cycle in increments of 1/24th of a tidal cycle. In the inset of each is the phase of the tide.
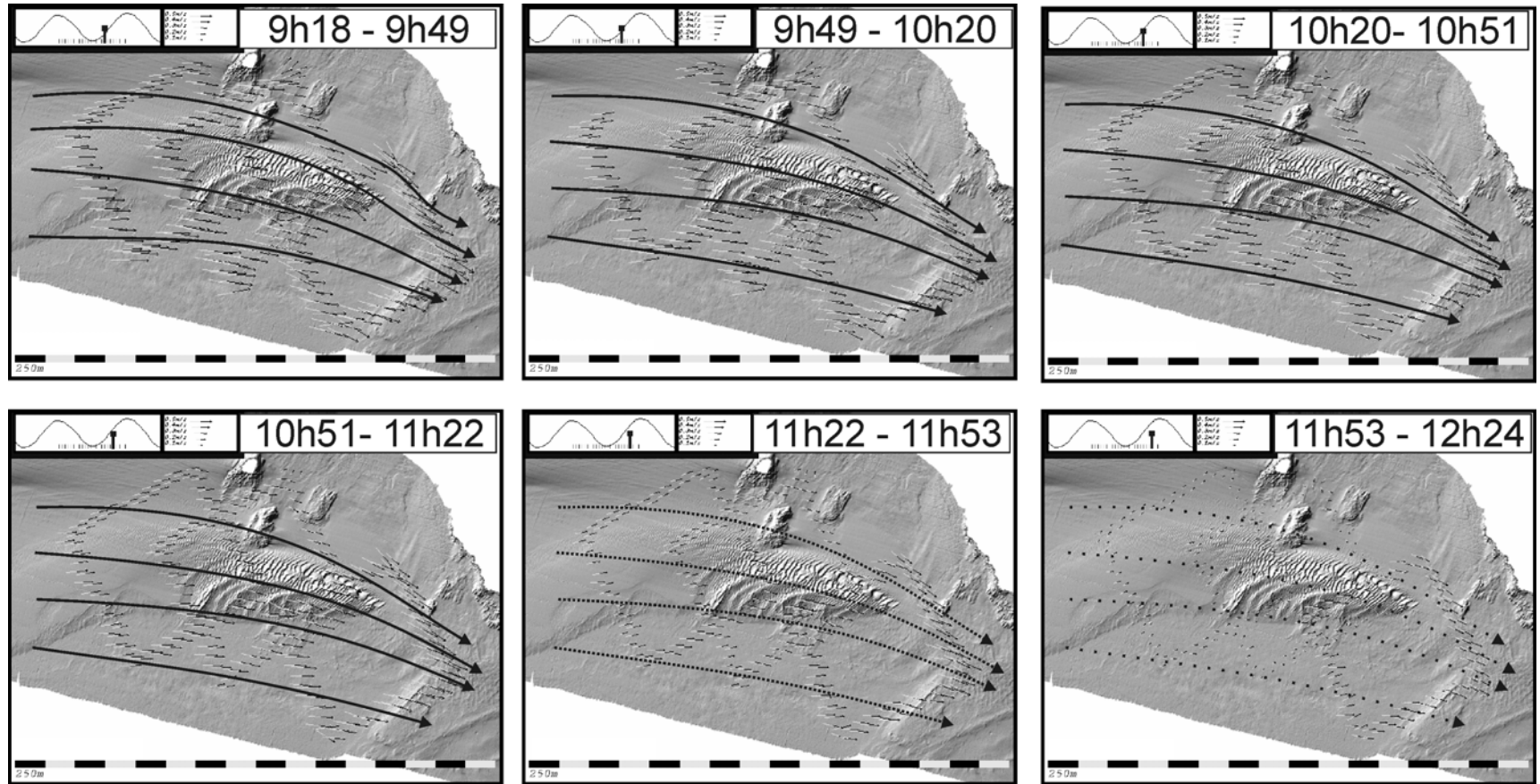
Figure 3.18 Interpretation of the last quarter of a tidal cycle in increments of 1/24th of a tidal cycle. In the inset of each is the phase of the tide. During this period, fresher water incurred from the advected plume of the Saint John River (to be discussed in Section 3.4.4)

The interpretation starts just after high water as weak (15 cm/s, depth-averaged) ebb currents flow down the Bay of Fundy and around the headland in a WNW direction. The ebb currents steadily increase until at around 90 minutes after high tide when depth-averaged currents offshore reach their maximum of at least[*] 110 cm/s. At this time, high shear (note high velocity gradient at this time in the lee of the headland in Figure 3.19) causes the ebb currents close to the headland to pull away from the headland leaving the eye of the incipient eddy in its lee.
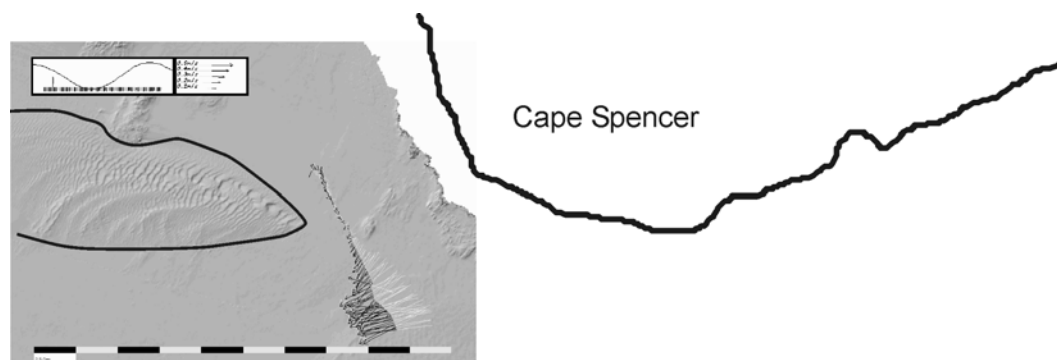
Figure 3.19 Raw data showing lateral shear of peak ebb currents. The area of slack water in the lee of the headland is part of the eye of the incipient tidal eddy.

From 2h04 to 5h10, the localized circulation of the tidal eddy is seen to be steadily advected in a south-south-westerly direction across the sand bank. The effect of this localized circulation means that even during the falling tide, currents over the sand bank still flow towards the headland in the "flooding" direction. The eddy takes the form of an ellipse stretching out downstream of the headland rather than a neat circular vortex. This is especially noticeable between 3h06 and 4h08 From 5h10 until 6h43 (bearing in mind that low water occurs at roughly 6h12), spatial curvature (or vorticity) of the current

---

[*] "at least" because the currents in Figure 3.19 were measured close to a neap tide (see Figure 3.8 (right)) and so reflect minimum peak currents close to the headland.

vectors shows that the tidal eddy still has an effect on the current field of the sand bank during this time.

As the tide rises after low water the vorticity of the current field decreases, and the streamlines straighten out. Flood currents are now seen to be uniform in strength across the sand bank although inspection of the contoured currents in Figure 3.20 shows that there is a marked increase in velocity gradient as the currents approach the headland where they increase in strength due to the Venturi effect. The series ends as the flood currents are seen to diminish at slack water around high tide.
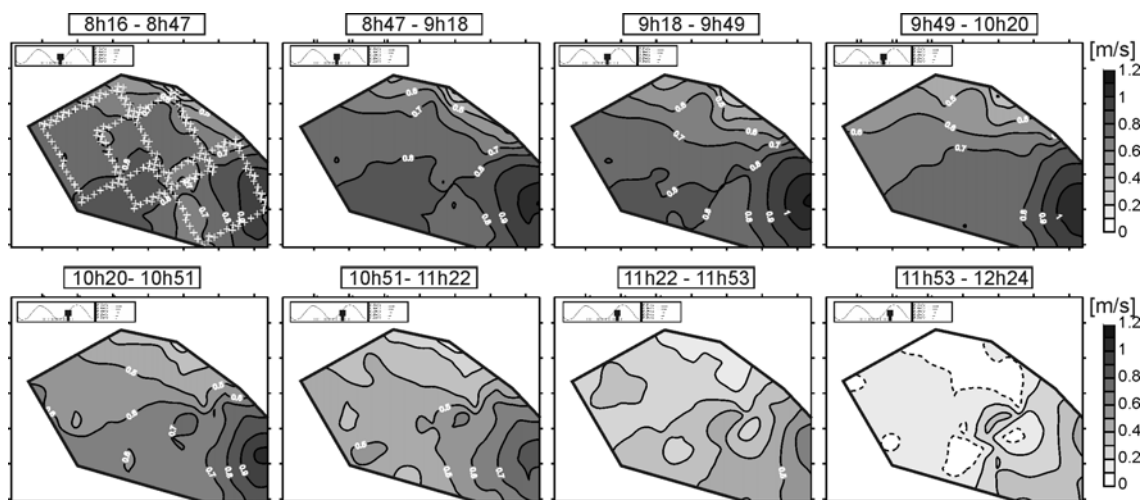
Figure 3.20 Contoured magnitude of currents between 8h16 and 12h24 in Figure 3.17 and Figure 3.18. Flow is from left to right. Acceleration of currents around the headland and subsequent slackening is plainly seen in the lower right hand of the figures.

3.4.1.1   Spatial Hydrograph Variation.

Another useful method is inspecting the change in current magnitude and azimuth at a point over the tidal cycle or "hydrograph", to use a term from surface hydrology. Previous to the use of ADCPs on moving platforms, inspection of the change in flow at a point was the main mode of analysis of currents through the use of arrays of bottom-mounted or buoy-mounted current meters. A relevant example of such an application is *Dyer and*

Huntley [1999], where current meters were situated inshore and offshore of a banner bank in Devon. The use of an ADCP on a moving platform, is analogous to using many such current meters and so is capable of greater spatial resolution of current variability, although lesser temporal resolution is achievable than stationary current meters because the frequency of repeat current measurements at a point depends on the speed of the vessel and the perimeter of the track line.

Figure 3.21 , Figure 3.22 and Figure 3.23 show the observed depth-averaged currents measured at points moving along one side of a diamond from inshore to offshore. Immediately obvious is the marked increase in the strength of currents flowing away from the headland as we move seaward at the initiation of the falling tide (see dotted arrows at bottom of Figure 3.21 , Figure 3.22 and Figure 3.23). This is due to the rotational effect of the tidal eddy that causes inshore currents, initially flowing away from the headland, to diminish almost as soon as they are initiated and then increase in the opposite direction while currents farther offshore are continuing to flow in the opposite direction. Therefore, the time at which currents flowing away from the headland start to decrease is taken as the time the eddy begins to have an effect. This time is denoted by the downward arrows in each of the three figures and it is clear that the time between when the eddy is initiated inshore to the time when the eddy affects the whole current field is quite short, just over one hour.
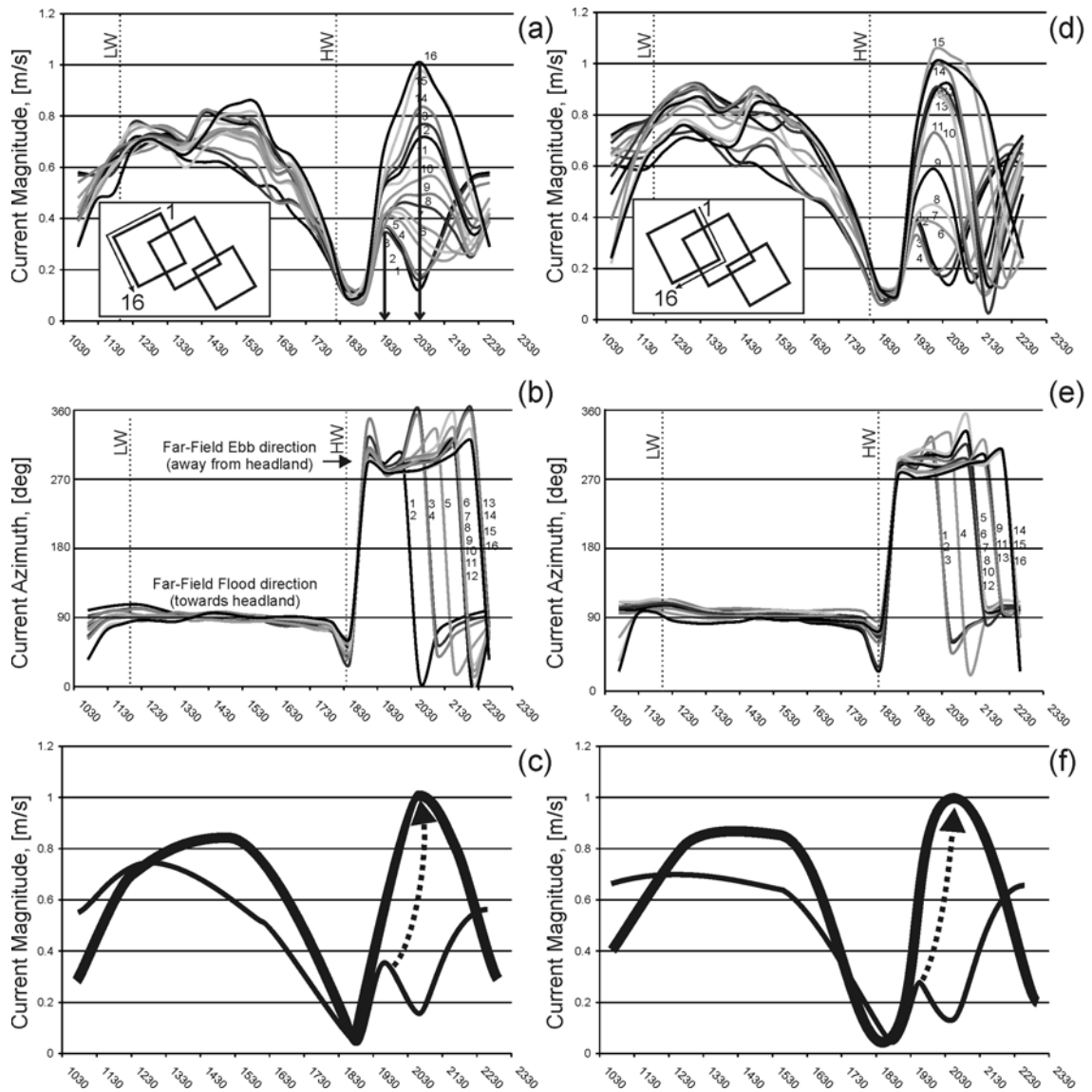
Figure 3.21 Offshore variation of currents in eastern diamond. Increasing numbers denote increasing distance offshore. Inset shows location of current measurement points. Downward straight arrows in (a) denote time the eddy begins to affect the current field. Bottom charts show interpretation of innermost hydrograph (lighter line) and outermost hydrograph (heavier line). Dotted line shows increasing peak of currents flowing away from the headland moving to seaward. Also shown is time of observed low and high waters at Saint John tide gauge.
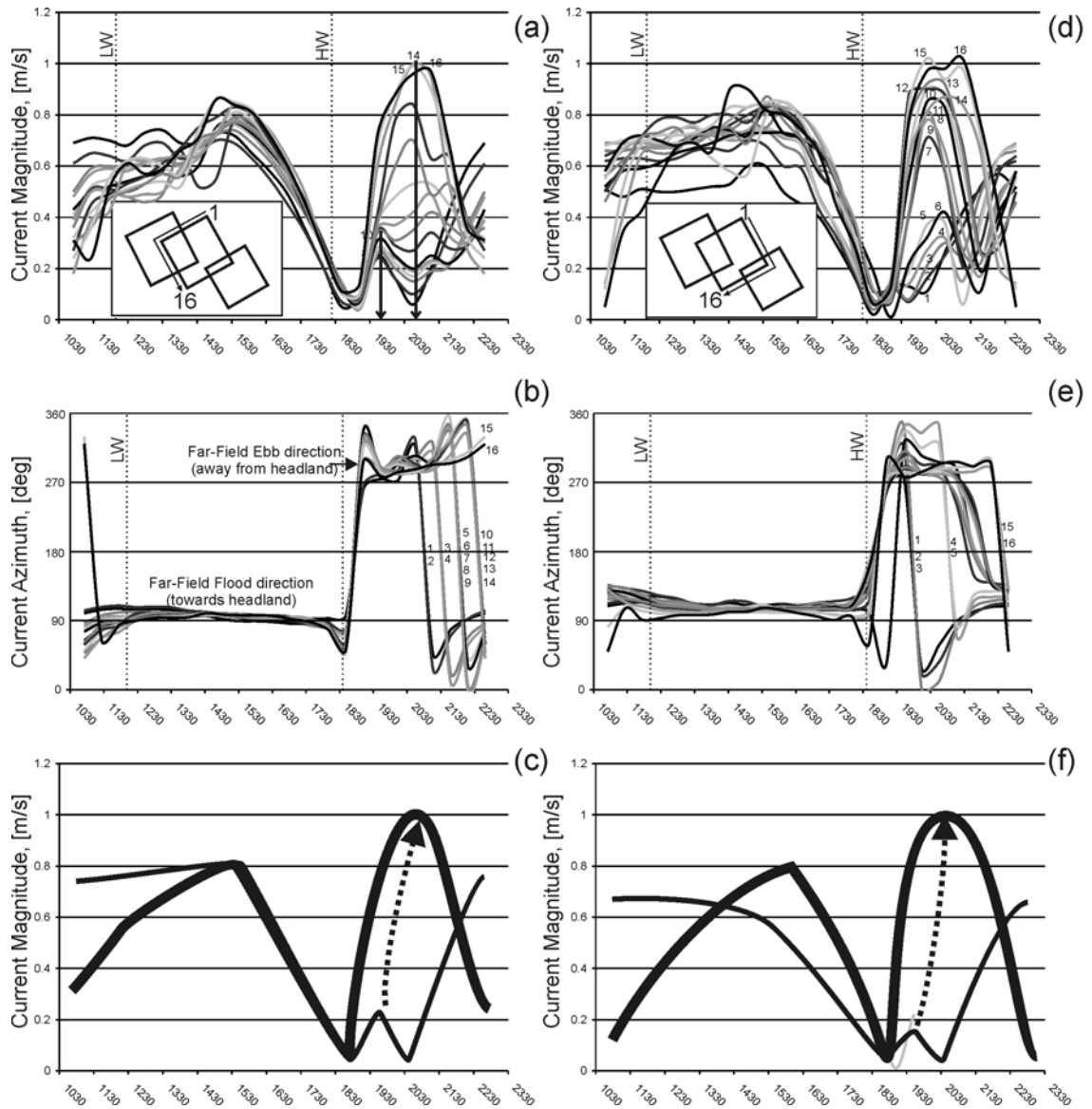
Figure 3.22 Offshore variation of currents in
central diamond with interpretation.
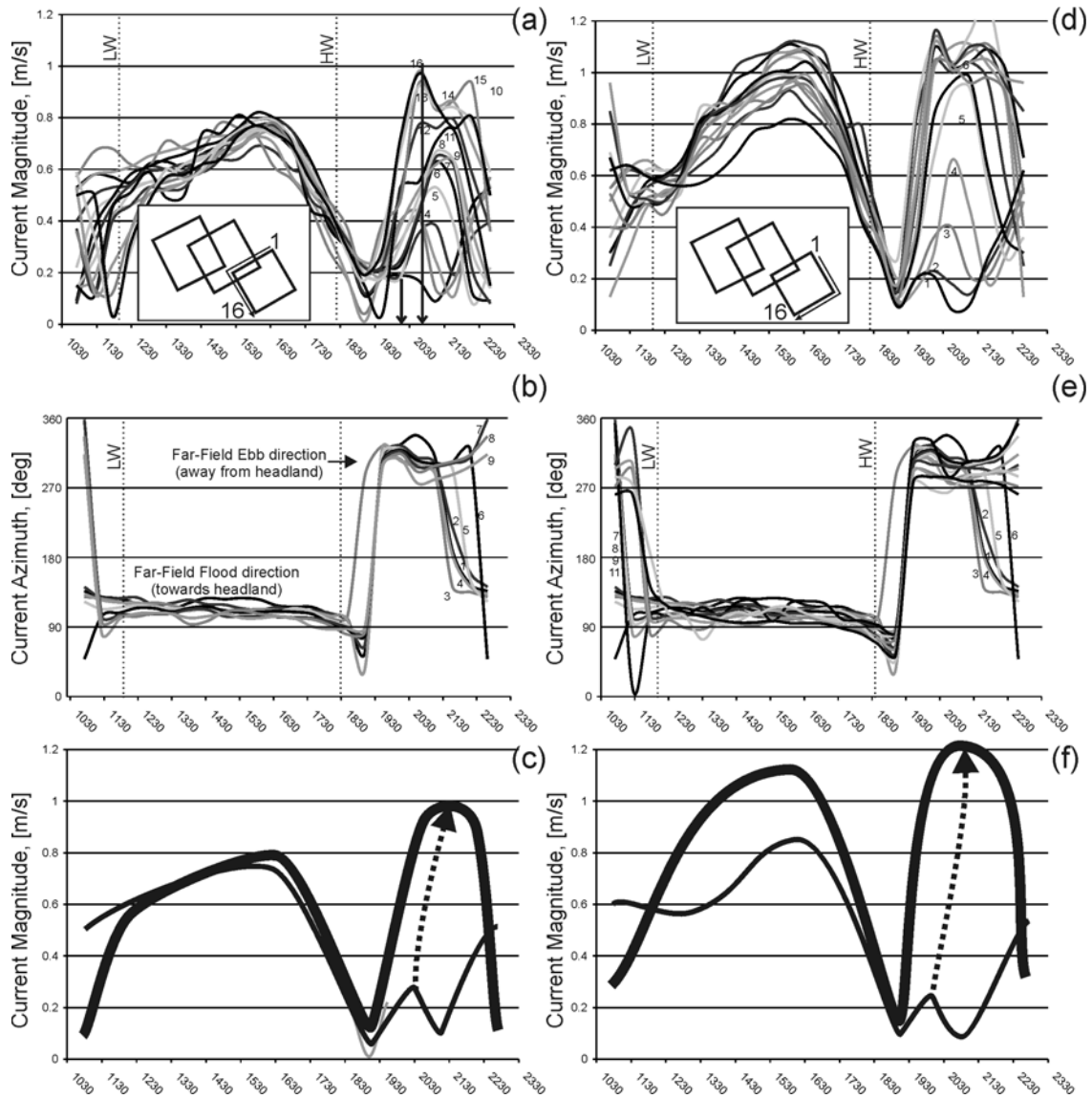
Figure 3.23 Offshore variation of currents in western diamond with interpretation.

Figure 3.24 shows typical hydrographs at key points around the field area. The general picture is that inshore currents flowing toward the headland are 3-4 times greater than inshore currents flowing in the opposite direction. Currents flowing towards the headland are also longer in duration than opposing currents. In contrast, offshore currents are greater magnitude flowing away from the headland although still shorter in duration.
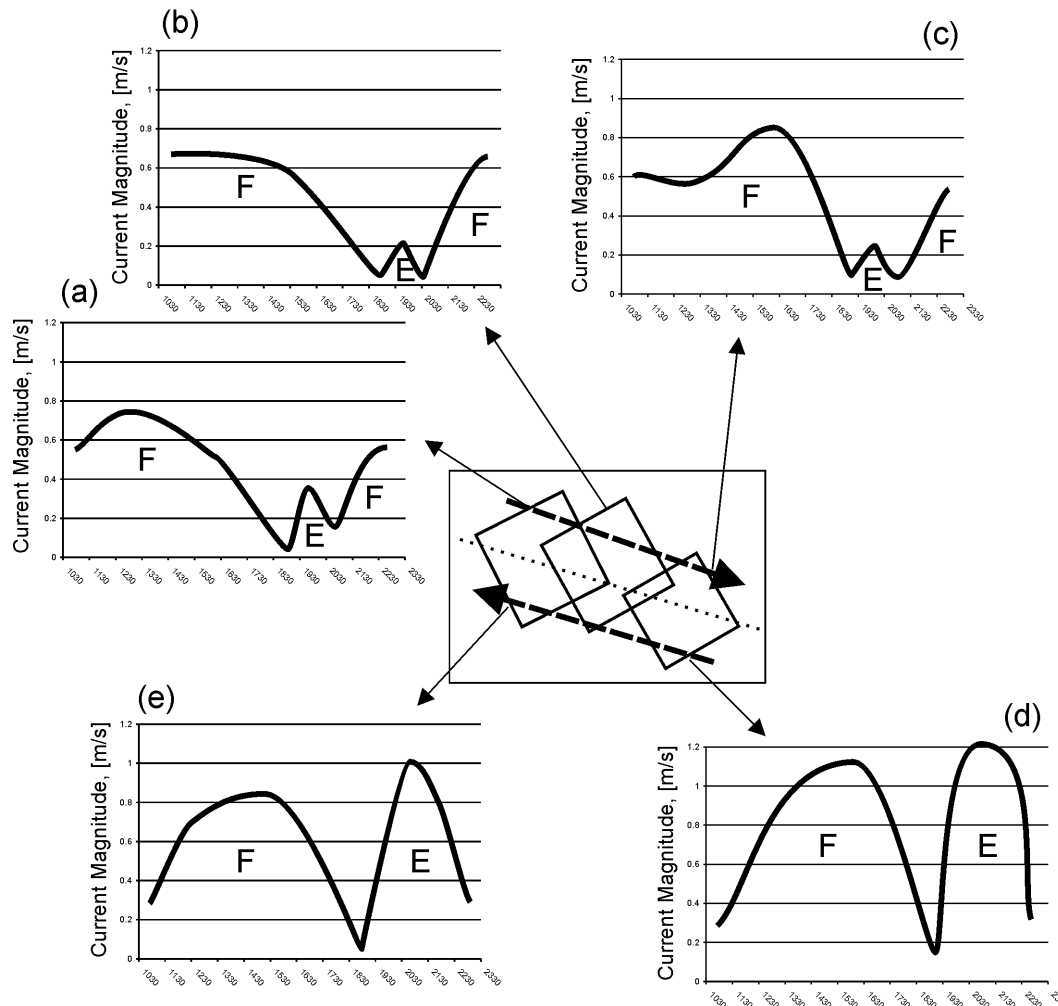
Figure 3.24 Summary interpretation of current magnitude variation over the field area. Currents flowing in the ebb direction ("E") markedly decrease in strength inshore. Dashed arrows show direction of peak currents, which will be shown in a later chapter to indicate net sediment transport direction. Dotted line schematically indicates line of bedload reversal.

The current pattern in Figure 3.24 has implications for sediment transport: according to *Johnson et al.* [1982], sediment transport is expected to be oriented parallel to the peak current direction. Using modelled peak current direction as an indicator of net bedload transport direction, *Bastos et al.* [2002] noticed that the headland associated sand banks lay only within a well defined area, the so called "line of bedload reversal" (indicated on Figure 3.24), that separated zones of opposing peak currents. This concept will be explored at the end of this thesis.

3.4.2. Current Ellipses

Figure 3.25 shows the result of fitting ellipses to the current vector at a point over the

tidal cycle. As mentioned in Section 3.3.2.2, only those ellipses calculated from at least

97% of the tidal cycle were plotted to eliminate biased ellipses.
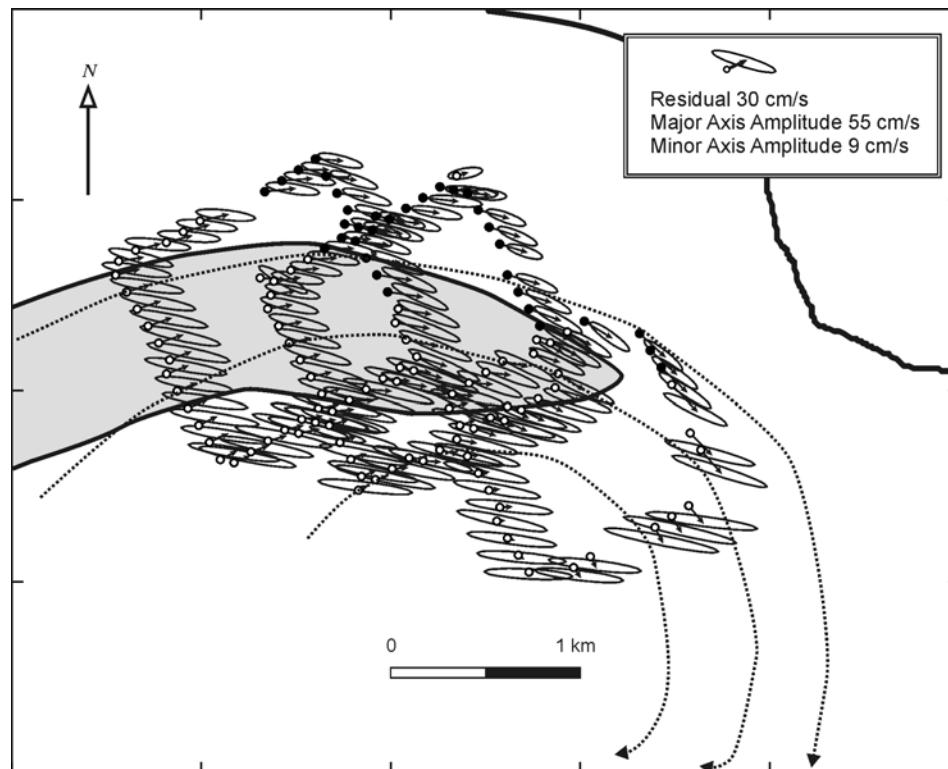
Figure 3.25 Map showing current ellipses and residual current where 96% of tidal cycle was sampled.
Dotted lines depict interpretation of residual eddy based on residual current vector curvature. Sand bank
denoted by the filled grey shape.

The three tidal cycles successfully resolved part of the residual "eddy" (the interpreted

dotted line in the figure). This feature is a result of the advection of the transient tidal

eddy from the lee of the headland to offshore and has been observed in the tidally

averaged current fields around other headlands [*Pingree*, 1978; *Imasato*, 1983; *Geyer and

Signell*, 1990]. It is notable that the sand bank itself lies shoreward and off-centre of the

residual eddy, contrary to *Pingree and Maddock* [1979] who said that banner banks should

form at the centre of residual eddies. However, the sand bank location agrees with the

mathematical model of banner bank formation put forward by *Signell and Harris* [2000].
Signell and Harris [2000] and *Bastos et al.* [2002] state that this residual eddy,
proportional to the tidally integrated instantaneous current, has theoretically little impact
on sediment transport because net sediment transport depends primarily on the tidally
integrated *cube* of the instantaneous current. Practically, this means that just because the
residual current vectors in Figure 3.25 do not reverse in direction moving offshore, does
not mean that sediment transport does not reverse. This latter has implications for the
sediment transport discussion in Chapter 7.
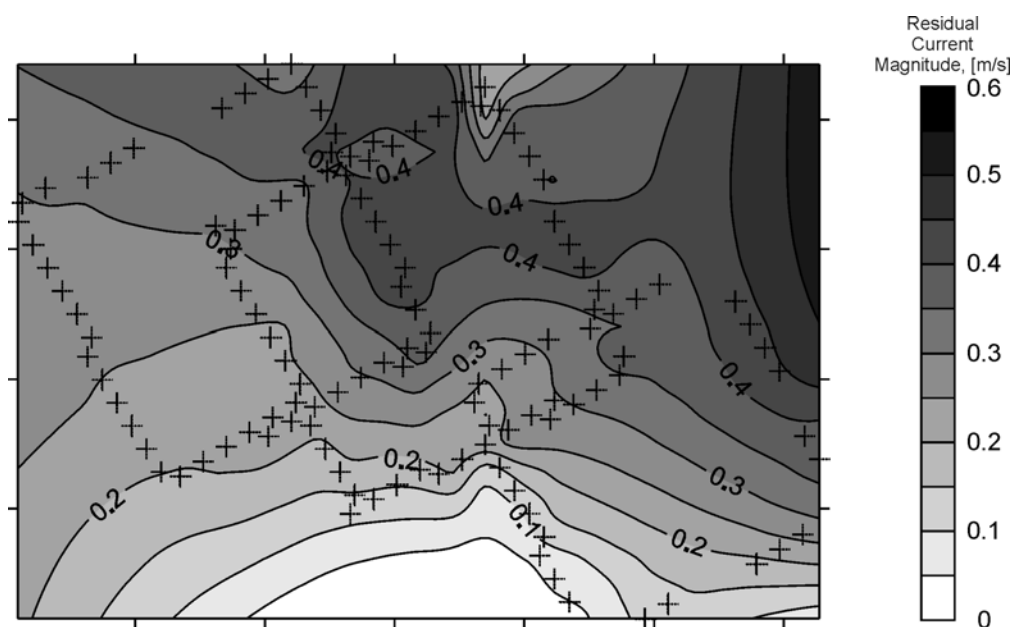
Figure 3.26 Contour map of residual current magnitude. Crosses denote sample points where at least 23/24 of the tidal cycle was sampled.

Residual current magnitude is seen to increase from the residual eddy centre where
residual current approaches zero to 40 - 45 cm/s in a broad zone stretching from over the
large sand dunes to adjacent to the headland itself (Figure 3.26), such a trend was also
noted by *Geyer and Signell* [1990]. This increase of residual current strength reflects the

increase in tidal asymmetry as we move closer to the headland because tidal currents in this region rarely reverse from the flooding direction.

In contrast to residual current magnitude, the tidal current amplitude, i.e. the semi-major axis of the tidal ellipse, is observed to increase to seaward from 25 cm/s in the lee of the headland to over 75 cm/s at a point close to the tip of the headland (Figure 3.27) and to over 65 cm/s at seaward portions of Diamonds 1 and 2. The general increase in tidal current amplitude towards the tip of the headland is a reflection of the Venturi Effect induced amplitude increase on either phase of the tide.
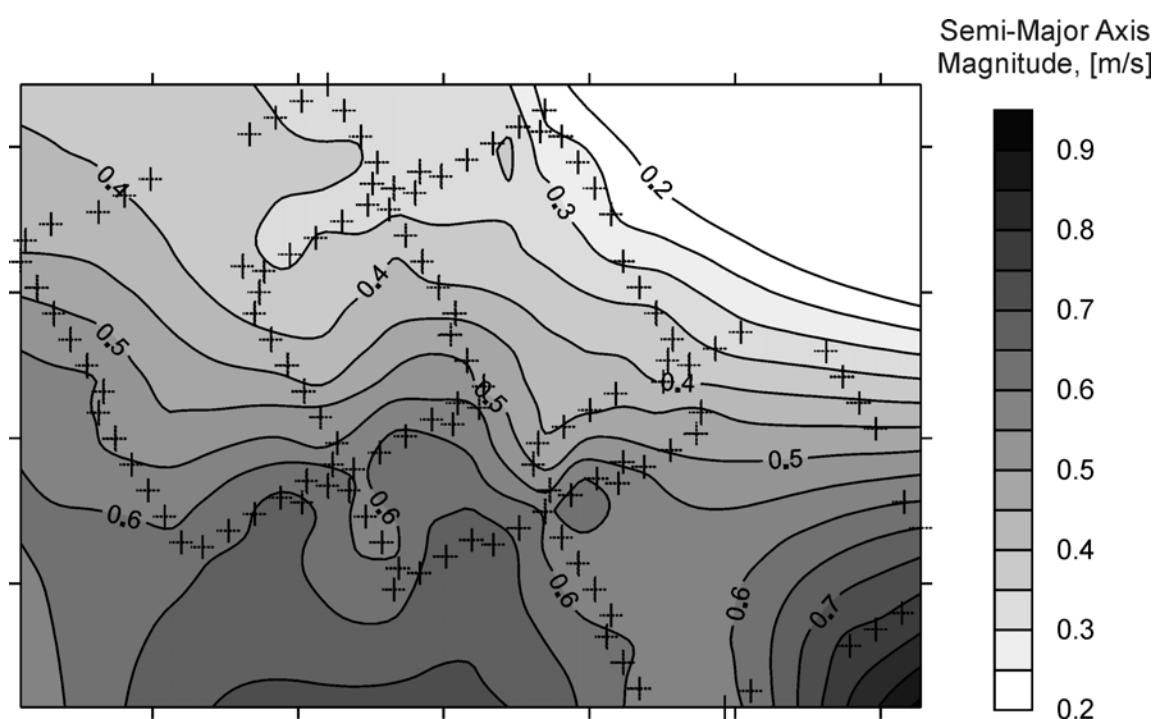
Figure 3.27 Contour map of semi-major axis magnitude. The kinks in the contours are due to the fact that tidal currents were sampled on different phases of the spring-neap cycle.

Comparison of the residual current magnitude and the magnitude of the semi-major axis of the current ellipse reveals a region where the tide current amplitude is less than the residual current, i.e. according to the current ellipses, there is a region in the lee of the headland where tidal current does not reverse, just oscillates between slack and peak flood.

This implies that in the lee of the headland, the current regime is almost unidirectional (Figure 3.28 (right)). The current regime in this zone could explain the presence of the relatively large, markedly asymmetric dunes where the zone overlaps the sand bank (Figure 3.28 (left)).
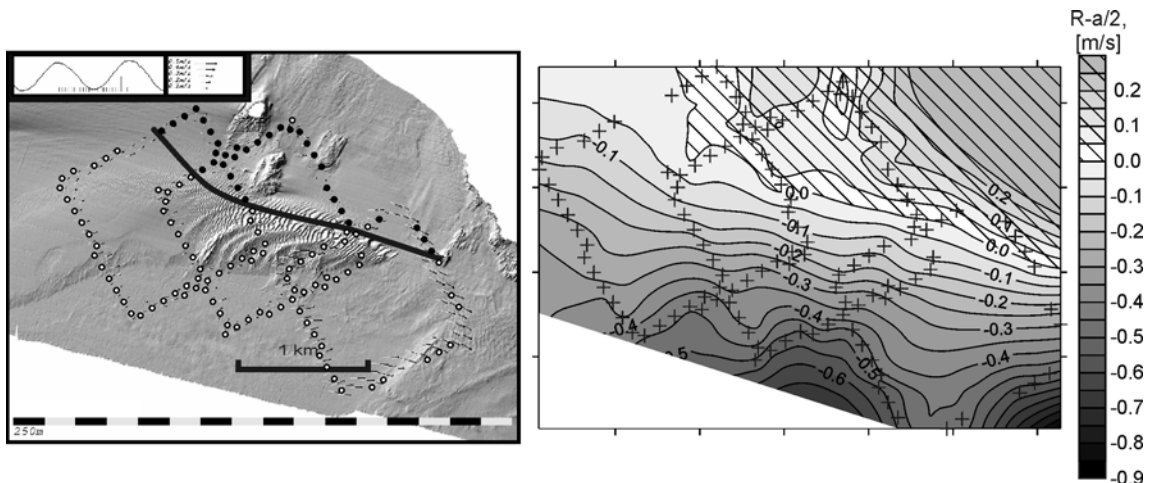
Figure 3.28 (Left) The zone of unidirectional currents in the lee of the headland represented by solid dots; the empty dots represent regions where tidal oscillation is greater than the residual magnitude. (Right) Contours of difference between residual current and semi-major axis, the hatched area denotes unidirectional region.

3.4.3. Current Profile Analysis

Figure 3.29 to Figure 3.33 show the ratio of the water speed, $U(z)$, relative to the depth-averaged velocity, $\bar{U}$ plotted against the fractional height of the water column, as described in Section 3.3.2.2. The different symbols correspond to different averaged profiles at discrete regions along a transect, i.e. all profiles taken within the black dot A in Figure 3.14 are averaged together to produce a single averaged profile. Note how the number of points changes with the height of the water column over the tidal cycle because the bin size is a fixed dimension (1 metre in this case). Note also how the A, B, etc. in Figure 3.29 to Figure 3.33 correspond to different phases of the tidal cycle and not to different locations along a transect as in the schematic diagram Figure 3.14.

Inspection of the figures reveals that the observed data conform to predicted power law values to different degrees over the tidal cycle. When the currents in the study region are flowing predominantly towards the headland (in the "flood" direction, positive values of the inset hydrograph), the water column conforms well to predicted with over 90% of the observed data falling within ±15% of the predicted curve. This indicates that the major influence on the current velocity profile is bottom friction. During the period when the flooding currents are decreasing to just after maximum ebb current, the water column does not conform as well to the predicted values. Inertia of the water mass as the flow is decreasing is hypothesised to explain why the velocity profiles do not conform to the predicted profile during this time. Since the theoretical predicted profile is based on steady flow irrotational conditions in a river, it is to be expected that any reversal in the current could induce an inertial effect on the velocity profile, this phenomenon has also been noted by *Van den Berg* [1987] in an estuarine environment with strong tidal asymmetry. In addition, the ebb currents are rotational, again contrary to the steady irrotational assumption upon which the predicted velocity profile rests. Soulsby [1997] paraphrased the preceding arguments by stating that the logarithmic current velocity profile assumption is invalid within ~1 hour either side of slack water. Concurring with this statement is the observation that Figure 3.30(D) and Figure 3.31(E,F), which exhibit the greatest departure from predicted, are within 50 minutes before and ~90 minutes after slack before ebb.
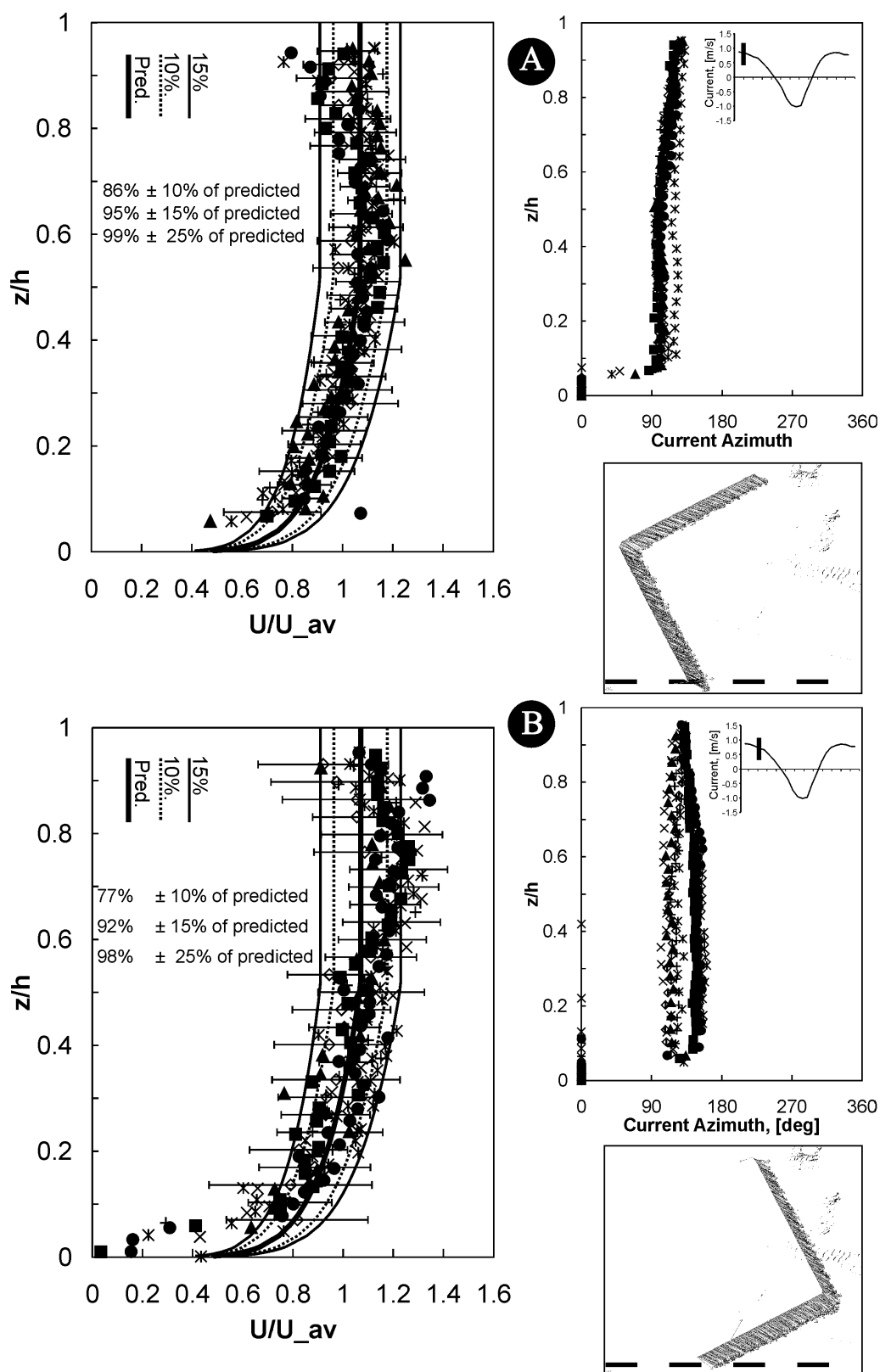
Figure 3.29 Normalized velocity magnitude profiles (left); current azimuth profiles (top right in each) and horizontal variation of depth-averaged current azimuth (bottom right in each). A: Peak Flood (PF); B: PF + 1 hour.
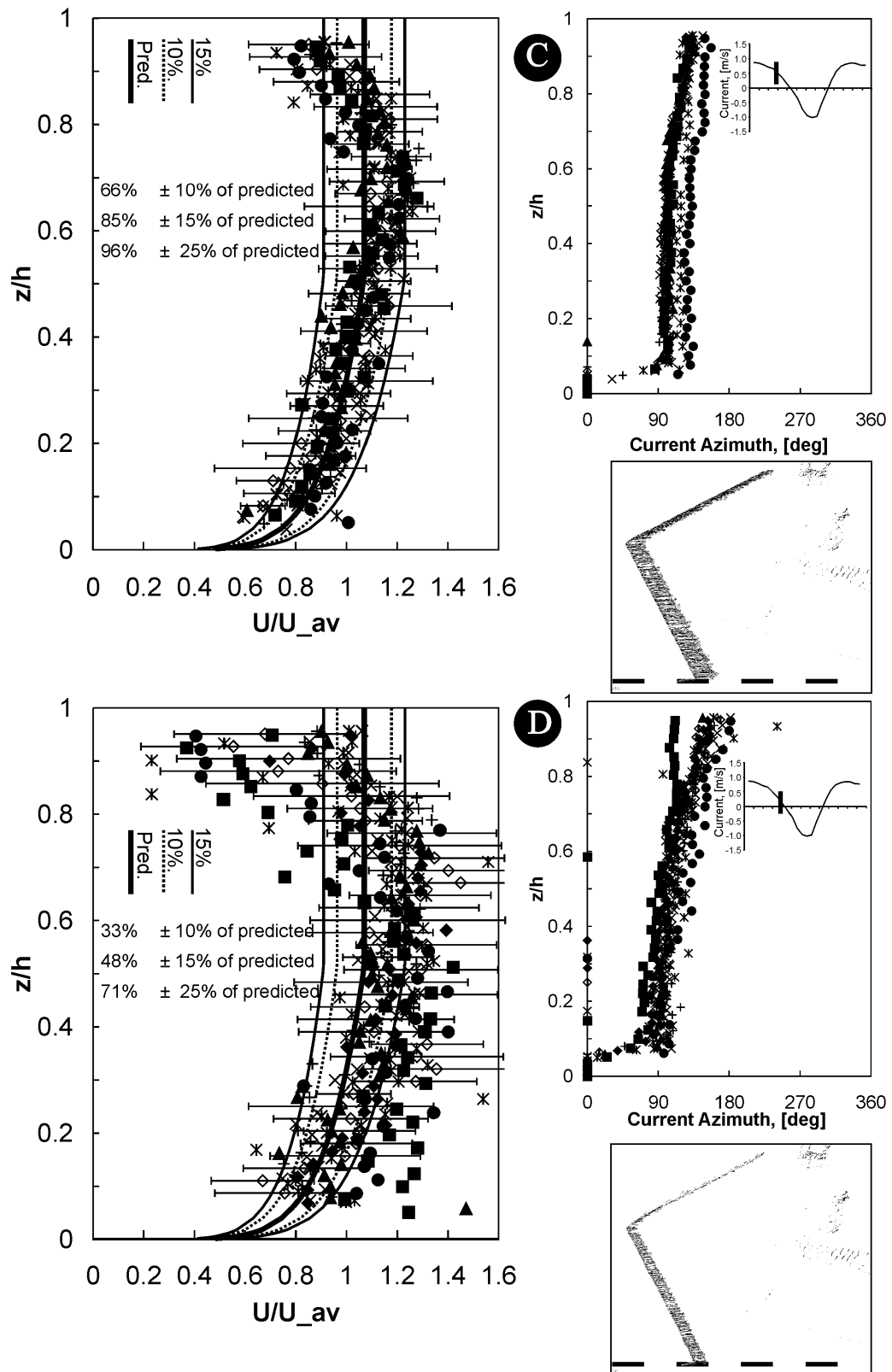
Figure 3.30 Normalized velocity magnitude profiles (left); current azimuth profiles (top right in each) and horizontal variation of depth-averaged current azimuth (bottom right in each). C: PF + 1hr50; D: PF + 2hr55.
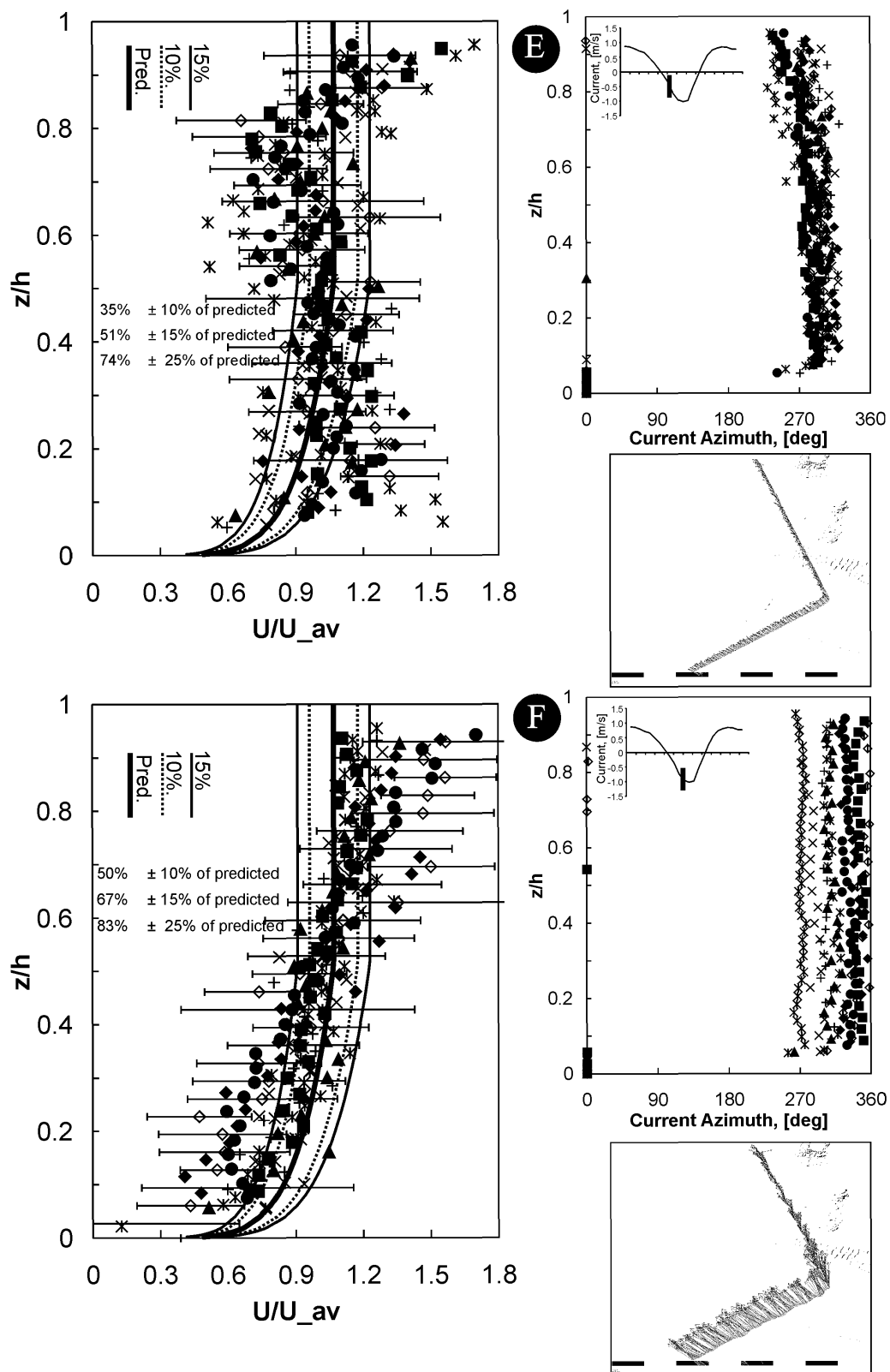
Figure 3.31 Normalized velocity magnitude profiles (left); current azimuth profiles (top right in each) and horizontal variation of depth-averaged current azimuth (bottom right in each). E: PF + 4hr15; F: PF + 5hr20.
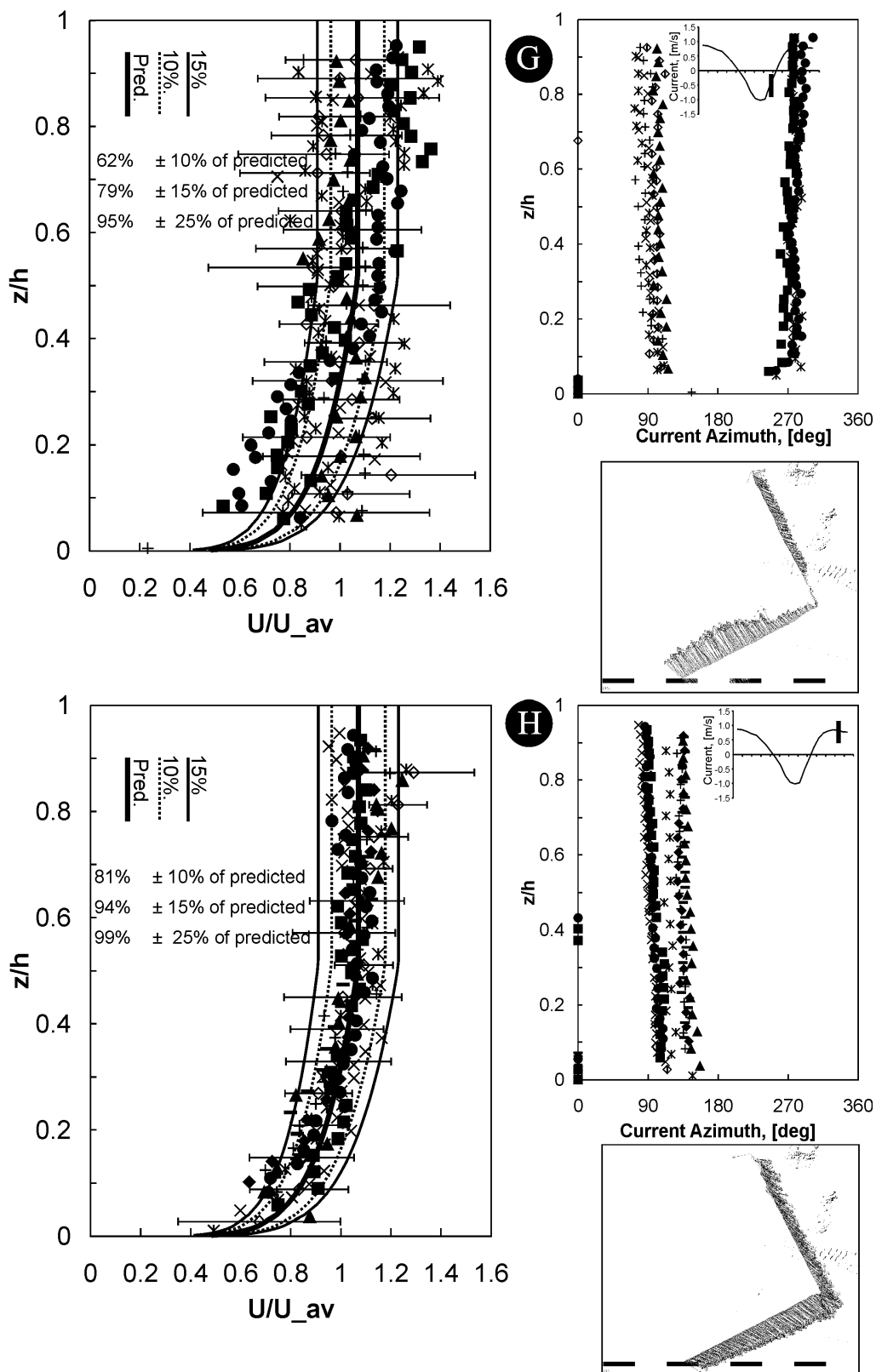
Figure 3.32 Normalized velocity magnitude profiles (left); current azimuth profiles (top right in each) and horizontal variation of depth-averaged current azimuth (bottom right in each). G: PF + 6hr50; H: PF + 10hr20.
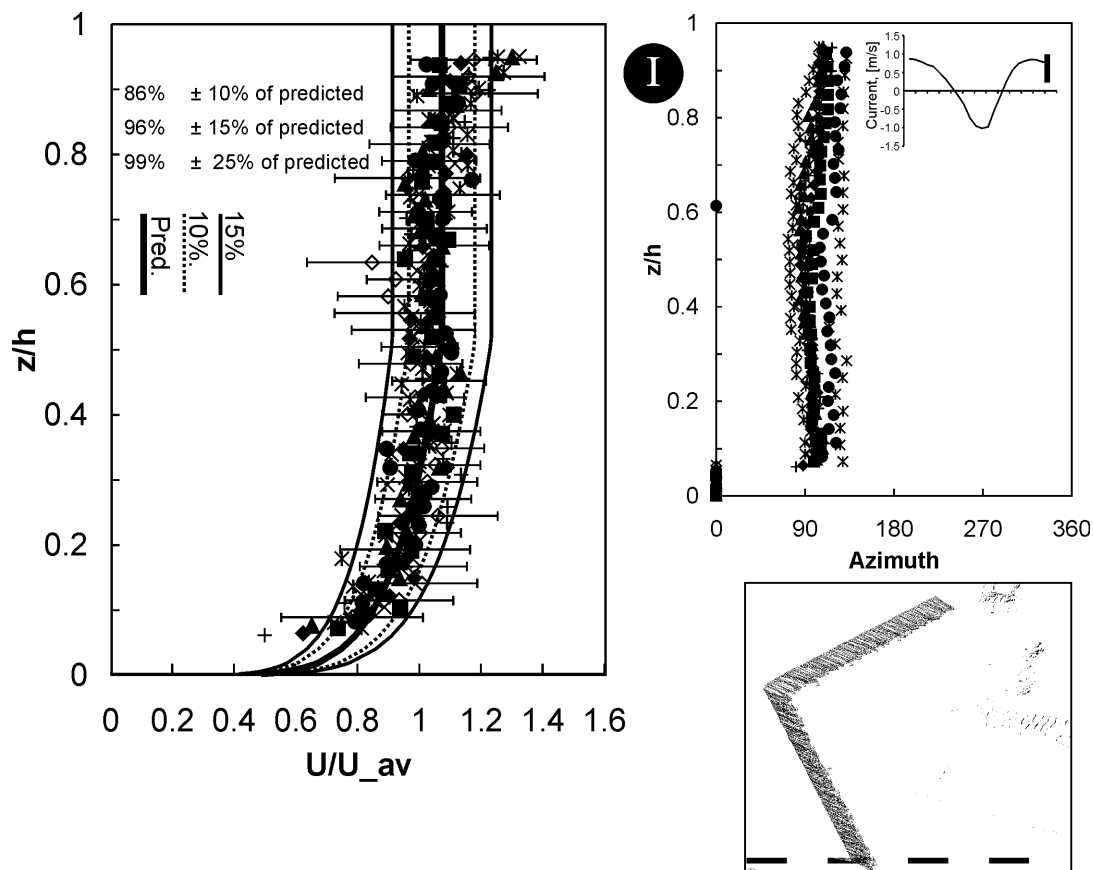
Figure 3.33 Normalized velocity magnitude profiles (left); current azimuth profiles (top right in each) and horizontal variation of depth-averaged current azimuth (bottom right in each). PF + 12hr10.

3.4.4. Salinity and temperature profiles

To investigate the possible influence of the Saint John River on the water structure,

CTD profiles were carried out at regular intervals over one of the tidal cycles.

Interestingly, it was evident that on the flooding tide the freshwater plume of the Saint

River had an influence on the water structure over the sand bank.

Figure 3.34 shows a graphical time-wise interpolation of the temperature (left) and

salinity (right) data. The top and bottom images correspond to the dips taken in the

shoreward and seaward corners of Diamond 3. The dips were taken almost continuously

over the tidal cycle (the frequency of dipping is shown at the bottom of the figure). From

examining the changing physical properties of the water, it becomes apparent that even

though there is little or no change in the current vectors at the commencement of fresher water incursion (compare Figure 3.17 with Figure 3.18, the latter the period of fresher water incursion), the *provenance* of these currents is different.
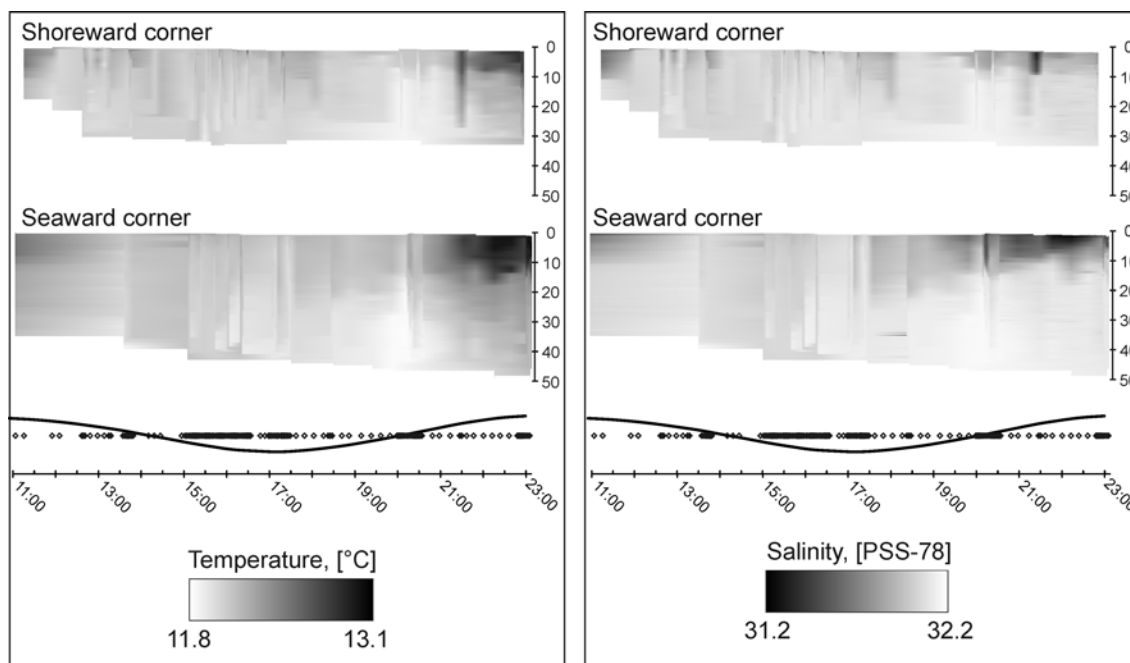
Figure 3.34 Time-wise interpolated temperature (°C) and salinity profiles (practical salinity units, where 35 is standard open ocean salinity) (left and right respectively) taken during the 2003 tidal cycle. Times are UTC. Solid line denotes observed tidal elevation from Saint John tide gauge.

The main thing to notice is the change in salinity and temperature of the upper 20 m of the water column over the tidal cycle. This change begins at around 2000 hrs, three hours before slack before ebb (this is more clearly seen in the deeper dips taken at the seaward end of a circuit in Figure 3.34 (bottom)), about one hour after low water when irrotational currents coming from the vicinity of Saint John Harbour begin to advect the brackish water from the primary "plume" that had leaked into the Bay of Fundy from the Saint John River on the preceding falling tide.

At 2300 hrs, which in fact is the only time during the tidal cycle when the water mass is simultaneously at slack, this stratification of the water column is at its most obvious.

Salinity and temperature are plainly related; the advected brackish water has a minimum salinity of one practical salinity unit less than and a temperature of ~0.8 °C greater than the background values for those quantities. Since river water tends to be warmer and, of course, fresher than seawater, this latter observation is to be expected of an advected river plume.

This latter stratification of the water column corresponds in time and depth with the anomalously slow surface waters in Figure 3.29, Figure 3.30 and Figure 3.33, indicating that mixing and transferral of momentum between the water masses is not happening because of the density contrast between the two masses.

3.5.   Field observations in the context of the mathematical model

To see whether Signell's model could be applied to the Mispec Bay eddy, geometrical parameters, as described in Equation (3.7) (p. 55), of Cape Spencer were calculated. Signell's model strictly applies to symmetric headlands but assuming that the down-current side of the headland causes the separation (not strictly true since the up-current side of headland induces a Venturi Effect acceleration of current); the model is forced here to apply to the asymmetric headland Cape Spencer. Here, a pair of different coaxial ellipses can be fitted to the headland for flooding and ebbing currents since a substantial down-current embayment only exists for the ebbing current.

EBB   FLOOD

a=1.50 km   a=1.5 km

b_{Ebb}=0.85 km b_{Fld}=2.5 km

α~1.8   α~0.6
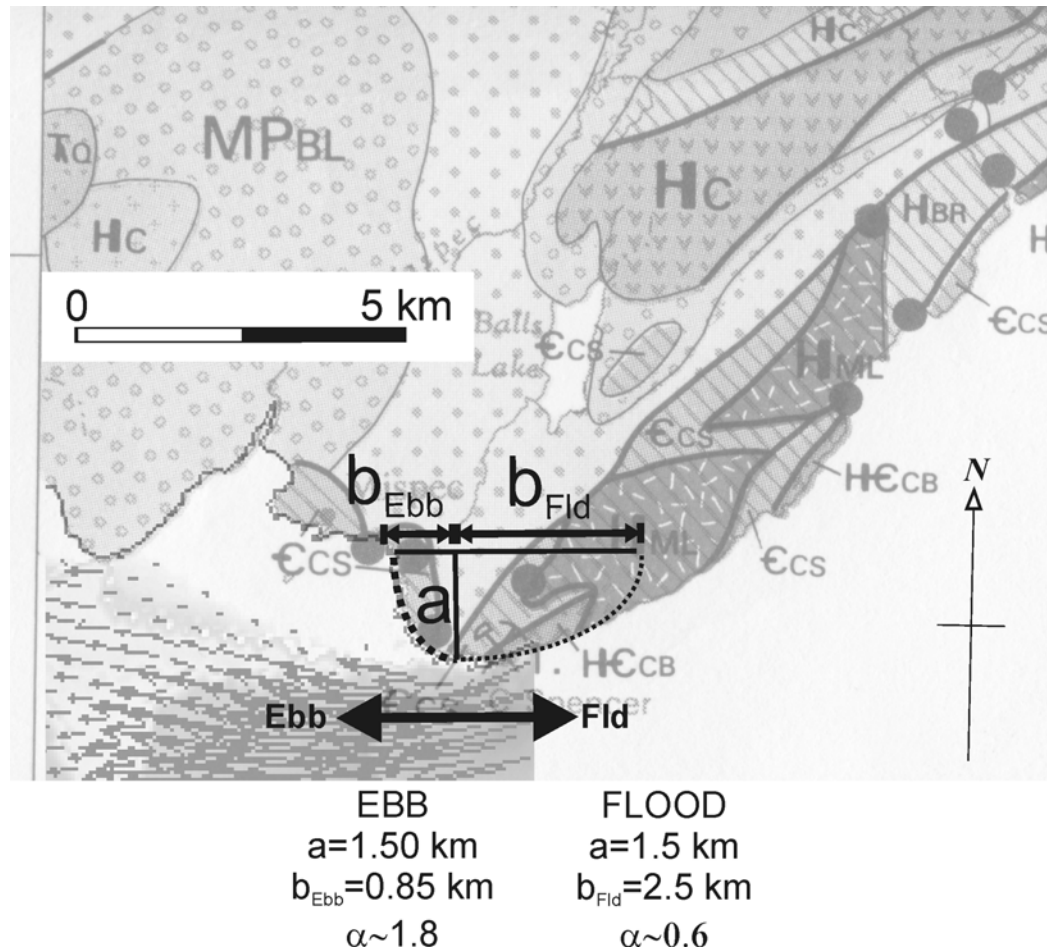
Figure 3.35 Fitting two coaxial ellipses to the outline of Cape Spencer.

Table 3.2 Parameters used to calculate frictional length scale, tidal excursion and aspect ratio of Cape Spencer for ebbing currents.

a, [km]	1.50	U_0, [m/s]	0.4 – 1.3
b, [km]	0.85	σ_{M2}, [s']	0.00014
H, [m]	35	l_f, [km]	3.1
z_0,[mm]	0.3	l_t, [km]	5.7 – 18.5
C_D	5.5E-03	α	1.8

An ellipse with current-normal and current-parallel axes of 1.5 and 0.85 km

respectively was fitted by eye to the headland (Figure 3.35) for the ebb currents with the

constraint, as in Signell's model, that the shore-normal axis was normal to the currents

flowing around the headland. The modelled currents of *Li et al.* [2003] were used for the

orientation of the latter since these predictions encompassed Cape Spencer completely. For ebbing currents, the headland aspect ratio is estimated to be ~1.8. An ellipse with shore-normal and shore-parallel axes of 1.5 and 2.5 km was fitted to the headland for flooding currents; however in this case, the aspect ratio is 0.6 and less than 4/3 implying that major eddy generation by flow separation is impossible for flooding currents.

The value of the drag coefficient was calculated from a roughness length of 0.3 mm (later Equation (4.2)), an accepted value for a substrate of sand/gravel [*Soulsby*, 1997], which is the dominant seabed type around the headland. The spring neap range of the far-field tidal amplitude was taken to be 0.4 – 1.2 m/s after tidal current predictions (Figure 3.8). Ratios of advection to friction and advection to local acceleration were calculated from Equation (3.7) to be 12 and 6 – 17 (because of spring-neap range) respectively. Reference to Figure 3.6 reveals that the Mispec Bay eddy is comfortably classified as a Case one eddy, implying that bottom friction will dissipate the eddy before the onset of the next tidal cycle. This matches favourably with the observation of the tidal eddy (Figure 3.15 and Figure 3.16), which shows the eddy to be dissipated before the onset of the flood tide.

As stated earlier, it is not strictly valid to apply Signell's model to an asymmetric headland since the model allows for: (1) up-current Venturi Effect acceleration and (2) subsequent down-current deceleration, both directly dependant on single values of aspect ratio, α, and alongshore extent, b. For Cape Spencer on the falling tide, the former induces a down-current deceleration corresponding to the ellipse with minor axis b_{Ebb} but there is no up-current Venturi Effect induced acceleration corresponding to such an

elliptical outline, rather there is theoretically lesser up-current acceleration of the ebb currents corresponding to an ellipse with longer minor axis b_{Fld}. Nevertheless, the observation of the dependence of aspect ratio on the phase of tide at the least predicts the possibility and impossibility of *major* eddy advection on the falling tide and rising tide respectively. If it is accepted that tidal eddies affect the sediment transport regime around the headland, then the latter hydrodynamic prediction matches with the observation of a pair of morphologically different sand banks either side of the Cape. This will be examined thoroughly in Chapter 7.

3.6. Conclusion

Analysis of ADCP current data has revealed the substantial disturbing effect of Cape Spencer on the current regime in Mispec Bay.

The net effect of Cape Spencer on the current regime in Mispec Bay is that: (a) the sheltering effect of the Cape causes currents flowing away from it to decrease to landward; (b) the rotational effect of the tidal eddy causes ebbing currents over the sand bank to flow in the 'flood' direction, i.e. towards the headland, which in turn causes the tidally averaged (residual) currents to be oriented strongly towards the headland over the sand bank and (c) tidal currents flowing towards the headland increase strongly in amplitude as they approach Cape Spencer from Mispec Bay. The tidally averaged residual is greater than the semi-major axis of the current ellipse over the large asymmetric dunes on the shallow part of the sand bank indicating that flow in this region is almost unidirectional. The high degree of asymmetry of these large dunes corroborates with this observation of unidirectional currents.

The tidal current velocity profile conforms well to the predicted, bottom-friction controlled, logarithmic profile (approximated by a power law profile) when currents are uniform across the field area. Approaching slack before ebb, the only time there is simultaneous slack water in this region, the advection of the Saint John River plume (detected by CTD dips over a tidal cycle) induces slight stratification of water column and affects the current velocity profile by causing it to depart from predicted in shallow depths (note stratification induced kinks within top 30% of water column in Figure 3.29, Figure 3.30 and Figure 3.33). Figure 3.30(D) and Figure 3.31 show that resisting inertia of the water column around slack water causes larger departures from the logarithmic profile. This is to be expected since current velocity profiles are not expected to conform around slack water [*Soulsby*, 1997].

An eddy forms on the falling tide in Mispec Bay because Cape Spencer is pronounced enough, and of sufficiently small along shore extent to advect vorticity due to an adverse pressure gradient down-current of the headland. Both the tidal excursion and frictional length scales are sufficiently large enough so the vorticity can be advected downstream as a single large eddy that decays over the course of a tidal cycle (Case one eddy). On the flooding tide, the asymmetry of Cape Spencer causes it to have an aspect ratio less than 4/3 meaning that major eddy generation as a result of flow separation is impossible.

C h a p t e r   4 :   G r o u n d t r u t h i n g

Any study that deals with predictions and measurements of sediment transport requires knowledge of seabed type and variability. For these reasons, a comprehensive ground-truthing program of bottom sampling and towed video was carried out. Knowledge of grain size statistical parameters, especially the median grain size, is necessary to predict sediment transport rate and compare with independent predictions of sediment transport rate derived from bedform migration (Chapter 5). The spatial distribution of grain size parameters may also be used to define possible sediment transport pathways. Underwater video was carried out ancillary to an investigation of lobster population density in Saint John Harbour. The aim was to see whether active bedload and/or suspended load transport could be observed and also to observe the substrate type.

4.1. Importance of Groundtruthing Data

Figure 4.1 illustrates the importance of the groundtruthing data (sediment sampling or photography) collected in this work, especially bottom sampling, to the eventual calculation of sediment transport rate and also sediment transport direction.
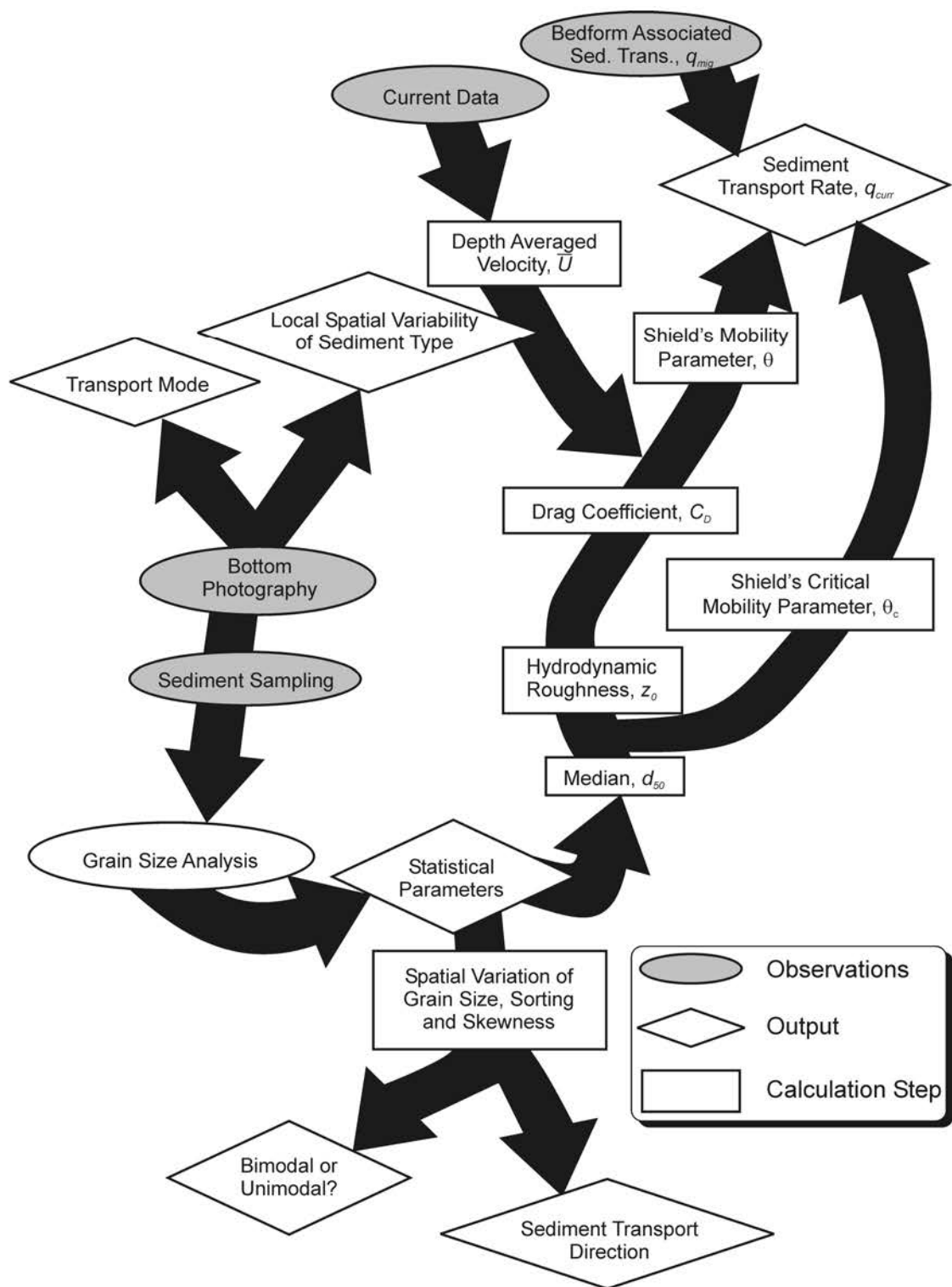
Figure 4.1 Schematic diagram illustrating the importance of ground-truthing to a sediment transport study.

4.1.1. Sediment Transport Rate

Knowledge of median grain size is necessary to determine the theoretical critical shear

stress (or critical current speed) immediately above which the sediment is transported.

Neglecting the effect of particle shape, the larger the grain size, the higher the shear stress

required to mobilize it. The effects of differing viscosity and density contrast are

accounted for by using the dimensionless grain size, D_*, (see equation in (Figure 4.2). The

dimensionless critical shear stress, θ_{cr}, is usually determined by referring to an empirical

chart of dimensionless critical shear stress against dimensionless grain size, such as that of

Shields [1936] (Figure 4.2). *Soulsby* [1997] formulated a useful algebraic expression of

this chart expressing θ_{cr} as a function of D_* and this was used to determine critical shear

stresses described later in this thesis.
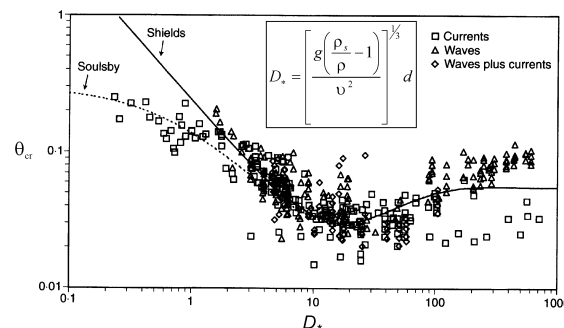
Figure 4.2 Modified version of Shields' critical shear stress plot (from *Soulsby* [1997]). The x- and y-axes are dimensionless variables of grain size and of critical shear stress ("threshold Shields parameter") respectively. Also shown is the expression used to calculate dimensionless grain size, D_*, where υ is kinematic viscosity.

In addition to determining *critical* shear stress, for a flat bed, knowledge of the grain

size together with knowledge of the current speed, is necessary to determine the *actual*

shear stress experienced at the bed, τ_0. This is because grain size directly controls the

hydrodynamic 'roughness', z_0, of the water sediment interface (4.1), which in turn

influences the degree of turbulence of the water column above the bed and the greater the

turbulence, the greater the frictional interaction of the flow with the bed [*Open University*, 1999]. This is because the shear stress is theoretically proportional to the vertical current velocity gradient[*], which is linked to the water turbulence. This effect of roughness on the interaction of the flow with the bed is parameterised to form the drag coefficient, C_D (4.2).

$$z_0 = \frac{d_{50}}{12} \dots \text{Hydrodynamic Roughness} \tag{4.1}$$

$$C_D = \left[\frac{\kappa}{1 + \ln\left(\frac{z_0}{h}\right)} \right]^2 \dots \text{Drag Coefficient} \tag{4.2}$$

$$\tau_0 = \rho C_D \bar{u}^2 \dots \text{Current Shear Stress} \tag{4.3}$$

$$\theta = \frac{\tau_0}{g\rho\left(\frac{\rho_s}{\rho} - 1\right)d_{50}} \dots \text{Shields Mobility Parameter} \tag{4.4}$$

$$q_b = f(\theta, \theta_{cr}) \dots \text{Bedload Transport Rate} \tag{4.5}$$

where

$d_{50} = \text{median grain size, [m]}$

$\kappa = \text{Von Karman's constant} = 0.4$

$h = \text{water depth, [m]}$

$\tau_0 = \text{bottom Shear Stress, [N.m}^{-2}]$

$g = \text{acceleration due to gravity, [m.s}^{-2}]$

$\rho, \rho_s = \text{densities of water and sediment, [kg.m}^{-3}]$

[*]Note that (4.3) is an alternative *empirical* expression for shear stress related to the depth-averaged velocity, not the vertical current velocity gradient.

Once the actual bottom shear stress, τ_0, is calculated (4.3), it is converted to the non-dimensional Shields mobility parameter, θ, (4.4), which takes into account median grain size as well as the density contrast between water and sediment. The bedload transport rate, q_b, which depends on how much the actual shear stress is greater than the critical shear stress, or the "excess shear stress", is then calculated according to (4.5). Over the years, many researchers have proposed different equations to calculate bedload transport rate but they are usually of the form of Equations (4.6) or (4.7), depending on whether shear stress or current are being used. Examples of such equations are employed in Section 6.2 to predict sediment transport.

$$q_b \propto \theta_{excess}^{1.5} \tag{4.6}$$

$$q_b \propto u_{excess}^{3} \tag{4.7}$$

4.1.2. Sediment Transport Direction

In addition to the prediction of sediment transport rate, sediment sampling is important to the identification of sediment transport pathways. Much research has been done on spatial analysis of statistical grain size parameters, most notably by *McLaren* [1981], *McLaren and Bowles* [1985; 1991] and *Gao and Collins* [1991; 1992]. *McLaren and Bowles* [1985] were the first to propose using trends of *combinations* of grain size parameters to determine sediment transport directions, as opposed to trends in grain size variation only. By inspection of downstream trends of grain size, μ, sorting, σ, and skewness, *Sk*, in flumes, they empirically identified that out of eight possible combinations of these parameters, only two particular combinations were indicative of derivation of sediment from location A to location B.

$$\sigma_B \leq \sigma_A \text{ AND} \begin{cases} \text{Case 1}: \mu_B < \mu_A \text{ AND } Sk_B \geq Sk_A \\ \text{OR} \\ \text{Case 2}: \mu_B > \mu_A \text{ AND } Sk_B \leq Sk_A \end{cases} \qquad (4.8)$$

If a downstream sample B is derived from an upstream sample A, B will always be better sorted and B will be either finer and finer skewed (Case 1) or coarser and coarser skewed (case 2) (4.8). To reason this scientifically: if B is a *deposit,* i.e. energy is decreasing downstream, it will be seen that which one of Case one or Case two applies depends on how A was initially eroded. If A was eroded in an energy regime sufficient to erode grain sizes *greater* than the mean grain size of A, then relatively larger grain sizes will be transported as load and then deposited downstream as a relatively coarser sample B (case 2). However, if A was eroded in a lower energy regime, then grain sizes *less* than the mean grain size will be eroded and then deposited as a relatively finer sample B (case 1). In contrast, if B is a *lag* deposit, i.e. now energy is increasing downstream, then the sample B may be thought of as the residual sediment of A after it is eroded. Note that in this latter situation, Case 1, i.e. coarsening downstream still applies.

Gao and Collins [1992], identified that Case one and Case two above were better thought of as the *most probable* combinations of grain size parameters indicating sediment transport since other combinations of grain-size parameters could be randomly possible and proposed a probabilistic technique based on the definition of sediment "transport vectors". Their technique identifies the length of a "vector" at location A as signifying its importance as a sediment source. Vectors are calculated in the following manner:

1. A truth table (Figure 4.3) describing whether transport between points is possible on the basis of Equation (4.8) *and* the distance between the points is

less than a pre-determined critical radius. Separate truth tables are compiled for Case one and Case 2. Unit vectors are then drawn between sample points if there is a TRUE in the respective position in the matrix (Figure 4.3(a)).

2. If more than one unit vector exists at a sample point, they are summed (Figure 4.3(b)).

3. All vectors within a radius of the critical distance of a given sample point are vectorially averaged at that point. This step is intended to average out random noisy vectors (Figure 4.3(c))

4. If the magnitudes of the trend vectors from the last step are longer than a statistically determined magnitude, they are retained; otherwise they are removed (Figure 4.3(d)).

	1	2	3	4	5
1					✓
2	✓				
3		✓			
4					
5	✓				
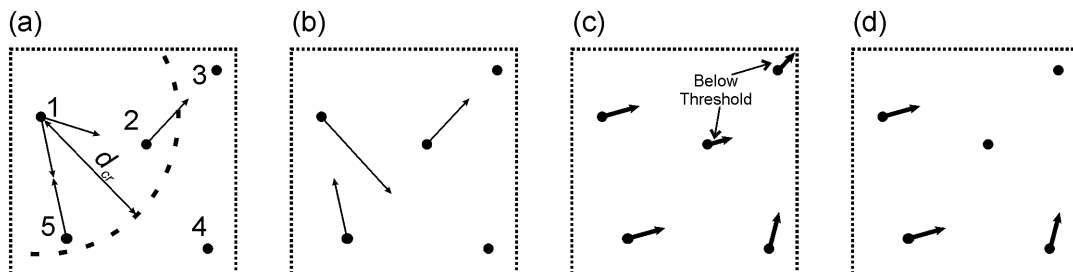
Figure 4.3 Diagram showing truth table and how trend vectors are plotted.

To determine whether the calculated trend vector lengths are significant, *Gao and Collins* [1992] randomly reallocated the grain size parameters, e.g. the grain size, sorting and skewness of sample 3 would be re-allocated to position 1. In this way, a new truth table is created and steps 1-3 are repeated. A number of such random allocations are carried out, the magnitudes of all the random vectors are plotted in a frequency diagram, and the 95% confidence critical vector is calculated according to the mean and standard deviation of the randomly re-allocated trend vector magnitudes (95% interval = mean + 1.96 x s.d.).

4.2. Data Acquisition and Processing

4.2.1. Sediment Sampling

On 14th August 2003, the UNB research vessel, *Mary O*, was deployed to conduct the sediment sampling program since she possessed a winch with which a grab could be deployed. A Shipek grab, on loan from GSC (Atlantic), capable of sampling up to 1.8 kg of sediment down to ~ 8 cm depth, was used for sampling purposes. Co-ordinates defining the outline of the sand bank and the extent of the study area were entered into navigation software and sampling was conducted within and around the sand bank with an average spacing of 260 m. From 30 grab attempts, seven yielded samples too small to be sieved (but nevertheless were identified by eye) and three came up empty (i.e. the door had swung shut but no sample was inside, possibly indicating bedrock substrate). The 20 remaining samples were measured through 14 standard sieves with aperture sizes ranging from 37.5 mm down to 75 micron (or, from cobbles down to very fine sand); six of these samples had very high clay content and so had their fine fractions measured by hydrometer analysis.

Two methods of determining the grain size parameters were employed: the central moment method that uses as input the histogram of weight percentage fractions and the American Standards and Testing Method for grain size analysis [*ASTM_D-422-63*, 2002] that uses readings of cumulative percentage finer that are read off a cumulative percentage chart. The results of both of these estimates of grain size and sorting were compared for consistency. The average difference in the grain size estimate between the two methods was 0.07 phi with a standard deviation of 0.18 phi and the equivalent figures for sorting were -0.21 phi and 0.24 phi. This meant that the two methods compared favourably for their standardised estimates of grain size (e.g. "coarse sand" or "very coarse sand"), whilst the standardised classifications estimates of sorting disagreed by at most one classification, e.g. one method classified a sample as "poorly sorted" and the other method classified it as "very poorly sorted".

4.2.2. Bottom Video

A digital video camera, designed and built by Mike Strong (St. Andrews Marine Biological Station) (Figure 4.4), was deployed from the Canadian Coastguard vessel *Hart* between 1150 to 1425 AST at the commencement of ebb currents (slack before ebb was at 1200 AST) on the 24$^{\text{th}}$ September 2003. A heavy shackle was fastened to the front of the tripod to weigh down the front and point the camera at the seabed. A cable fed video to a monitor and tape recording unit on board so the altitude of the tripod could be controlled by hand for optimal viewing of the seabed. The vessel's position was also displayed on the monitor and recorded as an image onto the tape (and ultimately transferred to DVD); the camera was deployed while the vessel was drifting. Given the fact that the maximum cable out was 40 m and the homogeneity of the seafloor for a given transect, the position

of the camera was taken to be the position of the vessel. A pair of laser pointers with their

beams set parallel and 25 cm apart was mounted on the frame to give a scale reference for

the 2D image on the monitor. This assembly was designed primarily as a tool for

"presence or absence" inspections of biota. The lack of a magnetic compass or depth

gauge made its application for this geological investigation strictly qualitative.
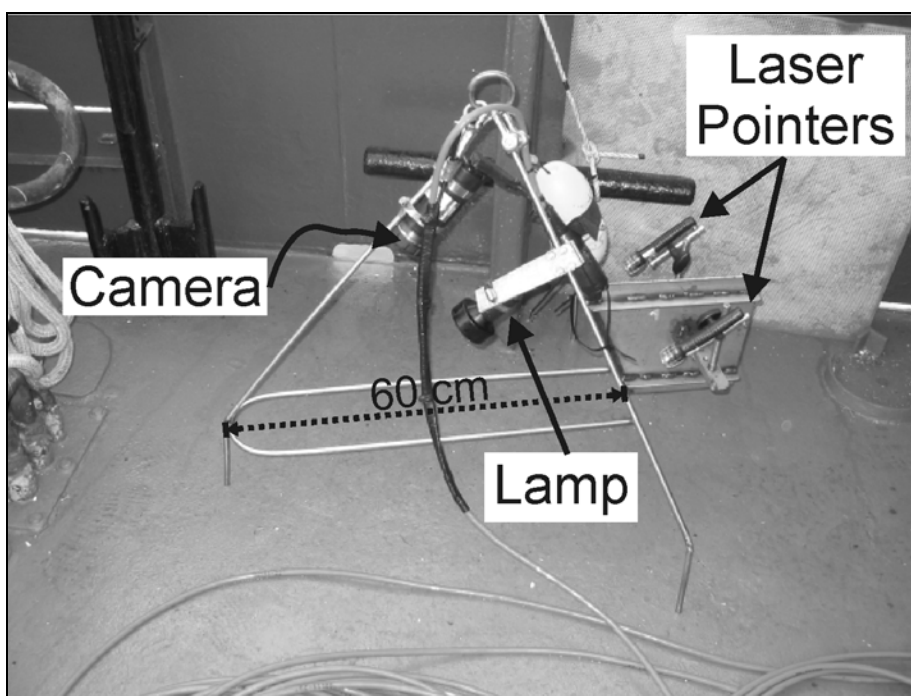
Figure 4.4 Annotated photo of the video assembly.

4.3. Results

4.3.1. Sediment Sampling

Five distinct sedimentary facies were identified on a plot of grain size against sorting

(Figure 4.5): (Facies A) grey, moderately well sorted medium sand and fine shelly sand

(eight samples, mean grain size 0.33 mm); (B) poorly sorted, coarse skewed, bimodal

coarse sand and gravel (four samples including one visually classified); (C) dark brown,

very poorly sorted, fine skewed, very fine sand and silt with coal and wood fragments and

sparse shells and pebbles (six samples; mean grain size 0.06 mm); (D) very coarse sand

and gravel (two samples; mean grain size 4.1 mm) and (E) well sorted very coarse sand (one sample; mean grain size 1.3 mm).

These five classes were well defined spatially (Figure 4.6): All of the samples taken on the sand bank fall into Facies A. Facies B encompasses coarse samples taken proximal to the sand bank, two of which (samples 7 and 24) were markedly bimodal medium sand and gravel (Figure 4.7). Sample 26 was too small to be sieved but was visually classified as a mixture of sand and gravel, i.e. facies B. The samples comprising facies C were taken off the north and north-western edge of the sand bank, between Mispec Point and Black Rock. The pebbles and granules of Facies D were only found adjacent to Cape Spencer. Facies E was only made up of one sample and was found one kilometre from the dunes on the sand bank on the other side of Cape Spencer. Its coarser grain size has implications for the sediment transport regime around Cape Spencer that will be discussed in Chapter 7.

All of the facies A samples in the western tail of the sand bank (samples 19, 20 and 30) had quite high mud (defined as particles smaller than 70 micron) contents (compared to the other facies A samples) ranging from 3 – 3.9 wt%. However, sample 16 of facies A, in the interior of the sand bank, had an anomalously high mud content of almost 13 wt%. Walnut sized 'clumps' of clay, rather than disseminated mud, were evident from inspection of this sample. Facies B also had medium to high mud contents ranging from 2 – 9 wt%. Facies D and E located proximal to Cape Spencer were quite clean of fines and had relatively low clay contents of 0.5 – 1.5 wt%.
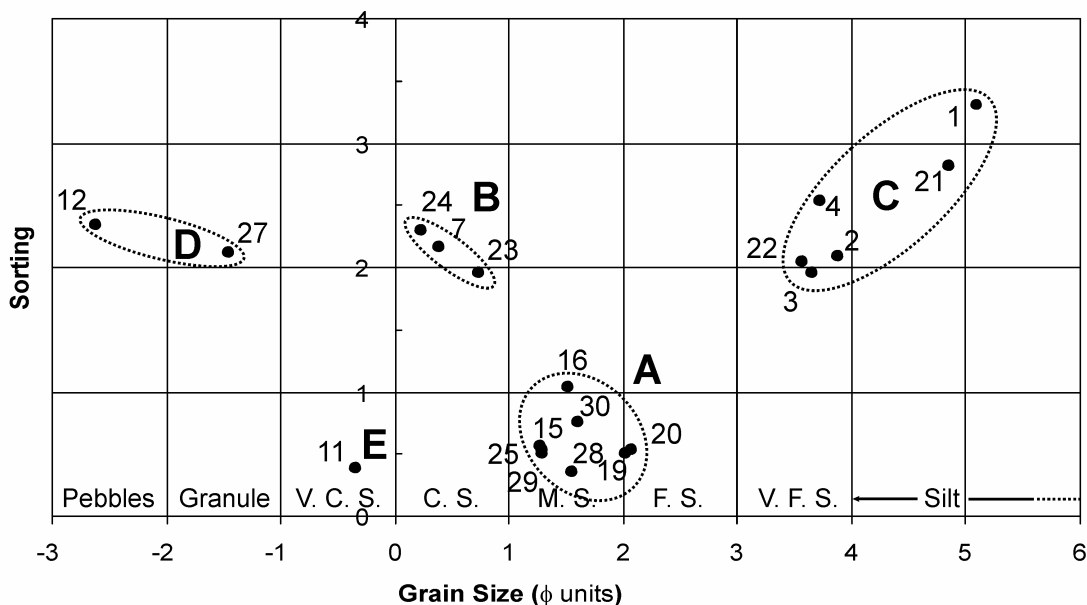
Figure 4.5 Plot of mean grain size against sorting. Grain size classifications are listed along the ϕ axis.

Figure 4.6 shows a simple spatial interpretation of sedimentary facies in Mispec Bay based on the correlation of bathymetric texture and sediment type and then visually inspecting an EM-3000 multibeam backscatter image from an October 2000 GSC survey to extend the class boundaries. Note how the eastward extent of facies C landward of the sand bank has been interpreted to continue across the sand bank so that there is overlap between the muddy facies C and the sandy facies A (this is justified because of the high fines contents of samples 19, 20, 23, 24 and 30); this reflects some mixing between the mud facies and the sediments making up the bank. The bimodal sand and gravel facies B is interpreted to be nothing other than overlap between the sandy facies A and the gravelly facies D. The sand content of facies B is likely to decrease with distance from the sand bank and it is difficult with this simple visual inspection of backscatter to be confident about how far it extends away from the sand bank. This is the reason for the uncertainty in the extent of the overlap between facies A and D in Figure 4.6(b).
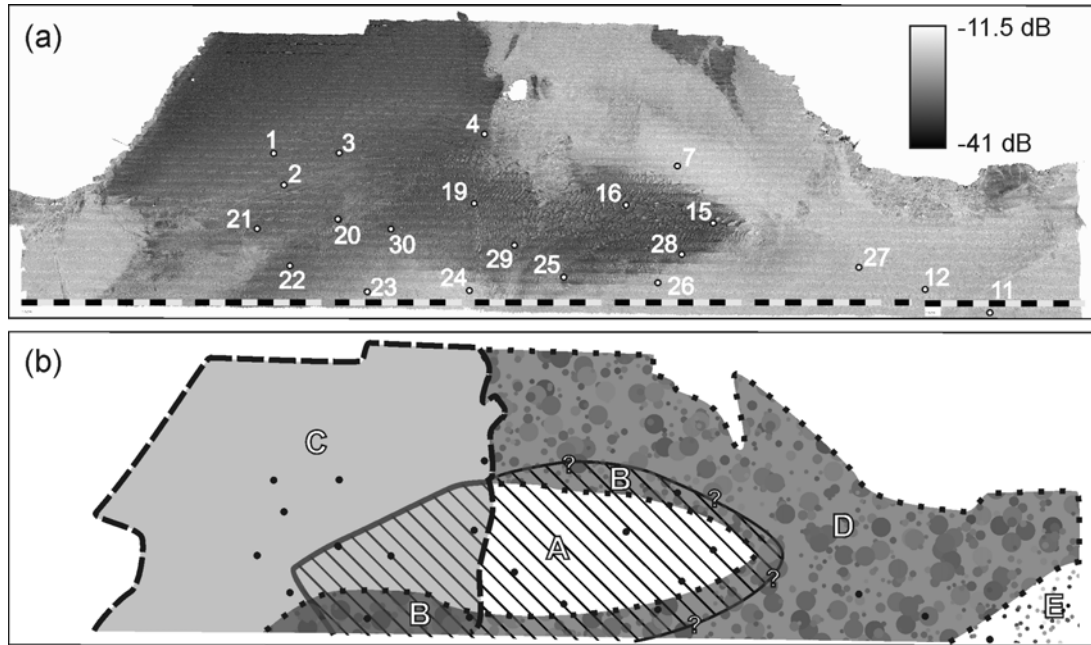
Figure 4.6(a) Simrad EM3000 backscatter of the study area with sample locations; (b) A visual interpretation of backscatter and bathymetric texture (dunes, flat, etc.) data guided using groundtruthing data: Facies A enclosed by solid line; C, short dashed line; D, dotted line and E no line. Facies B is within the overlap between A and D.
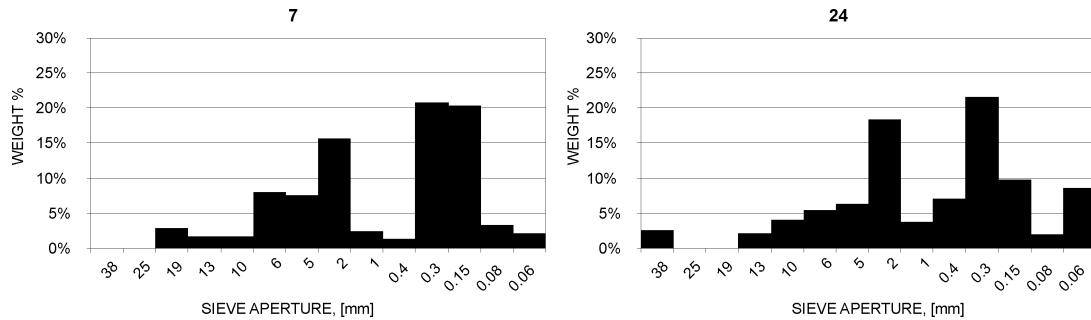
Figure 4.7 Bimodal samples of facies B.

4.3.2. Trend Vectors

Trend vectors and significant vector lengths were calculated as described in Section 4.2.1. A critical distance of 1500 m was used, i.e. only sample locations within 1500 m of each other were compared. The procedure of *McLaren and Bowles* [1985] and *Vanwesenbeeck and Lanckneus* [2000], where vectors satisfying either case one or two were drawn separately (Figure 4.8(a-c, d-f)), was followed. The critical vector length for the fining downstream case one was found to be 0.82 at the 95% confidence interval and only two vectors from the poorly sorted coarse gravel and cobbles of facies B were found

to be significant at this level. This means that sediment within 1500 m of these samples may be regarded as deposits derived from these headland proximal locations. The critical vector length for the coarsening downstream case two was found to be 0.46 at the 95% confidence interval and all six migration vectors from the muddy sediments of facies C were found to be significant at this level. The implication of this result is that the samples within 1500 m of these samples may be regarded as *either* being lags derived from the mud *or* deposits arising from erosion of the mud with sufficient energy to erode grain sizes larger than the mean grain size of the mud (see Section 4.1.2). Notably there were no significant trend vectors on the sand bank itself. This is because the sand bank is quite uniform in terms of grain size, sorting and skewness. Clearly, the trend vector method, which relies on consistent trends in grain size, sorting and skewness, cannot be used on the sand bank to determine sediment transport direction.
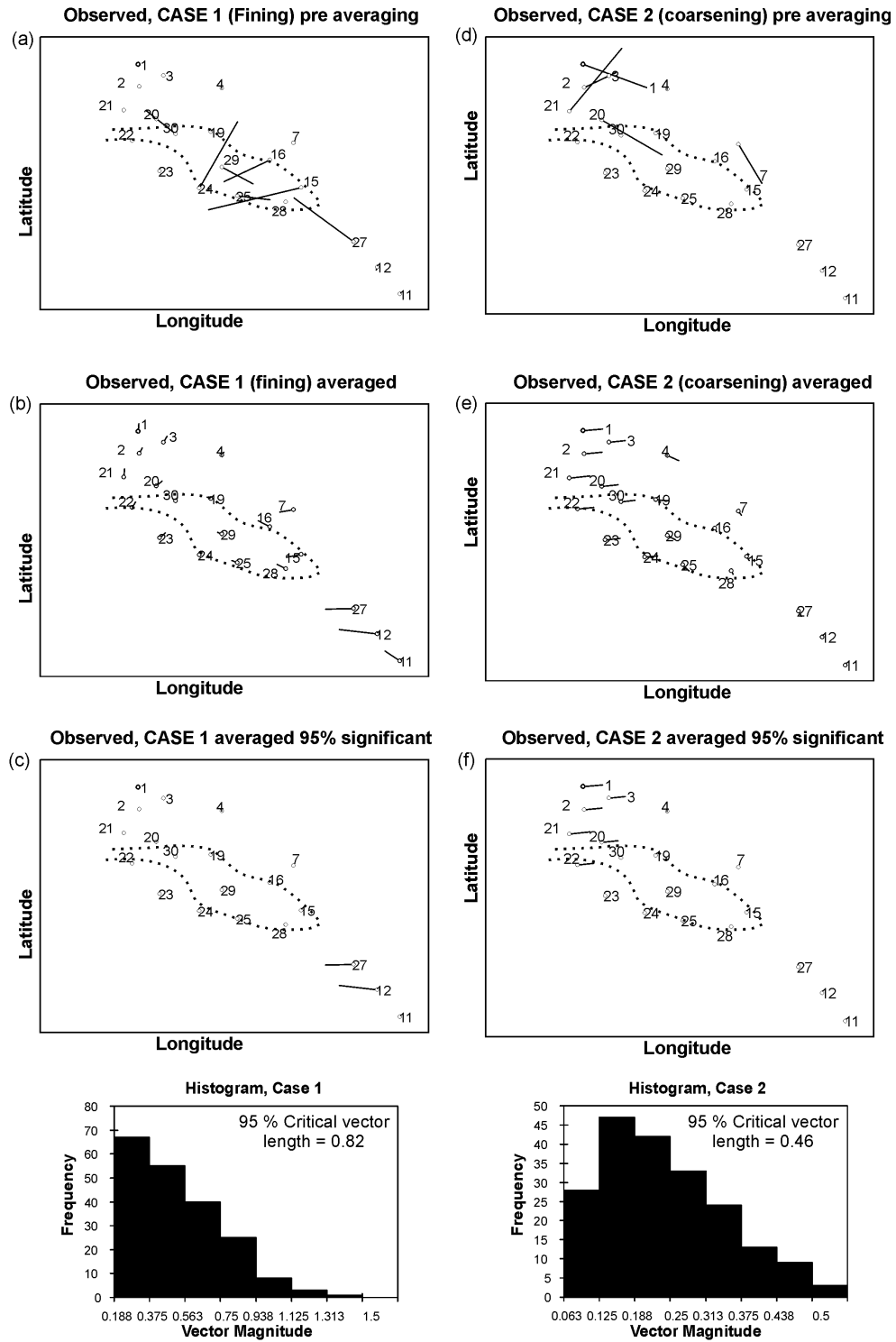
Figure 4.8 Results of calculating trend vectors. Left column depicts the stages (corresponding to Figure 4.3(b-d)) of calculating the trend vectors for Case one and right column depicts the calculation of Case 2. Note different horizontal scales in magnitude histograms.

4.3.3. Bottom Video
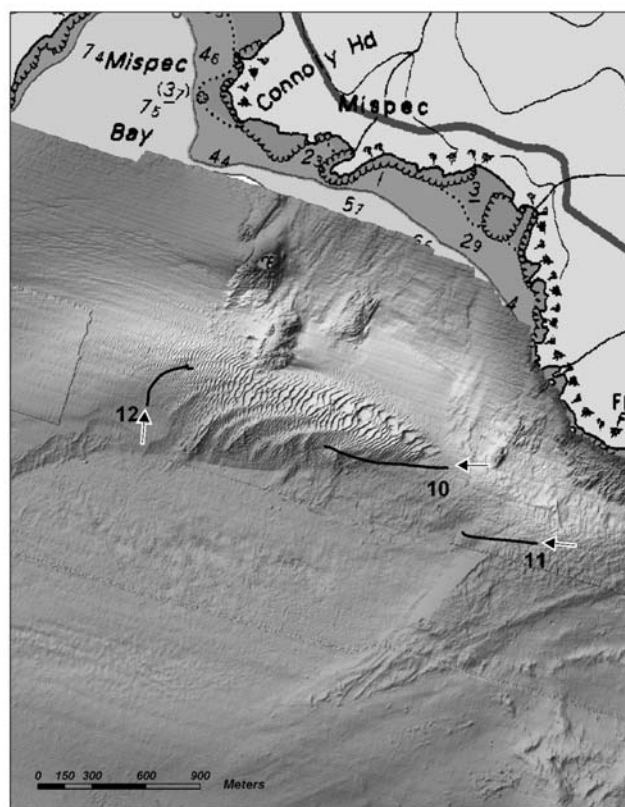
Figure 4.9 The three bottom photography transects carried out on *Hart* in October 2003. Arrows indicate transect direction (Figure courtesy of Eric Patton, GSC (Atlantic)).

Three video transects were carried over the field area (Figure 4.9). In terms of data quality, backscattering of light from particles in the water column meant that the brightness of the lamp could not be turned to its maximum level and this in turn meant that the seafloor could only be viewed by standing the apparatus stationary on the seafloor. In addition, relative movement between the drifting vessel and the light camera frame meant that such stationary periods of observation on the seafloor greater than five seconds were impossible because the vessel began to drag the camera or the currents began to topple the frame. This meant that the camera had to be 'hopped' along the seafloor by pulling and releasing the cable so the video footage is more like a series of snapshots of the seafloor

rather than an uninterrupted movie of the seafloor. Bearing this in mind, the following observations were made during the transects (going east to west):

Transect 11

This transect was made close to Cape Spencer at a water depth of around 35 m. Boulders were quite extensive in the early part of this transect (Figure 4.10) although they petered out to cobbles with interstitial finer sediments towards the end (Figure 4.11).
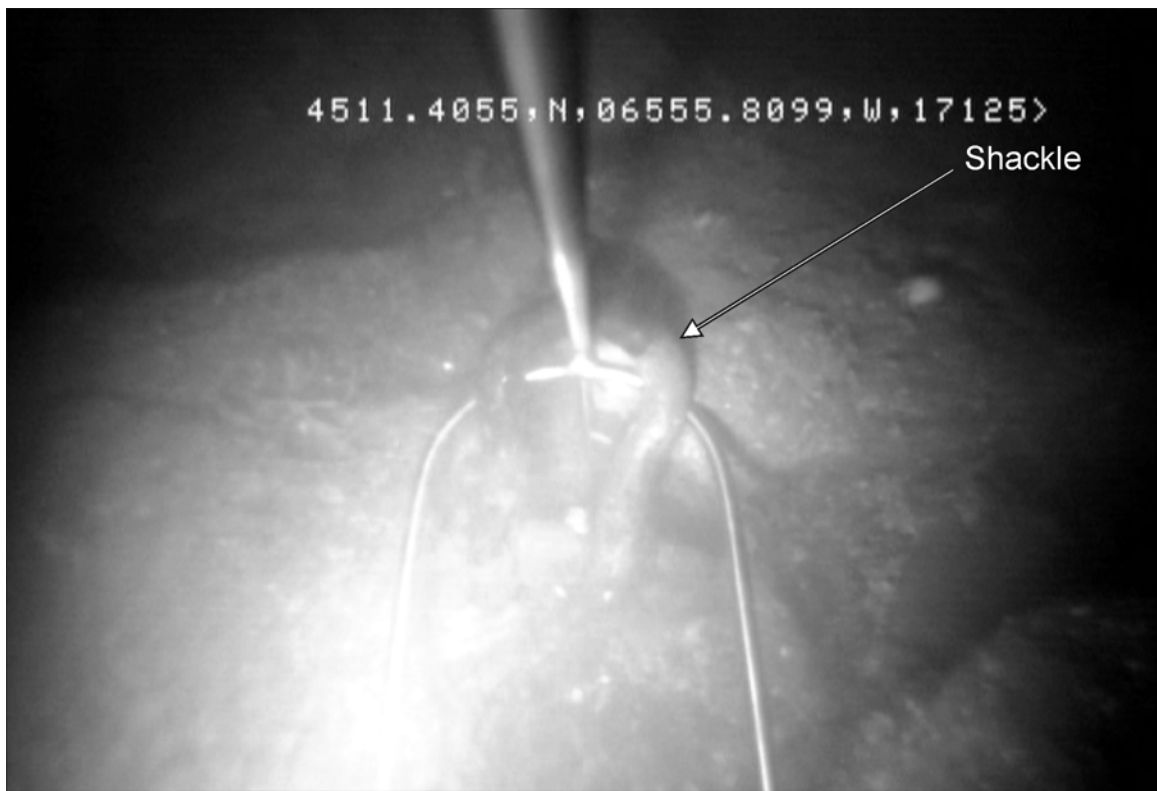
Figure 4.10 Video still showing boulders encountered at start of transect.

The boulders and cobbles were encrusted with barnacles and *in situ* seaweed throughout. Patches of shell hash were also observed with no boulders or cobbles present. The seabed was quite rich in biota with some starfish and a lobster observed.

Figure 4.11 Barnacle encrusted angular cobbles observed towards end of transect.

Disaggregated seaweed fronds and suspended matter were present throughout; in some cases, suspended sediment was dense enough that it occluded observation of the seafloor.

Transect 10

This transect crossed from the featureless bathymetry of the seafloor surrounding the sand bank onto the deep part of the sand bank. The start of the transect showed the seabed to be scattered with angular barnacle-encrusted cobbles, some with weed growing on them (Figure 4.12).

4511.6483,N,06556.2294,W,15594>

Figure 4.12 Video still showing barnacle covered boulder at start of transect 10 before crossing on to sand bank.

Moving on to the sand bank proper, cobbles became absent and 'carpets' of disaggregated seaweed fronds moving over very soft (evinced by how easily the legs of the camera sank into the sediment) asymmetrically rippled sand became the dominant seabed character (Figure 4.13). Active bedload and suspended load transport was observed and sediment thrown up by the landing of the camera was swiftly transported away. Disaggregated fronds moving in carpets and singly were present throughout.

4511.6854,N,06556.5978,W,16192>

Figure 4.13 Video still of sand ripples showing homogeneously coloured seabed in transect 10.

Towards the end of transect 10, in the interior of the sand bank, sand echinoderms became more prevalent (Figure 4.14).

Figure 4.14 Picture of echinoderms encountered towards the end of transect 10.

<u>Transect 12</u>

This transect was carried out at a depth of ~30 m over the smaller sand waves of the western tail of the sand bank close to the mud of facies C while the vessel was drifting with the clockwise ebb tidal eddy. The track of this transect in Figure 4.9 shows the turning effect of the eddy on the ship's track. The early part of this transect was characterized by relatively flat sand with a preponderance of broken up shells and echinoderms (Figure 4.15). In some places, the ripples present were poorly developed, possibly indicating increased cohesiveness in the sediment, which can impede bedload transport and bedform formation [*Mitchener and Torfs*, 1996]. A third of the way into the transect, shells became less prevalent and ~2 cm high (relative to one of the legs of the camera) sand ripples became better defined.

Figure 4.15 Picture of shelly substrate at the start of transect 12 with a lobster at top-right of picture.
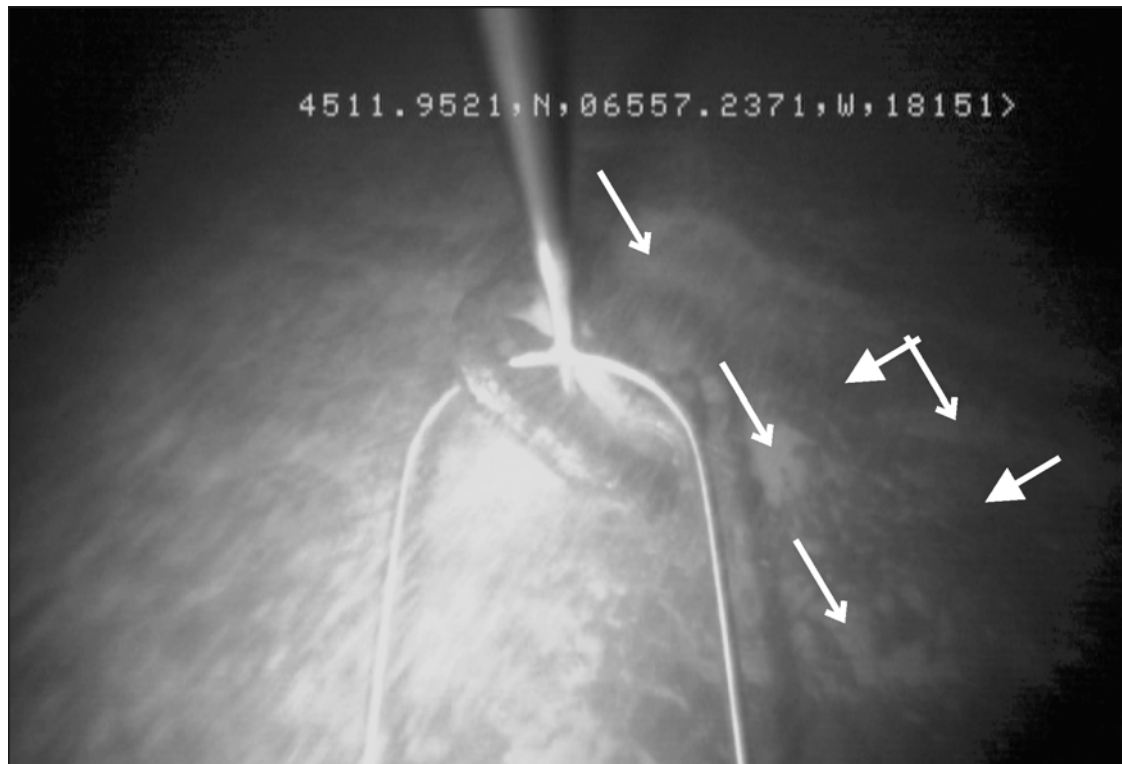
Figure 4.16 Picture of mottled shell-free seabed characteristic of transect 12. Filled and open arrows point to darker (muddier) and lighter (sandier) areas of the seafloor respectively.

A solitary lobster was also observed. Some weed was observed to be growing *in situ* and some disaggregated weed was being moved along by the currents, although much less than at transects 10 and 11. Interestingly, the sandy substrate was marked throughout the transect with light and dark stripes (Figure 4.16), possibly indicating varying clay content and a soft drink can (!) was observed. Currents moved the camera around but active bedload transport was not observed.

4.4.   Interpretation

Bottom sampling and video evidence both point to contrasting sedimentological conditions in the field area: mud, cohesive sand, incohesive sand and angular cobbles. Such a configuration of sediment facies has been noted around other banner banks: Skerries Bank in Start Bay, Devon, U.K. [*Hails*, 1975] and the numerous banks around Isle of Portland also in Devon [*Bastos et al.*, 2002]. However, the Portland banks are different to the Mispec Bay bank since for the former, the seabed around is more scoured and is quite bedrock dominated.

Without core information, it is hard to corroborate the hypothesis of typical headland associated facies made by *Bastos et al.* [2002], namely a regional gravelly facies that is in places overlain by medium sand (in the Mispec Bay case, the only such deposit would be the sand bank itself) that grades to mud with increasing distance from the headland. In 2002, a number of 3.5 kHz shallow seismic profiles were executed in Mispec Bay to resolve the base of the sand bank and any vertical structure but there was little penetration of the substrate. However, comparison of the histograms of Figure 4.7 and Figure 4.17 shows that the bank proximal facies B may be considered to be a mixture of gravel similar

to the facies D immediately around the headland and sand from the sand bank (facies A), therefore the idea of a regional strata of gravel that is overlain by the sand bank is a plausible one.
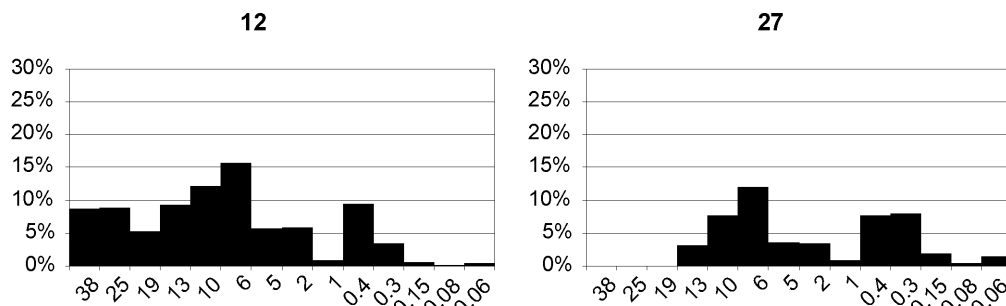
Figure 4.17 Histograms of the gravel facies D.

With regard to sediment sources and pathways, increased clay content of the facies A samples in the west part of the sand bank; trend vectors (Figure 4.8(left column)); and the striped nature of the seabed in the west part of the sand bank (revealed by bottom video) has three possible explanations: either (a) the sand on the sand bank is derived from *in situ* mud after the finest fraction has been removed by tidal currents yet still retains high weight percent mud or (b) sand that is deposited in this locality is becoming reworked with *in situ* mud by tidal currents or (c) sand that is deposited in this locality is being draped by mud transported from facies C. It is possible that all of these mechanisms are at work. Nevertheless, the relatively high content of clay in this west part of the sand bank explains why the ripples are relatively small in size in this locality since clay content is thought to hinder bedform formation due to increased cohesiveness of the substrate [*Mitchener and Torfs*, 1996; *Van Ledden and Wang*, 2001]. The walnut sized clumps of clay found in the anomalous sample in the interior of the sand bank could be the result of the tearing of the mud from up-current during periods of storm erosion because it has been reported that catastrophic erosion of mud is characterized as "aggregates or clumps of

material being detached from the bed and mostly transported as bedload" [*Mitchener and Torfs*, 1996].

The presence of terrigenous wood fragments and charcoal indicate that the mud itself is land derived and is possibly a flocculated deposit from the Saint John River (the discoloured plume of the Saint John River has been observed to stretch past Mispec Point both on satellite images). However, another explanation of the existence of wood and charcoal could be the annual dumping for the last 40 years of dredged sediments from the mouth of the Saint John river by the city of Saint John at a site ~3.5 km north-west of where the mud was detected. A mathematical model of sediment dispersion and transport of Saint John Harbour predicts that sediment at the dumpsite could be transported into Mispec Bay [*Li et al.,* 2003]. It is likely that both direct fluvial flocculation and dumpsite dispersal are mechanisms by which terrigenous sediment makes its way into facies C.

<u>Geological classification of surficial sediments</u>

Figure 4.18 Fader's 1977 surfical geology map of the Bay of Fundy around the Saint John Harbour area. The Sambro Sand is unit 9b and the LaHave Clay is unit 10c. The black rectangular area denotes the study area.

The two main distinctive facies in the field area, the muddy facies C and the gravelly facies D correspond well both spatially and qualitatively with the accepted description of Bay of Fundy surficial sediments. The surficial sediment map of *Fader et al.* [1977] describes a "silty sandy clay", the LaHave clay, 3.5 km offshore of Mispec Pt. (Figure 4.18) where facies C was observed and sand and angular gravel of the Sambro Sand close to where facies D was observed. Both of these contemporaneous deposits are hypothesised to be derived from the winnowing of the Scotian Shelf Drift, a glacial till that stretches from the mouth of the Bay of Fundy to the Saint John-Digby line, winnowing that happened during the late postglacial sea-level rise. In the Gulf of Maine and Bay of Fundy, the LaHave clay is supposed to be a deposit of the clay fraction of the glacial till [*Fader et al.*, 1977] and the Sambro sand supposed to be the residual gravel lag, a so-called "modified till" or "transgressive lag". The Sambro sand, itself a residual lag deposit, has been in turn reworked throughout the Bay of Fundy and here the Sambro sand is characterized by extensive fields of sand waves and isolated megaripples [*Fader et al.*, 1977].

Facies C could therefore be analogous to the LaHave clay but with present day fluvial input from the Saint John River; in fact, in the past the LaHave clay in the Bay of Fundy has been dubbed the Saint John (River) Delta [*Fader et al.*, 1977]. Facies D could correspond to the sand and angular gravels of the Sambro sand.

The Mispec Bay banner bank is probably also associated with the Sambro sand, albeit in this case the formative process is coastal sediment transport, not deep marine as is the case for the Sambro sand associated dunes in the Bay of Fundy. Mathematical modelling of banner bank formation [*Signell and Harris*, 2000] predict that they are initially

composed of sediment derived from the seabed around the headland, i.e. in the Cape

Spencer case, the sand fraction of the Sambro sand. However, because of the unusual

proximity of the easily eroded LaHave Clay, the latter may be a source of some of the

sediment that makes up the banner bank.

Chapter 5: Migration Measurement

5.1. Introduction

The following chapter is an updated version of *Duffy and Hughes-Clarke* [2005].

Digital terrain models (DTMs) compiled from high-density multibeam echosounder (MBES) soundings are currently the highest resolution representations of the morphology of a given area of seafloor. Airborne sounding techniques, such as LIDAR, can be more efficient than MBES techniques in the time it takes to survey an area but the poor sounding density and large sounding footprint area result in DTMs that are lower in resolution than MBES DTMs. Also unlike multibeam, LIDAR is limited to surveying in shallow non-turbid water so areas where active sediment transport is taking place may not be surveyed using this technique.

As stated in Chapter 2, Figure 3.six multibeam surveys of the Mispec Bay banner bank were conducted with the intention of measuring the rate of migration of the sand dunes on the bank. Obviously, the scale of detectable displacement is controlled by the justifiable resolution of the DTM. The latter depends on the multibeam sounding density which in turn depends on factors such as water depth, beam footprint area, across-track beam spacing, ping rate and vessel speed (discussed in Chapter 2). The presence of static bodies within the study area, such as bedrock outcrops, helped confirm the precise registration of successive surveys and ensured that detected displacements are real and not artifacts. With such a dataset, gaining knowledge of the mechanisms forming and maintaining the bank was of particular interest.

More generally, measurements of the dynamic behaviour of bedforms are of immediate relevance to hydrographers wishing to optimize repetitive survey frequency [*Le Bot and Idier*, 2000] and have been used by workers to calibrate their mathematical models [*Besio et al.*, 2004; *Nemeth et al.*, 2004]. Knowledge of bedform migration rate can also be combined with parameters describing the shape, height and composition of bedforms to calculate bedload transport rate [*Van den Berg*, 1987; *Ten Brinke et al.*, 1999; *Wilbers and Ten Brinke*, 2003; *Hoekstra et al.*, 2004; *Van Lancker et al.*, 2004]. *Duffy et al.* [2005] compare the bedform associated bedload transport rates observed on this sand bank with predicted rates derived from observed depth-averaged currents.

A number of different approaches to measuring sand dune migration have been taken over the years. *Langhorne* [1982] took a direct measurement approach, staked out a large sand wave on the Skerries Bank in Start Bay, Devon and employed divers to make continual measurements of the sand wave morphology over many tidal cycles. *Dorst* [2004] applied principles of geodetic deformation analysis to networks of point soundings in a hydrographic approach to determine the degree, type and statistical significance of seabed dynamics. *Lindenbergh* [2004] also took a geodetic deformation approach and used the model of a propagating sinusoidal wave which necessitated assumptions that dune spacing and celerity do not change in space. *Knaapen* [2005] observed the migration of bedforms through analysis of 22 multibeam surveys of a small (75 m by 750 m) area and measured migration by visually comparing extracted crest lines and trough lines. *Knaapen* [2005] carried out 14 multibeam surveys in September 2001, four surveys in April 2002 and four surveys in September 2002 with all surveys done at a reduced speed of four knots.

How does one take advantage of the total coverage afforded by modern sonar techniques to detect change? One approach is simply to view the DTMs as frames in a movie and observe how the bedforms migrate *Rubin* [2000]. However, it is difficult and user-intensive to interpret and quantify the degree of migration especially if the bed configuration is complex and the study area is large.
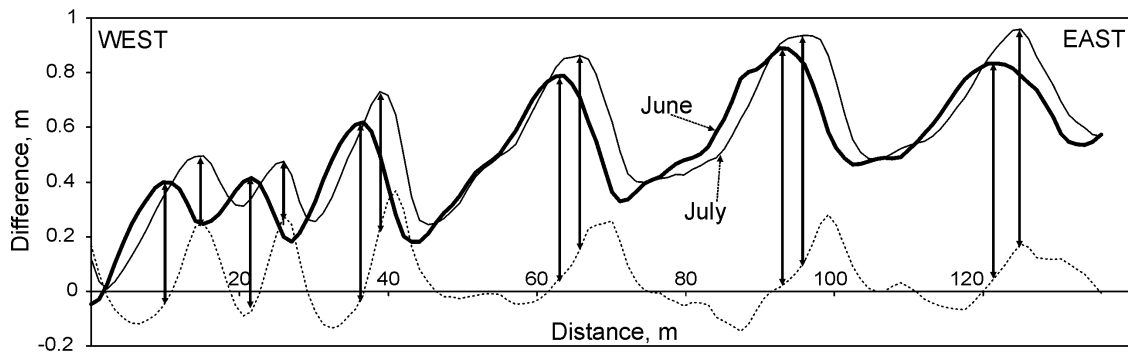
Figure 5.1 Depth cross-sections and cross-section through a difference DTM.

Since detecting the change of a DTM from one period to another is of interest, the DTMs may be subtracted and the resulting isopach map may be interpreted to show how the crests of the bedforms changed. In Figure 5.1, two cross-sections are displayed from the June and July surveys together with the difference between them. The arrows point out the positions of the crests at the different times. It is apparent that the difference cross-section bears little quantitative information about the displacement of the crests. This method is more suited to assessing volumetric change due to bedform migration. However, since such a volumetric method is based on subtracting absolute depth values at a point, the results are subject to motion related artifacts such as long period heave and tidal errors.

In this chapter, it is proposed to make full use of all the data in the DTM to determine how the bedforms have migrated with no *a priori* assumptions of dune spacing or spatial distribution of celerity. Not only the displacement of the *crest* is examined; such a measurement is limited in precision to the resolution of the DTM, which in turn is limited by the sounding footprint area. Furthermore, sand dunes may deform as they migrate so that the crest displacement may not necessarily equal the displacement of the center of mass of the dune [*Middleton and Southard*, 1984]. Instead, the relative position of the best match of a window of an image describing the shape of the DTM at time t_0 is sought at time t_1. The method described in this development uses slope images as the data set and so is insensitive to long period heave and tidal errors. In addition, cross-correlation of slope images emphasises the alignment of crest-line curvature, which most precisely defines a bedform displacement.

Discrete cross-correlation methods are widely used to analyze temporal, spatial, and spatio-temporal data series. Temporal cross-correlation is used in seismic data processing to distinguish a known signal from noise [*Kearey and Brooks*, 1996]. Spatial cross-correlation has been applied to pattern recognition in the motion picture industry [*Lewis*, 1995] and to image detection and registration in the remote sensing field [*Pratt*, 1991]. *Delacourt et al.*, [2004] recently applied a digital cross-correlation technique to stereo-photographs with the aim of measuring the three-dimensional displacement of a prominent landslide in south central France. In Particle Image Velocimetry, a cross-correlation technique is applied to a succession of digital images of a particle seeded flow to elucidate motion vectors [*Willert and Gharib*, 1991; *Jambunathan et al.*, 1995; *Raffel et al.*, 1998].

This chapter will concern itself with an application of a cross-correlation technique to consecutive DTMs of actively migrating sand dunes in Mispec Bay, Saint John, New Brunswick. Section 5.2 deals with the mathematics of cross-correlation and its specific application in this research. Section 5.3 describes factors relating to the temporal resolution of the dataset. Section 5.4 describes the results of different correlation pick types and the impact of morphology on migration measurement. Section 5.5 will be an interpretation of the migration vector field. Sections 5.6 and 5.7 are discussion and conclusion.

5.2. Theory and Implementation

The spatial cross-correlation technique may be used to locate the point where two spatial datasets are most similar. The cross-correlation coefficient quantifies the strength of correlation of two discrete datasets and is the sum of the products of overlapping pixels (5.1), where $f(x,y)$ and $g(x,y)$ are windowed discrete spatial variables with dimensions (W_x, W_y). The cross-correlation coefficient calculation is iterated by incrementing and decrementing the relative displacement in the x and y directions by k and l respectively:

$$r_{k,l} = \sum_{x=0}^{W_x} \sum_{y=0}^{W_y} f(x,y)g(x-k,y-l)$$

$$(-M \le k \le M)$$

$$(-N \le l \le N)$$

$$-\infty < r_{k,l} < \infty$$

All variables are integers   (5.1)

$$r = \begin{bmatrix} r_{-M,N} & \cdots & \cdots & \cdots & r_{M,N} \\ \vdots & & & r_{k_{MAX},l_{MAX}} & \vdots \\ \vdots & & r_{0,0} & & \vdots \\ \vdots & & & & \vdots \\ r_{-M,-N} & \cdots & \cdots & \cdots & r_{M,-N} \end{bmatrix}$$

The position of the maximum of the resulting *2M+1* by *2N+1* matrix (*M* and *N* being

the search radii), *(k$_{MAX}$, l$_{MAX}$)*, is the displacement of *g* relative to *f* where they are highest

correlated. However two factors affect the effective implementation of Equation (5.1): (a)

bright spots or dark spots in *g*, e.g. due to outlier soundings, will bias the maximum

correlation value towards these areas so that a high *r* value may just reflect these

anomalous spots; (b) the magnitude of *r* is linked to the size of the window *(W$_x$,W$_y$)* so is

not useful for comparisons with different window sizes. *r* is therefore normalised to the

two dimensional correlation coefficient, *R*, as illustrated in Equation (5.2).

$$R_{k,l} = \frac{\sum_{x=0}^{W_x} \sum_{y=0}^{W_y} \left[f(x,y)-\overline{f}\right]\left[g(x-k,y-l)-\overline{g}_{k,l}\right]}{\sqrt{\sum_{x=0}^{W_x} \sum_{y=0}^{W_y} \left[f(x,y)-\overline{f}\right]^2 \sum_{x=0}^{W_x} \sum_{y=0}^{W_y} \left[g(x-k,y-l)-\overline{g}_{k,l}\right]^2}}$$ (5.2)

$$-1 \le R_{k,l} \le +1$$

Equation (5.2) is the expression used in this development to calculate the correlation

between *f* and *g*. Note how only the mean of *g* needs to be calculated at each lag value

(k,l); the mean of *f* is independent of lag value since it is the pattern sought in *g* and need

only be calculated once at the start of the iteration.

Figure 5.2 illustrates the relationship between f, g, and the entire dataset dim_x by dim_y. Once the matrix of normalised cross-correlation, R, is fully populated, the windows f and g are advanced to the next position in the dataset. Figure 5.2 also shows f at the next positions in the x and y directions by the dotted rectangles. In this case there is 50% overlap of windows in both the x and y directions to ensure there is redundancy of measurement.
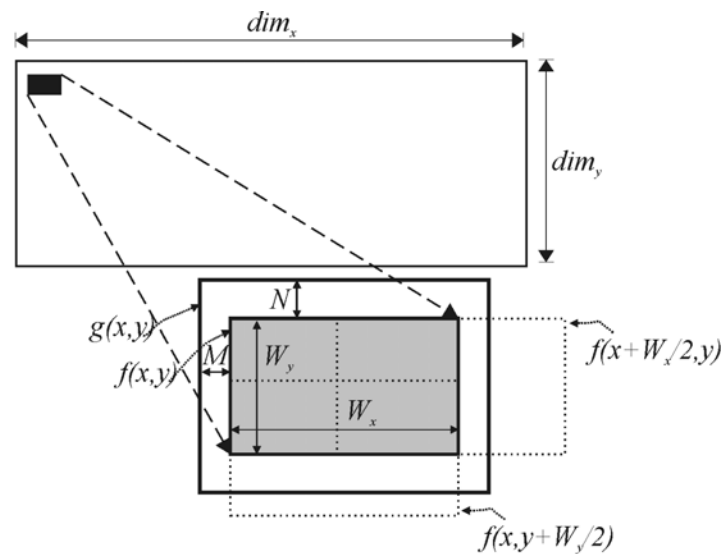
Figure 5.2 Diagram of f, g and the dataset.

5.2.1. Selecting the Window Size and Search Parameter

Some pre-analysis of the migration vector fields and the shape of the correlograms are necessary so that suitable values for the window size and search parameter can be chosen. Conceptually, the window size must be large enough so that it just encompasses a unique area of seafloor. If the window size is not large enough, then spurious displacement vectors will result. Therefore, the window size must be chosen to be just large enough so that the number of outliers of migration vectors is minimised. The search parameter is

chosen by examining a sample of correlograms taken throughout the field area as described in the following section.

5.2.2. Selecting the Migration Vector

Up to this point the implementation of cross-correlation is no different to that done in Particle Image Velocimetry (PIV) with one major exception: in PIV the fields of cross-correlated pixels are assumed to be random, therefore in the cross-correlation matrix there will be a single circular point maximum to which a translation vector can be drawn.

In the application of cross-correlation discussed here, a linear feature is cross-correlated with another linear feature that has been displaced. Depending on the sinuosity of this crest line, the resulting cross-correlation matrix will not have an obvious point maximum but an elliptical maximum or a correlation 'ridge'. This correlation morphology has important implications for the choice of migration vector as will be seen later.

In Figure 5.3(c), actual output resulting from cross-correlating a 30 by 30 pixel subwindow with a search size of ± 16 in the x and y directions is displayed. The following methods of measuring the displacement of bedforms were tested:

(i) By taking the offset of the maximum correlation;

(ii) By accounting for the shape of the cross-correlation peak by taking the weighted centroid (linearly weighted according to the ratio $R_{k,l}/R_{max}$) of the part of the array greater than a certain threshold value, hereafter called the "threshold region". *Raffel et al.* [1998] describes this method in the context of PIV to be suitable for broad threshold regions with

particle images less than 1.5 pixels in size. These criteria are met by the application of cross-correlation presented here in which typical threshold regions are made up of 50 values (for search size of $\pm$ 10 pixels) and the 'particles' in this case are equal to one pixel.

(iii) By taking account of the spatial trend of the cross-correlation peak by calculating a weighted line of best fit on the points making up the threshold region and then locating the point on the line which is closest to the zero lag position. This forces the migration vector to have an orientation normal to the average orientation of matching crest lines at the different times, i.e. in the event of no change in orientation of the crest lines, the migration vector will be perpendicular to the crest line. This is an acceptable assumption for 2-D dunes in a uniform flow field since it is widely accepted that in such a situation the dune crests lie perpendicular and migrate parallel to the mean sediment transport direction [*Belderson*, 1982; *Rubin and Hunter*, 1987].
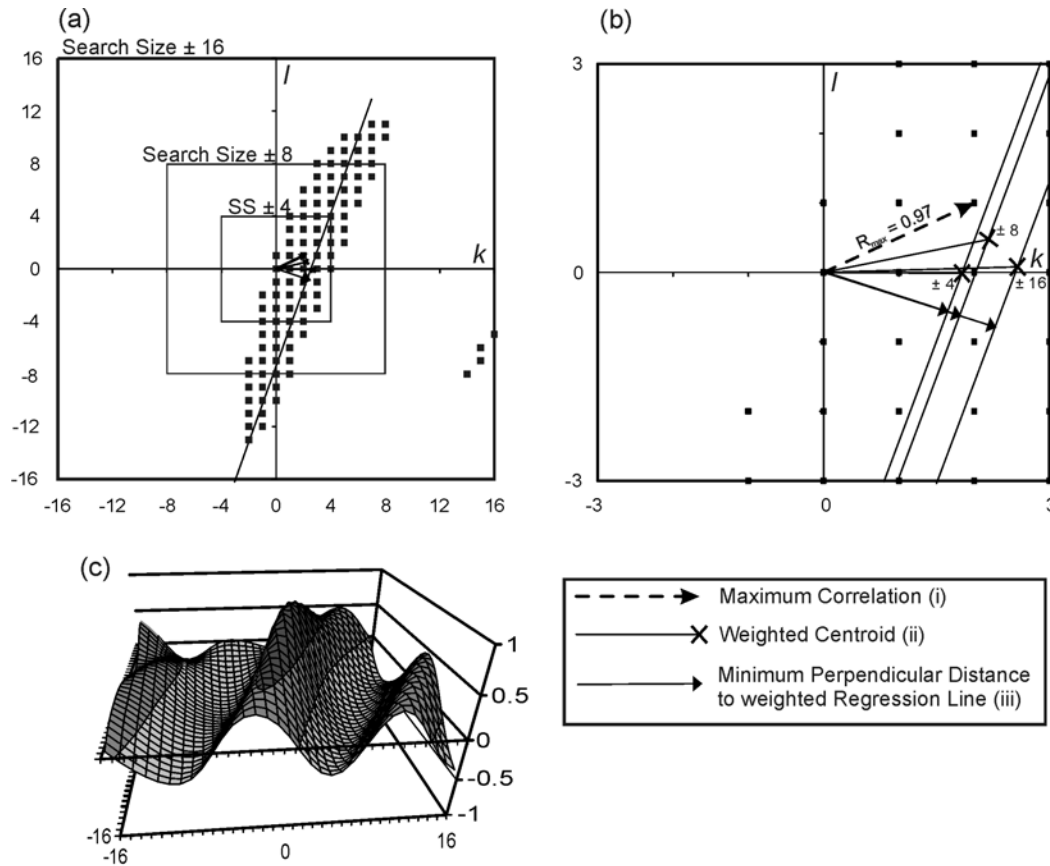
Figure 5.3 Different outputs of the spatial correlation algorithm using a 30 by 30 pixel (equals 30 by 30 m for this dataset) window with search sizes of M,N =4, 8, and 16 pixels. (a) shows the part of the cross-correlation array where $R_{k,l}$ is greater than the threshold value, the concentric rectangles show what part of the cross-correlation array is captured with the different search sizes; (b) is a close-up view of the different cross-correlation picks at the different search sizes. Note the erratic centroid pick as the threshold region becomes more populated with each increment of search size and note the static maximum correlation pick. Also shown are the weighted regression lines calculated as the search size is incremented and shown are the minimum perpendicular distance points to those lines; (c) shows the shape of the variogram.

The function of the threshold region is to define the shape of the base of the cross-correlation maximum. The authors found that a threshold value equal to the maximum correlation value divided by $\sqrt{2}$ satisfactorily described the plan view of correlation peak. The implications for this choice will be discussed later.

An important advantage of using one of the methods (ii) or (iii) is that displacements finer than the pixel size of the data sets may be resolved, unlike the maximum

displacement, method (i),which is constrained to integer displacements in the x and y directions. This is because the cross-correlogram, *R*, may be considered a discretised continuous correlation surface and the actual peak of this function lies between the pixels [*Sjödahl*, 1994]. For this reason, method (i) is limited in accuracy and precision. Method (ii) is a method of interpolating for the true correlation peak. Method (iii) is a new method proposed here and is specific to the cross-correlation of linear features in that emphasis is given to the linear trend of the cross-correlogram in addition to the correlation magnitude. Figure 5.3 (a,b) illustrates the different methods to elucidate a migration vector. It is immediately evident that methods (ii) and (iii) are sensitive to different degrees on the number of points in the threshold region. This number depends on both the threshold value and the search size (see the concentric squares in Figure 5.3(a) enclosing different threshold regions for different search sizes). The centroid picks are erratic in azimuth and magnitude up until the threshold region is fully populated (represented by the black squares in the figure). Any wider searching is not needed because either it will not increase the number of points in the threshold region or it could detrimentally incorporate high correlation points from a proximal crest thereby getting a false lock (four such outliers at a search size greater than ± 14 pixels are depicted in the lower right quadrant of Figure 5.3(a)). To minimize such spatial aliasing errors, the code was modified to only carry out the centroiding operation on the correlation ridge that is closest to the zero displacement position. The implication of the latter is that our survey frequency is such that spatial aliasing is not a problem: the bedforms have not migrated greater than half their spacing in the survey interval and the relevant correlation ridge is therefore the one closest to the origin.

However even if the threshold region is fully populated and the migration vector based on the weighted centroid method is stable, it is readily seen that a change in the threshold value can again cause the azimuth and magnitude of the vector to vary especially if the crest line has low sinuosity at the scale of the correlation window. In this latter case, high *R* values (greater than 90% of the maximum correlation value) can persist along the crest line at time t_2, affecting the position of the weighted centroid since the threshold region is not well-defined (Figure 5.4(a) shows the correlogram resulting in this case). It is clear that describing the migration of a *straight-crested* sand dune by fixing on its morphology (as the weighted centroid method does) is ambiguous and sensitive to input parameters. The linear regression method (iii) surmounts this latter problem of unstable azimuths by making the assumption that migration is perpendicular to the crests. This assumption of crest-perpendicular migration is a fair one only if competent currents are uniform along the crest [*Dietrich and Smith*, 1984; *Rubin and Hunter*, 1985; *Rubin and Hunter*, 1987]. Current cycles conducted over the sand bank have revealed that uniform currents over the 2D dunes flow 80% of the tidal cycle towards the headland [*Duffy et al.*, 2004]; this strengthens the argument that these straight crested dunes migrate perpendicular to their crests. Migration vectors arising from this method are in general less subject to variation in magnitude than vectors calculated from the centroid method and their azimuth is already fixed. However, they are insensitive to marked crest-oblique migration.
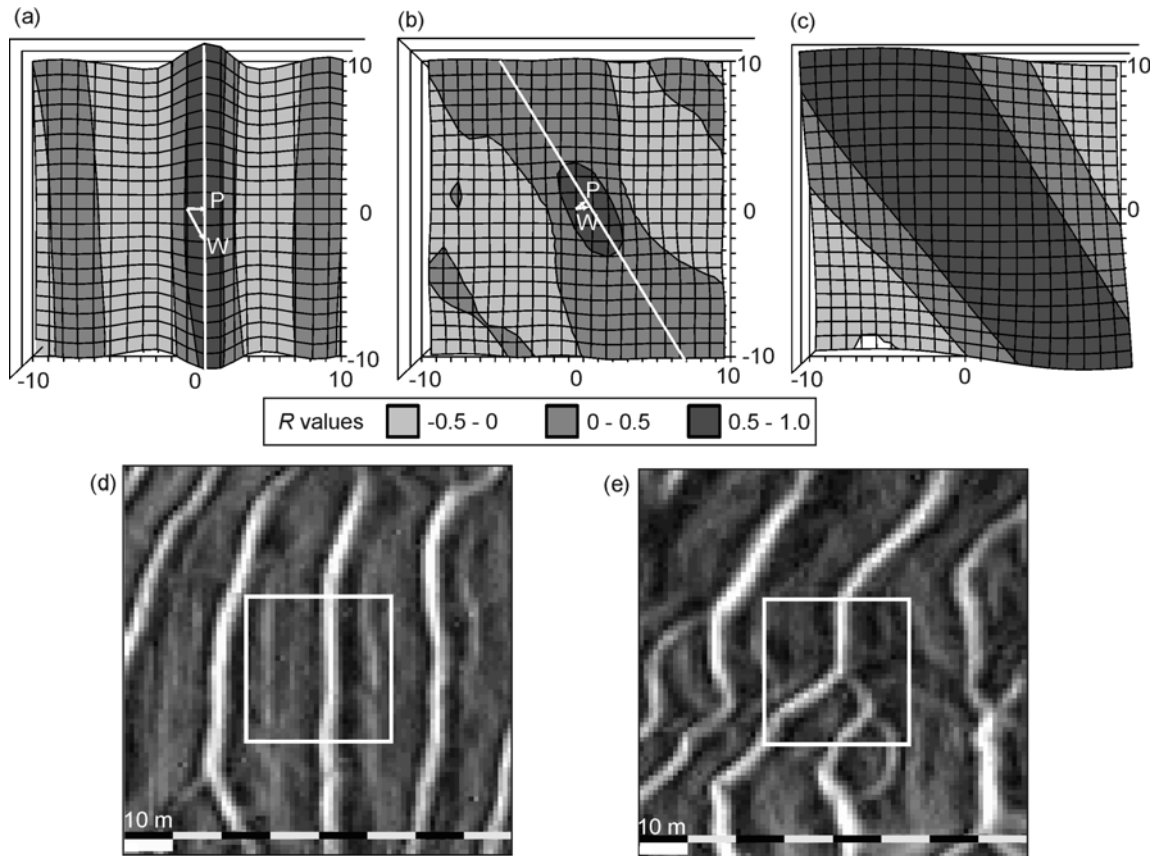
Figure 5.4 Figure shows the different correlation morphologies of: (a) a straight crested dune, using maximum slope of surface as the data type; (b), a bifurcating dune, using slope of surface as the data type; (c), the same bifurcating sand dune, using depth as the data type. The slopes of the straight crested dune (d) and bifurcating dune (e) are also shown with the correlation window outlined in white. P and W denote perpendicular regression and weighted centroid vectors respectively.

For dunes with three dimensional features such as sinuosity, bifurcations or terminations in the window of interest, the locus of such high R values is an enclosed ellipse rather than a line. Figure 5.4(b) shows the shape of the correlation function for sand dune with a bifurcation. In this case the centroid method is a more reliable indicator of displacement since there is a better-defined peak to which a stable vector may be drawn.

To summarize: the weighted centroid vector method may be used in all cases except where there are straight crested dunes, then the perpendicular method is more suitable.

5.2.3. Data pre-processing
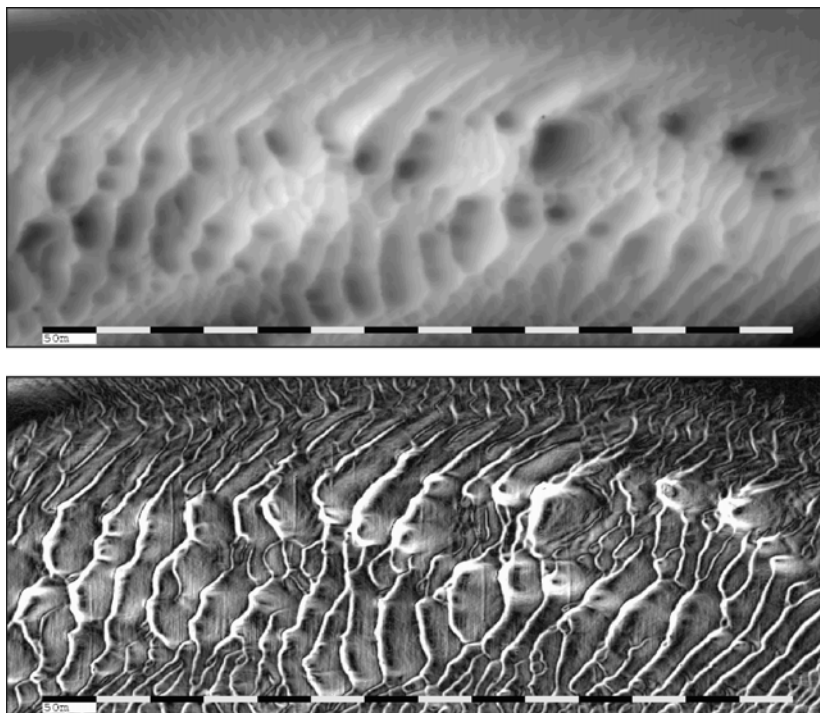
Figure 5.5 Different representations of the seafloor. (TOP) Eight bit digitized depth showing slowly varying pixel values on the sand dunes; (BOTTOM) Spatial gradient of bathymetry emphasizing dune morphology.

The type of representation of the bathymetric surface is of paramount importance to the detection of migration of bedforms. The cross-correlation algorithm works best when the input data contains regions of rapidly varying pixel shade. However, the features of interest, bedforms, are characterized by large areas of slowly changing depth (Figure 5.5(top)). If the cross-correlation is executed on this representation of the bathymetric surface, then a very broad correlogram results, in which the centroid or regression vector pick would be unreliable (Figure 5.4(c)). Clearly, this data type does not help picking where the crests of the dunes are most highly correlated. Using software developed by Ocean Mapping Group, *addSUN*, various representations of the DTM morphology were experimented with. Although sun illuminated representations emphasised dune morphology satisfactorily, the resulting migration vector was found to be dependent on the

azimuth of the virtual sun. The *-omni* option in *addSUN* generates an image of the slope of the DTM at a point; this data type showed no change in migration vector since there were no extra parameters in the slope calculation, such as azimuth or elevation of a virtual sun.

An image showing the slope at a pixel to emphasize the dune morphology was therefore used (Figure 5.5 (bottom)). The correlogram of the dune using this data type (Figure 5.4(b)), shows how much better defined the correlation peak is when using the slope data as input.

When we make this slope image, we lose any depth information of the dataset. This is acceptable since the focus of this chapter is the horizontal migration of the sand dunes, not the vertical change due to accretion or deflation. Inspection of depth cross-sections showed that vertical shifts in bathymetry not due to migration of the dunes were at the limit of the vertical accuracy of the dataset due to datum and tidal issues and therefore difficult to quantify. Furthermore, since the Mispec Bank appears not to have grown or decreased over the last four years, it is reasonable to assume that the bank is in dynamic equilibrium with respect to thickness and there is therefore negligible vertical change over the period of investigation.

5.3.   Dataset Temporal Resolution

Multibeam acquisition and processing for a single survey has been described in detail in Chapter 2. How the surveying frequency was decided will now be discussed. The active nature of the sand dunes on the bank was discovered through inspection of four Geological Survey of Canada cruises conducted at six month intervals in 2000 and 2001.

Although the slow moving dunes could be tracked over the 6-month interval, the fast

moving dunes could not be tracked with much confidence since their migration rate was

greater than half of their spacing per sample period. Therefore, a more frequent interval

was chosen to capture the movement of these fast moving dunes. Table 5.1 gives the

intervals between the surveys with the duration of a single survey lasting seven hours.

Table 5.1 Dates of Multibeam surveys with intervals.

Date	24/4/2002	18/5/2002	30/6/2002	1/8/2002	27/8/2002	2/10/2002
Interval between surveys (days)	–	24	43	32	26	36

To rule out possible measured dune displacements due to dune crest oscillations over a

tidal cycle such as those noted by direct measurements of a sand dune conducted by

Langhorne [1982], a separate hydrographic survey of a small area of the sand bank was

carried out during the execution of the ADCP cycle of the 4th October 2002 in which the

same area of seafloor was passed over every 30 minutes. No dune migration within the

resolution of the instrument was noted over this survey so the necessary assumption can be

made that detected migration is due to tidally integrated sediment transport rather than

short-term crest oscillations.

Bedrock outcrops in the area confirmed proper registration of the monthly DTMs.

Maximum apparent displacements of these outcrops were of the order of 1.5 m; this was

observed for the April-May interval, thereafter apparent displacements were not resolvable

on the one metre DTM.

5.4.   Results

Pre-analysis was first carried out to determine optimal cross-correlation window and search sizes. Optimum window size was sought by trial and error. A small window size caused spurious vectors since the windows did not contain a unique portion of the seafloor. A square window size of side 30 pixels (equal to 30 meters for this DTM) produced the most uniform vector field over the entire sand bank. A series of small dunes that fall within a single large window are assumed to not move independently over such a short length scale. Their migration may therefore be described by a single vector.

Selecting search size was not so straightforward for reasons outlined in Section 5.2.2. In the case of vectors calculated by the centroid and linear regression methods, their directions and azimuths were dependent on search size up until the elliptical threshold region was fully populated, found to be on average ± 10 pixels. Although as Figure 5.4(a) shows, even with such a search size the centroid vectors in the case of straight crested dunes will not be stable.

For the fore-going reasons, experimentation with different correlation pick types was done with a window size of 30 pixels and a search parameter of ± 10 pixels. Vectors were displayed using the –*currents* (because the output from the correlation code is formatted the same as a currents data file) option in *jview*, general data viewing software developed by Ocean Mapping Group. Where output from this code is displayed (Figure 5.6, Figure 5.8 and Figure 5.12), a single migration vector is represented by a two-tone arrow where the transition between white and black represents the origin of the vector.

5.4.1. Experimenting with different correlation pick types
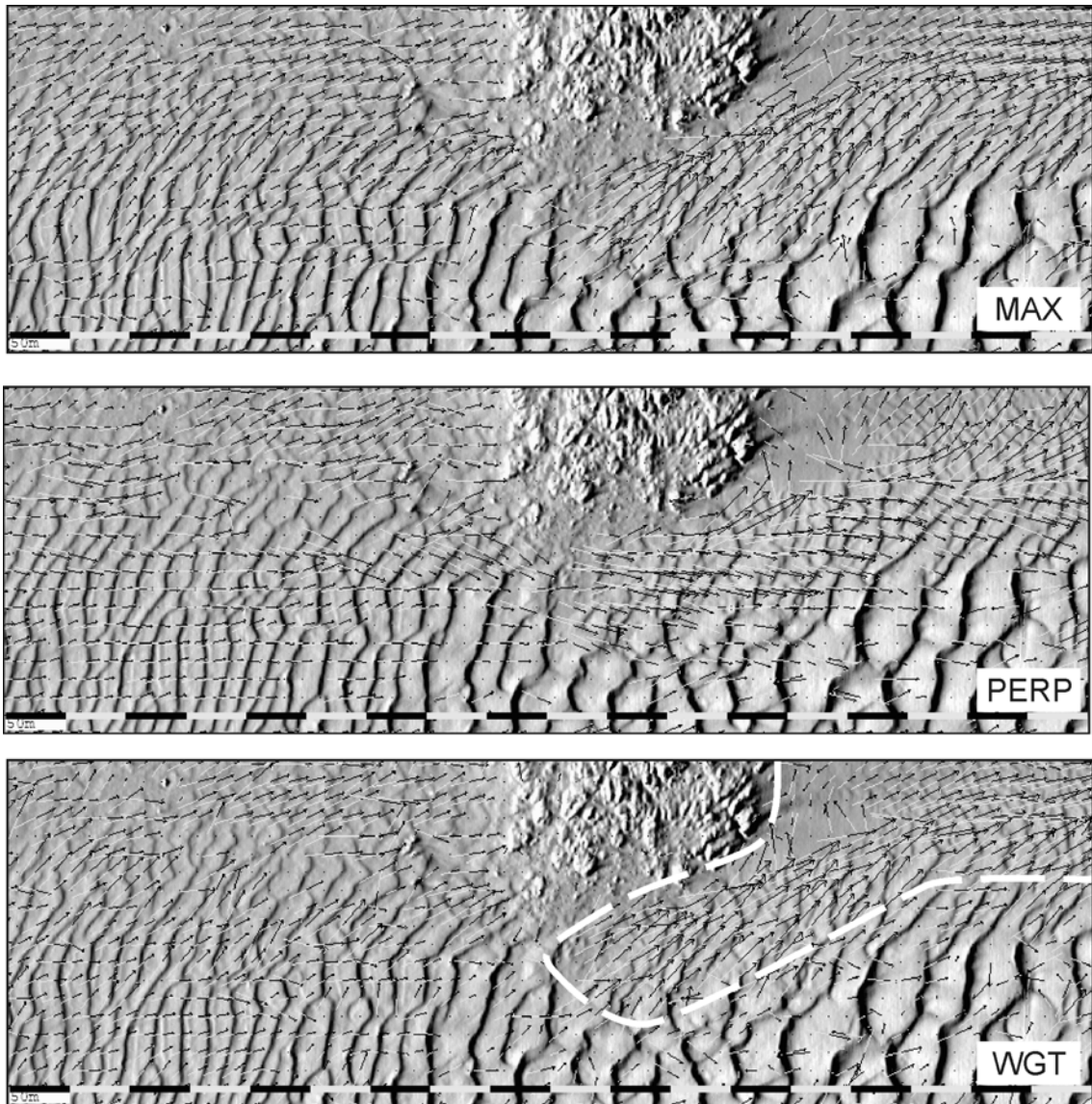
Figure 5.6 Different correlation picks on the dunes for a window size of 30 by 30 and search size of ± 10. Vectors are averaged from five vector fields with a ~1 month interval. TOP: picking the maximum correlation (method i); CENTER: picking the minimum perpendicular distance to the regression line (method iii); BOTTOM: picking the weighted centroid (method ii).

In Figure 5.6 monthly averaged outputs for running the algorithm with the three

different options (maximum correlation (method i), threshold region line of best fit

(method iii)) and weighted centroid (method (ii)) are shown. For ease of explanation in

the text, the order of method ii and method iii have been reversed.

Maximum correlation (method i)

As outlined by *Sjödahl* [1994] and *Raffel et al.* [1998], it makes little sense theoretically to use this vector type (Figure 5.6 (top)) since the vector is constrained to integer pixel displacements in the x and y directions. In addition, since the threshold region may be quite broad and a well-defined sharp peak does not exist, statistically it makes more sense to take into account the shape of the threshold region when calculating the migration vectors.

Regression line of correlation array (method iii)

These vectors were almost everywhere perpendicular to the crest lines, since they were forced to be so by the minimum perpendicular distance to the regression line of the threshold region condition. Vector subtraction of the regression line vectors from the weighted centroid vectors demonstrated that in regions of the sand bank with *three-dimensional* dunes, there was only one area where the weighted centroid vectors were systematically different from the regression vectors; this indicates that crest oblique migration was happening there. In the regions of *straight* crested dunes, there was some random difference between the regression vectors and weighted centroid vectors for reasons outlined in Section 5.2.2.

Correlation array weighted centroid (method ii)

As stated, vector subtraction between regression and centroid vector revealed the presence of crest oblique migration. This area is outlined with the white dashed line in Figure 5.6 (bottom). Bedforms that were migrating perpendicular to their crests and parallel to the sediment transport direction migrate into this region where the current

suddenly changes in direction and magnitude, because of acceleration around the bedrock obstacle. This induces the sediment transport direction to change across a distance too short for the bedforms to adjust as they migrate, causing crest-oblique migration. This phenomenon has been postulated for submarine dunes by *Rubin* [1998], observed in river meanders by *Dietrich and Smith* [1984] and in sub-aerial dunes by *Rubin and Hunter* [1985]. As far as the author is aware, this is the first time crest-oblique migration has been observed in a marine environment. The fact that in this region the bedforms are sinuous and in some cases terminate in the window makes their correlation morphology better defined and more trustworthy in this situation as described in Section 5.2.2.

5.4.2. Migration velocities

To calculate migration rates, the calculated displacement vectors were converted to average migration velocities (in m/month, where one month = 30 days) by taking account of the survey interval (Table 5.1). To make use of the fact that the separate migration velocity fields from the five survey intervals were in effect five different observations of the same phenomenon, they were then temporally averaged together to produce a more coherent vector field describing the migration regime of the sand bank. This averaging process reduced the prominence of spurious migration vectors in featureless seafloor while maintaining the true migration vector field.

Outliers can be removed from the averaged vector field by removing all vectors at a certain point that have a standard deviation of azimuth greater than a certain amount. This method was useful for removing noisy vectors that had erratic azimuths in each of the five vector fields. In this work, vectors that had standard deviations of azimuth of greater than 60° were filtered out. This resulted in the elimination of most of the vectors in the

featureless seabed and vectors where there was negligible systematic detectable movement. This latter point does not imply that there is no active sediment transport in this region. Rather, the correlation technique which depends on a systematic trackable feature, fails to measure bedform migration in these regions. In the next chapter, migration rates are combined with bedform heights to give an estimate of bedload transport on the banner bank. The bedload estimates thus calculated are limited to the region of dune features; bedload *not* expressed as migrating bedforms is indeterminate with this technique.

5.4.3. Temporal Aliasing

The previous discussion of migration vector calculation has assumed that there is a roughly monthly interval between the cross-correlated surveys. Of course, this places a limit on the smallest displacement that can be measured between the cross-correlated surveys; if the dune crest moves less than a pixel during the interval, then no displacement will be detected (this is often the case for the slower moving larger dunes) while the displacement of faster moving dunes will be detected. Ideally, resolution of these slower moving dunes and the faster moving dunes would be done simultaneously; this is done by varying the time period between cross-correlated surveys.
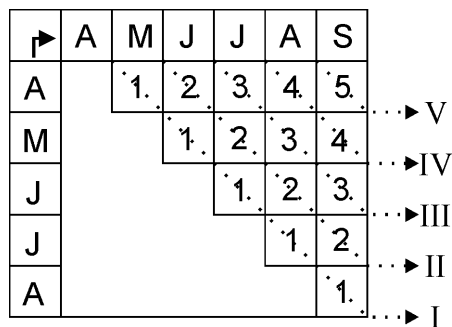
Figure 5.7 Illustration of choice of survey interval. The solid arrow denotes the cross-correlation operation. Vector averaging of the different intervals is denoted by the dotted arrows

How this is done practically is illustrated in Figure 5.7. Five temporally averaged

weighted centroid vector fields are derived and displayed in Figure 5.8: the first (I) being

made up of the average of five roughly one-month intervals; the last (V) being made up of

a single five month interval.
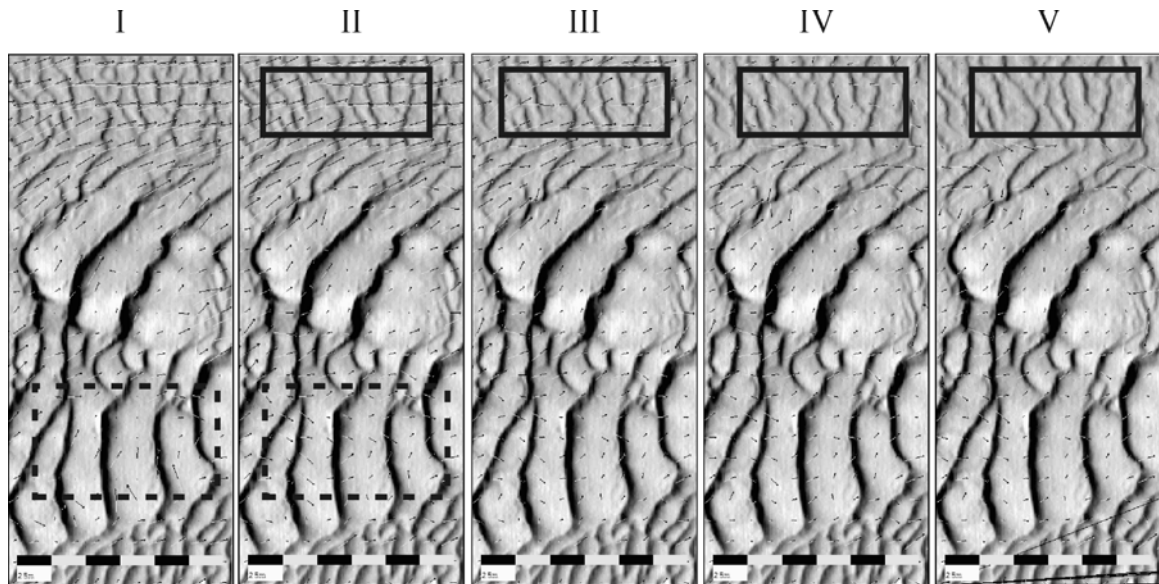
Figure 5.8 Sample averaged weighted centroid vectors from vectors fields I to V resulting from choosing intervals as described in Figure 5.7. Comparison of dashed squares shows better resolution of slow moving large dunes, i.e. more vectors. Solid squares demarcate loss of lock effect due to temporal aliasing in fast moving dunes.

From inspection of the solid rectangles in Figure 5.8, it is clear that the weighted

centroid vector fields derived by averaging the displacements over greater than two

months begin to "lose lock" on the fast moving dunes because of temporal aliasing. A

concession needed to be made between resolution of slow movements and loss of lock of

faster dunes and this was found to be the two-monthly interval field.

This observation compares favourably with theoretical temporal aliasing calculations:

for instance, the small dunes in the western part of the sand bank have a spacing of 12 m

and average migration rates of 2 m/month. This means that to avoid aliasing, the survey

period must be shorter than three months. Given the fact that the DTM is of finite

resolution, a interval of two months satisfies this condition. This two-monthly vector field is used for sediment transport calculation in the next chapter.

5.4.4. Migration Vector Precision and Accuracy

We used DGPS positioning which gave our horizontal position to within 1.5 m at 95% level of accuracy, as quoted by the manufacturer. A number of stages of averaging in the processing of migration vectors make them more accurate:

The compilation of the DTM by binning the soundings into a 1 m grid averages out the horizontal errors of the soundings within that bin, making the averaged horizontal position of the averaged sounding more accurate. The fact that some of the soundings in a single bin are from different survey lines at different times helps minimize potentially correlated bias errors due to multipath.

Since the DTM is quantised into 30 m by 30 m units, outliers in horizontal position within this large window have less of an impact. In addition, this window size encompasses multibeam soundings from multiple opposing survey lines along which biases are unlikely to be correlated.

Considering the vector field as a whole, overlapping successive correlation windows in the x and y direction increases the 'signal to noise' ratio of the vector field by increasing the redundancy of displacement measurement.

Since each vector field is based on only two observations of state of the sand bank, stacking the migration vectors considerably increases their accuracy. Filtering based on

standard deviations of azimuth and magnitude helps eliminate vectors in areas where no migration is occurring or no bedforms are present.

To find out which of the correlation pick methods were most accurate in terms of migration magnitude, the Cartesian displacement was measured of a sample of dunes throughout the sand bank between the April survey and the September survey and taking into account the interval, calculated their average migration rate between those two periods. The Cartesian displacement was calculated by picking a distinctive feature on a dune crest, such as a bifurcation, and measuring its displacement between the April and September surveys. The precision of this 'eye-balling' of the Cartesian migration rate is one pixel from the April survey to the September survey which translates to 0.20 m/month.

Although, the azimuth of the weighted centroid vector could vary with the threshold value, its magnitude and the magnitude of the regression vectors were very close to the Cartesian migration rate, both being within $\pm$ 0.40 m/month of the Cartesian rate. The technique successfully resolved average migration rates down to 0.8 m/month, the latter rate resolved from cross-correlating 2 month intervals to detect such slowly migrating dunes.

5.5. Interpretation

As pointed out in the introduction, the underlying justification of this development was to better understand sediment transport processes of the banner bank. To that end, the following pertinent observations could now be made as a result of this method.
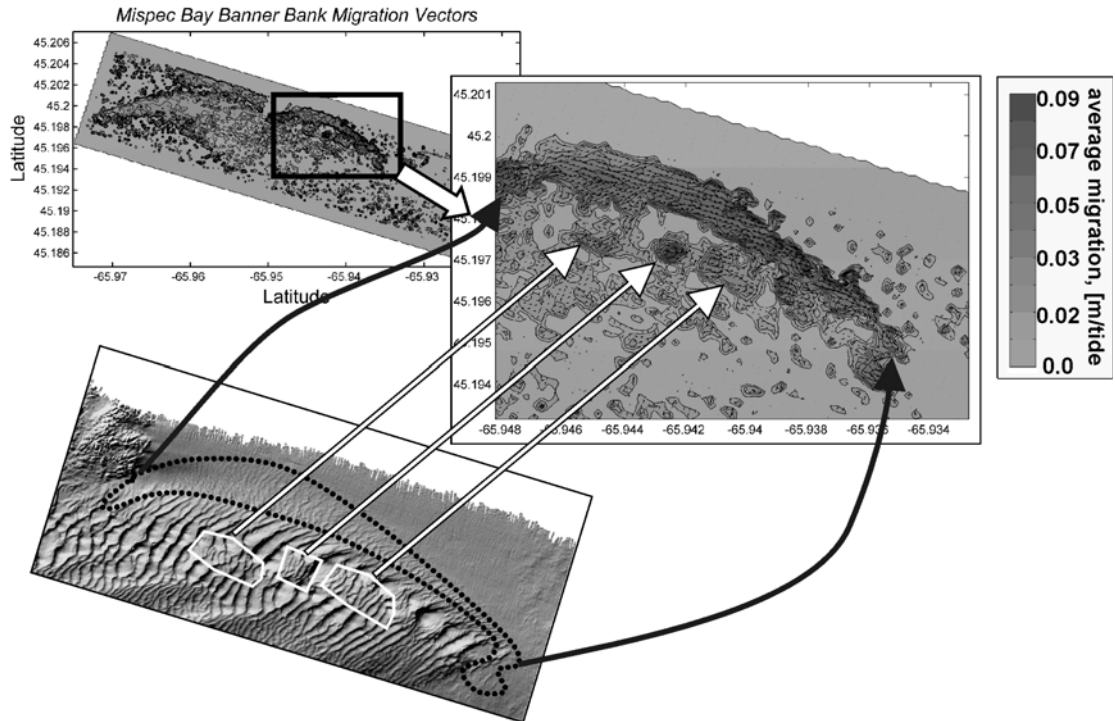
Figure 5.9 Overview contour map, with detail of tip, of average migration rate with vectors superimposed. Also shown in lower left-hand is a shaded relief map showing locations of migration "hot-spots".
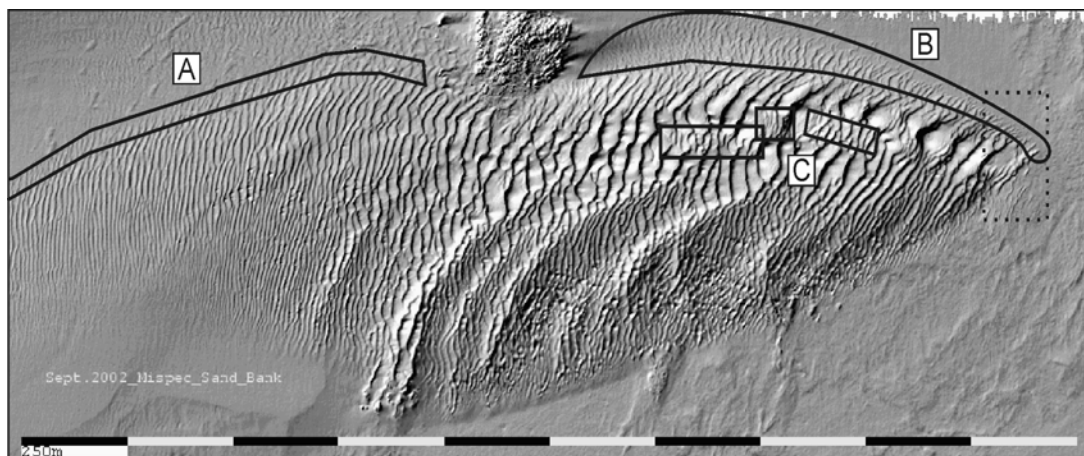
Figure 5.10 Overview of the sand bank with the areas of most active migration outlined in black. The dotted rectangle is the location of Figure 5.12.

Inspection of the migration vector field of this banner bank reveals substantial spatial variability of movement (Figure 5.9). Overall, the dunes of spacing 20 m are the most active with mean and peak migration rates of 3.0 and 4.5 m/month. Note that these bedforms are only 30 cm in height; this shows the power of using the DTM slope data, rather than bathymetry, in this instance. These active dunes occur where the sand bank

laterally peters out to featureless seabed to the north (area A in the figure); in the base of a shallow channel feature that delimits the north-western part of the sand bank (area B); and at a number of flat patches in the sand bank where the depth is shallower than 27 m below mean water level (areas C). The larger (50 m spacing, 3 m high) dunes on the sand bank proper migrate slower with average migration rates of 0.9-1.1 m/month

A lateral increase in the net bedload transport vector in areas A and B is theorised to cause the increase in migration velocities towards the landward periphery of the sand bank where sand is transported either in suspension or as an undetectable sheet flow along the seabed; this will be dealt with in more detail in Chapter 7. As described in Chapter 4, sediment sampling has indicated that that seafloor landward of the sand bank is composed of bimodal medium sand and gravel whereas the sand bank itself is composed of moderately well sorted medium sand and fine sand. Therefore, it is proposed that immediately landward of areas A and B the net bedload transport vector is sufficiently large to wash away the 30 cm high bedforms and form the bimodal lag deposit, over which sediment is transported as a sheet grain flow. Area B possibly also has a locally increased net sediment transport due to the channelised nature of the bottom flow.

Where the sand bank comes to a narrow 'tip' close to the headland, there is evidence of bedforms becoming barchanoid in planform before being obliterated as the peak dominant current moves into the suspension regime proper and sediment begins to be suspended (Figure 5.12). Figure 5.11 illustrates typical frictional velocity variation over a tidal cycle derived from observed depth averaged current data close to the sand bank tip. Also shown are suspension threshold values for typical grain sizes on the sand bank. It is evident that during the peak flooding phase, sediment begins to become suspended,

decreasing the amount carried along the bed. It is worth noting that this frictional velocity variation is for observed currents around the neap tide (Figure 3.8) and so represents close to the minimum peak threshold velocity value over the spring neap cycle. The resulting change in bedform morphology is characteristic of increasing down-current net sediment transport towards the headland and could be evidence of a 'bedload parting zone' surrounding the headland as described by *Kenyon et al* [1981]. Such a bedload parting zone has been hypothesised to exist in the vicinity of another headland, Portland Bill, U.K., by *Bastos et al.* [2002] on the basis of surficial geology and current modeling.
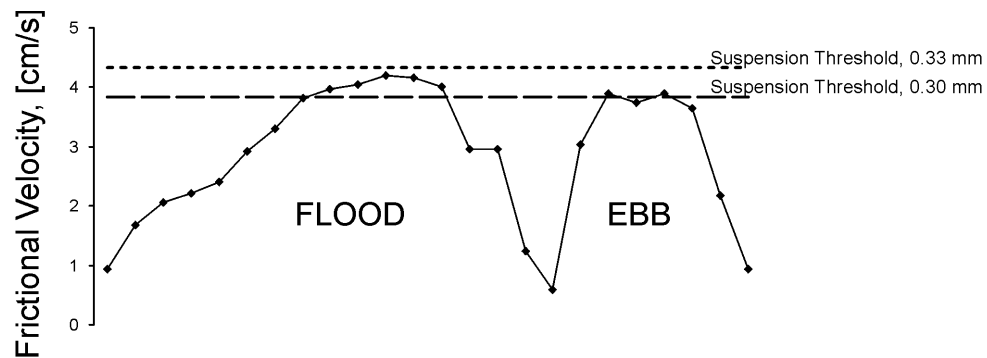
Figure 5.11 Predicted frictional velocity variation over an observed tidal current measurement cycle close to the tip of the sand bank. A hydrodynamic roughness value of 0.3 mm, typical of a sand/gravel substrate [*Soulsby*, 1997], was chosen to estimate the frictional velocity at the bed. Also shown are the suspension thresholds for typical grain size on the sand bank.

Moving towards the tip of the sand bank from area C, which is the highest part of the sand bank, the sand bank gradually tapers in thickness. The relative elevation of area C increases its exposure to wave action, which may explain the presence of swiftly migrating bedforms in that area (Figure 5.9).
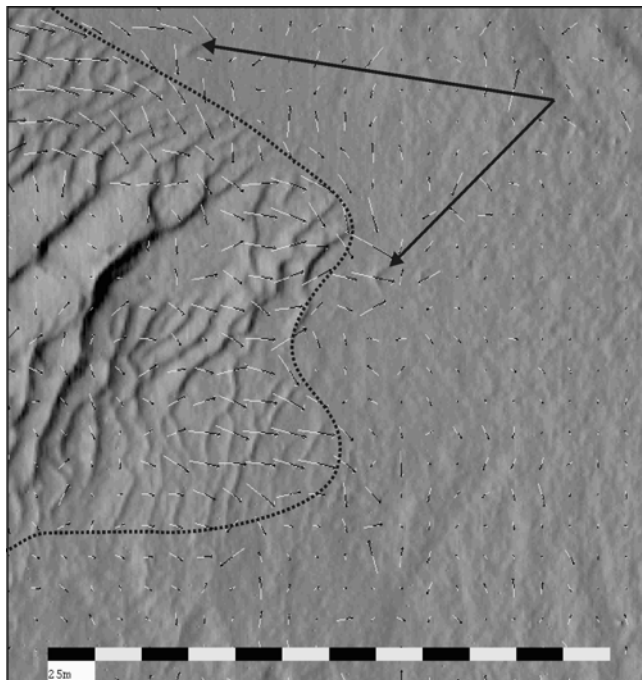
Figure 5.12 Picture showing accelerated migration of bedforms in two lobes at the tip of the sand bank. The weighted centroid vectors in these areas indicate migration rates of up to 3 m/month. The sand bank is demarcated by the dotted line. The arrows point out some examples of barchanoid dunes found in Area B.

5.6. Discussion

Both perpendicular regression and weighted centroid methods of picking the end of the migration vector are accurate to within ± 0.5 pixel per month. Table 5.2 summarizes vector applicability to dune type. The crest perpendicular vectors must be used in the event of straight crested dunes because the centroid pick, which depends on the existence of a unique trackable feature, cannot be used in this case. However, the crest-perpendicular migration assumption is only valid for uniform competent flow conditions. Indeed, as noted by *Rubin and Hunter* [1987], without knowledge of the current field, it is impossible to determine migration directions of straight crested dunes from remotely sensed images. The centroid pick must be used in all other cases, e.g. sinuous dunes, bifurcating dunes or dune crests that terminate in the correlation window so that oblique migration, if present, may be detected. Inspection of the linearity of the correlograms is therefore necessary to decide which one of the two vectors is representative. This latter

step has been automated by making the selection of centroid or regression vector be dependant on the ratio of the long axis to the short axis of the threshold region.

Table 5.2 Summary table of migration vector applicability to dune morphology and crest-relative migration direction.

Dune Type	3D, Crest Perpendicular	3D, Crest Oblique	2D, Crest Perpendicular	2D, Crest Oblique
Regression vector	Y	N	Y	N
Weighted Centroid vector	Y	Y	N	N

Since a correlation vector is based on a threshold region, and describes a region of 'best-fit' between successive images of (the slope of) a dune, it better reflects the horizontal translation of the volume of a sand dune rather than a method which relies purely on the translation of a dune crest. This is especially true of dunes which have deformed after their migration, as noted by *Middleton et al* [1984] and observed by *Langhorne* [1982].

Treating the five month to month vector fields of translation as separate observations of the same phenomenon enables 'stacking' of the vectors to produce vectors of migration rate. This enables us to get a clearer and more accurate picture of the average migration regime on the sand bank than a single observation.

The more observations of the sand bank done, the better the accuracy of the migration vectors providing the frequency of surveying is adequate to avoid temporal aliasing of sand dune migration. This means that the survey frequency must be high enough so that sand dunes with the highest ratio of migration rate to spacing do not migrate more than half their spacing in the survey interval. In this case, simultaneous resolution of both high

and low migration velocities was only achieved by averaging two-monthly vector fields, otherwise either slow dunes were not resolved or fast dunes were aliased.

In this experiment, a Simrad EM-3000 multibeam with a 1.5° by 1.5° nadir beamwidth was used. The use of a higher resolution multibeam, such as the Reson Seabat 8125 with a nadir beamwidth of 0.5° by 1.0°, would of course enable finer detail to be resolved which would enable the tracking of smaller scale features such as ripples climbing on the backs of larger dunes. If migration is to be detected at this scale, high precision horizontal positioning such as RTK-GPS becomes necessary and the vessel's speed must be decreased to ensure high along-track sounding density. There is also the possibility that crest oscillations that may occur over a tidal cycle could be detected. The vector field output for the motion of the dunes described in this chapter should not be different with a higher resolution sonar. Any difference could be due to tidal crest oscillations resolved by the higher resolution multibeam.

5.7.   Conclusion

The technique described in this chapter successfully reproduced a credible migration vector field on a sand bank through analysis of successive slope images compiled from dense, high resolution multibeam sounding data. The migration of even small (30 cm high) dunes was resolved since the data input into the algorithm described the slope rather than absolute depth and the survey frequency was high enough so that the fastest moving bedforms had not moved greater than half their spacing during the survey interval (i.e. aliasing was not an issue). The assumption of crest perpendicular migration was found to be invalid in the part of the sand bank down current of a bedrock obstacle where non-

uniform currents are experienced but valid in the region of straight crested dunes in the interior of the sand bank where currents are uniform.

The technique described here has been applied to data sets other than the Mispec Bay dataset. Migration vectors were successfully extracted from repeat surveys carried out in Puget Sound [*K. Iwanowska (GSC (Pacific))*, pers. comm.] and in an unnamed Norwegian Fjord [*O. Christensen (Norwegian Geological Survey)*, pers. comm.].

The determined migration rates now enable estimation of bedload transport rate, to be dealt with in the next chapter.

Chapter 6: Bedload Transport Estimation

In this chapter, the method of estimation of bedform associated sediment transport will be detailed. This entails the combination of migration rate data, already discussed, with the sand dune morphometric parameters of height and form factor. In order to test these bedform associated sediment transport figures for reasonableness, they will be compared with numerical predictions using observed currents and grain sizes. Therefore, in this chapter, the different disciplines applied in previous chapters are brought together in order to test the hypothesis that repetitive multibeam surveying may be used to estimate bedload transport rates.

It should be pointed out the general technique of using bedform migration rates to assess bedload transport is not new. The technique has been successfully tested in rivers or estuarine areas [*Engel and Lau*, 1980; *Van den Berg*, 1987; *Jinchi*, 1992; *Ten Brinke et al.*, 1999; *Wilbers and Ten Brinke*, 2003] and occasionally in the open sea [*Langhorne*, 1981; *Huntley et al.*, 1991; *Knaapen*, 2005], all with simultaneous near bottom current measurements. The methods of measuring bedform displacement vary from repeat single beam surveying every day for six days around periods of high river discharge [*Van den Berg*, 1987]; six months of sidescan sonar images [*Van den Berg*, 1987]; 12 months of multibeam surveys in which a small sand dune field was surveyed multiple times every six months [*Knaapen*, 2005]; employing divers for almost daily measurement of a large sand dune during spring and neap tides [*Langhorne*, 1982]; daily levelling of two transects over an intertidal bedform-covered shoal for a period of 12 days [*Larcombe and Jago*, 1996] and a bottom mounted camera taking photographs at two hourly intervals for a period of

three days [*Huntley et al.*, 1991]. In this chapter, comparison of bedform associated sediment transport rate based on much longer (~30 day) time intervals with bedload transport rate deduced from tidal current observations will be attempted.

Another method of estimating bedload using repeat observations of bedforms is subtraction of successive depth observations [*Langhorne*, 1982; *Huntley et al.*, 1991]. Such an observation will give a direct volumetric measurement of sediment eroded from the lee and deposited on the stoss side; however, these observations require excellent vertical control and in the past these observations have been direct bed measurements [*Langhorne*, 1982] or repeated stationary photography [*Huntley et al.*, 1991]. For multibeam sonar to apply this technique, an accurate height measurement such as that afforded by RTK-GPS would be required so that vertical errors due to tide and heave artefacts could be accounted for. This was attempted without success in this work but it is argued that the bedload estimation technique developed in this thesis is more widely applicable since it does not require RTK-GPS.

6.1. Theory and Implementation of Bedform Associated Sediment Transport

The sediment transport rate expressed as a migrating bedform may be quantified as the transport rate necessary to transport the volume of the sand dune in the time for it to travel one wavelength [*Simons et al.*, 1965].

$$q_{b,mig} = \frac{(\text{Volume per unit Crest Length})}{(\text{Time to displace one wavelength})} = \frac{(z_{crest} - z_0)f\lambda}{\lambda/c}$$

$$q_{b,mig} = cfH$$

$q_{b,mig}$ = average bedload transport rate over one dune wavelength

z_{crest} = depth to dune crest

(6.1)

z_0 = depth to point of zero bedload transport (assumed to be trough)

λ = dune wavelength

f = form factor

c = dune migration rate

A more rigorous derivation of this is given in Appendix B.

Implicit in (6.1) is that all the sediment is transported by erosion from the stoss side of the bedform, transport over the crest and then subsequent deposition on its lee side. If this was not the only mode of bedload transport, along a train of bedforms there would a "background" bedload transport, q_{0b}, not expressed through bedform migration and superimposed upon the spatially varying sediment transport expressed as migrating bedforms. Such "sediment bypassing" (dashed arrow in Figure 6.1), where sediment leaps from the crest onto the stoss side of the down-current dune [*Larcombe and Jago*, 1996], is predicted to become significant at higher flow stages [*Huntley et al.*, 1991] and increases the discrepancy between bedform associated sediment transport and actual bedload transport. For this reason, if knowledge of typical maximum local flow stage is not available, then $q_{b,mig}$ must always be considered to be a lower estimator of bedload transport [*Knaapen*, 2005].
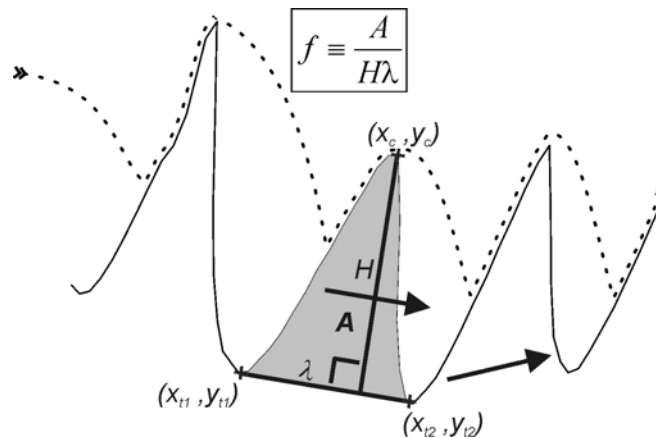
Figure 6.1 Calculation of height and form factor for the cross-section of a dune. Heavy solid arrows show bulk migration parallel to the base of the dunes. Dashed arrow depicts sediment bypassing where sediment is not trapped in the lee of the dune so this sediment transport is not expressed as dune migration.

It should also be pointed out a further sufficient condition for the validity of the assumption of equality of bedform associated sediment transport and actual bedload transport is that sediment is transported in the same direction as the bedform is migrating. This is not the case at very high flow rates where "anti-dunes" occur. In this latter extreme case, sometimes observed in rivers and shallow streams crossing beaches, bedforms migrate upstream because of erosion from the lee side and subsequent deposition on the stoss side of the next dune downstream [*Van Rijn*, 1993]. Therefore, sediment is transported downstream but the bedforms migrate upstream so the assumption of equality of bedform associated transport and bedload transport is false, however, this situation is rarely encountered in marine environments, with the possible exception of at the base of turbidity currents.

As is evident from (6.1), three quantities are necessary to calculate the bedload transport expressed in the migration of a sand dune. Migration speed as been comprehensively dealt with in the previous chapter so the form factor and dune height are the remaining parameters that need to be quantified. The dune height is here defined as

the perpendicular distance from the crest of a dune onto the line joining the troughs either side of the crest as illustrated in Figure 6.1 and Equation (6.2).

$$h = \frac{\left|(x_{t2} - x_{t1})(y_{t1} - y_c) - (y_{t2} - y_{t1})(x_{t1} - x_c)\right|}{\sqrt{(x_{t2} - x_{t1})^2 + (y_{t2} - y_{t1})^2}}$$

$$f \equiv \frac{A}{bh}$$

(6.2)

This definition has also been employed by *Wilbers and Ten Brinke* [2003] and is the most logical definition of dune height since it accounts for dunes where their troughs are not on the same level. The height defined in this manner is the imaginary line through which the section of the dune must move perpendicularly, e.g. for a large scale sloping surface the dune will move along this sloping surface normal to the height defined here (arrows in Figure 6.1).
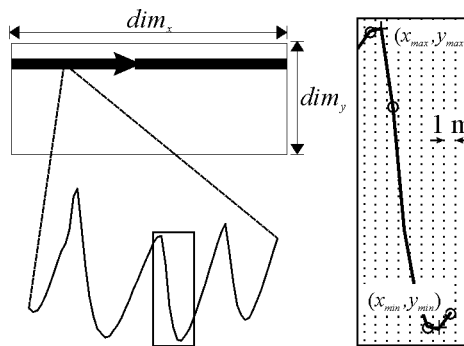
Figure 6.2 Diagram depicting the detection of the position and height of local maxima and minima in a dune profile.

Calculation of dune height and form factor therefore requires the positions and depths of all the local maxima and minima of the sand bank. This process is described in Figure 6.2 and is achieved by scanning through a depth DTM row by row and storing the value and position of each local maximum and minimum. An image of the height of the dunes is the output of this code.

The form factor is calculated by numerically integrating the area A (Figure 6.1) by a trapezoidal approximation and dividing by the product of the length of the baseline and the perpendicular height. A value of 0.5 means that the cross-section of the dune may be approximated by a triangle. However, a dune section need not be a pure triangle to have a form factor of 0.5 (Figure 6.3 (right)).
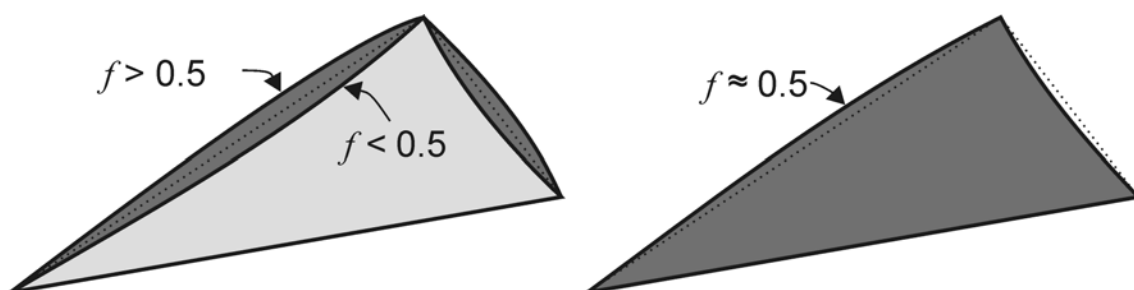
Figure 6.3 Schematic illustration of form factor.

To calculate the sediment transport rate, the average magnitude of the migration vectors in the vicinity of the pixel in question is multiplied by the form factor and the local dune height, taking into account assumed porosity (40%) and assumed density (2650 kg/m^3). The average of the migration magnitudes is used because as stated in Section 5.2, the migration of a given area of seafloor is measured on four separate occasions because of the overlap between cross-correlation search areas. The hatched area in Figure 6.4 is an example of such an area; there are four different vectors pertaining to that region and the average of the magnitudes of these vectors is used to calculate the bedload transport in this region. Implicit in this averaging process is the reasonable assumption that the azimuths of the migration vectors do not change drastically over the scale of the overlap between adjacent search areas.
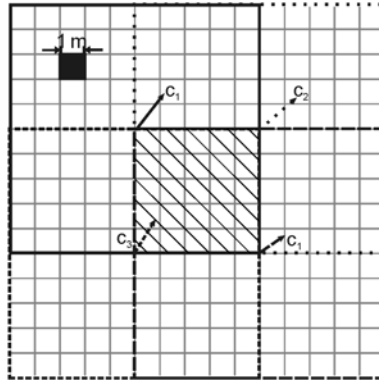
Figure 6.4 Illustration of averaging of migration vector magnitude in order to calculate bedload transport rate. c_1, c_2, c_3 and c_4 describe the migration of the seabed delineated by the large squares centered on the vectors. All the pixels (grid squares) in the hatched area are allocated the value of the average of the magnitudes of the migration vectors c_1, c_2, c_3 and c_4.

6.2. Hydrodynamic Predictions of Bedload Transport

To investigate the usefulness of the bedform associated sediment transport measurement as described in this chapter, various general hydrodynamic predictors of bedload transport, q_b, and a specific numerical model of the field area were used to compare with the "observed" bedform associated sediment transport rate.

A number of formulae for dimensionless bedload transport, Φ, have been proposed, many of which can be expressed in terms of the Shields mobility parameter, θ, and Shields critical mobility parameter, θ_{cr} (6.3). Equation (6.4) illustrates how the bedload transport is calculated from the dimensionless bedload transport by accounting for the effects of gravity, density contrast and median grain size

$$\Phi = f(\theta, \theta_{cr}) \tag{6.3}$$

$$q_b = \Phi\left(\sqrt{\left[g(\rho_s/\rho - 1)d_{50}^{\,3} \right]} \right) \tag{6.4}$$

Shields Parameter, θ, in (6.3) above was defined in Chapter 4 (Equation (4.4), p. 99) and the critical mobility parameter, θ_{cr}, is calculated from the algebraic expression

proposed by [*Soulsby*, 1997] for Figure 4.2 (p. 98). It should be noted that although the

formulae following were developed for steady flows in rivers, they can still be used for

tidal flows because the response time of a sand grain in bedload motion is very short

compared to the tidal period [*Soulsby*, 1997].

Hydrodynamic predictors are quite variable, with variations of up to a factor of four

for identical input parameters [*Soulsby*, 1997]. Three empirical predictors were chosen

and the reasons for the choice are given:

1. The formulation of *Nielsen* [1992], Equation (6.5) was chosen because it is

    consistently the largest of the hydrodynamic predictors in use [*Soulsby*, 1997]

    and will prove a useful upper limit to expected bedload transport rate.

$$\Phi_N = 12\sqrt{\theta}\left(\theta - \theta_{cr}\right) \tag{6.5}$$

2. The formulation of *Madsen* [1991], Equation (6.6) was chosen because it does

    not make the simplifying assumption that the grains are in continuous contact

    with the bed. More realistically, it allows for momentum transfer through

    saltation and thus can be used at higher flow rates when saltation occurs.

$$\Phi_M = 9.5\left(\sqrt{\theta} - 0.7\sqrt{\theta_{cr}}\right)\left(\theta - \theta_{cr}\right) \tag{6.6}$$

3. The modified Kalinske-Frijlink formulation, Equation (6.7)was used by *Van*

    den Berg [1987] in a study similar to this one, where bedform associated

    sediment transport rates were compared with predicted values using the latter

    formulation. In this formula the bedload transport rate is calculated directly.

$$q_{b,K} = 5\rho_s d \sqrt{dg(\rho_s/\rho - 1)}\theta e^{-0.27/\theta} \tag{6.7}$$

Equation (6.4) is used to calculate $q_{b,N}$ and $q_{b,M}$ from their dimensionless equivalents, Φ_N and Φ_M.

6.2.1. Method

Observed depth-averaged currents, the median grain size of the sand bank and measured depths were used to calculate the instantaneous bottom shear stress in order to calculate the instantaneous Shields mobility parameter, θ. The Shields mobility parameter, together with the critical Shields mobility parameter, θ_{cr}, (above which motion is initiated), are then used to predict the instantaneous bedload transport. This instantaneous bedload transport is then integrated over the tidal cycle (taking into account opposing sediment transport directions with opposing currents) to give the bedload in units of kg/m/tide to make this figure directly comparable to the observed bedform associated sediment transport rate.

6.3. Results

6.3.1. Bedform Associated Sediment Transport

The map of sand dune height is shown in Figure 6.5. The continuous height data has been binned into eight intervals so the regions with similar heights can be more easily identified.
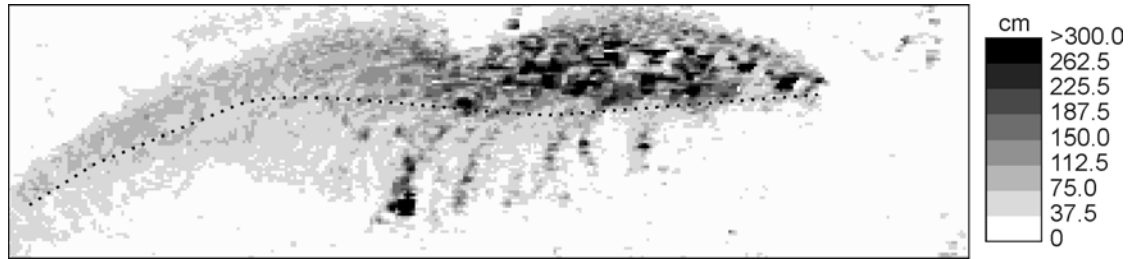
Figure 6.5 Sand dune height plot. Dotted line demarcates the shoreward extent of the small dunes in the deep water.

Two patterns in dune height on the sand bank are readily observed. Firstly, dune height increases eight-fold towards the tip of the sand bank, reaching a maximum height of four metres. Secondly, the smallest dunes are found only in a thin band over the landward edge of the sand bank and in deeper water seaward of the dotted line in the figure.

The map of form factor is shown in Figure 6.6. Analysis of the form factor frequency plot gives a mean form factor of 0.49 with a standard deviation of 0.1.
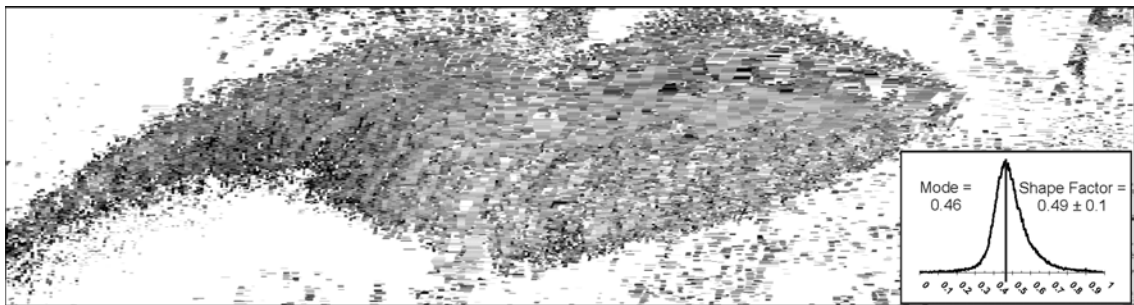
Figure 6.6 Plot of form factor showing frequency plot of values.

The most frequently occurring form factor (the mode) is 0.46. Any variation in form factor of the order of the standard deviation will not have a large effect on the calculation of bedform associated sediment transport; therefore the calculation of Equation (6.1) was done assuming a form factor value of 0.5.
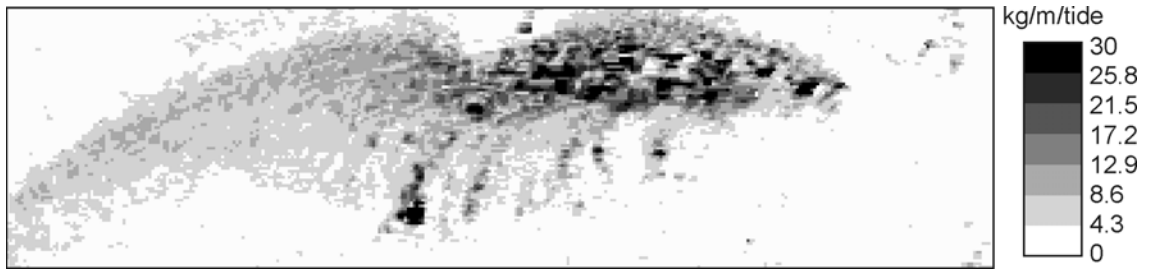
Figure 6.7 Bedload Transport plot.

Figure 6.7 shows the result of calculation of Equation (6.1), the bedform associated sediment transport. Comparison of Figure 6.5 and Figure 6.7 reveals that much of the variability on bedform associated bedload transport is due to variability in bedform height. Even though larger bedforms move slower (see Figure 5.8 (II) p. 144), their greater height ensures that they move larger volumes of sediment than the swiftly migrating smaller (only 30 cm high) dunes. The peak bedform associated bedload transport is therefore estimated to be 30 kg/m/tide. Comparison of this figure with numerically predicted figures will be made in Section 6.4

6.3.2. Numerically Predicted Sediment Transport

6.3.2.1 General Formulae
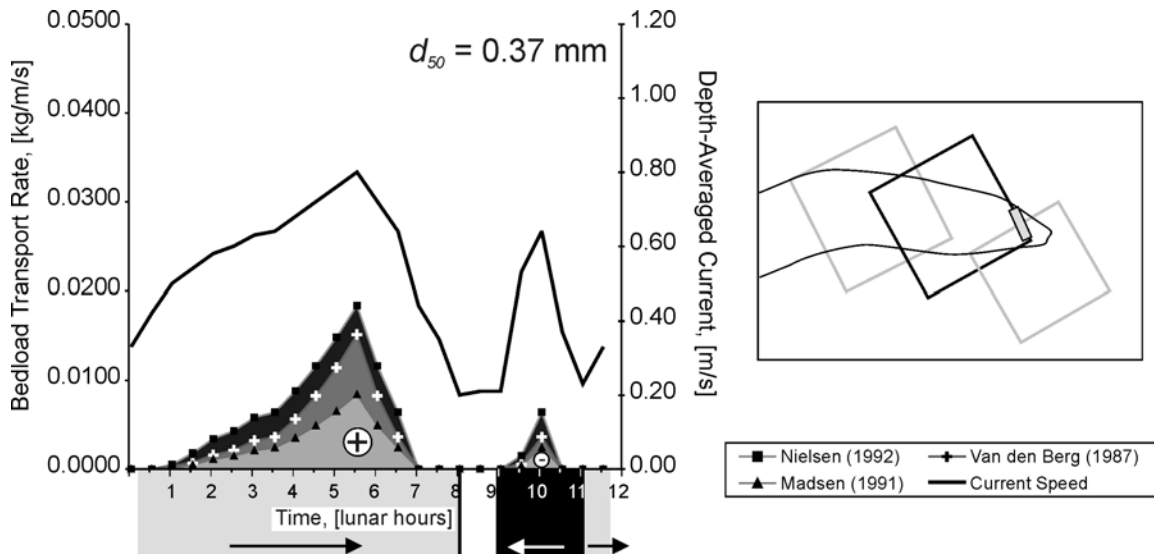
Figure 6.8 Typical average spring neap current magnitudes over the large dunes on the sand bank together with predicted instantaneous bedload transport rates. Arrows denote note additive (during flood) and subtractive (during ebb) sediment transport.

As will be discussed later, the bedform associated sediment transport rate is best thought of as being a spring-neap cycle averaged figure. Therefore, care must be taken so that the currents used to calculate the Shields mobility parameter are representative of average spring-neap conditions. Figure 3.8 (p. 60) shows that the current measured by Diamond 2 may be taken to be representative of average spring neap conditions. The tidal current measurement points of Diamond 2 were chosen over the high bedform associated bedload transport values (small grey box in Figure 6.8(right)), to see if these values could be replicated. Figure 6.8 shows the predicted instantaneous bedload transport rate based on Equations (6.5), (6.6) and (6.7).

Table 6.1. Tidally integrated bedload transport rates at the point defined in Figure 6.8.

	Tidally integrated bedload, [kg/m/tide]	Discrepancy Ratio
Nielson (1992)	214	~ 7
Kalinske-Frijlink (1951)	149	~ 5
Madsen (1991)	90	3
Bedform Associated Value	30	1

Table 6.1 displays the tidally integrated bedload transport values (the areas under the curves in Figure 6.8), taking into account the fact that sediment transport away from the headland during the ebb tide is subtractive. The table also lists the ratio of the mathematically predicted value to the bedform associated value.

6.3.2.2   Region Specific Numerical Model

A sediment transport model SEDTRANS96 [*Li and Amos*, 2001] was used by [*Li et al.*, 2003] to predict how dredge spoils dumped in Saint John Harbour and approaches would be dispersed by the current regime. This sediment transport model used regional current predictions from a depth-averaged hydrodynamic model and observed grain size at the Black Pt. dumpsite. Conveniently, Mispec Bay was also modeled and the total sediment transport rate predicted for this area.
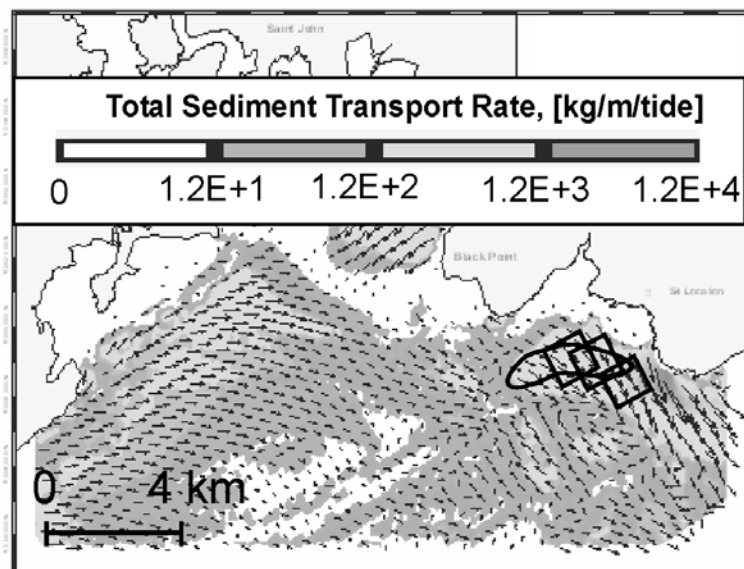
Figure 6.9 Predicted total sediment transport rate averaged over one spring tide in Saint John Harbour area after *Li et al.* [2003]. Legend has been modified to show units in kg/m/tide rather than m³/m/s.

This research predicted *total* sediment transport rates averaged over one spring tide of between 120 to 1200 kg/m/tide over Mispec Bay sand bank. It was estimated that bedload constituted ~20% of total sediment transport rate and therefore bedload transport rate was predicted to be between 24 and 240 kg/m/tide over Mispec bank for an assumed grain size of 0.22 mm.

6.4. Discussion

Given the fact that the Li's predicted rate is based on modeled spring tide conditions, this value should be representative of *maximum* sediment transport rate over a tidal cycle. In contrast, the bedform associated transport rate of 30 kg/m/tide is based on the averaged per tide displacement measured at points in time separated by periods of 67, 75, 58 and 62 days (these are the intervals of the vectors comparing every second survey as discussed in Section 5.4.3 page 143). If it is accepted that bedforms move discontinuously along the seafloor with the displacement related to both the period of time the bottom shear stress exceeds the threshold and the magnitude of the peak shear stress, then it follows that

bedform migration must be governed by the 14 day periodically varying peak currents of the spring-neap cycle with maximum bedform displacements happening during spring tide. It is proposed here that bedform associated sediment transport rate, which is based on average displacement over 4.8, 5.4, 4.1 and 4.4 spring-neap cycles, is representative of the rate averaged over a spring-neap cycle and so is expected to be lower than the maximum rate that was predicted by Li. Therefore, it is stated that the observation of peak spring-neap averaged bedload transport of 30 kg/m/tide agrees favourably with the specific model of Mispec Bay, which predicted spring bedload transport rates of between 24 to 240 kg/m/tide.

Given the range of the values (90 to 214 kg/m/tide) of average spring-neap transport for the general models, it seems fair to make the statement that the bedform-associated spring-neap averaged rate is at worst within 7 times of the highest prediction and at best within three times of Madsen's prediction. However, some attempt will be made to explain the discrepancy.

A major underlying assumption of the current related bedload transport rate is that calculation of Shields parameter using the depth-averaged velocity is based on a logarithmic velocity profile. Section 3.4.3 (page 83) shows that the velocity profile conforms well to the power law approximation of the logarithmic velocity profile although there is some non-conformity either side of slack water. Most sediment transport is hypothesised to occur on the flood tide anyway so the non-logarithmic profile on the ebb should not substantially affect the net sediment transport rate.

Another possible reason why the bedform associated transport rate underestimates the numerical predictions is that there could be substantial sediment bypassing as depicted in Figure 6.1 and not being expressed as dune migration. According to *Huntley et al.* [1991], the bedform migration method worked best when bedload dominated suspended sediment transport. At the transition between bedload domination and suspended sediment domination, sediment bypassing was hypothesised to increase when bedform relief decreases as the bed shear stress increased and ripples began to be washed out. *Huntley et al.* [1991] estimated a maximum sediment bypassing rate of 150% (such bypassing would bring the bedform associated transport figure up to 75 kg/m/tide). However, this is only a "guesstimate", and it was therefore suggested that the bedform migration method should only be used when bedload transport dominated suspended sediment transport so the assumption of negligible sediment bypassing remains valid. Nevertheless, at the least it may be said that the bedform associated sediment transport rate is in general a good lower estimate of bedload transport rate.

Chapter 7: Sediment Transport Processes on the Cape Spencer Sand Bodies

In order to put the observations made in this research in a marine geological context, it is first necessary to summarize the latest theories on banner bank formation and maintenance. *Dyer and Huntley* [1999] described qualitatively how bedload reversal was a sufficient condition for the regional accumulation of sediment and banner bank formation. They also stated that banner banks were likely only formed post sea level rise, since that produced relatively sudden disequilibrium conditions in coastal sediments with respect to hydrodynamics. *Signell and Harris* [2000] formulated mathematical models of banner bank initiation and formation, using the observations of *Geyer and Signell* [1990] for calibration. *Bastos et al.* [2002] utilised groundtruthing, modelled currents, side-scan sonar and digitized hydrographic charts to formulate a conceptual model of post formation banner bank maintenance.

In this chapter, the actual observations of hydrodynamics and sediment transport will be used to field-test the models of *Bastos et al.* [2002] and *Signell and Harris* [2000] and to then posit a specific conceptual model of the Cape Spencer sand bodies.

7.1. Literature Review

7.1.1. Headlands and Banner Bank Initiation

The aim of *Signell and Harris* [2000] was to rigorously test the claim of *Pingree and Maddock* [1979], that banner banks were formed in the centre of so-called "residual

eddies"[*] by a "tidal stirring" effect analogous to the settling of tea leaves at the centre of the bottom of a stirred tea cup caused by an inward directed pressure gradient force, *PG* in Figure 7.1. The asymmetry in size of the sand banks either side of the Portland Bill was attributed by *Pingree and Maddock* [1979] to the Coriolis Effect, *Cor* in Figure 7.1, having a subtractive or additive effect on either side of the headland because the residual eddies apparently counter-rotate on either side. This causes the inward directed, sediment carrying, pressure gradient force to have different magnitudes on either side (Figure 7.1).
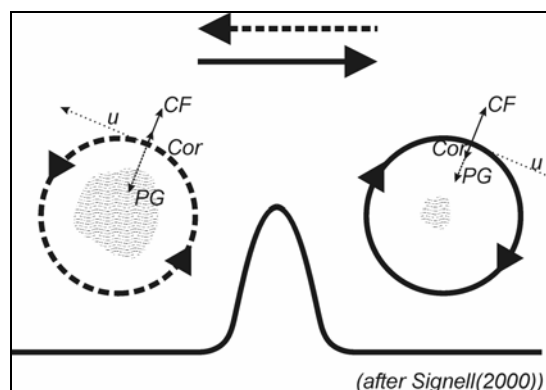
Figure 7.1 Tidal stirring hypothesis put forward by *Pingree* [1978]. **PG** represents the pressure gradient force, which balances the Coriolis force, **Cor**, and the centrifugal force arising from the curvature of the flow, **CF**. The residual eddies are shown either side of the headland. Situation shown is in the northern hemisphere. On the left side of the headland, **PG** = **CF** + **Cor**, whereas on the right side, the Coriolis force is in the opposite direction because of the opposite sense of rotation, here **PG** = **CF** - **Cor**. Note the lesser pressure gradient force where the Coriolis force opposes the centrifugal force.

The findings from *Signell and Harris* [2000] are summarised as follows:

1. Initially, the pair of sand banks is comprised of sediment eroded from the seabed around the headland where the bedload transport rate is at a maximum on the up-current side of the headland. The sand is initially deposited close to the centre of the residual eddy (Figure 7.2(a)), but as the seabed around the headland becomes increasingly depleted of sediment the sand bank increases in

---

[*]The "residual eddy" is the vector field resulting from tidally averaging the instantaneous vector field of the tidal eddy.

area and thickness and gradually migrates away from the centre of the residual

eddy to a stable position in the lee of the headland (Figure 7.2(b,c)). The

modelled banner bank reaches a maximum thickness close to its tip before

tapering off towards its tip.
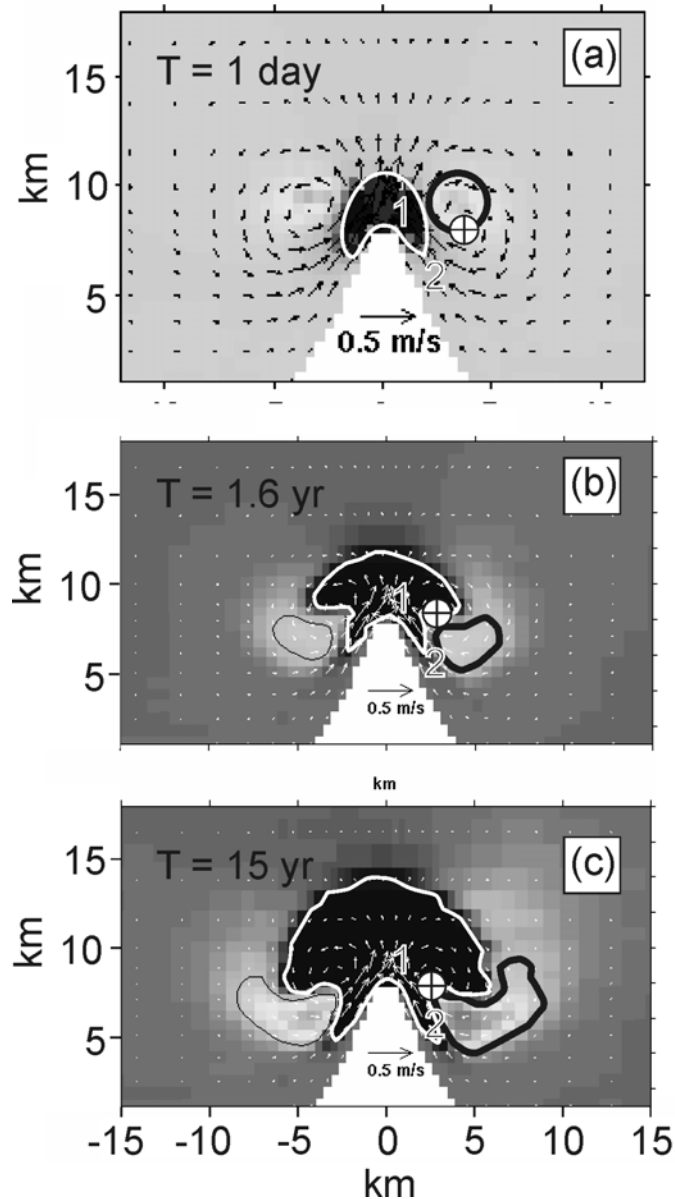
Figure 7.2 Temporal evolution of the banner banks of *Signell and Harris* [2000]. At each stage, one of the banner banks is outlined in black and the scoured area in white. The centre of the residual eddy is denoted by the cross. "1" and "2" refer to the regions of erosion on different phases of the tide and are explained in Section 7.2.3.

2. As the sediment source became exhausted, the banks ceased to grow and then reached an equilibrium state (i.e. did not increase or decrease in size) with the local bottom shear stress regime.

3. The Coriolis Effect was simulated and was not found to cause visible asymmetry in size of the modelled sand banks. The obvious asymmetry in size of the Portland Bill banks (for which was posed the "tidal stirring" hypothesis) was instead ascribed to spatially persistent non-periodic phenomena such as the prevailing wind direction driving waves from one direction.

The main conclusion of this work was that there was a dubious connection between the tidally averaged current field and banner bank formation; this was because the strongly non-linear (cubic) relationship between sediment transport and current strength meant that the temporally averaged current vector did not relate to the net sediment transport vector. There was a stronger connection between the instantaneous current field (and therefore the instantaneous shear stress and sediment transport field) and banner bank formation. Therefore, banner bank formation was instead ascribed to both the cumulative effect of instantaneous patterns of bedload transport vector convergence (causing deposition) and divergence (causing erosion) over the tidal cycle together with the changing sediment supply conditions as the seabed becomes depleted.

7.1.2. Headlands and Banner Bank maintenance

Whereas *Signell and Harris* [2000] modelled the formation of a banner bank by examining the net effect of instantaneous bedload convergence and divergence over many tidal cycles, *Bastos et al.* [2002] and *Bastos et al.* [2003] used field evidence and predicted

instantaneous bedload transport over a tidal cycle to formulate a conceptual model that explained headland associated sedimentary facies (including the mobile sands of banner banks). This conceptual model dealt more with the active, long-term, sedimentary processes associated with headlands rather than the formative processes described by *Signell and Harris* [2000].

Bastos et al. [2002] noted that towards the headland there was a coarsening sequence of the distinct sedimentary facies of sandy mud, mobile sand and then scoured bedrock or gravel. Such a sequence of facies in the open sea is theorized to indicate increasing magnitude of peak instantaneous bedload transport with the region of scoured rock or gravel being dubbed a "bedload parting zone" [*Stride*, 1963; *Harris et al.*, 1995].
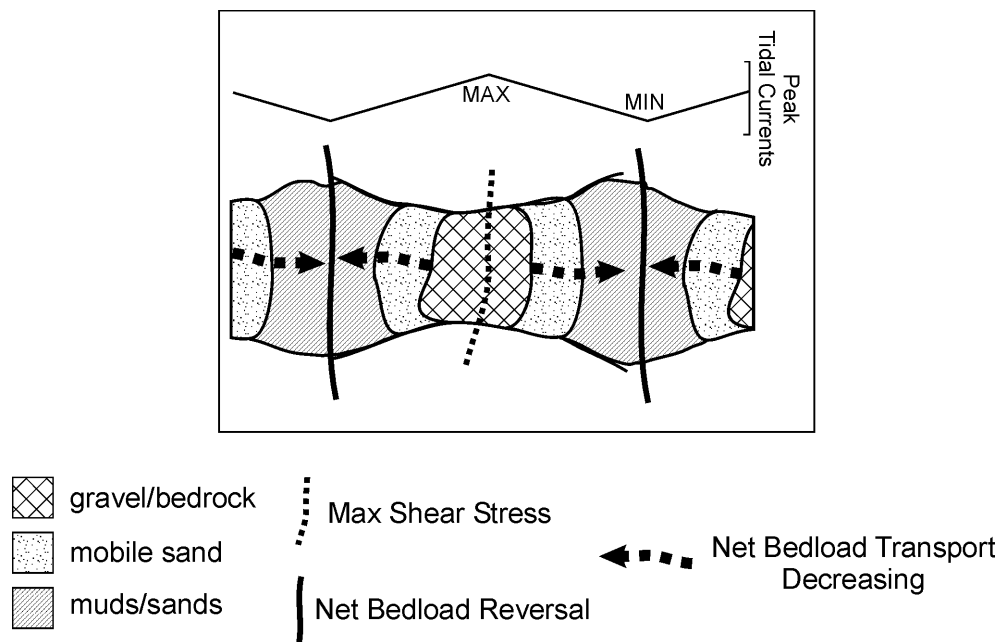
Figure 7.3 Sequence of sedimentary facies on either side of a bedload parting (BLP) in the open sea (after [*Harris et al.*, 1995]).

Figure 7.3 shows an ideal bedload parting (BLP) in the open sea; such a situation can exist at the seabed below a tidal nodal point (amphidromic point) located close to a coastline where the regional peak bottom stress (and therefore the regional peak

instantaneous bedload transport) reaches a local maximum at all phases of the tide [*Harris et al.*, 1995]. Since peak tidal current amplitude decreases away from the amphidromic point, net sediment transport also decreases away from the amphidromic point. Sediments are hypothesised to move down this sediment transport gradient in a diffusive manner over long timescales (hundreds to thousands of years), causing the eventual development of a scour zone at the BLP at the edge of which the coarser sediments are deposited, and finer sediments are deposited as mud farther away. For a true BLP, the asymmetries of the dunes either side of the BLP will indicate net sediment transport *away* from the scour zone and the scale of the scour zone will be greater than the maximum tidal excursion and so will form a barrier to net sediment transport.

However, it is theoretically possible to transport sediments *up* the gradient of the magnitude of sediment transport vector, i.e. opposite in direction to the dotted arrows in Figure 7.3. Such a process is thought to eventually cause the scour zone in the Dover Strait [*Harris et al.*, 1995]. Up-gradient transport of sediment is also supposed to be active in the embayments around the headland Portland Bill. This process will maintain the same facies sequence as Figure 7.3 but dune facing directions will be towards the scour zone, not away. This up-gradient sediment transport was central to the conceptual model of post-formation banner bank maintenance of *Bastos et al.* [2002]. *Bastos et al.* [2002] proposed that tidal asymmetry arising from the hydrodynamic disturbance caused by the headland caused a pair of lines of bedload reversal either side of the headland inshore of which sediment transport increased down-current and offshore of which sediment transport decreased down-current (Figure 7.4). The latter conceptual model will now be described in more detail. *Bastos et al.* [2002] utilised the hypothesis of *Johnson et*

al. [1982], namely that since instantaneous bedload transport is proportional to the cube of excess current velocity, a general rule of thumb is that the direction of the *net*, i.e. tidally integrated, bedload transport vector is the same as the direction of the peak current vector over the tidal cycle. It follows that the long-term net sediment transport vector is parallel to the peak spring tidal current, i.e. parallel to the spring flood or spring ebb current.

This latter rule was used to infer the direction of net bedload transport vectors from predicted peak spring current vectors from a hydrodynamic model. Assuming that the magnitudes of the net bedload transport vectors were proportional to the calculated peak instantaneous bedload transport vectors (using *Gadd et al.* [1978]), examination of the spatial pattern of the net bedload transport vectors revealed that there were two distinct zones on either side of a headland: an "inner zone", where the net bedload transport vector increased in magnitude towards the headland and an "outer zone", where the net bedload transport vector decreased in magnitude away from the headland (Figure 7.4). These zones were an expression of the tidal asymmetry induced by the headland: in the inner zone, peak tidal currents were oriented towards the headland; in the outer zone, peak tidal currents were oriented away from the headland.

The line between these two zones was called the line of "net bedload convergence" by *Bastos et al.* [2002] but in this thesis it seems clearer to refer to this line as one of net bedload reversal since *all* the bedload vectors in the outer zone exhibit "convergence" in the strictest mathematical sense, i.e. decreasing magnitude down-current. According to *Dyer and Huntley* [1999], net bedload reversal is a sufficient condition for there to be a regional accumulation of sediment. This latter point is more to do with the initial formation of the sand bank; however, the line of bedload reversal also constitutes a virtual

barrier parallel to which sediment is channelled as a steady state "river of sand" (to use a

useful analogy from *Inman* [2003]).
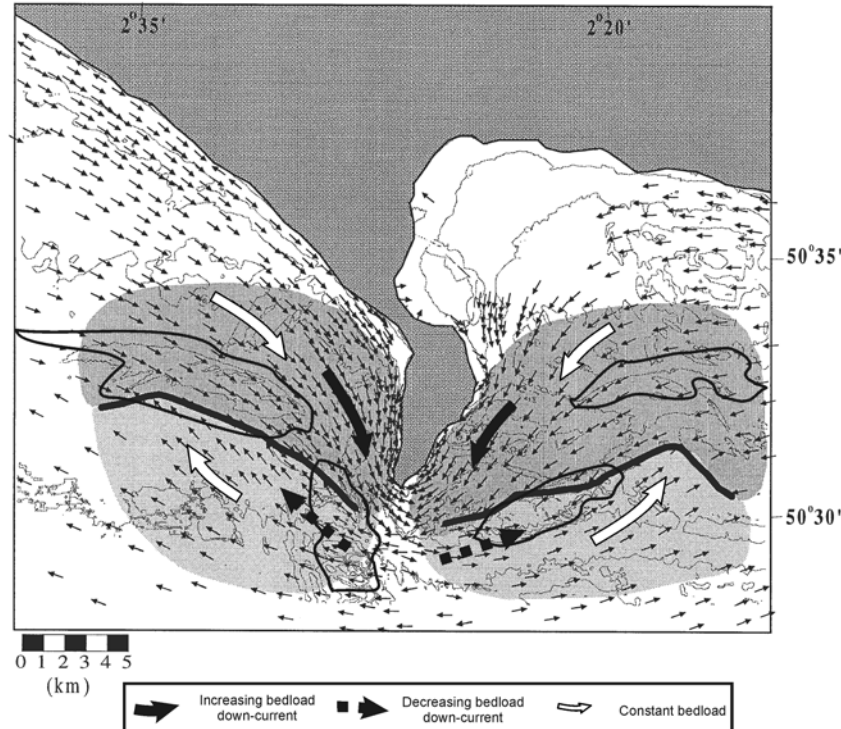
Figure 7.4 Illustration of configuration of the two pairs of Portland Bill banks (outlined in black) with shaded zones of bedload transport (calculated using modeled peak spring currents) towards headland (dark gray) and away from headland (light gray). The line between the gray zones is the line denoting bedload reversal. Dotted block arrows are analogous to the dotted arrows in Figure 7.3 (modified after *Bastos et al.* [2002] and *Bastos et al.* [2003]).

Coarse sand being transported within the *outer* zone is deposited close to the headland

while *finer* sand is transported back to the tail of the banner bank because bedload

transport rate *decreases* down-current; according to Bastos, this process caused the

formation of the pair of sand bodies closest the tip of the Portland Bill (Figure 7.4).

Maximum net bedload transport exists proximal to the headland itself and a scour zone

therefore exists where no deposition takes place. Note that this scour zone is not strictly a

BLP since net bedload transport is not everywhere oriented away from the scour zone

[*Harris et al.*, 1995]. Hence, *Bastos et al.* [2002] referred to a scour zone rather than to a BLP.

The interpretation of model predicted net bedload transport vectors in Figure 7.4 was confirmed by *Bastos et al.* [2002] through inspection of sand dune asymmetries (steep side facing direction of net bedload transport). Agreeing with *Signell and Harris* [2000], the point was made that the residual current field was not as relevant to sediment transport as the instantaneous patterns of bedload transport throughout the tidal cycle.

7.2.   Application of the Models to the Cape Spencer sand bodies

In order to place the observations made in this thesis in the context of the foregoing models, relevant descriptions of observations of the Mispec sand bank and its complement on the other side of Cape Spencer, "Sand-Body Two", will now follow.

7.2.1. Description of Sand-Body Two

Since no repeat observations were carried out on Sand-Body Two, no dynamic information about sand dune migration is available although analysis of facing directions will give information about net sediment transport directions.
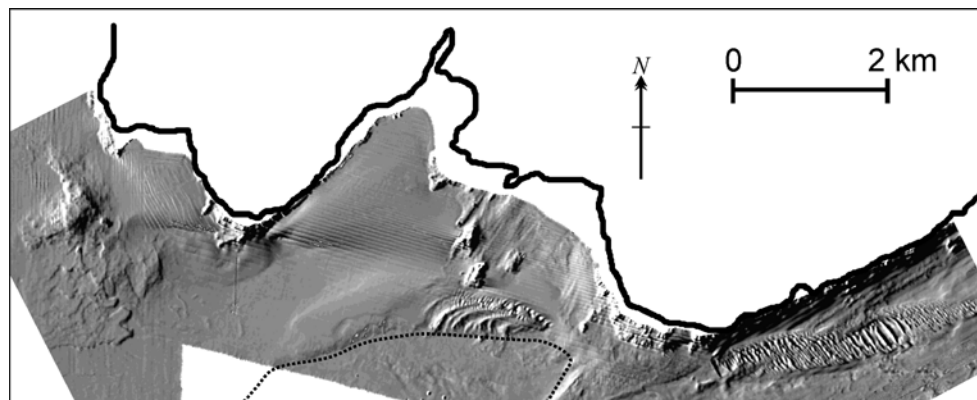
Figure 7.5 Relative locations of the sand bodies either side of Cape Spencer. The Saint John Harbor dumpsite is seen on the extreme left. Dotted line denotes edge of scoured zone around Cape Spencer. Multibeam data processed by Ian Church, Ocean Mapping Group.

Table 7.1. Comparison of the sand bodies.

	Mispec Bank	Sand-Body Two
Area, [km^2]	1.2	2.6
Depth Range below C.D., [m]	22 - 40	25 – 55
Estimated max thickness, [m]	8	2 - 3
Dune height range, [m]	0.3 – 3.5	1 – 7

Sand-Body Two is quite different to the Mispec Banner bank (Table 7.1). The most striking difference is that whereas the Mispec Bay bank is a definite bank, i.e. a positive topographic feature on the seabed, the other body is more a sheet of sand composed of large bedforms so is not strictly a bank. Figure 7.6 illustrates this point: subtraction of topographic contours from the interpolated regional contours beneath the banks (represented by the white dotted lines in the figure) give an estimated maximum thickness of 8 m for the Mispec Bank but only 2 m for Sand-Body Two. There is a depression in the middle of Sand-Body Two (indicated in Figure 7.6) where the sand bank is deeper than the regional contours. This is interpreted to be where erosion has exposed the more easily eroded mud facies that underlies the gravel in this region [*Fader et al.*, 1977].
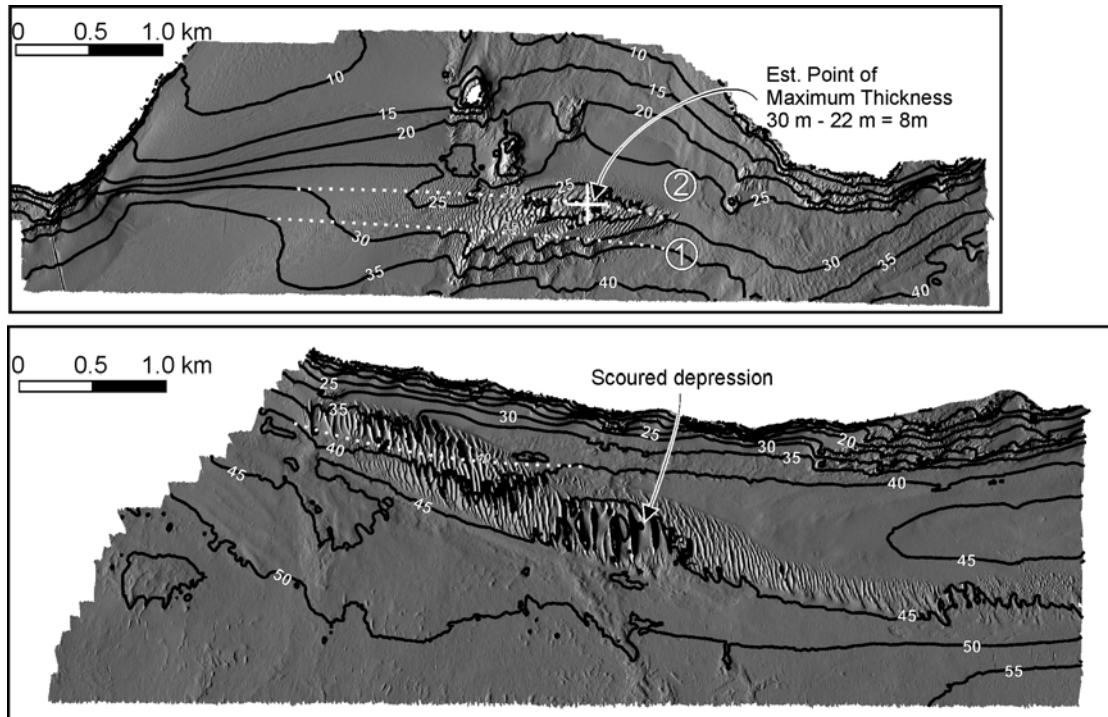
Figure 7.6 Contrasting topography of the Cape Spencer sand-bodies. Interpolated regional contours are represented by the white dotted lines. (TOP) the Mispec sand with interpolated 30 and 35 metre contours (labeled in small italics) and estimated point of maximum thickness; (BOTTOM) Sand-Body Two, estimated to be 2 – 3 m in thickness. Also indicated is the scoured depression.

In terms of composition, the only groundtruthing pertaining to Sand-Body Two was the "outlier" sample 11 (Figure 4.5, p. 107), which was well sorted very coarse sand and was roughly one kilometre from the body in question (Figure 7.7). The backscatter character of Sand-Body Two is also overall higher than the Mispec sand bank, possibly indicating overall coarser grain size. This coarser grain size compared to the Mispec bank could indicate relatively high peak bottom shear stresses over Sand-Body Two.
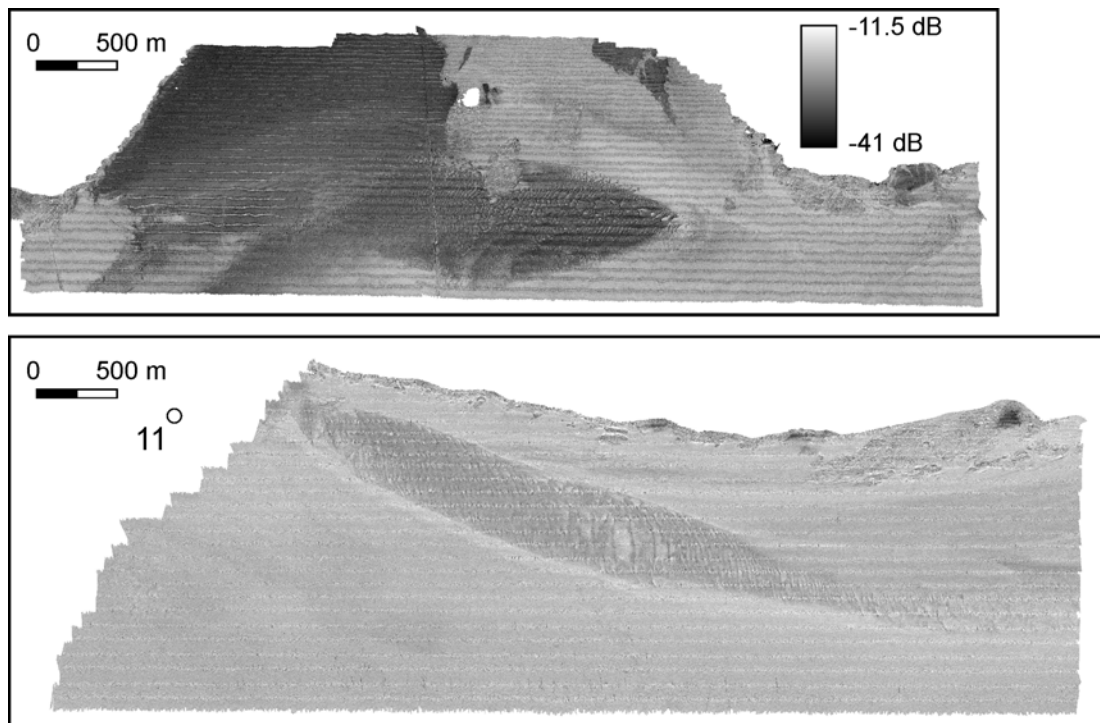
Figure 7.7 Contrasting backscatter strengths of the sand bodies. Note higher backscatter on Sand-Body Two relative to the Mispec bank. The location of sample 11 in relation to Sand-Body Two is also shown.

Inspection of facing directions of the dunes close to the shoreward edge of Sand-Body Two shows the dunes to be markedly asymmetric and indicating net sediment transport towards Cape Spencer (transect A in Figure 7.8 and white solid arrows in Figure 7.9(a,b)). The dunes become symmetric in the interior of the sand bank indicating that the sediment transport in opposing directions is equal so net sediment transport is close to zero in the interior. On the seaward side of Sand-Body Two, the degree of asymmetry is much less than on the shoreward edge and only the larger dunes indicate that net sediment transport is opposite in direction but probably not as great in magnitude (transect B in Figure 7.8 and white dotted arrows in Figure 7.9(a,b)). In Shambles Bank, Portland Bill, U.K., such opposing dune facing directions also exist and, together with computed net bedload transport from a single ADCP tidal cycle observation, led *Bastos et al.* [2004] to propose that a line of net bedload reversal ran through the bank.
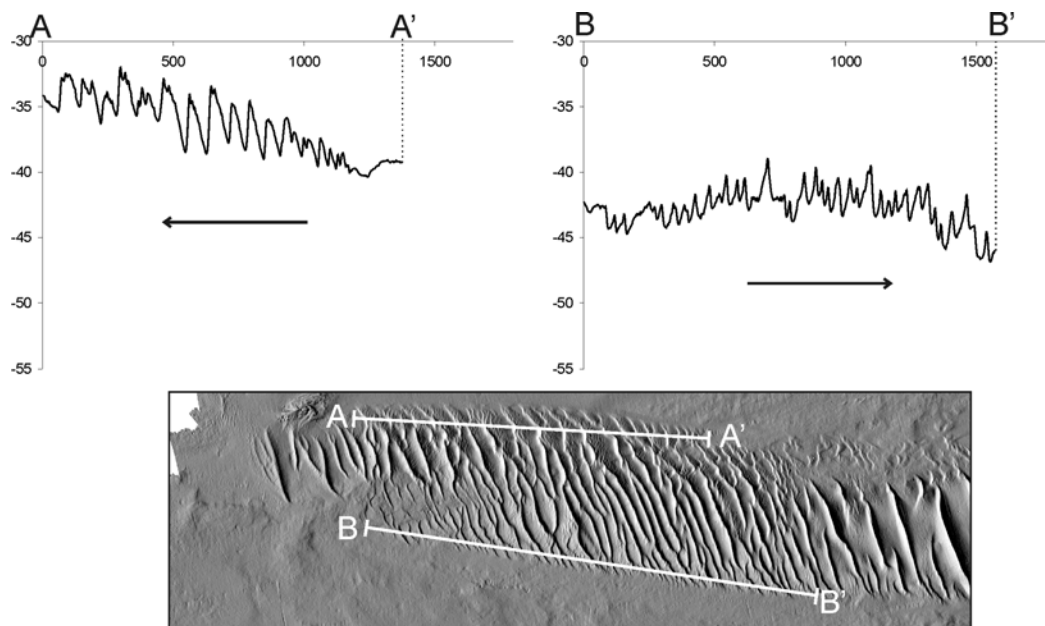
Figure 7.8 Cross sections of Sand-Body Two showing contrasting dune facing directions on the landward and seaward sides.

At the distal end (away from the headland) of Sand-Body Two, the sand dunes are seen to propagate along a relatively narrow "tail"; the morphology of the dunes is also observed to change towards the end of the tail Figure 7.9(c,d). This lenticular dune shape has been noted elsewhere in the Bay of Fundy, where the Sambro Sand is a thin veneer overlying glacial mud (Emerald Silt) [*Greenberg et al.*, 1997]. The surficial geology map of *Fader et al.* [1977] indicates that such a veneer exists very close to Sand-Body Two. Dunes migrating onto this thin gravel veneer induce scouring around their bases, which when eroded down to the easily (relative to the coarse sand of the dunes themselves) eroded Emerald Silt cause the migrating dunes to develop moats and become isolated along-crest [*G. Fader (GSC (Atlantic)),* pers. comm.]. If this hypothesis is correct, the lenticular shape is then a product of differential erosion. It is speculated that a similar process probably initiated the depression in the middle of Sand-Body Two.
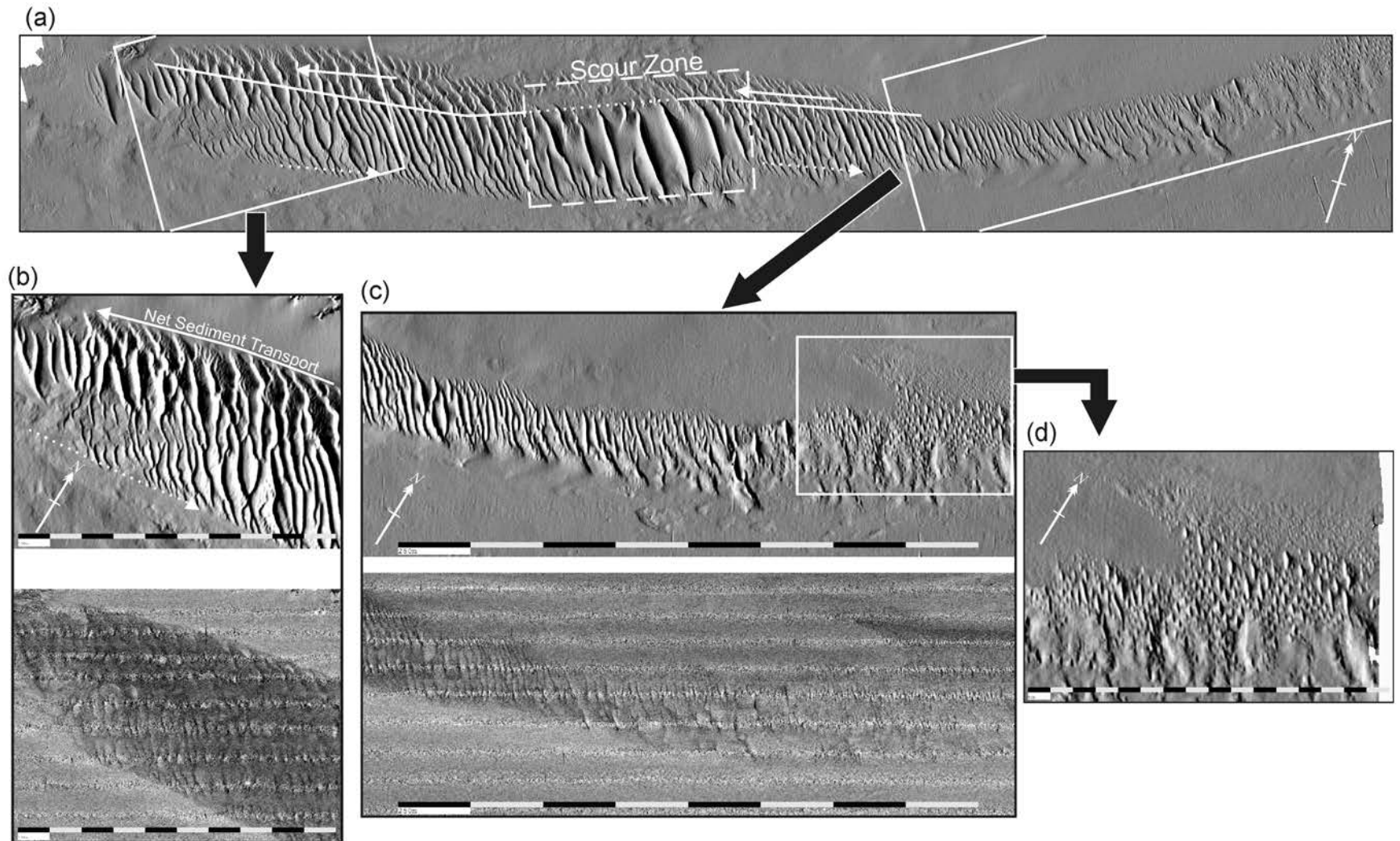
Figure 7.9 Sun illuminated and backscatter images of Sand-Body Two. (a) Overview; (b) sun illuminated and backscatter image of a close-up of the tip, dark backscatter denotes well-sorted sand compared to surrounding gravel; (c) sun illuminated and backscatter image of the 'tail' of the sand body and (d) close-up of lenticular ripples.

7.2.2. Description of Mispec Bay Observations

As stated, *Bastos et al.* [2002] used modelled currents and bedload transport rates to formulate the conceptual model. In Chapter 6, observed currents were used to calculate bedload transport rate. In order to test the conceptual model, the distinct zones of opposing bedload transport must be also present in Mispec Bay.
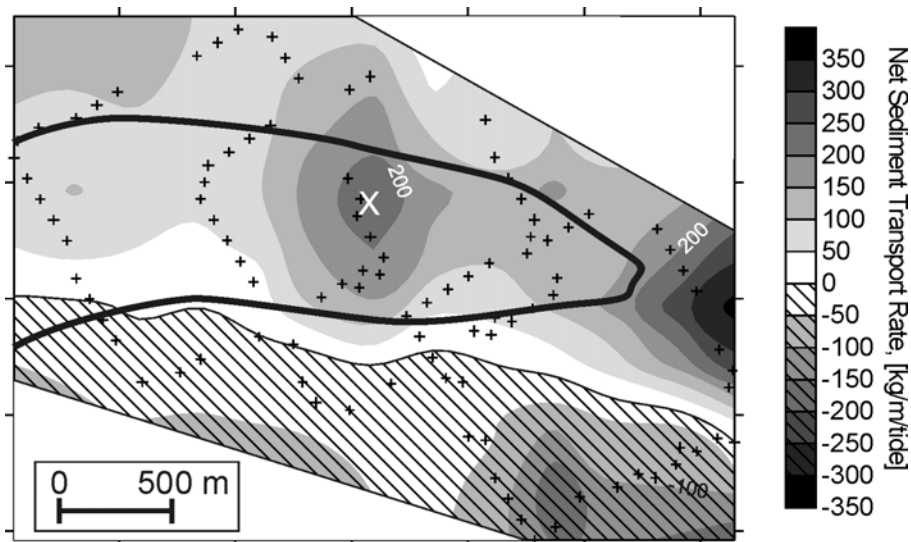
Figure 7.10 Predicted bedload transport rate over the sand bank (outlined in the figure) for median grain size of 0.37 mm. Positive values indicate net transport towards the headland; negative values indicate net transport away from the headland. Interpolation is restricted to the region of ADCP observations

Figure 7.10 shows tidally integrated predicted bedload transport calculated using observed currents and depths. Currents were projected onto the flood axis direction to enable subtraction of flood from ebb transport components. The formulation of Madsen [1991] (Equation (6.6), p. 161) was chosen because it was closest to the bedform associated sediment transport value.

The maximum in the figure denoted by the large "X" is attributed to the fact that its constituent data points (from Diamond 1 (Figure 3.7)) were sampled closest to the spring tide and so have the highest degree of net sediment transport relative to Diamond 2, which also sampled points in this region. Since the figure plots a quantity which is proportional

to the cube of the current speed, variability in current strength over the spring-neap cycle is to blame for this local maximum. It's worth noting that the maximum in sediment transport near the headland is calculated from the near neap currents of Diamond 3 and could possibly indicate minimum sediment transport conditions in this location over the spring-neap cycle.

Evidently, the tidal asymmetry arising as a result of the Mispec Bay tidal eddy has an impact on the net bedload transport. Firstly, over the sand bank, the effect of the long duration of currents flowing towards the headland coupled with the paucity of opposing currents induces bedload transport to be oriented towards the headland. Secondly, the sheltering effect of both Black Point and Cape Spencer on the tidal amplitude in Mispec Bay causes the flood amplitude to decrease landward of the sand bank (Figure 3.27, p. 82). The latter induces bedload transport to decrease landward of the sand bank. Thirdly, the acceleration of currents flowing in this direction as they approach the headland means that bedload transport rates increase markedly close to the headland.

Seaward of the sand bank, bedload transport is seen to reverse because of the "short sharp" jet of water from the vicinity of the headland on the ebbing tide. The magnitude of net sediment transport is observed to decrease down-current in the hatched area of Figure 7.10 because the tidal eddy reverses current flowing away from the headland. Therefore this region of high sediment transport oriented away from the headland is highly localized. The resolution of this outer zone is compromised because of the lack of current observations farther seaward of the sand bank.

Therefore current observations confirm the existence of the line of net bedload reversal predicted by *Bastos et al.* [2002] that delimits the seaward edge of the sand bank. Net bedload transport over the sand bank is oriented towards the headland with the magnitude increasing close to the bank tip and towards the headland. This observation is corroborated by the bedform associated sediment transport rates (Figure 6.7, p. 164), which show a gradual increase in bedload transport to 30 kg/m/tide in the shallow part of the sand bank (roughly within the 25 m contour). Decreasing cohesiveness and shoaling depth help to increase local bedform associated bedload transport because the effect of waves and currents is then enhanced. Decreasing bank thickness and the presence of large scours in the lees of dunes between this shallow region and the tip of the sand bank also implies increasing net sediment transport, and possibly increased suspended sediment transport.

7.2.3. Conceptual Model of the Cape Spencer sand bodies

Dyer and Huntley [1999] suggested that it helps to consider the formative and maintenance processes of banner banks as being separate with the formative process ceasing once the sediment source is exhausted. *Dyer and Huntley* [1999] also suggest that sea level rise is a necessary condition for the formation of sand banks.

Therefore, it is proposed that the formative process, modelled by *Signell and Harris* [2000], commenced in the late post-glacial when the glacial till in the Bay of Fundy, already elevated due to early post-glacial isostatic rebound, began to be reworked by the commencement of increased tidal currents. This happened at the onset of present-day circulation in the Bay of Fundy, 6000 BP, when the sea rose higher than Georges Bank and Browns Bank due to eustatic sea-level rise thus creating the necessary resonance in

the Bay of Fundy to cause increased tidal ranges and currents (before 8000 BP tidal range in the Bay of Fundy was estimated to be 2 m) [*Fader et al.*, 1977].

The coast and coastal sediments were then not in equilibrium with the new hydrodynamic regime and were eroded: (1) from around the headland tip, by ebb currents shooting off the headland tip and (2) from the sides of the headland, by both the reversing currents of the tidal eddy and flood currents (compare Areas "1" and "2" in Figure 7.2 with the same in Figure 7.6 (TOP)). Eroded sediments were deposited in between these two zones of erosion in a region of net bedload reversal to form the Mispec banner bank. As time went on, the scour zone became progressively larger and the volume and height of the sand bank increased until all the sediment around the headland had been eroded away and deposited on the sand banks. This large scour is evident in Figure 7.5 within the dotted line (compare this real scoured zone with the modelled scour zone in Figure 7.2(c)). The potential sediment supply has now been exhausted and the sediments around the headland are now in equilibrium with the hydrodynamic regime.

It is proposed here that the banks are in steady state equilibrium (this is also hypothesised for banner banks in general by *Dyer and Huntley* [1999] and *Signell and Harris* [2000]), since the banner banks are still in a region of non-zero sediment transport. Given the tidal excursion of 6 – 18.5 km (Table 3.2, p. 92) and the length of Mispec Bay (~5 km), it is conceivable that sediment advected from the sand bank tip could end up being channelled through the outer zone and deposited back on the tail of the Mispec bank on the next phase of the tide, in addition, there may also be a sediment contribution from the mud facies in the western part of Mispec Bay.

Therefore, there are two separate components to Mispec Bank: (1) the large-scale, boomerang shaped, positive topographic feature of the sand bank itself, a result of local erosion and subsequent deposition of the sediments around the headland and (2) the present day "river of sand" [*Inman*, 2003] continually flowing over the top of the sand bank in response to non-zero sediment transport oriented towards the headland. Since the sand bank has not been observed to change in size, process two is a steady state process with sediment possibly being circulated around the sand bank.

In Section 3.5 (p. 91), Cape Spencer was stated to be a markedly asymmetric headland, having current relative elliptical aspect ratios of ~1.8 and ~0.6 on ebb and flood phases respectively. In addition, Cape Spencer possesses a much shorter along shore extent on the ebb (~0.85 km compared to ~2.5 km (Figure 3.35, p.92)). It was stated that this contrasting geometry has an effect on vorticity advection down-current of Cape Spencer on the flood and ebb phases of the tide, i.e. a major eddy is advected only in Mispec Bay.

Previous models [*Signell and Harris*, 2000; *Bastos et al.*, 2002; *Bastos*, 2003; *Bastos et al.*, 2004] have considered the effects of a symmetric headland on its proximal net sediment transport regime. These effects are summarised in Figure 7.11(a). The important point to note is that in this case the effects of the headland are felt simultaneously on both the up-current and down-current sides. For instance, on the up-current side of the headland the currents accelerate due to the Venturi effect while simultaneously on the down-current side, the effect of the tidal eddy strips current flowing away from the headland and reverses it to enhance flow towards the headland. The net effect on net sediment transport is illustrated in Figure 7.11(a); there is a local maximum

in sediment transport rate proximal to the headland tip. Inshore sediment is moved within

a region of increasing net sediment transport towards the scour zone with the gradient of

the magnitude of net sediment transport suddenly increasing getting closer to the headland

(this tapers off the tip of the banner bank) and offshore sediment is moved within a region

of decreasing net sediment transport away from the scour zone and a pair of sand banks is

deposited close to the headland tip.
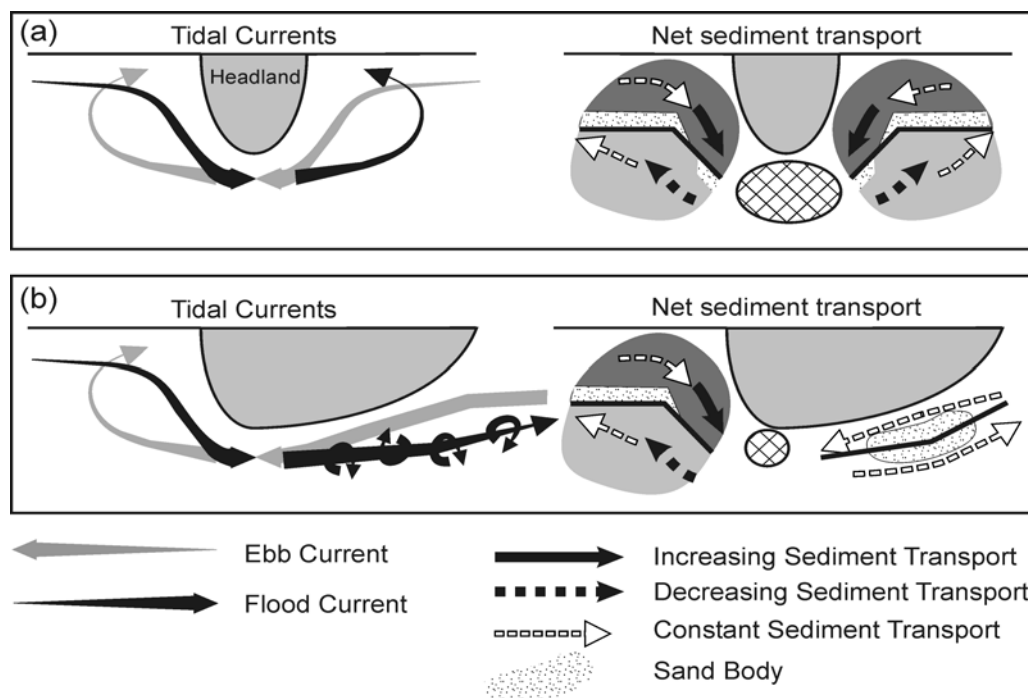
Figure 7.11 (a) Net sediment transport associated with a symmetric headland; (b) proposed net sediment transport associated with an asymmetric headland. Width of tidal current vectors denotes current magnitude.

For an asymmetric headland such as Cape Spencer, only half of the latter description

applies (Figure 7.11(b)), e.g. on the flooding tide the accelerated current approaching the

headland is *not* associated with a major eddy down-current because there is no 'abrupt'

embayment on the down-current side of the headland on this phase of the tide. However,

since there is a maximum in current speed at the headland tip, the flood current does

decelerate somewhat down-current and this may induce minor vortices down-current of

the headland. Likewise, the ebb tidal eddy is *not* associated with up-current Venturi effect induced acceleration; rather the far-field ebb current suddenly decelerates into the tidal eddy. The net effect of this current field on the sediment transport regime is illustrated in (Figure 7.11(b)).

A line of bedload reversal is interpreted to exist along the seaward edge of Mispec Bank, inshore of which net sediment transport vector increases in magnitude towards the headland and offshore of which the sediment transport vector decreases in magnitude moving away from the headland. Through Sand-Body Two a weaker bedload reversal exists inshore of which sediment transport rate remains constant towards the headland and offshore of which sediment transport rate decreases or remains constant moving away from the headland. Sand-Body Two may be considered analogous to Shambles Bank, in that the line of bedload reversal runs through the sand bank [*Bastos et al.*, 2004]. A scour zone exists close to the headland tip but is smaller than the symmetric headland case because the maximum sediment transport rate is only located there on the flooding tide.

The sediment on Sand-Body Two is coarser and better sorted, indicating higher peak shear stress in this region compared to the Mispec bank but the constant spatial gradient of net sediment transport ensures that Sand-Body Two eroded away.

7.3.   Conclusion

On the basis of observed data and using the models of *Signell and Harris*, [2000], *Bastos et al.* [2002] and *Bastos et al.* [2003] as starting points, a conceptual model specific to the Cape Spencer sand bodies has been put forward. The conceptual model explains some of the observed phenomena of the Cape Spencer sand bodies:

- The contrast in relief of the pair of sand bodies is ascribed to the fact that the presence of a major tidal eddy in Mispec Bay makes the formational model of *Signell and Harris* [2000] applicable only here. This model predicts the banner bank to be shoreward of the residual eddy centre and for the thickness of the bank to increase to a maximum close to the bank tip (Figure 7.2) before the bank tapers (both in horizontal extent and in thickness) to a narrow point because of locally increased net sediment transport in the inshore region (due to Venturi) and in the offshore region (due to current shooting from the headland tip) of the sand bank. Because of the lack of a tidal eddy on the other side of Cape Spencer, there is no strong bedload reversal and the latter formational process did not happen to the same degree. However, here a weak bedload reversal does exist because of slight tidal asymmetry in this region. Therefore, coarse sediment advected around Cape Spencer is deposited around the bedload reversal but here expresses itself as a relatively thin sheet of coarser sand.

- Sand-Body Two is coarser grained and better sorted because the peak bottom shear stress is predicted to be greater over Sand-Body Two than over Mispec Bank. As proposed in the conceptual model, even though peak bottom shear stress is higher, sediment transport gradients are small, evinced by the fact that Sand-Body Two can exist without being eroded away.

- Sand-Body Two possesses opposing net sediment transport vectors (evinced by opposing dune facing directions) because the bedload reversal passes

through the latter. The inshore edge possesses dunes that are more asymmetric than the seaward edge, indicating that tidal asymmetry is greater inshore than offshore. The dunes are more symmetric in the interior where net bedload transport is zero, i.e. current excursions are large but equal and opposite.

C h a p t e r   8 :   C o n c l u s i o n

8.1. Summary of Major Work Done

The two main aims of this research, namely to test whether repetitive multibeam surveying could be used to quantify bedload transport and to test the applicability of existing models of banner banks, necessitated a multi-disciplinary thesis that addresses the three-fold nature of the subject matter.

OBSERVATIONS

1. Hydrodynamics

Hydrodynamics is one of the vital components of the system under investigation. Real hydrodynamic data: (1) enables validation of banner bank models, which implicitly refer to the current field in their assumptions of sediment transport behaviour, and (2) provides a dataset to validate bedform associated bedload transport values. To this end, three M2 current measurement cycles were carried out in 2002 and 2003. For (1) above, the following analyses were carried out:

- Generation of a series of synoptic maps of current field over a full tidal cycle;

- Analysis of tidal current behaviour at distinct points around the study area;

- Analysis of spatial variation of tidal current elliptical parameters (the latter derived from code developed by the author) and residual currents;

- Hydrodynamic parameter estimation of Cape Spencer and its locality and inspection of applicability of the headland separation model of *Signell and Geyer* [1991].

2. Groundtruthing

Surficial sedimentology is another major component of the system under investigation and groundtruthing was carried out for similar reasons as hydrodynamic analysis, i.e. to validate models of banner bank formation and to quantify predicted sediment transport from current data. The following analyses were carried out:

- Sieve analysis, which provided median grain size necessary to predict sediment transport using hydrodynamic bedload predictors.

- Classification of grab samples on the basis of degree of sorting and grain size, together with multibeam backscatter and bathymetric texture information, enabled spatial classification of distinct sedimentary facies. This enabled validation of an existing conceptual model of a banner bank [*Bastos et al.*, 2002] that alleged a coarsening sequence of facies towards the headland.

- Spatial analysis of variation of grain size parameters (after *Gao and Collins* [1992]) that enabled resolution of "transport vectors", which indicated preferred sediment transport directions.

- Bottom photography allowed the discovery of the mottled nature of the seabed in the west part of the sand bank, interpreted to reflect increased mud content of the substrate in this locality. This observation, together with the visual

observation of decreased sediment transport, allowed the important deduction that the increased mud content hindered sediment transport and bedform migration.

3. Migration Measurement

Six consecutive multibeam surveys of Mispec Bank were carried out from April to September 2002 to investigate the dynamism of its sand dunes. To this end, intensive software development has been done in this thesis: a new *application* of spatial correlation has been proposed whereby migration vectors are derived from successive bathymetric slope images and a new *method* (the perpendicular regression of the correlogram) of tracking straight crested dunes has been developed.

ANALYSIS

1. Bedload Transport Estimation

More code was developed to derive estimates of bedload transport from repeated bathymetric observations. Code was written to: (a) extract dune crest-lines and trough-lines; (b) calculate form factors of the dunes on the sand bank; (c) calculate the perpendicular height of the dunes relative to the line joining the troughs on either side of a crest and (d) estimate the bedform associated sediment transport rate by multiplying the dune height by the magnitude of the dune velocity and the form factor (a uniform form factor of 0.5 was felt to be justified in this work).

To check the latter bedform associated sediment transport rate, it was compared with, firstly, a number of different empirical predictors (Equations (6.5), (6.6) and (6.7)) of

bedload transport using observed currents and median grain size and, secondly, a region specific numerical model [*Li et al.*, 2003].

2. Conceptual Model Development

The second major aim of this work was to formulate a conceptual model of the Cape Spencer sand bodies. This was done by applying another conceptual model [*Bastos et al.*, 2002; *Bastos*, 2003] but modifying it for application to the Cape Spencer by accounting for the lack of high gradients in sediment transport rate adjacent to Sand-Body 2.

8.2. Conclusions and Recommendations

A method of using repetitive multibeam surveying to estimate bedload transport has been developed and tested. In addition, a number of conclusions pertaining to the local hydrodynamics and local sediment transport are made.

Comparison of crest-perpendicular and weighted centroid migration vectors revealed the widely held assumption of crest-perpendicular dune migration to be invalid for the 3D dunes around Black Rock. This is the result of the non-uniform along crest currents, generated when water accelerates around the obstacle. As far as the author is aware, this is the first time this has been observed in a marine environment although previous observations of this phenomenon have been made inside river meanders.

Repeat multibeam surveys of the sand dunes have drawn attention to the spatial variability of migration rate that can exist around a sand bank. However, this spatial migration variability has little effect on bedload transport variability around the sand bank

since this thesis has shown that bedform height is the major parameter that determines the change in bedload transport around the bank.

The output from the bedload transport estimation technique developed in this thesis falls in the range, albeit an order of magnitude range, predicted with a region specific mathematical model [*Li et al.*, 2003] and was 3 – 7 times less than empirical model predictions using observed currents, grain size and depth. With a "guesstimated" extreme sediment bypassing rate 150% [*Huntley et al.*, 1991], the bedform associated bedload was 1.2 – 3.8 less than the empirical model predictions. With reference to these results, the hypothesis that "repetitive multibeam surveying may be used to estimate bedload transport in a tidal environment" can therefore be accepted with the following conditions:

1. The repeat survey frequency must be high enough to that aliasing of fast moving dunes is avoided (as described on p. 144).

2. The bedform associated bedload transport values must be considered to be representative of the average bedload transport over the survey interval, e.g. spring-neap averaged rate in this thesis.

3. The accuracy of the technique increases with decreasing dimensionless shear stress (Shields Parameter). With lower values of Shields Parameter, bedload transport that is not expressed as bedform migration, i.e. sediment bypassing as described in Section 6.1, p. 156, is not expected to be significant. Otherwise, for higher values of Shields Parameter, the bedform associated transport technique constitutes a lower limit to bedload transport.

4. The accuracy of the migration detection technique increases with the number of observations of the migrating bedforms. However, this assumes that the quantity of interest, i.e. the spring-neap averaged bedload transport rate, is stationary. If this is not the case, e.g. with an annual storm event or seasonal change in wave activity, then the sediment transport rate must be considered to be an annually, as opposed to spring-neap cycle, averaged sediment transport.

5. Connected with the latter point, the bedload measurement technique described in this thesis, which is based on horizontal displacement of bedforms of known dimension, assumes steady state sediment transport, i.e. any bed level change over the survey interval not due to the migration of bedforms is assumed to be negligible.

6. By definition, the technique relies on the existence of migrating bedforms. Bedload transport happening during sheet flow conditions cannot be measured with this technique. As stated in point three above, sediment bypassing of ripples is a similar unmeasurable quantity, therefore the bedform associated bedload transport value is in general a lower limit.

This technique has good potential since it makes full use of 2D data rather than single-beam lines or 1D sections through a DTM, as has been done in the past.

The logarithmic current velocity profile assumption is valid when the water column velocity is steady during the flood. Either side of slack before flood, the current velocity profile does not conform to the logarithmic profile due to the inertia of the water column which, by definition, resists the tidal reversal in current velocity.

The asymmetric coastline of Cape Spencer has an impact on its local current field with respect to tidal eddy advection and consequently sand bank development. With respect to ebbing currents, the coastline of Cape Spencer has an elliptical aspect ratio greater then the threshold, 4/3, necessary to advect a major tidal eddy; in contrast, the elliptical aspect ratio is less than this threshold for flood currents so a major eddy is not advected although some minor vortices are anticipated to stream from the headland tip on the flooding tide. Thus, the tidal eddy advected in Mispec Bay locally induces major tidal asymmetry, with a line of net bedload reversal separating the regions of flood dominated bedload and ebb dominated bedload. Mispec bank has built up inshore of this line and sediment is continually advected from its tip, where there is an increasing net sediment transport rate; a portion of this sediment ends up being redeposited on the distal end of the bank only to be recirculated around the bank. However, on the other side of Cape Spencer, the lack of a major tidal eddy induces lesser tidal asymmetry either side of a line of bedload reversal; the sand body here is consequently lower in elevation because there is less potential for sediment accretion.

8.3. Suggestions for future research directions

Whilst the author recognises the unusually rich dataset that was available, there is always the desire for more data. At least two more tidal current measurement cycles would have been useful to better resolve the outer zone described in Chapter 7 and also around Cape Spencer itself to quantify the maximum current speeds in this region. Tidal cycle measurements over Sand-Body Two would especially have been useful to investigate the nature of the current field on the flooding tide.

Better bottom photography would have been useful. A stationary bottom-mounted platform such as the *RALPH* system owned by the Geological Survey of Canada (Atlantic) could be usefully deployed to estimate the amount of suspended sediment transport and also to provide independent observations of sediment bypassing of bedforms, if any. Specific locations of interest would be in the lee of the bedrock obstacle to investigate the nature of the bedform migration and in the muddy facies C to investigate whether winnowing of the mud is happening.

Use of fluorescent tracers would be a very worthwhile, although practically difficult, exercise. Two plugs of sand "tagged" with differently coloured fluorescent dyes and with a similar grain size distribution to facies A and E could be inserted by divers into the Cape Spencer sand bodies; the former into the Mispec bank around peak flooding currents and the latter into Sand-Body Two around peak ebbing currents. Then, an intensive sediment sampling program[*] would have to be undertaken over the sand banks to investigate whether (a) there is evidence of sediment recirculation around a particular sand bank and (b) there is evidence of sediment exchange or net sediment transport between the sand banks.

Hydrodynamic and sediment transport modelling around Cape Spencer, similar to the hydrodynamic and sediment transport model of the symmetric headland Portland Bill [*Bastos*, 2003], would be a useful exercise. A high resolution grid capable of resolving the rapid spatial change in current velocity close to the headland tip would need to be used to accurately resolve the tidal eddy. This exercise would also test the impact of the headland

[*] see *McComb and Black* [2003] where ~1200 samples were analysed for fluorescence over 10 months of sampling

asymmetry on the surrounding current field and if this impact varies over the spring-neap cycle. Sediment transport modelling over a spring-neap cycle, as opposed to only over a spring tidal cycle, would enable better testing of the spring-neap averaged bedform associated bedload value.

Future use of dependable RTK heights would eliminate much of the noise (see p. 155) superimposed on the difference DTMs derived from subtraction of successive bathymetric surfaces. These accurate difference DTMs could be used to: (1) confirm the accuracy of the bedload transport values calculated from bedform migration and (2) would also resolve net accretion or deflation.

R e f e r e n c e s

1 Allen, J.R.L. (1985). *Principles of Physical Sedimentology*, 271 pp., George Allen & Unwin, London.

2 ASTM_D-422-63 (2002). Standard Test Method for Particle-Size Analysis of Soils, ASTM International.

3 Bastos, A., N.H. Kenyon, and M. Collins (2002). "Sedimentary Processes, Bedforms and Facies, Associated with a Coastal Headland: Portland Bill, Southern U.K." *Marine Geology*, 187, pp. 235-258.

4 Bastos, A.C. (2003). "Water and Sediment Movement around a Coastal Headland: Portland Bill, Southern U.K." *Ocean Dynamics*, 53, pp. 309-321.

5 Bastos, A.C., D. Paphitis, and M.B. Collins (2004). "Short-Term Dynamics and Maintenance Processes of Headland-Associated Sandbanks: Shambles Bank, English Channel, U.K." *Estuarine, Coastal and Shelf Science*, 59, pp. 33-47.

6 Belderson, R.H. Bedforms, in *Offshore Tidal Sands: Processes and Deposits*, edited by A.H. Stride, pp. 27-55, Chapman and Hall Ltd., New York, 1982.

7 Besio, G., P. Blondeaux, M. Brocchini, and G. Vittori (2004). "On the Modeling of Sand Wave Migration." *Journal of Geophysical Research*, 109(C04018), Citation # (4digit no), doi:10.1029/2002JC001622.

8 Butman, B., P.S. Alexander, C.K. Harris, P.A. Traykovski, M.B. Ten Brinke, F.S. Lightsom, and M.A. Martini (2002). Oceanographic Observations in the Hudson Shelf Valley, December 1999 - April 2000: Data Report, in *U.S. Geological Survey Open-File Report 02-217*, USGS.

9 Delacourt, C., P. Allemand, B. Casson, and H. Vadon (2004). "Velocity Field of the 'La Clapiere" Landslide Measured by the Correlation of Aerial and Quickbird Satellite Images." *Geophysical Research Letters*, 31(15), pp. L15619.

10 Dietrich, W.E., and J.D. Smith (1984). "Bed Load Transport in a River Meander." *Water Resources Research*, 20(10), pp. 1355-1380.

11 Dorst, L.L. (2004). "Geodetic Deformation Analysis: A New Method of the Estimation of Seabed Dynamics." *Marine Sandwave and River Dune Dynamics II, International Workshop*, University of Twente, Enschede, The Netherlands.

12 Duff, P.M.D. (1994). *Holme's Principles of Physical Geology*, 4th ed., Chapman & Hall.

13 Duffy, G.P., and J.E. Hughes-Clarke (2005). "Application of Spatial Cross-Correlation to Detection of Migration of Submarine Sand Dunes." *Journal of Geophysical Research - Earth Surface*, Special Section on Marine Dune and River Dune Dynamics, 110(F4), Citation # (4digit no), 10.1029/2004JF000192.

14 Duffy, G.P., J.E. Hughes-Clarke, and D.R. Parrott (2005). "Bedforms and Associated Sand Transport on a Banner Bank, Saint John, Nb." *Geological Association of Canada - Mineralogical Association of Canada*, Halifax.

15 Duffy, G.P., J.E. Hughes-Clarke, and R. Parrott (2004). "Application of Current Measurement and Time Lapsed Bathymetric Multibeam Surveying to Investigation of a Banner Bank, Mispec Bay, New Brunswick, Canada." pp. 72-78, *Marine Sandwave Dynamics and River Dune Dynamics II, International Workshop*, University of Twente, Enschede, The Netherlands, 1 - 2 April, S.H.O.M.

16 Dyer, K.R., and D.A. Huntley (1999). "The Origin, Classification and Modelling of Sand Banks and Ridges." *Continental Shelf Research*, 19, pp. 1285-1330.

17 Engel, P., and Y.L. Lau (1980). "Computation of Bedload by Dune Tracking." *ASCE Journal of the Hydraulics Division*, 106(369-380).

18 Fader, G.B., L.H. King, and B. MacLean (1977). Surficial Geology of the Eastern Gulf of Maine and Bay of Fundy, in *Geological Survey of Canada Papers 76-17*, pp. 23, Ottawa, Canada.

19 Gadd, P.E., J.W. Lavelle, and D.J.P. Swift (1978). "Estimates of Sand Transport on the New York Shelf Using near-Bottom Current Meter Observations." *Journal of Sedimentary Petrology*, 48(1), pp. 239-252.

20 Gao, S., and M. Collins (1991). "A Critique of the "Mclaren Method" for Defining Sediment Transport Paths - Discussion." *Journal of Sedimentary Petrology*, 61(1), pp. 143-146.

21 Gao, S., and M. Collins (1992). "Net Sediment Transport Patterns Inferred from Grain-Size Trends, Based Upon Definition of "Transport Vectors"." *Sedimentary Geology*, 80, pp. 47-60.

22 Geyer, W.R., and R. Signell (1990). "Measurements of Tidal Flow around a Headland with a Shipboard Acoustic Doppler Current Profiler." *Journal of Geophysical Research*, 95(C3), pp. 3189-3197.

23 Greenberg, D.A. (1979). "A Numerical Model Investigation of Tidal Phenomena in the Bay of Fundy and Gulf of Maine." *Marine Geodesy*, 2, pp. 161-187.

24 Greenberg, D.A., B.D. Petrie, G.R. Daborn, and G.B. Fader (1997). "The Physical Environment of the Bay of Fundy." pp. 11 - 34, *Bay of Fundy Issues: A Scientific Overview*, Wolfville, N.S., January 29 - February 1, 1996, Environment Canada.

25 Hails, J.R. (1975). "Sediment Distribution and Quaternary History." *Journal of Geological Society of London*, 131, pp. 19-35.

26 Hanes, D.M., C.E. Vincent, D.A. Huntley, and T.E. Clarke (1988). "Acoustic Measurements of Suspended Sand Concentrations." *Marine Geology*, 81, pp. 185-196.

27 Hare, R. (1995). "Depth and Postioning Error Budgets for Multibeam Echosounding." *International Hydrographic Review*, LXXII(2), pp. 35 - 69.

28 Harris, P.T., C. Pattiaratchi, M. Collins, and R.W. Dalrymple What Is a Bedload Parting?, in *Tidal Signatures in Modern and Ancient Sediments*, edited by B.W. Flemming, and A. Bartholoma, Blackwell, 1995.

29 Hoekstra, P., P. Bell, P. van Santen, N. Roode, F. Levoy, and R. Whitehouse (2004). "Bedform Migration and Bedload Transport on an Intertidal Shoal." *Continental Shelf Research*, 24, pp. 1249-1269.

30 Hughes-Clarke, J.E. (1998). "The Effect of Fine Scale Seabed Morphology and Texture on the Fidelity of Swath Bathymetric Sounding Data." pp. 168-181, *Canadian Hydrographic Conference*, Victoria, Canada, March 10-12, Canadian Hydrographic Service.

31 Hughes-Clarke, J.E. (2003). "A Reassessment of Vessel Coordinate Systems: What Is It That We Are Really Aligning?" pp. 1-12, *US Hydrographic Conference*, Biloxi, Mississippi, US Hydrographic Service.

32 Huntley, D.A., C.L. Amos, J.J. Williams, and J.D. Humphery (1991). "Estimating Bedload Transport on Continental Shelves by Observations of Ripple Migration - an Assessment." *Euromech 262- Sand Transport in Rivers, Estuaries and the Sea*, Wallingford, U.K., A.A. Balkema, Rotterdam, The Netherlands.

33 Huntley, D.A., and D.M. Hanes (1987). "Direct Measurements of Suspended Sediment Transport." *Coastal Sediments '87*, New Orleans, ASCE.

34 Imasato, N. (1983). "What Is Tide-Induced Current?" *Journal of Physical Oceanography*, 13(7), pp. 1307-1317.

35 Inman, D. Littoral Cells, in *Encyclopedia of Coastal Science*, edited by M. Schwartz, Kluwer Academic Publishers, Dordrecht, The Netherlands, 2003.

36 Jambunathan, K., X.Y. Ju, B.N. Dobbins, and S. Ashforth-Frost (1995). "An Improved Cross Correlation Technique for Particle Image Velocimetry." *Measurement Science and Technology*, 6, pp. 507-514.

37 Jinchi, H. (1992). "Application of Sandwave Measurements in Calculating Bed Load Discharge." pp. 63-70, *Erosion and Sediment Transport Monitoring Programmes in River Basins*, Oslo, International Association of Hydrological Sciences.

38 Johnson, M.A., N.H. Kenyon, R.H. Belderson, and A.H. Stride Sand Transport, in *Offshore Tidal Sands: Processes and Deposits*, edited by A.H. Stride, Chapman and Hall, London, 1982.

39 Kearey, P., and M. Brooks (1996). *An Introduction to Geophysical Exploration*, 2nd ed.

40 Kenyon, N.H., R.H. Belderson, A.H. Stride, and M.A. Johnson (1981). "Offshore Tidal Sand Banks as Indicators of Net Sand Transport and as Potential Deposits." *Special Publication of the International Association of Sedimentologists*, 5, pp. 257-268.

41 Knaapen, M.A.F. (2004). "Measuring Sand Wave Migration in the Field. Comparison of Different Data Sources and an Error Analysis." *Marine Sandwave Dynamics and River Dune Dynamics II, International Workshop*, University of Twente, Enschede, The Netherlands.

42 Knaapen, M.A.F. (2005). "Quantifying Bedform Migration Using Multi-Beam Sonar." *Geo-Marine Letters*, Citation # (4digit no), 10.1007/s00367-005-0005-z.

43 Langhorne, D.N. (1981). "An Evaluation of Bagnold's Dimensionless Coefficient of Proportionality Using Measurements of Sandwave Movement." *Marine Geology*, 43, pp. 49-64.

44 Langhorne, D.N. (1982). "A Study of the Dynamics of a Marine Sandwave." *Sedimentology*, 29(4), pp. 571-594.

45 Larcombe, P., and C.F. Jago (1996). "The Morphological Dynamics of Intertidal Megaripples in the Mawdach Estuary, North Wales, and the Implications for Palaeoflow Reconstructions." *Sedimentology*, 43, pp. 541-559.

46 Le Bot, S., and D. Idier (2000). "Dune Dynamics: From Field Measurements to Numerical Modelling. Application to Bathymetric Survey Frequency in the Calais-Dover Strait." *Marine Sandwave Dynamics*, Lille, France, 2000.

47 Lewis, J.P. (1995). "Fast Template Matching." pp. 120-123, *Vision Interface '95*, Quebec City, Canadian Image Processing and Pattern Recognition Society.

48 Li, M.Z., and C.L. Amos (2001). "Sedtrans96: The Upgraded and Better Calibrated Sediment-Transport Model for Continental Shelves." *Computers & Geosciences*, 27, pp. 619-645.

49 Li, M.Z., R. Parrott, and Z. Yang (2003). "Stability and Dispersion of Dredged Material at the Black Point Offshore Disposal Site, Saint John Harbour, New Brunswick." *Canadian Coastal Conference*, Queen's University, Donald Gordon Centre, Kingston, ON, Canada, Canadian Coastal Science and Engineering Association.

50 Lindenbergh, R. (2004). "Parameter Estimation and Deformation Analysis of Sand Waves and Mega Ripples." *Marine Sandwave Dynamics and River Dune Dynamics II, International Workshop*, University of Twente, Enschede, The Netherlands.

51 Madsen, O.S. (1991). "Mechanics of Cohesionless Sediment Transport in Coastal Waters." pp. 15-27, *Coastal Sediments '91*, American Society of Civil Engineers.

52 McComb, P., and K. Black (2003). "Detailed Observations of Littoral Transport Using Artificial Sediment Tracer, in a High-Energy, Rocky Reef and Iron Sand Environment." *Journal of Coastal Research*, 21(2), Citation # (4digit no), 10.2112/03.

53 McLaren, P. (1981). "An Interpretation of Trends in Grain Size Measures." *Journal of Sedimentary Petrology*, 51(2), pp. 611-624.

54 McLaren, P., and D. Bowles (1985). "The Effects of Sediment Transport on Grain-Size Distributions." *Journal of Sedimentary Petrology*, 55(4), pp. 457-470.

55 McLaren, P., and D. Bowles (1991). "A Critique of the "Mclaren Method" for Defining Sediment Transport Paths - Reply." *Journal of Sedimentary Petrology*, 61(1), pp. 147.

56 McLaren, P., M. Collins, S. Gao, and R.I.L. Powys (1993). "Sediment Dynamics of the Severn Estuary and Inner Bristol Channel." *Journal of Geological Society of London*, 150, pp. 589-603.

57 Middleton, G.V., and J.B. Southard (1984). *Mechanics of Sediment Movement*, 2nd ed.

58 Mitchener, H., and H. Torfs (1996). "Erosion of Mud/Sand Mixtures." *Coastal Engineering*, 29, pp. 1-25.

59 Nemeth, A.A., S.J.M.H. Hulscher, and R.M.J. Van Damme (2004). "Modelling Sand Wave Migration and Height, Comparing Model Results and Data." pp. 352, *Marine Sandwave Dynamics and River Dune Dynamics II, International Workshop*, University of Twente, Enschede, The Netherlands.

60 Nielsen, P. (1992). *Coastal Bottom Boundary Layers and Sediment Transport*, World Scientific Publishing, Singapore.

61 Open University, O.C.T. (1999). *Waves, Tides and Shallow-Water Processes*, 227 pp., 2nd ed.

62 Park, M.-J., and D.-P. Wang (2000). "Tidal Vorticity around a Coastal Promontory." *Journal of Oceanography*, 56(3), pp. 261-273.

63 Pingree, R.D. (1978). "The Formation of the Shambles and Other Banks by Tidal Stirring of the Seas." *Journal of Marine Biological Association of the United Kingdom*, 58, pp. 211-226.

64 Pingree, R.D., and L. Maddock (1979). "The Tidal Physics of Headland Flows and Offshore Tidal Bank Formation." *Marine Geology*, 32, pp. 269-289.

65 Pratt, W.K. (1991). *Digital Image Processing*, 2nd ed.

66 Raffel, M., C.E. Willert, and J. Kompenhans (1998). *Particle Image Velocimetry, a Practical Guide*, Springer-Verlag, Berlin.

67 Randall, D.A. (2004). The Shallow Water Equations, in *Selected Nuggets*, lecture notes on derivation of shallow water equations including derivation of vorticity equation, pp. 219-230, http://kiwi.atmos.colostate.edu/group/dave/#pubs.

68 RD-Instruments (1996). *Acoustic Doppler Current Profiler, Principles of Operation a Practical Primer*, 52 pp., 2nd ed., San Diego.

69 Ridderinkhof, H., and J.T.F. Zimmerman Residual Currents in the Western Dutch Wadden Sea, in *Residual Currents and Long-Term Transport*, edited by R.T. Cheng, pp. 93-104, Springer-Verlag, New York, 1990.

70 Robinson, I.S. Tidally Induced Residual Flows, in *Physical Oceanography of Coastal and Shelf Seas*, edited by B. Johns, pp. 321-357, Elsevier, Amsterdam, 1983.

71 Rubin, D.M. (1998). *Cross-Bedding, Bedforms, and Paleocurrents*, SEPM, Tulsa, Oklahoma.

72 Rubin, D.M. (2000). "Time-Lapse Movies of Migrating Bedforms." *Marine Sandwave Dynamics, International Workshop*, University of Lille, France.

73 Rubin, D.M., and R.E. Hunter (1985). "Why Deposits of Longitudinal Dunes Are Rarely Recognised in the Geologic Record." *Sedimentology*, 32, pp. 147-157.

74 Rubin, D.M., and R.E. Hunter (1987). "Bedform Alignment in Directionally Varying Flows." *Science*, 237, pp. 276-278.

75 Sankaranarayanan, S., and D.F. McCay (2003). "Three-Dimensional Modeling of Tidal Circulation in Bay of Fundy." *Journal of Waterway, Port, Coastal and Ocean Engineering*, 129(3), pp. 114-123.

76 Schlichting, H. (1968). *Boundary Layer Theory*, 747 pp., 6th ed., McGraw-Hill.

77 Shields, A. (1936). "Anwendung Der Ähnlichkeits-Mechanik Und Der Turbulenz-Furschung Auf Die Geschiebebewegung." *Preußische Versuchsanstalt für Wasserbau und Schiffbau*, 26.

78 Signell, R., and W.R. Geyer (1991). "Transient Eddy Formation around Headlands." *Journal of Geophysical Research*, 96(C2), pp. 2561-2575.

79 Signell, R.P., and C.K. Harris (2000). "Modelling Sand Bank Formation around Tidal Headlands." *Estuarine and Coastal Modeling, 6th Int. Conf.*, New Orleans, LA.

80 Simons, D.B., E.V. Richardson, and C.F. Nordin (1965). Bedload Equation for Ripples and Dunes, in *US Geological Survey Professional Paper 462-H*, pp. 9, Washington.

81 Sjödahl, M. (1994). "Electronic Speckle Photography: Increased Accuracy by Nonintegral Pixel Shifting." *Applied Optics*, 33(28), pp. 6667-6673.

82 Soulsby, R.L. (1997). *Dynamics of Marine Sands*, 249 pp., Thomas Telford.

83 Stride, A.H. (1963). "Current Swept Sea Floors near the Southern Half of Great Britain." *Q. J. Geol. Soc. London*, 119, pp. 175-199.

84 Ten Brinke, W.B.M., A.W.E. Wilbers, and C. Wesseling (1999). "Dune Growth, Decay and Migration Rates During a Large-Magnitude Flood at a Sand and Mixed Sand-Gravel Bed in the Dutch Rhine River System." *Special Publication of the International Association of Sedimentologists*, 28, pp. 15-32.

85 Van den Berg, J.H. (1987). "Bedform Migration and Bed-Load Transport in Some Rivers and Tidal Environments." *Sedimentology*, 34, pp. 681-698.

86 Van Lancker, V., J. Lanckneus, S. Hearn, P. Hoekstra, F. Levoy, J. Miles, G. Moerkerke, O. Monfort, and R. Whitehouse (2004). "Coastal and Nearshore Morphology, Bedforms and Sediment Transport Pathways at Teignmouth (U.K.)." *Continental Shelf Research*, 24, pp. 1171-1202.

87 Van Ledden, M., and Z.B. Wang (2001). "Sand-Mud Morphodynamics in an Estuary." pp. 505-514, *2nd Symposium on River, Coastal and Estuarine Morphodynamics Conference*, Obihiro, Japan.

88 Van Rijn, L.C. (1993). *Principles of Sediment Transport in Rivers, Estuaries and Coastal Seas*, Aqua Publications, Amsterdam.

89 Vanwesenbeeck, V., and J. Lanckneus (2000). "Residual Sediment Transport Paths on a Tidal Sand Bank: A Comparision between the Modified Mclaren Model and Bedform Analysis." *Journal of Sedimentary Research*, 70(3), pp. 470-477.

90 Wilbers, A.W.E., and W.B.M. Ten Brinke (2003). "The Response of Subaqueous Dunes to Floods in Sand and Gravel Bed Reaches of the Dutch Rhine." *Sedimentology*, 50(6), pp. 1013-1034.

91 Wilkinson, R.H., E.J. Moore, and A.P. Salkield Photogrammetry in Sediment Transport Studies, in *Underwater Photography and Television for Scientists*,

edited by J.D. George, G.I. Lythgoe, and J.N. Lythgoe, Clarendon Press, Oxford, 1985.

92 Willert, C.E., and M. Gharib (1991). "Digital Particle Image Velocimetry." *Experiments in Fluids*, 10, pp. 181-193.

Appendix A: Derivation of Frictional Torques

It will be proven that:

$$-C_D\left[\nabla\times\frac{|\mathbf{u}|}{H}\mathbf{u}\right]\bullet\hat{\mathbf{k}}=-C_D\frac{|\mathbf{u}|}{H^2}\left[\mathbf{u}\times\nabla H\right]\bullet\hat{\mathbf{k}}+C_D\frac{1}{H}\left[\mathbf{u}\times\nabla|\mathbf{u}|\right]\bullet\hat{\mathbf{k}}-C_D\frac{|\mathbf{u}|}{H}\zeta \qquad (A.1)$$

Note that the LHS may be written in the form *curl(f*A)*, where *f* and *A* are scalar and vector fields respectively. Now the vector calculus identity

$$\nabla\times f\mathbf{A}=\left(\nabla f\right)\times\mathbf{A}+f\left(\nabla\times\mathbf{A}\right). \qquad (A.2)$$

may be used to rewrite the LHS as

$$-C_D\left[\nabla\times\frac{|\mathbf{u}|}{H}\mathbf{u}\right]\bullet\hat{\mathbf{k}}=-C_D\left[\left(\nabla\frac{|\mathbf{u}|}{H}\right)\times\mathbf{u}\right]\bullet\hat{\mathbf{k}}-C_D\frac{|\mathbf{u}|}{H}\zeta , \qquad (A.3)$$

where ζ is the vorticity magnitude, $(\nabla\times\mathbf{u})\bullet\mathbf{k}$. The last term on the RHS of (A.2) is term III of (3.5) but the first term on the RHS still has to be broken up to complete the derivation. This is achieved by using the vector calculus product rule *grad(f*g) = grad(f)*g+f*grad(g)*, where *f* and *g* are scalar fields:

$$-C_D\left[\nabla\times\frac{|\mathbf{u}|}{H}\mathbf{u}\right]\bullet\hat{\mathbf{k}}=-C_D\left[\left(\frac{1}{H}\nabla|\mathbf{u}|+|\mathbf{u}|\nabla\frac{1}{H}\right)\times\mathbf{u}\right]\bullet\hat{\mathbf{k}}-C_D\frac{|\mathbf{u}|}{H}\zeta . \qquad (A.4)$$

Now the *grad(1/H)* needs to be broken up so the relative directions of the speed gradient and depth gradient can be seen. This is done by using the vector calculus chain rule:

$$\nabla f(g) = f'(g)\nabla g \,, \tag{A.5}$$

and thus rewriting (A.4) as

$$-C_D\left[\nabla \times \frac{|\mathbf{u}|}{H}\mathbf{u}\right]\bullet \hat{\mathbf{k}} = -C_D\left[\left(\frac{1}{H}\nabla|\mathbf{u}| - |\mathbf{u}|\frac{1}{H^2}\nabla H\right)\times \mathbf{u}\right]\bullet \hat{\mathbf{k}} - C_D\frac{|\mathbf{u}|}{H}\zeta \,. \tag{A.6}$$

Now it is evident that because the vectors of speed gradient and depth gradient point in opposite directions, when flow is around a shoaling headland (see Figure 3.3 (b,c)), they are added rather than subtracted. Expanding the [( ) ×$\mathbf{u}$] term on the RHS of (A.6) and using the cross-product identity $\mathbf{A} \times \mathbf{B} = -\mathbf{B} \times \mathbf{A}$ yields

$$-C_D\left[\nabla \times \frac{|\mathbf{u}|}{H}\mathbf{u}\right]\bullet \hat{\mathbf{k}} = C_D\frac{1}{H}\mathbf{u}\times \nabla|\mathbf{u}| \bullet \hat{\mathbf{k}} - C_D|\mathbf{u}|\frac{1}{H^2}\mathbf{u}\times \nabla H \bullet \hat{\mathbf{k}} - C_D\frac{|\mathbf{u}|}{H}\zeta \,, \tag{A.7}$$

which is equal to (A.1). In the special case of flow around a headland, the generated vorticities due to speed and slope torque are both positive.

Appendix B: Derivation of Bedform Associated Sediment Transport

A formulation for bedload transport from the migration of dunes may be derived as follows based on derivations from *Allen* [1985], and *Van den Berg* [1987]:

When the spatial gradient, q_b, of bedload transport at a point increases, the bed level, z, is eroded; conversely, when the spatial gradient of bedload transport decreases, the bed level is accreted. This is simply the continuity of mass law and may be expressed mathematically as:

$$\frac{\partial q_b}{\partial x} + \frac{\partial z}{\partial t} = 0 \qquad (B.1)$$
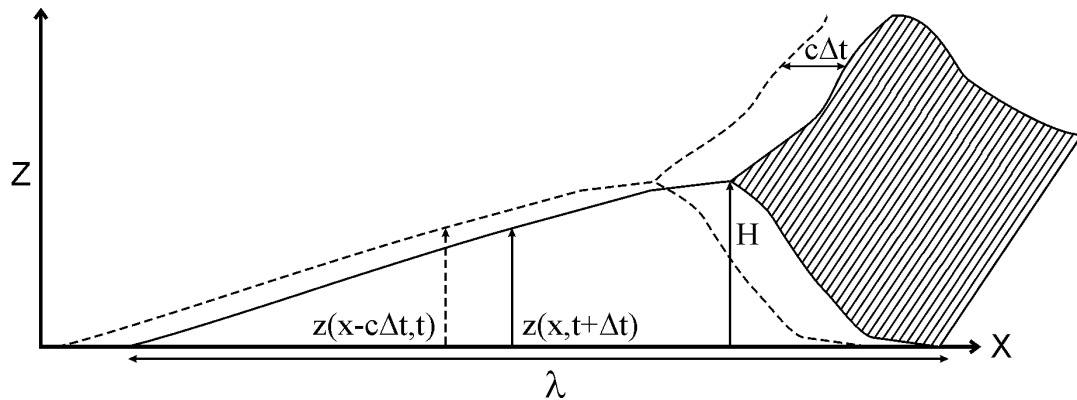

Figure B.1 Schematic diagram showing the migration of a dune with a migration rate c.

Where q_b is the volumetric bedload transport or, the volume of sediment transport per unit width of the bed per unit time [m^3/m/s]. Assuming undeformed propagation of the dunes at a migration rate ("celerity") of $c = \Delta x / \Delta t$ (Figure B.1) then:

$$z(x, t + \Delta t) = z(x - c\Delta t, t) \qquad (B.2)$$

This may also be expressed as:

$$z(x,t)+\frac{\partial z}{\partial t}\Delta t = z(x,t)-\frac{\partial z}{\partial x}\Delta x \qquad (\text{B.3})$$

Cancelling out common terms and substituting $\Delta x/\Delta t = c$:

$$\frac{\partial z}{\partial t} = -\frac{\partial z}{\partial x}\frac{\Delta x}{\Delta t}$$
$$\frac{\partial z}{\partial t} = -c\frac{\partial z}{\partial x} \qquad (\text{B.4})$$

Substituting (B.4) in to (B.1):

$$\frac{\partial q_{b,mig}}{\partial x} - c\frac{\partial z}{\partial x} = 0 \qquad (\text{B.5})$$

To calculate the bedload transport at a point, (B.5) is integrated to a variable x:

$$q_{b,mig}(x) = -c\int_0^x \frac{\partial z}{\partial x}dx = c\big(z(x)-z_{q=0}\big) \qquad (\text{B.6})$$

This gives the important, somewhat unintuitive, result that that the bedload transport rate at a point is linearly proportional to the elevation of that point above the level of zero bedload transport, $z_{q=0}$ (here taken to be the level of the trough). Since z cannot exceed the bedform height, H, the maximum local bedload transport rate over the dune is at the crest and is cH. Over a train of bedforms the bedload transport expressed as dune migration therefore varies in a spatially periodic way. The bedload transport rate over one dune wavelength (and therefore the bedload transport rate over a train of bedforms) results from the averaging of eqn. (B.6) over one dune wavelength, λ:

$$q_{b,mig} = \frac{1}{\lambda}\int_0^\lambda q_{b,mig}(x)dx = \frac{c}{\lambda}\int_0^\lambda (z(x)-z_0)dx = \frac{c}{\lambda}A = \frac{c}{\lambda}fH\lambda = cfH \qquad \text{(B.7)}$$

(B.7) evaluates to the volume per unit crest-length of the dune, or the cross-sectional area of the dune in Figure B.1 times the celerity. This area is proportional to the product of λ and H; the coefficient is the form factor, f, which, in the event of pure triangular dunes will be ½.

Curriculum Vitae

Candidate's full name: Garret Patrick Duffy

Universities attended: University of Dublin (Trinity College),
Dublin, Ireland,
September 1993 – April 1997,
B.A. (Earth Science);

University of Durham,
Durham, U.K.,
September 1998 – September 1999,
M.Sc. (Geophysics);

Refereed Publications:

Duffy, G.P., and J.E. Hughes-Clarke (2005). "Application of Spatial Cross-Correlation to Detection of Migration of Submarine Sand Dunes." *Journal of Geophysical Research - Earth Surface*, Special Section on Marine Dune and River Dune Dynamics, 110(F4), F04S12, 10.1029/2004JF000192.

Magazine Articles:

Duffy, G.P., and J.E. Hughes-Clarke (2004). "Application of Spatial Cross-Correlation to Detection of Migration of Submarine Sand Dunes." *Sea Technology*, October, pp. 53-57.

Conference Papers:

Duffy, G.P., and J.E. Hughes-Clarke (2005). "Bedform Celerity and Sediment Transport on a Banner Bank, Saint John, New Brunswick." 15 pp., *12th Canadian Coastal Conference*, Dartmouth, N.S. November 6 - 9.

Duffy, G.P., J.E. Hughes-Clarke, and R. Parrott (2004). "Application of Current Measurement and Time Lapsed Bathymetric Multibeam Surveying to Investigation of a Banner Bank, Mispec Bay, New Brunswick, Canada." pp. 72-78, *Marine Sandwave Dynamics and River Dune Dynamics II, International Workshop*, University of Twente, Enschede, The Netherlands, 1 - 2 April, S.H.O.M.

Conference Presentations:

Duffy, G.P., J.E. Hughes-Clarke, and D.R. Parrott (2005). "Bedforms and Associated Sand Transport on a Banner Bank, Saint John, N.B." *Geological Association of Canada - Mineralogical Association of Canada*, Halifax.

Duffy, G.P., J.E. Hughes-Clarke, and R. Parrott (2004). "Monitoring Change between Time-Lapsed Multibeam Surveys Using Spatial Cross-Correlation." *32nd International Geological Congress*, Florence, Italy, August 20 – 28.

Duffy, G.P., and J.E. Hughes-Clarke (2004). "Measurement of Bedform Migration Rate by Application of Spatial Correlation." *Canadian Hydrographic Conference*, Ottawa, ON.

Duffy, G.P., J.E. Hughes-Clarke, and R. Parrott (2003). "Monitoring the Temporal Behaviour of the Submarine Sand Dunes of Mispec Bay, Saint John, N.B., through Use of Monthly Multibeam Acoustic Surveys." *1st Joint Meeting, Geological Society of America North-eastern Section and Atlantic Geoscience Society*, Halifax, Nova Scotia, March 27-29.